Corrosion Behaviour of CoCrMo in Simulated Biological Environments

Blake John Thornley

Submitted in accordance with the requirements for the degree of

Doctor of Philosophy

The University of Leeds
School of Mechanical Engineering
Leeds, UK

June 2021

The candidate confirms that the work submitted is his own and that appropriate credit has been given where reference has been made to the work of others. The contribution of the candidate and the other authors to this work has been explicitly indicated below. The candidate confirms that appropriate credit has been given within the thesis where reference has been made to the work of others.

In the following papers listed, the primary author has undertaken all of the experimental studies, the evaluation of data, and the preparation and submission of the publications.

Papers contributing to this thesis:

- B. Thornley, A.R. Beadling, M. Bryant, A. Neville," Investigation into the Repassivation Kinetics of CoCrMo for Applications in a Simulated Biological Environment," NACE International, 2019

- B. Thornley, A.R. Beadling, M. Bryant, A. Neville," Investigation into the Repassivation Process of CoCrMo in a Simulated Biological Environment" Corrosion, 2020, 76(6), pp.539 – 552

- B. Thornley, A.R. Beadling, A. Neville, M. Bryant," Key Metal-Ion Protein Interactions Vital for Functional Total Joint Replacement Biomedical Interfaces," Submitted to Scientific Reports

- B. Thornley, A.R. Beadling, A. Neville, M. Bryant," Electrochemical, Chemical and physical interactions of phosphates and BSA with CoCrMo biomedical alloys," Submitted to Electrochemica Acta

Acknowledgements

First and foremost, I am incredibly grateful to my PhD supervisors, Dr Michael Bryant, Prof Anne Neville, and Dr Andrew Robert Beadling. The work would not be what it is today without their invaluable support and tutelage. I would like to extend my thanks to several staff members who aided in the production of this research: Dr Benjamin Johnson (XPS), Dr Chun Wang (AFM), John Harrington (FIB), Dr Zabeada Aslam (TEM), Stuart Micklethwaite (SEM) and Dr Adrian Cunliffe (ICP-MS). I would also like to thank my partner Anna for her constant support and listening to countless presentations. Lastly, I would like to thank my parents and brother for their encouragement and support during my time in Leeds.

Abstract

A proven treatment for patients suffering from musculoskeletal issues is orthopaedic surgery. Metal-on-metal devices have been popular over the last 50 years due to low wear rates and excellent corrosion resistance. However, due to recent findings of metal dissolution into the body, their subsequent use has been in decline and are barely used today. This leads to adverse effects within the patient as well as weakening the structural integrity of the alloy. Understanding the mechanisms behind this phenomenon are vital to improving the functionality of these implants as due to their low wear rates they are viable for the ever-growing younger population who require an implant.

A thorough investigation into the electrochemical behaviour of cobalt-chromium-molybdenum alloys in simulated bodily fluids has been undertaken, looking in detail at the specific interactions that bovine serum albumin has with the alloy. A range of electrochemical and surface characterisation techniques were adopted to undertake this research. Analysis of the electrolyte post-test was also conducted to determine the dissolution of the alloy under specific conditions.

Obtained results have indicated that the presence of inorganic/organic species affects the corrosion resistance and dissolution of the metal. The presence of bovine serum albumin has been shown to be two-fold: it can inhibit the access of oxidants to the alloy leading the adsorbed organic layer/passive film to be weaker, increasing the corrosion rate but can alter the passive film due to the molecule being a cathodic inhibitor increasing the resistance of corrosion in the passive domain. During an electrochemical repassivation phase, the presence of bovine serum albumin is seen to inhibit the repassivation rate alongside altering the composition of the reformed passive film and ratios of metallic ions released into the environment. The affinity of bovine serum albumin with molybdenum has been identified to be due to the formation of a highly thermodynamically favoured Mo-S bond.

From the findings presented, a clearer understanding of the electrochemical interactions that take place within the body have been obtained. This is crucial for further understanding and predicting in-vivo performance.

Table of Contents

List of Tables

List of Figures

List of Equations

Nomenclature

AES	Auger Electron Spectroscopy
AFM	Atomic Force Microscopy
ARMD	Adverse Reactions to Metal Debris
ASTM	The American Society for Testing and Materials
CD	Circular Dichroism
CoCrMo	Cobalt Chromium Molybdenum
EDX	Energy Dispersive X-Ray Spectroscopy
EELS	Electron Energy Loss Spectroscopy
FCC	Face Centred Cubic
FDA	Food and Drug Administration (USA)
HC	High Carbon content
HCP	Hexagonal Close Packed
HFM	High Field Model
HNSS	High Nitrogen Stainless Steel
ICP-MS	Inductively Coupled Plasma-Mass Spectroscopy
LC	Low Carbon content
MHRA	Medicines and Healthcare products Regulation Agency (UK)
M	Metal
MoM	Metal-on-Metal
NaCl	Sodium Chloride
NMR	Nuclear Magnetic Resonance
M_w	Molecular Weight
PDM	Point Defect Model

ROS	Reactive Oxygen Species
SEM	Scanning Electron Microscopy
THR	Total Hip Replacement
TJR	Total Joint Replacement
WLI	White Light Interferometry
XPS	X-Rat Photoelectron Spectroscopy

Protein Terminology

Ala	Alanine
Asp	Aspartate
BSA	Bovine Serum Albumin
His	Histidine
HSA	Human Serum Albumin
MBS	Multi Ligand Binding Site
NTS	Nitrogen Terminal Site

Electrochemistry

Θ	Area Fraction Covered by Oxide
A	Area Exposed to the Electrolyte
a_p	Activity of the Products
a_r	Activity of the Reactants
c	Dissolution Rate
C	Capacitance
C_{dl}	Double Layer Capacitance
CE	Counter Electrode
CPE	Constant Phase Element
d	Thickness of the Film
ε	Relative Dielectric of the Film

ε_0	Permittivity of the Vacuum
E^o	Standard Cell Potential
E_0	Potential of the Amplitude of the Wave
E_a	Activation Energy
E_b	Breakdown Potential
E_{cell}	Potential Difference between a Cell
E_{corr}	Corrosion Potential
Epp	Passivation Potential
Er	Repassivation Potential
EAS	Electrochemically Active Species
EDL	Electric Double Layer
EIS	Electrochemical Impedance Spectroscopy
EMF	Electromotive Force
$E(t)$	Sinusoidal Potential
F	Faradays Constant
ΔG^o	Gibbs Free Energy Change
ΔG_{red}	Gibbs Free Energy Change at Equilibrium
h	Planck's Constant
ΔH^o	Change in Enthalpy
$\Delta H^{\ddagger}$	Change in Activation Enthalpy
i_{corr}	Corrosion Current Density
i_0^{diss}	Dissolution Exchange Current Density
i_{film}	Rate of Film Growth
$I(t)$	Sinusoidal Current
K	Equilibrium Constant

L_{ss}	Steady State Film Thickness
n	Valence of the Ion
N	Avogadro's Number
OCP	Open Circuit Potential
ρ	Density of the Film
R	Ideal Gas Constant
R_{ct}	Charge Transfer Resistance
R_s	Resistance of the Solution
RE	Reference Electrode
ΔS^o	Change in Entropy
$\Delta S^{\ddagger}$	Change in the Activation Enthalpy
SHE	Standard Hydrogen Electrode
T	Temperature
v	Total Volume of Oxide to Grow
ω	Radial Frequency
W	Warburg Diffusion
WE	Working Electrode
Z	Impedance

Tribocorrosion

α	Asperity Factor
β	Abrasive Asperity
C	Material Lost only to Corrosion
H	Hardness
S	Synergy due to Wear and Corrosion
ΔS_w	Contribution to the Synergy due to Wear
ΔS_c	Contribution to the Synergy due to Corrosion

T	Total Material Lost to Tribocorrosion
V_{chem}	Volume of Material Lost to Corrosion
V_{mech}	Volume of Material Lost to Mechanical Wear
V_{total}	Total Volume of Material Lost

Chapter 1
Introduction

1.1 Motivation

Total joint replacement (TJR) consists of substituting a human joint with an artificial device, which is needed as a long-term solution for arthritic and congenital diseases. These devices have been used consistently since the 1950s, with advancements in technology now putting TJR as being one of the most successful surgical procedures in the modern age.

The National Joint Registry for England, Wales, and Northern Ireland (NJR) reported that there were over 95,000 primary hip replacements conducted within 2019, with osteoarthritis accounting for 90% of these replacements [1]. This disease is the most common form of joint arthritis and disability, mainly involving the knee and hip joints. It leads to joint pain, stiffness, and inhibition to movement by affecting all of the joint structures, including the synovial membrane, cartilage and bone [2]. Currently, in the UK, about 8.5 million people are living with this disease [1,2].

Metal-on-metal (MoM) implants have come under scrutiny in recent years due to the accelerated release of metal ions into the patient, which stems from mechanical abrasion and corrosion of the surface, exposing the extremely reactive bulk alloy [3]. This can then lead the material to degrade over the lifetime of the implant, which can have adverse effects on the patient as the degraded products may adversely react with the patient alongside weakening the integrity of the implant [4]. These effects were noted in 2010 by the regulatory agencies in the UK (MHRA) and USA (FDA), with alerts being issued and the subsequent usage of these bearings being in decline since 2012 [5,6].

1.2 Aims and Objectives

This doctoral thesis investigates the corrosion behaviour of the biomedical alloy cobalt-chromium-molybdenum (CoCrMo) in a protein containing environment. This involved an extensive electrochemical study of the alloy alongside post-test surface analysis to understand further the surface chemistry and interactions that occur.

Electrochemical characterisation of the alloy was undertaken to be able to understand the effect of specific species (inorganic, organic) and varying conditions that the alloy could be exposed to. Post-test surface characterisation was used primarily to investigate changes to the passive film, which gives the alloy its corrosion resistance, and how specific species interact with the surface of the alloy. By relating these findings to the electrochemical data, a deeper understanding of the prevailing mechanisms was reached. The key emphasis was placed upon the corrosion products from CoCrMo and how they interact with the protein-containing environment.

Specific objectives were as follows:

- Investigate how the presence of Bovine Serum Albumin affects the morphology, corrosion behaviour and dissolution rates of CoCrMo under specific electrochemical conditions (cathodic, passive, and trans-passive).
- Utilise surface characterisation techniques to compare a CoCrMo passive film's composition and protectivity before and after an electrochemical repassivation phase.
- Characterise the binding interactions between Bovine Serum Albumin and the metal ions of CoCrMo, relating the findings to the dissolution data enabling the affinities of each metal ion protein interaction to be determined.

1.3 Structure of the Thesis

This thesis consists of 9 chapters, including this introductory chapter. **Chapter 2** contains an extensive review of the corrosion process with supporting literature concerning the application of biomaterials with a specific focus on CoCrMo alloys. The materials and experimental methodology for the research undertaken are presented in **Chapter 3**. The following chapters present the experimental work carried out throughout this project: **Chapter 4** presents the electrochemical study of CoCrMo, **Chapter 5** displays physical and chemical changes to the surface of CoCrMo after electrochemical testing, **Chapter 6** characterises the quantity of metal ion dissolution from CoCrMo under specific conditions, and **Chapter 7** quantifies the bonding interactions between CoCrMo and Bovine Serum Albumin. These chapters present the experimental findings as well as discussing the findings and giving concluding remarks. **Chapter 8** brings all the results chapters together, discussing the

findings obtained and critiquing with the literature. **Chapter 9** presents the main conclusions of this project, general limitations to the conducted work and suggests possible further work.

Chapter 2
Literature Review

This literature review aims to give a critical overview of the essential components associated with this research. The fundamentals of corrosion will be explained, followed by the design and history of the hip replacement. Specific emphasis will be placed upon the CoCrMo alloy used, covering in detail the passive film's role, the effects of alloy degradation, and the alloy's interaction with its surrounding environment.

2.1 Introduction

Throughout history, materials have been utilised to help treat the human body. The earliest noted reports date back to the Egyptians and Roman times, where linen was utilised for sutures with gold and iron used in dental applications [7]. Due to incredible advancements in technology in the last century, biomaterials have enhanced the life quality of people across the globe, ranging from alterations to the muscular and skeletal systems to the insertion of stents to reopen blocked passageways within the body. Figure 2.1 summarises the major applications of biomaterials today, with there currently being over 50 different materials in a variety of different devices [3].

Biomaterials are defined as any synthetic or natural materials that are expected to be in contact with living tissue or a biological environment [3,7]. Today these materials can generally be classified into four main groups: metals, ceramics, polymers and engineered composites (a combination of two or more of the previous groups). The most important feature of a biomaterial is its biocompatibility, which is the ability of the material to perform its desired function without inflicting any undesirable local or systematic issues within the body [7]. The application of the device and its required properties are vital in determining which material the device should be made of.

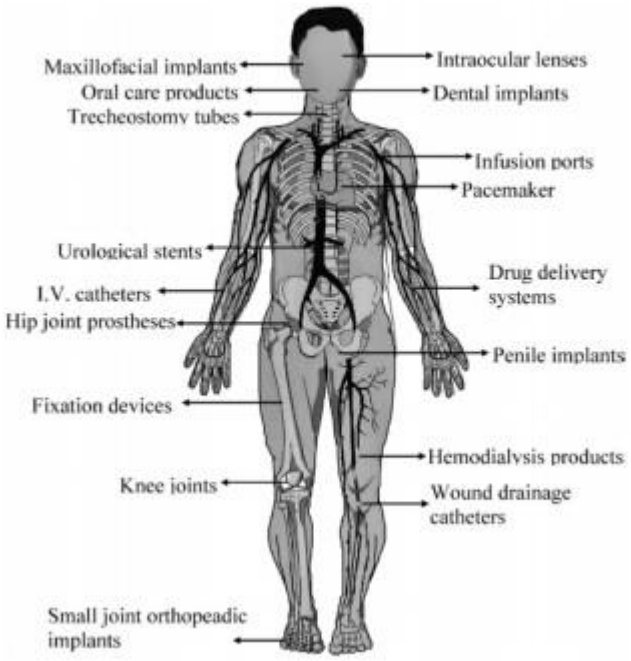

Figure 2.1 The major applications of biomaterials within the human body [3]

2.2 The Hip

2.2.1 General Background

The natural hip consists of the femur head, which articulates against the acetabular cup within the acetabulum. For a motion to occur smoothly, cartilage forms the surface between the acetabular cup and femoral head, lowering friction and acting as a shock absorber due to its elastic nature. Arthritis affects this layer of cartilage, making it weaker and thinner by either a degenerative process (osteoarthritis) or inflammation of the synovial membrane (rheumatoid arthritis) [2]. If a specific part of the joint is damaged, repairs to that particular area could be undertaken.

A hip replacement is needed when the joint has become damaged to the point at which motion is painful or limited; this can be from arthritis, osteolysis, deformation or an injury. In this situation, the damaged joint is entirely removed and replaced with a prosthesis, commonly referred to as total hip replacement (THR).

Annually there are around 200,000 total hip and knee replacements carried out in England and Wales alone, which typically have a lifespan of between 10 – 15 years [1]. Approximately 58% of these replacements occur in women, with the leading causes being osteoarthritis and obesity [1]. There has been a drastic rise in the need for a hip replacement in people aged under 60; demand has risen by 76% over the last decade in England, with the numbers rising from 10,000 to 18,000 [8]. S. Kurtz et al. [9] predicted in 2009 that the projected relative proportion of the younger patient population could rise to between 50-55% for both primary hip and knee replacements by 2030, with projected revision rates for hip replacements being 35% whereas for knee revision it is ~60% (Figure 2.2). Revision surgery is known to be a highly complex procedure with a higher rate of intraoperative fractures in comparison to initial implantation placing a higher urgency on the need of developing safer longer-lasting implants which are better functioning due to increased activity of the joint [10,11].

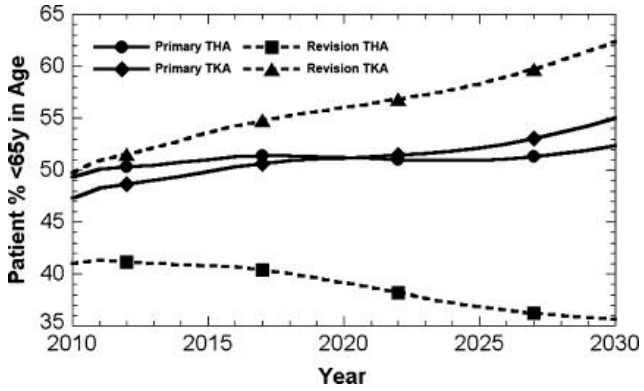

Figure 2.2 Indicates projections for the increases in patients under 65 that would require a hip/knee replacement or revision to an existing joint replacement [9]

2.2.2 Medical Procedure for Total Hip Replacement

For THR, the damaged head of the femur is removed with a metal stem being inserted into the hollow centre of the femur; this is either cemented or done via a place fit [12]. On top of this inserted metal stem, either a metal/ceramic ball is attached, which acts as the femoral head [10,12]. A metal socket replaces the acetabulum with a spacer (metal, plastic, ceramic), enabling

smooth movement between the surfaces [12]. For a metal-on-metal device, both the ball and socket components are made from metal.

The correct counter face, combination of materials, finish of the surface, diameter of the femoral head, and clearance are important features to minimise the implant's friction, wear, and corrosion within a patient [10].

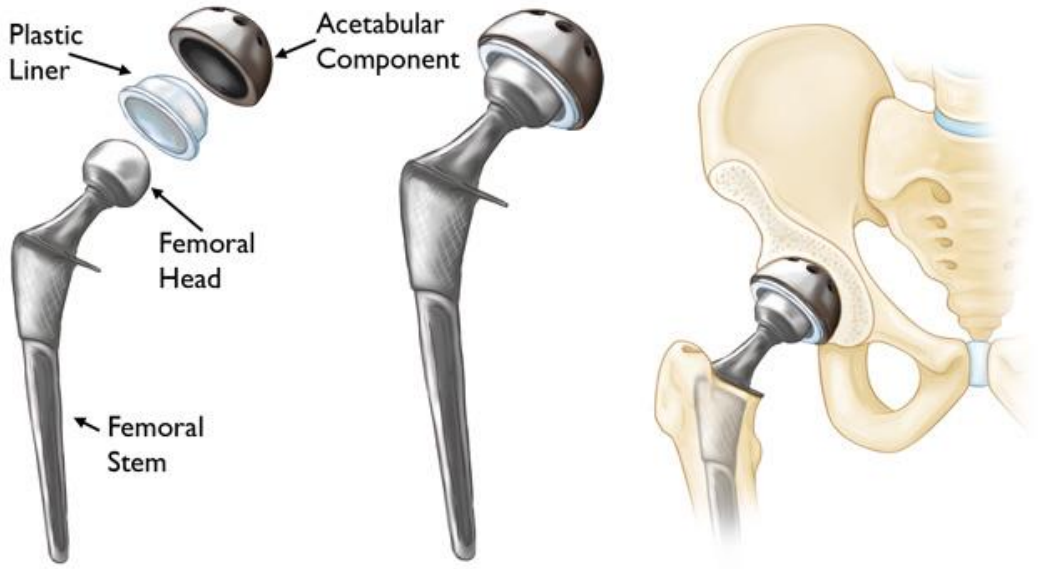

Figure 2.3 Shows the components of an artificial hip replacement [12]

2.2.3 Timeline of Total Hip Replacements

Since the first reported hip replacement was undertaken by Glück in 1891, which comprised of a ball and socket joint made of ivory, there have been many iterations of the prosthetic replacement utilising different materials [13]. Examples of the possible combinations are indicated in Figure 2.4.

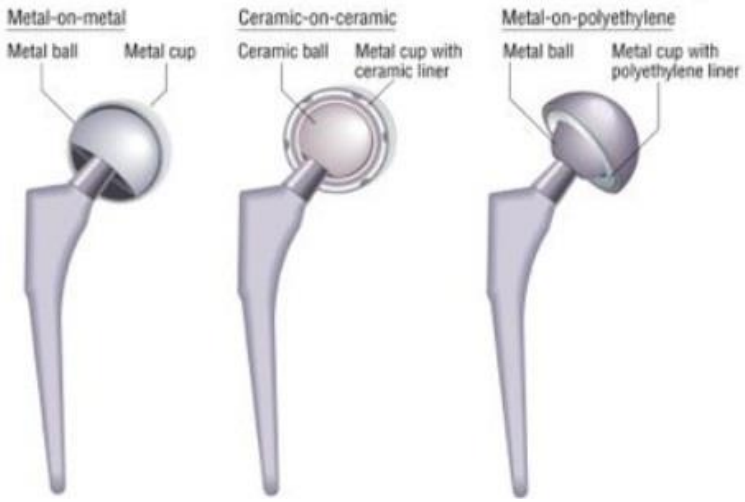

Figure 2.4 Depicts the different hip replacement combinations that have been used [14]

2.2.3.1 First Gen Metal-on-Metal

The English surgeon, G.K McKee, was the first person that regularly used metal on metal prosthesis [15]. In 1953, he modified the Thompson stem (a hemiarthroplasty used for fracture treatment), so it consisted of a new acetabulum of cobalt-chromium [13]. The model didn't perform as desired, though, the first series obtained a 10% failure rate by four years [15]. P. Ring built upon McKee's initial model but didn't use bone cement to hold the joint in place [16]. Early results for this model were not promising either though, displaying the same problems as the first model with the main cause of failure for these joints being loosening of components and the release of wear particles [15,16].

2.2.3.2 Metal-on-Polymer

In the 1960s, the materials and techniques for a hip replacement saw some advances due to J. Charnley [13]. He managed to develop a low friction device that was made up of a metal femoral stem with a polytetrafluorethylene (PTFE) component, which was used for seating the joint in place by acrylic bone cement [17]. There were also some slight design alterations, with the size of the femoral head being reduced to minimise the amount of wear the device would endure in its lifetime [17]. This design has been hailed as the 'gold standard' for THR and is still heavily used to this day [13].

The polyethene cup is seen as an issue for the replacement, with debris being released into the body and limiting the lifetime of the replacement [13]. The size of the debris particles were mainly sub-micron which led to immunological effects within the body [17].

2.2.3.3 Ceramic-on-Ceramic

This type of implant was introduced by the French surgeon Pierre Boutin in 1970 and was mainly used throughout central Europe. Ceramic was introduced to help address issues of friction and wear that occurred with other popular materials at this time; for orthopaedics, the ceramic consisted of either alumina or zirconia [13].

The ceramic-based implant was a good choice for active young patients due to the low wear rate. Riska et al. [18] conducted tests amongst 143 patients with these implants and noted no wear-related issues. Other known benefits are the high level of hardness of the implant, its resistance to scratches and the inert nature of its debris compared to metal or polymer. However, these implants are very expensive and require excellent surgical insertion technique as the contact surfaces are prone to chipping, which can lead to devastating wear of the implant [13].

2.2.3.4 Second Gen Metal-on-Metal

Metal-on-Metal joints made a comeback over the last 40 years due to there being a drastic need for a longer-lasting implant as more and more younger people are requiring an implant alongside the growing life expectancy of the population. The second-generation devices were produced from surgical grade CoCrMo due to their resistance to corrosion, biocompatibility, and low wear rates [19]. There are still many issues surrounding these implants, though, with metal ions being released from the alloys over time. This leads the material to degrade over the lifetime of the implant, which can have harmful effects on the patient, as the structure of the implant becomes compromised, and the degraded products may react adversely with the patient [13]. These effects were noted in 2010 by the regulatory agencies in the UK and USA, with alerts being issued and the subsequent usage of these bearings being in decline since 2012 [5,6].

2.2.3.5 Present Day

The NJR documented that there were almost 100,000 hip replacements issued during 2019, primarily being performed on females (~70%), with the average age being 69 [1]. A comparison of implant popularity since 2003 (Figure 2.5) indicates that the most common bearing for THR is Metal-on-Polyethylene [1,13]. There has been a steady rise in the quantity of Ceramic-on-Polyethylene (CoP) implants being used, which correlates to the decrease in Ceramic-on-Ceramic (CoC). The CoP consists of a ceramic femoral head with a polyethene acetabular, removing the squeaking sound and the fragility aspect of the CoC [20,21]. However, within the literature, this choice is seen as controversial, with CoC possessing lower wear rates [21,22]. As expected, the use of MoM hip replacements after initial findings of adverse effects (2008) declined and are barely used today [5,6].

a)

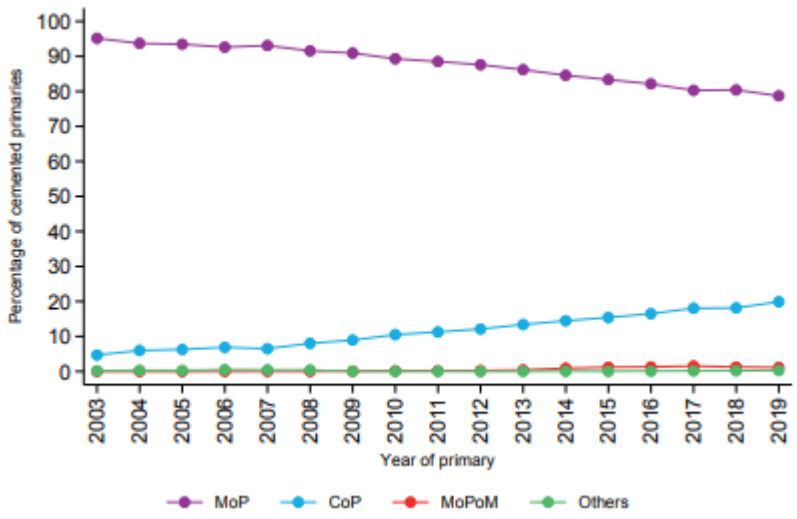

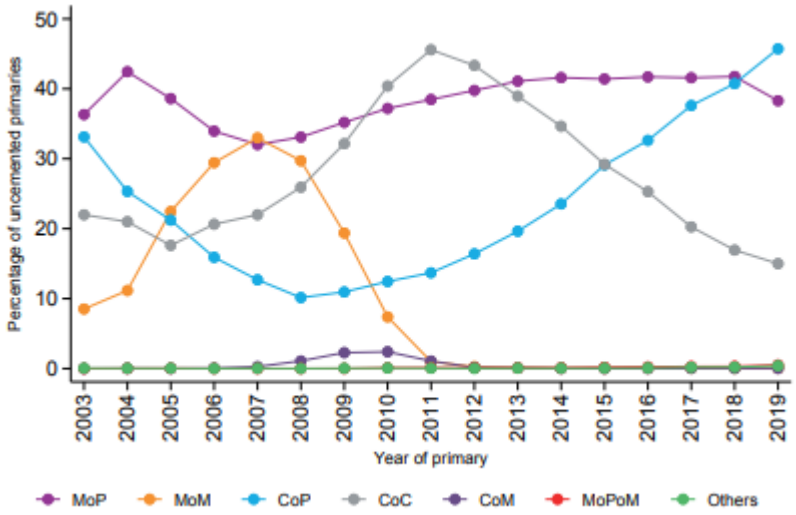

Figure 2.5 Temporal changes to the bearing surface of a hip replacement (a) Cemented Fit (b) Uncemented Fit [1]

2.3 Metals used in Hip Replacements

Metals are commonly used as biomaterials and are essential for orthopaedic implants due to their ductility, biocompatibility, and their high resistance to static/dynamic loads [23]. As the most vital qualities are its biocompatibility and its corrosion resistance, the most popular alloys used within the human body are Cobalt-based alloys, Iron-based alloys, or Titanium alloys. Alloys are usually used over pure metals as the mechanical properties are enhanced [24].

2.3.1 Cobalt-based alloys

Alloys of cobalt have been utilised in the fabrication of prostheses since the 1940s as they are regarded as highly biocompatible materials that possess excellent wear and corrosion resistance which is in part due to their passive nature [23,24]. Cobalt-based alloys are generally termed austenitic due to the high-temperature Face Centred Cubic (FCC) phase being stable at room temperature. However, due to the relatively low stacking fault energy of the alloy have been known to convert to Hexagonal Close Packed (HCP) when under applied stress/strain [25]. Z. Wang [26] observed different processed CoCrMo with XRD and TEM, finding that mechanically polished samples primarily exist in the FCC phase. Multiple sources have also indicated the role

shear plays in this re-orientation, stating that it can enhance the alloys tribocorrosion properties [27,28].

Other refractory metals (molybdenum, tungsten) are combined with cobalt to provide strengthening, aid the development of carbides, and enhance the alloys corrosion resistance [25]. The main cobalt-based alloy used within orthopaedic surgery is cast CoCrMo (Co 58 – 70%, Cr 27–30%, Mo 5–7%), which is favoured over wrought processed due to the complicated nature of the shapes, which cannot be machined [29]. The CoCrMo alloy is known to have excellent corrosion resistance, which is owed to its passive film properties. I. Milosev et al. [30] observed this layer using XPS, which spontaneously forms in air noted it to primarily consist of Cr_2O_3 with small contributions from Co and Mo oxides. Two distinct types of this CoCrMo exist which are based on their respective carbon levels: HC CoCrMo (High carbon content 0.05-0.35 wt.%) and LC CoCrMo (Low carbon content <0.05 wt.%) [24]. Different types of carbides are formed depending on this carbon content and the fabrication method of the alloy, including M_7C_3, M_2C and M_6C (M is the metal) [31]. The formation of extra carbides is desired when designing for sliding bearing surfaces as they provide further strengthening [24]. E. Benttini [32] observed carbide clusters on polished CoCrMo using AFM with a size of 30 – 40 μm with heights up to 50 nm.

2.3.2 Iron-based alloys

Stainless steels have been used in orthopaedics since the mid-1920s, with their biocompatibility within the body being proven for almost a century [33]. They are desirable due to a favourable combination of mechanical properties, corrosion resistance and cost-effectiveness [33,34].

For the majority of the last century, Stainless steel (UNS SS316L) was at the forefront of iron-based alloys used in orthopaedics due to its good mechanical properties, easy processing, and low cost [35,36]. Issues arose in these implants due to being denser and having higher elastic modulus compared to bone, leading to incompatibility of strength inducing stress [35]. These days the most commonly used iron-based alloy is HNSS (High Nitrogen Stainless Steel). Yamamoto et al. [37], was the first to develop this alloy by nitrogen adsorption treatment and observed a higher level of cytocompatibility than the 316L. Nitrogen was used to strengthen the mechanical and corrosion properties of the alloy whilst also replacing nickel. This was vital as the release

of nickel within the body causes inflammation and can lead to allergic reactions [35,36].

All variations of stainless steel alloys must contain a minimum of around 11% of chromium, as this is the amount needed to form a stable chromium oxide layer which gives the alloy is corrosion resistance [34]. With other elements being added depending on the required characteristics. A recognised flaw in stainless steel implants is that they are much more susceptible to crevice and pitting corrosion than other types of metal-on-metal joint, leading to high volumes of material loss from the alloy [33].

2.3.3 Titanium alloys

Titanium alloys are a more recent development, first being used as prostheses in the 1970s. Wilert et al. [38] defined these alloys as the choice of material for femoral based stems in 1996 due to their superior mechanical properties and biocompatibilities. Unlike the other alloys mentioned previously, they owe their corrosion resistance to the formation of a TiO_2 passive film (10 nm). Although these alloys have a lower modulus of elasticity which enhance their corrosion resistance due to lower shielding effects, the wear resistance of the alloys is much lower than that of the other alloys [39]. This is due to the poor shear strength and softness of the Ti metal, making it undesirable for load-bearing implants [39].

The two main titanium alloys currently in use are the commercially pure titanium (ci Ti) and Ti_6Al_4V, being utilised as replacements for hard tissue, e.g. artificial bones and dental implants [40]. The presence of aluminium and vanadium is needed to stabilise both the alpha and beta phases but has shown to possess issues with long term implants due to the presence of vanadium which has been shown to be extremely toxic [34,40].

2.3.4 Degradation of Metal implants within the body

Corrosion of metal implants within the body is of great concern as it leads to increased local concentrations of metal ions in the soft tissue around the implant [4,25]. Corrosion of the implant can cause fractures to occur more readily, which in turn accelerate ion release due to an increase in the surface area [7]. This is of particular concern to younger patients as they can be exposed to increased levels of metal ions for longer periods of time.

The toxicity of metals has been known throughout history, with both the Greeks and Romans recording both of benefits and toxic effects they possess.

Some metals that have been documented as carcinogenic in both humans and animals are as follows: Cobalt, Chromium, Copper, Nickel, Arsenic, Nickel and Cadmium [41]. Some metals such as Iron, Lead, Titanium and Zinc have been noted to induce tumours [41]. The extent and dose of exposure as well as the form of the metal determine the clinical consequence. There is a wide range of mechanisms that metal toxicity can undergo, including inhibiting enzymes, production of free radicals, disruption of cell function\structure as well as mutagenesis. Generation of reactive oxygen species (ROS) formed via detoxification mechanisms within the body may lead to damage of tissue which leads to the development of degenerative diseases such as cancer [41].

Wear of the implant is a different process which can also lead to metallic debris entering the body, which can have added detrimental effects to the patient. Catelas [42] determined the average size of wear debris from CoCrMo alloys was around 50 nm in length, predominantly being oval-shaped and consist of chromium (III) oxide. Patients with adverse reactions to metal debris (ARMD) typically have pain and pseudotumors, which can lead to antalgic gait (unnatural movement to avoid pain) [43,44]. Pseudotumors are either granulomatous, or cysts that develop in close proximity to the implanted alloy, an example of a cystic lesion around a hip replacement is shown in Figure 2.6 [44,45]. Over time the implant may become unstable with/without dislocation and need to be replaced; this is a unique mode of implant failure due to the associated soft tissue issues [43,44]. Matharu et al. [46] investigated the cause of 180 MoM hip replacements and determined that 61.7% of all revisions were due to the presence of pseudotumor which formed due to the presence of both wear and corrosion.

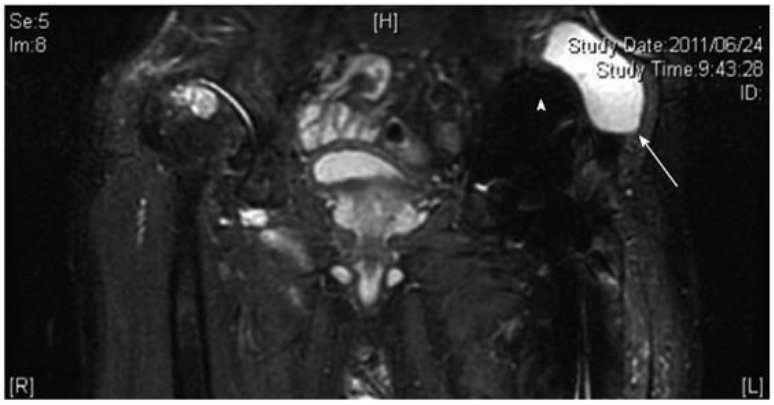

Figure 2.6 Indicates the formation of a cystic lesion within a male patient by use of Coronal short tau inversion recovery magnetic resonance [45]

As this research is focused around CoCrMo alloy's, more specific detail of the possible metal elements that could corrode into the body is discussed in the following sections to fully understand the interactions that metal ion dissolution can have on the patient.

2.3.4.1 Cobalt

Cobalt is vital for life, being a key component within Vitamin B12 which facilitates the production of healthy red blood cells. Although it is present naturally within the body, it is only present in extremely small quantities (1-2 mg) [47]. Metal ion dissolution from a CoCrMo alloy can disrupt this balance and lead to cobalt poisoning (>10 ug/l), leading to fever and inflammation [48]. Reports have shown that cobalt can bind strongly to proteins and cells, disrupting their natural process and behaving as a potential carcinogen seeing as it inhibits the repair of damaged DNA [49,50].

2.3.4.2 Chromium

Chromium is a naturally occurring heavy metal that exists primarily in its trivalent form, Cr(III) or hexavalent form Cr(VI). In its trivalent form, it has been shown to possess a weak affinity for cells, preferring to bind to proteins instead [34]. The hexavalent form has the opposite binding preference, as it has been shown to easily pass the membranes of cells but has a very weak binding affinity for proteins due to a lack of a specific binding site [50,51].

Naturally, due to wear and corrosion of the implant Cr(III) will be released into the body, as this is the primary constituent of the passive film [52]. This form of chromium has a relatively low toxicity level and is not considered carcinogenic [52]. However, the presence of high oxidising potential and low pH can lead to the oxidation of the trivalent form into the hexavalent. This form is of particular interest as its highly toxic and classed as a class I carcinogen [51]. Exposure to this ion can lead to various mutations in DNA and chromosomal damage [51,52].

2.3.4.3 Molybdenum

Biologically, molybdenum occurs as a trace metal within animals and plants, where it is essential in some enzymes as it acts as the metal hetero-atom within active sites. It is a transition metal that is capable of forming a wide range of oxidation states (II-VI). In humans, a low order of toxicity has been observed, but if levels are increased, then it can interfere with the body's copper uptake [53]. This occurs due to molybdenum preventing plasma

proteins from binding to copper and therefore increasing the amount of copper expelled by the body [53].

2.3.4.4 Electronic Properties

All of the three elements (Co, Cr, Mo) are located within the d-block of the periodic table, meaning they are categorized via their d orbitals (Figure 2.7). Elements within this part of the periodic table can exist in many different oxidation states due to the low energy gaps between transitions [54]. Configurations for the most common oxidation states of the elements in concordance with Aufbau's principle and Hund's rules are as follows : Co^{2+} [Ar] $3d^7$, Cr^{3+} [Ar] $3d^3$, Mo^{6+} [Kr].

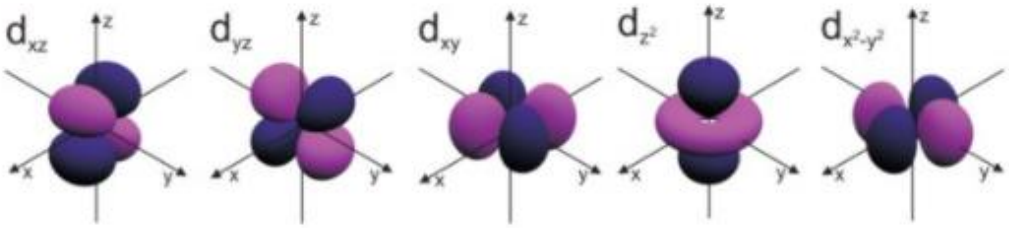

Figure 2.7 The orbital configurations for the d-block elements [55]

A compound is at its most stable when in accordance with the 18-electron rule, so upon release from the implant, the metal ion undergoes interactions with ligands. A ligand is defined as a molecule/ion that complexes to a metal ion, forming a co-ordination complex (Lewis base forms a dative bond, Lewis acid accepts an electron pair) [56]. The coordination of the ligands around the metal ion is governed by the size of the metal ion, steric hindrance between ligands and the interactions between the metal ion and the ligand [56]. These are key features that need to be considered when describing the metal–protein interactions. The most common co-ordinations are described in Table 2.1.

Table 2.1 Typical co-ordination structures for metal complexes

Shape	Co-ordination number	Bond Angle	Key Point	Example
Tetrahedral	4	109.5°	Common for d^0 and d^{10} ions	$[MoO_4]^{2-}$
Square Planar	4	90°	Typically seen for ions with a d^8 configuration	$[Ni(CN)_4]^{2-}$
Trigonal Bipyramidal	5	90°, 120°	Formed in the absence of ligands that enforce geometry	$Fe(CO)_5$
Octahedral	6	90°	Most common arrangement for metal complexes	$Mo(CO)_6$

2.4 Biological Environment

By looking at the environment of the implanted materials, it is easier to understand why the alloys undergo corrosion when implanted. The human body is mainly a saline aqueous environment that exists at approximately 37°C. Almost all of the mass of the body is made up of just six elements: Carbon, Hydrogen, Oxygen, Nitrogen, Calcium and Phosphorous. There is a complex mix of organic compounds, ions, and dissolved gases within the body, which vary depending on location [25]. Other bodily compounds that are known to affect in-vivo metals are chlorides, phosphates, and sulphates.

Body pH has been noted to fluctuate with respect to location and circumstance. For orthopaedics, the general pH ranges from 6.8 to 7.8 but has been seen to drop to as low as 4 when inflammation occurs [25,57]. Due to the acidic nature, this drop can induce trans-passive conditions, which leads to a higher rate of metal ion release as the passive film breakdowns [57].

2.4.1 Synovial Fluid

The native hip joint is encapsulated via a synovial membrane which generates synovial fluid. The role of this adhesive, non-Newtonian fluid is to heavily reduce friction during motion and provide stability by acting as a ‘seal’ alongside transporting nutrients to the hip [58]. This fluid is comprised of plasma, the same matrix as blood, which is non-cellular and is formed of around 95% water, with the remaining 5% being owed to hyaluronic acid, lubricin, proteinases and collagenases [25].

Following THR, a motion-induced pseudo synovial membrane generates between the bone and implant [59-61]. M. Kung [61] determined that the cells of the re-formed membrane were consistent with that of the original membrane. The produced fluid has comparable protein levels but was found to be less viscous [60,61]. However, this fluid allows for the successful functioning of the implant.

Human serum albumin (HSA) is the most abundant protein present in the fluid and therefore plays a great role in the environment/surface interactions of the implants [49,50]. This is due to its high mobility and concentration, so according to the laws of mass transportation, this protein arrives first at the metal implant, therefore, playing a key role in initial adsorption [62]. Albumin is a small globular protein that consists of 585 amino residues which are folded via the polypeptide chain giving the molecule three α-helical domains (I, II and III) [63,64]. Each domain is formed of two subdomains (A and B), with the molecule being cross-linked with 17 cystine residues; this occurs through eight disulfide bonds (one free thiol group). This protein displays a predominantly α-helical structure (74%), with the rest of the polypeptide occurring as turns within regions between subdomains and flexible regions [65]. A ribbon model of albumin displaying all of the domains and subdomains is shown in Figure

2.8. The principal cavities for ligand binding are located in subdomain IIA and IIIA [63].

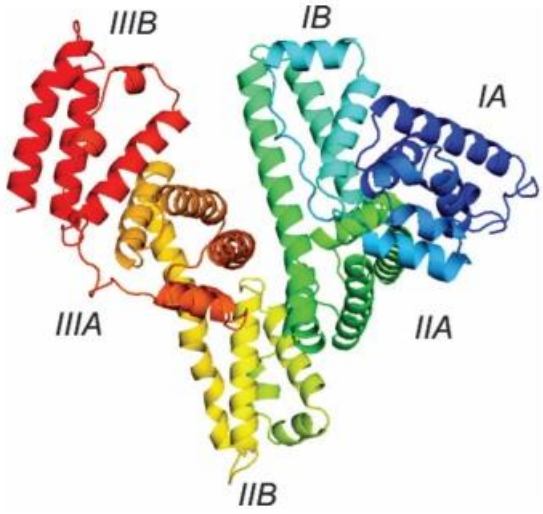

Figure 2.8 Schematic of an albumin molecule indicating the subdivision of HSA into domains (I, II and III) and subdomains (A and B) [63]

The main role of the protein within the body is to transport hormones, fatty acids, and other compounds [64]. This is enabled due to the versatility of the protein, which has four binding sites, all differing in size and specificity [66].

This versatility also means that the protein binds strongly to the variety of metal ions that are released from the implant (Section 2.3.4.4). Research has shown that the ions bind more strongly to albumin than to the other proteins present [49,50]. As the corroded products are consumed, the equilibrium across the electric double layer (EDL) is upset, leading to enhanced corrosion via either anodic or cathodic reactions [48].

2.4.2 Binding Sites of Albumin

Most of the mammalian albumins, including both Human and Bovine Serum Albumin (HSA/BSA), have four active sites throughout the molecule in which metal ions can bind. These are as follows: N Terminal Site (NTS), Multi Ligand Binding Site (MBS), Cys-34 Binding Site and Non-Localised Site B. All of these sites vary in size, structure, and specificity.

2.4.2.1 The N Terminal Site (NTS)

The NTS is composed of three residues in the sequence (Aspartate-Alanine-Histidine)(Asp-Ala-His) that can rotate around the peptide bond to form an

active site. This is enabled via the free terminal amine and histidine giving a four co-ordinate binding site, which prefers metal ions that are favourable in the square planar mode (d^8 configuration), e.g. Cu(II) and Ni(II) [66]. The metal ion is bound via the deprotonated amide nitrogen's of Ala and His chains, alongside the terminal amine and imidazole donor, as illustrated in Figure 2.9.

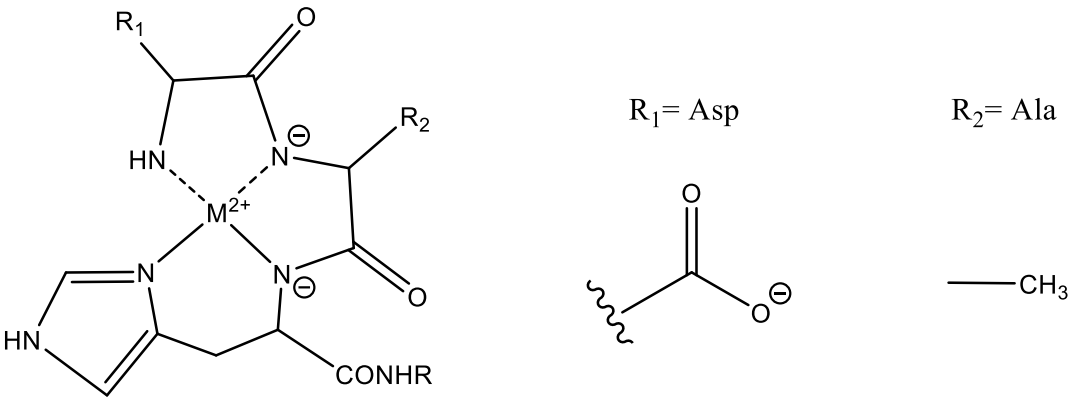

Figure 2.9 Schematic of the NTS binding site with a metal ion [66]

2.4.2.2 The Multi Binding Site (MBS) / Site A

This metal-binding site is known to have imidazole nitrogen present at the axial locations of the bipyramidal arrangement around the metal ion [66]. Ligand binding is also provided via the oxygen from a carbonyl and a carboxylate (domains I and II, respectively). The ion is also co-ordinated to a free L type ligand such as H_2O or Cl^-. Martins et al. [67] determined that Zn(II) and Cd(II) binds to this site by the use of NMR due to the presence of the two histidyl groups. Studies involving NMR, Raman and CD have also shown that there is an affinity for this site from both Cu(II) and Ni(II) [68-70].

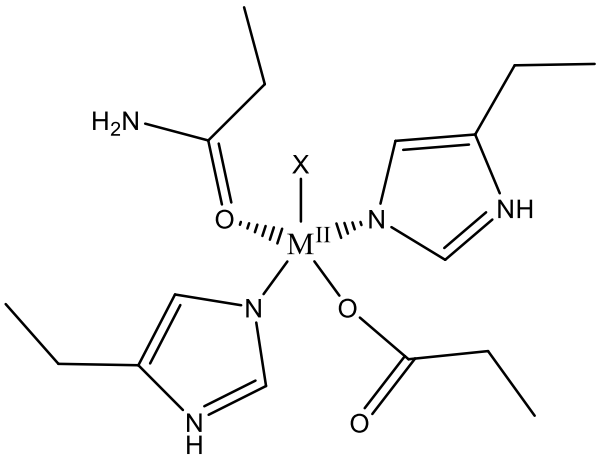

Where X = H_2O, Cl^-, etc

Figure 2.10 Schematic of the MBS with a metal ion [66]

2.4.2.3 The Reduced Cys-34 Binding Site

Albumin is held together by 17 disulphide bridges (R-S-S-R) which interconnects the α helices giving shape and structure to the proteins domains and subdomains. There is one thiolate form of Cys-34 residue, located in subdomain IA within a cleft of helices 2 and 3 (Figure 2.11) [66]. This location is suitable for coordination to a metal ion but due to spatial location isn't suitable for simultaneous coordination. Therefore, the site is specifically for those metal ions which can bind effectively to the albumin molecule via a single metal-sulphur bond due to its very high enthalpy [66]. Au(I) and Pt(II) are the most well-known metals that bind to this site [66].

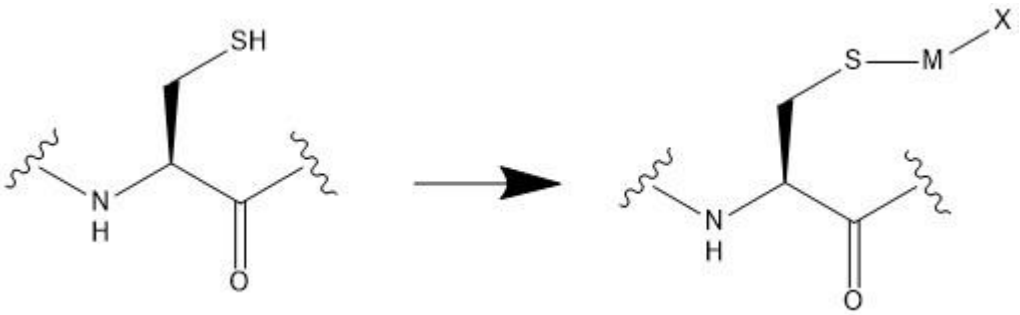

Where M is a metal ion

X is other ligated species

Figure 2.11 Schematic of the Cys34 binding site with a metal ion

2.4.2.4 The Non-Localised Site B

This site has not been localised in the literature so far; therefore, its location within the protein is unknown. From studies that were undertaken, it is known that only nitrogen ligand is involved with this not likely to be His-39 [66]. Recent studies have shown that Site B is the primary binding site for Mn(II) and Co(II) ions over the previously thought NTS and MBS [71,72].

2.4.3 Protein Interactions with Metals

One of the first events that occur when a metallic implant is submerged within biological media is the adsorption of a protein layer; it occurs immediately after water and ion adsorption [73,74]. However, the adsorption of protein molecules is a complex process, with the surface characteristics, stability of the protein and the pH and ionic strength of the environment affecting the process [75]. Typically the metallic biomaterials are covered in an air formed oxide layer (2 – 3 nm); for example, CoCrMo has a protective film comprised of Cr(III) oxide, so the protein interacts with this film instead of the bare metal. Characteristics of the oxide such as surface energy, hydrophobic/hydrophilic character, net charge, and roughness are key for the adsorption of proteins [75].

There have been multiple reports that have indicated that the performance of these metal implants are heavily reliant on the presence of proteins due to their tendency to form a biofilm on the surface of the alloy [76-78]. This film acts as a transient, solid lubricant that lowers the contribution of adhesion and abrasion to wear, with reports indicating that the thickness of the film formed ranges between 10-100 nm [76-78]. Yu Yan [79] stated that the overall state and thickness of the film are determined via the properties of the surface, such as wettability and topography.

Upon submersion, the proteins are attracted onto the surface of the metal via hydrophobic interactions, which can lead the protein to denature as the bonding interactions of the secondary and tertiary structures are disrupted [75,81]. Once present on the surface, the protein can then interact with the metal via electrostatic or covalent forces [81]. In CoCrMo alloys, the interactions of the metal and protein are said to stem from the affinity of the protein with molybdenum. Martin et al. [82] undertook corrosion studies on pure Co, Cr, Mo in protein-containing solutions with the film only being present on the molybdenum metal. The reasoning behind this is currently unknown, but it appears that the formation of this protective film is reliant on the BSA – molybdenum interactions and therefore the presence of Mo in the alloy.

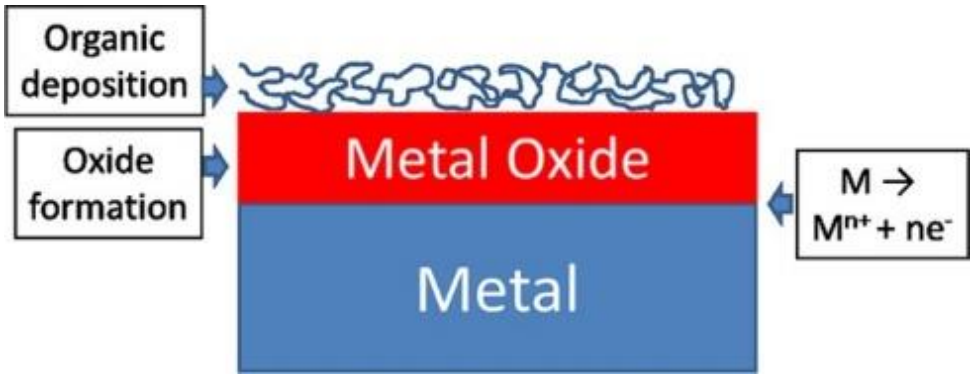

Figure 2.12 Shows the formation of a biofilm on the surface of a metal [82]

2.5 Corrosion

Corrosion is a natural process in which a material is degraded by its environment; this process occurs due to thermodynamic driving forces [83]. This is a purely electrochemical process that co-exists alongside mechanical processes in-vivo. This section will review the literature concerning the corrosion of biomedical alloys.

Metallic corrosion occurs due to an irreversible reduction-oxidation (redox) reaction between the alloy and an oxidising agent within the surrounding environment [83,84]. As implied, this consists of two reactions, which are both required to initiate and sustain metallic corrosion. The anodic oxidation reaction involves the ejection of electrons from metal atoms producing metal cations and free electrons. The reaction is depicted in Equation 2.1, where M is a metal.

Equation 2.1 The anodic reaction

$$M \rightarrow M^{n+} + ne^{-}$$

The cathodic reduction reaction is where an electrochemically active species (EAS) is reduced (gain of H/loss of O). The most common EAS within the body are solvated protons and dissolved oxygen, with the proceeding reaction being heavily dependent on the chemistry of the environment (Equation 2.2) [84].

Equation 2.2 The possible cathodic reactions

$$\frac{1}{2}O_2 + 2H^+ + 2e^- \rightarrow H_2O \qquad \text{Acidic Conditions (pH<7)}$$

$$\frac{1}{2}O_2 + H_2O + 2e^- \rightarrow 2OH^- \qquad \text{Alkaline Conditions (pH>7)}$$

$$H_2PO_4^- + 2H^+ + 2e^- \rightarrow H_2PO_3^- + H_2O \qquad \text{Phosphate Reduction}$$

$$2H^+ + 2e^- \rightarrow H_2 \qquad \text{Hydrogen Evolution}$$

The electric double layer (EDL) is considered to be a combination of a lattice of positive ions and mobile electrons, which behave like a gas [84]. The conductivity of the metal and other electronic properties are accounted for by these free electrons. When a metal is submerged within an electrolyte, hydration of the metal ions follows at the interface leading in a loss of metal ions, leaving the metal positively charged. As water is a dipolar molecule, when it adsorbs, it orients itself according to the charge at the surface of the metal; this causes the diffused ions to remain in close vicinity to the surface defined by the radius of their hydration shell [84]. This results in a charge separation at the interface, inducing a potential difference and an electrical capacitor at the metal-electrolyte interface, which can be manipulated to measure and quantify the corrosion of a metal. The charge distribution at this

interface is dependent on multiple factors: electronic properties of the metal, the chemisorption of anions and the adsorption of water molecules and hydrated cations [83,84]. This layer of charge separation is known as the EDL. Different models have been utilised to explain this distribution of charge at the interface; the simplest is known as the Helmholtz layer, which assumes that the compensation of excess charge by a monolayer of opposite charge with the potential dropping linearly over the double layer [84,85]. The Stern model is more advanced, with a schematic of this layer is shown in Figure 2.13; this model describes the distribution of charge in terms of a rigid inner layer with an outer diffusion layer [84,85].

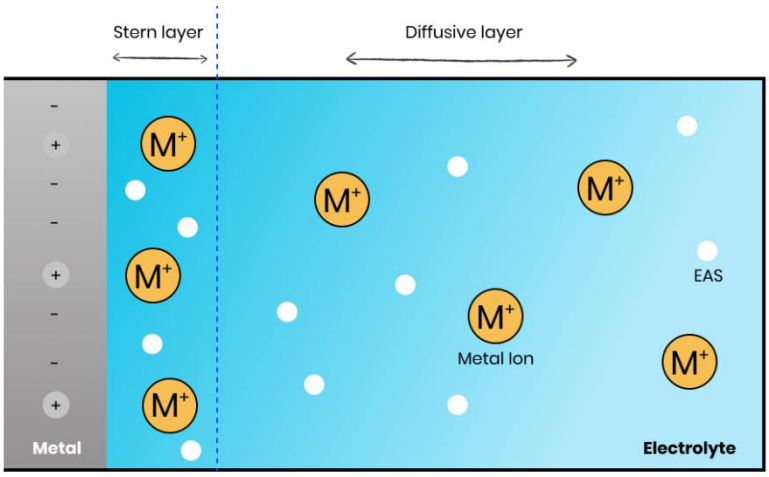

Figure 2.13 Representation of the double layer interface that exists when a metal is submerged in aqueous media. Adapted from [85]

The formation of this EDL can present complexities within biosystems due to the variety of different elements and compounds that exist within the human body (ions, inorganic species, proteins, cells). The presence of oxidising agents are reduced as they diffuse towards the layer and interact with free electrons, for example, the reduction of oxygen to form a passive film or the reduction of phosphates to form a phosphate layer. Before or after this charge transfer, mass transport phenomena can occur, which determine the concentration of the reactants and products at the surface of the electrode [85].

2.5.1 Thermodynamics of Corrosion

For corrosion of material to occur, there must be a thermodynamic driving force present. The Gibbs free energy change describes both the enthalpic

(ΔH^o) and entropic (ΔS^o) parts for a chemical reaction to occur. The equation for this process is shown in Equation 2.3:

Equation 2.3 The Gibbs-Helmholtz equation for the standard free energy of the reaction [86]

$$\Delta G^o = \Delta H^o - T\Delta S^o$$

For a reaction that didn't occur at standard state (1 atm, 298 K, pH 7), the Gibbs free energy equation is as shown in Equation 2.4.

Equation 2.4 Gibbs Free Energy change for the conditions of equilibrium (balanced rate of anodic and cathodic reactions) at a given temperature [86]

$$\Delta G_{red} = \Delta G^o + RTln(K)$$

Where ΔG_{red} is the free energy change for the reduction reactions, ΔG^o is the free energy change of the reaction, with K being the equilibrium constant. If the value of ΔG^o for the reaction is negative, then the reaction will occur spontaneously as there is a greater electromotive force present than what is needed for the reaction to occur. However, if the value is positive, then the reaction won't tend to occur.

During a corrosion reaction, there are two distinct thermodynamic driving forces in play; the chemical-related driving forces and the charge of separation, which occurs as a direct result of EDL formation due to hydration and migration of metal ions amongst other species [83,84]. This enables a measurable electrical potential across the metal-solution interface, which can be quantified via the following Equation:

Equation 2.5 Gibbs Free Energy change expressed in electrical terms [83]

$$\Delta G = -nFE_{cell}$$

Where n is the valance of the ion that takes part in the reaction and F being Faraday's constant (96,500 C/mol). E_{cell} is the difference in potential between the electrode in question and a reference electrode. The absolute potential cannot be monitored, so the potential must be referenced to a zero point which is defined from a reference electrode [80]. Even though any half-reaction can

be chosen for this point, the hydrogen-hydrogen ion reaction is universally accepted as it's relatively easy to establish a reversible hydrogen electrode [83-86]. The tendency for a reaction to complete can be determined by combing half-reactions. An example of the replacement reaction between copper and zinc is shown in Equation 2.6. If the reaction gives a positive electromotive force (EMF), then the reaction is spontaneous, with a negative EMF meaning the reaction is non-spontaneous. Displacement reactions are examples of redox reactions. In this example, the more reactive metal (Cu) reduces the ion of the more reactive metal (Zn^{2+}).

Equation 2.6 Copper and Zinc replacement reaction

$$Zn^{2+} + Cu \rightleftharpoons Zn + Cu^{2+}$$

$$E^{o}_{cell} = E^{o}_{Cathode} - E^{o}_{Anode} = 0.34 - (-0.76) = +1.10V$$

The electromotive series ranks some of the most common half-cell reactions according to their standard electrode potential; some selected examples are depicted in Table 2.2. This table enables multiple calculations for possible electrochemical reactions. It’s important to note that all of these potentials refer to electrodes with reactants at the unit activity of 25^{o}C.

Table 2.2 Electrochemical series of standard electrode potentials for some specified elements at 25°C [84]

Electrode	E° /V (SHE)
$\frac{1}{2}Cl_2(aq) + e^- \rightarrow Cl^-$	+1.40
$Pt^{2+} + 2e^- \rightarrow Pt(s)$	+1.19
$Fe^{3+} + e^- \rightarrow Fe^{2+}$	+0.77
$Cu^{2+} + 2e^- \rightarrow Cu(s)$	+0.34
$2H^+ + 2e^- \rightarrow H_2(g)$	0.00
$Mo^{3+} + 3e^- \rightarrow Mo(s)$	-0.20
$Co^{2+} + 2e^- \rightarrow Co(s)$	-0.28
$Fe^{2+} + 2e^- \rightarrow Fe(s)$	-0.44
$Cr^{3+} + 3e^- \rightarrow Cr(s)$	-0.76
$Zn^{2+} + 2e^- \rightarrow Zn(s)$	-0.76
$H_2O + e^- \rightarrow \frac{1}{2}H_2(g) + OH^-$	-0.83
$Na^+ + e^- \rightarrow Na(s)$	-2.71
$K^+ + e^- \rightarrow K(s)$	-2.94

This measured cell potential is often utilised as a semi-quantitative evaluation used to evaluate the tendency of cell corrosion when at open circuit potential (OCP). The Nernst equation can be derived via the substitution of Equation 2.4 into Equation 2.5. This describes the measurable electrical potential across an idealised metal-solution interface when at equilibrium. However, for systems not at equilibrium, the concluding term can become a reaction quotient (Q_c), this is a measure of the relative amounts of products and reactants at a specific point in time [25].

Equation 2.7 Nernst equation at equilibrium for a specific half-cell reduction process [83]

$$E = E^o - \frac{RT}{nF} Ln(\frac{a_p}{a_r})$$

Where E is the potential of the cell (V), E^o is the standard cell potential (V), R is the ideal gas constant ($JK^{-1}mol^{-1}$), T is the temperature (K), n is the quantity of electrons produced from the anodic half equation, F is Faradays constant ($Cmol^{-1}$) with a being the chemical reactivity of the products/reactants.

2.5.1.1 Determination of the Activation Energy

The Arrhenius equation provides a correlation between the activation energy of a reaction and the temperature. In chemistry terms, the activation energy is the minimum energy that needs to be overcome for a chemical reaction to proceed. The equation for this is shown in Equation 2.8; when applying to the corrosion process, it is possible to use i_{corr} (Acm^{-2}) instead of k as the i_{corr} is an equilibrium of the anodic and cathodic rates [87].

Equation 2.8 The Arrhenius equation [87]

$$k = Ae^{\frac{-E_a}{RT}}$$

Where, A is the pre-exponential factor, E_a is the activation energy (Jmol-1), T is the temperature of the system (K), and R is the ideal gas constant (8.314 $Jmol^{-1}K^{-1}$).

To obtain the activation energy, the logarithmic values of the corrosion current density are plotted against the inverse of temperature, see Equation 2.9. The gradient of the graph is equal to the activation energy of the reaction. Vidal et al. [88] obtained a linear relationship for investigating the effect of BSA adsorption in the presence of saline for CoCrMo (Figure 2.14), stating that BSA adsorbs via chemisorption as the E_a was 21 $kJmol^{-1}$.The higher the magnitude of the E_a the stronger the bonds formed, the type of adsorption can also be determined. The two main types that can occur are either physical or chemical. Physisorption typically is a very fast and reversible process due to small energy requirements (< 4.2$kJmol^{-1}$) as the forces that govern these interactions are weak, such as Van Der Waals, whereas chemisorption requires higher activation energies due to chemical bonds being formed between the species [89].

Equation 2.9 Logarithmic form of the Arrhenius equation that relates to the reaction rate

$$\frac{dlni_{corr}}{d\frac{1}{T}} = -\frac{E_a}{R}$$

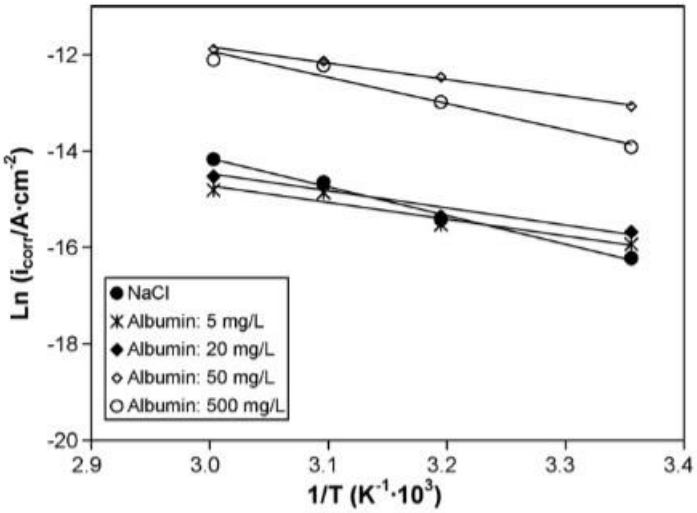

Figure 2.14 Effect of temperature and quantity of BSA on the corrosion rate of CoCrMo (Arrhenius plot) [88]

The Eyring equation (Equation 2.10) is based on transition state theory and, just like the Arrhenius equation, enables a relationship between the temperature and rate of reaction [88]. It is formed from combining Equation 2.8 and Equation 2.9 and enables the parameters of transition state activation to be determined [87].

Equation 2.10 The Eyring Equation (Linear form) [89,90]

$$lnk^{\ddagger} = \frac{RT}{Nh} e^{(\frac{\Delta S^{\ddagger}}{R})} e^{(\frac{-\Delta H^{\ddagger}}{RT})}$$

Where h is Planck's constant (6.63x10^{-34} Js), N is Avagadro's number (6.02x10^{23} mol^{-1}). This equation enables the activation enthalpy ($\Delta H^{\ddagger}$) and the activation entropy ($\Delta S^{\ddagger}$) to be determined from kinetic data obtained. From plotting $\ln(\frac{i_{corr}}{T})$ against $\frac{1}{T}$ gives a straight line with the slope being equal to $(-\frac{\Delta H^{\ddagger}}{R})$ and the intercept being $(ln\frac{R}{Nh} + \frac{\Delta S^{\ddagger}}{R})$.

The sign of the $\Delta H^{\ddagger}$ determines if the reaction that proceeds is either endothermic (-ve) or exothermic (+ve), with the sign of $\Delta S^{\ddagger}$ determining if the reaction is associative (-ve) or dissociative (+ve) [89,90]. An associative mechanism is where the process of adsorption leads to order through the complex formation of species; this also implies that no change occurs to the internal structure of the adsorbent [89,90].

2.5.2 Types of Corrosion

There are many different forms that corrosion can occur in depending on the material, electrolyte present and the conditions. They can either be general or localized in nature, where an attack is limited to specific areas of a structure. Fontana [91] presented a review of eight different types that can occur; this section will cover the types that are relevant for CoCrMo hip replacements.

2.5.2.1 Uniform Attack

This is the most common form of corrosion which is characterised via a chemical reaction that progresses evenly over the alloys exposed surface. This reaction leads to thinning of the alloy until failure occurs.

2.5.2.2 Pitting Corrosion

Pitting corrosion is a localised type of corrosion in which pits are formed on the alloy. This type of corrosion is autocatalytic due to metastable reactions occurring leading to the gradual formation of an active corrosion site [91]. Once a pit has formed, a local corrosion cell is established, making the pit active as anodic reactions take place within the pit, with surrounding areas acting as the cathode leading to more breakdown of the alloy, causing the pit to increase in size over time [91].

This is one of the most devastating types of corrosion, often leading to failure of the joint with relatively little material lost. Within biomedical devices, this is a problem often seen on the underside of screws and is even more prevalent in the presence of chloride ion containing environment [92]. Sikakurmar et al. [93] observed increased corrosion resistance to pitting in a saline environment with molybdenum addition.

2.5.2.3 Crevice Corrosion

In biomedical devices, crevice corrosion occurs within confined spaces or crevices where stagnant fluid can accumulate relative to the bulk solution [91,92]. Initially, both the anodic and cathodic reactions will happen uniformly within the system. Over time the fluid within the crevice will become oxygen-depleted, which cannot be replaced due to the nature of the crevice [91]. To enable the potential energy to be kept at a minimum within this crevice and to maintain the charge, reduction reactions will preferentially take place just outside of the crevice with negative ions moving from the bulk to the crevice [91]. This leads to a decrease in the pH within the crevice leading to an autocatalytic reaction. Research has shown that this type of corrosion can be limited by the appropriate design and material choice of the implant [92].

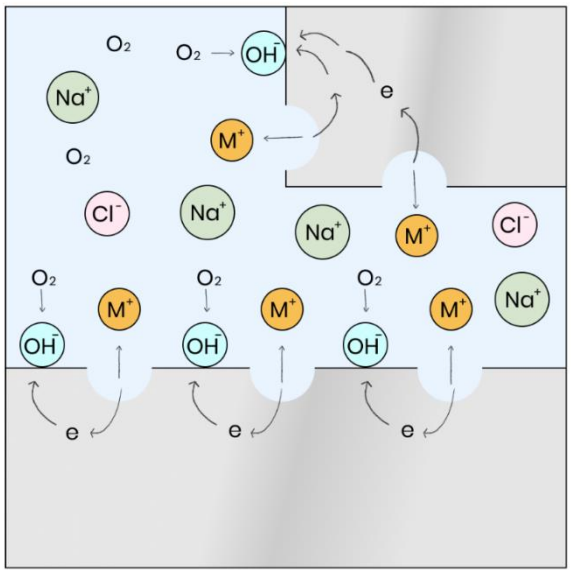

Figure 2.15 Schematic showing the process of crevice corrosion. Adapted from [91]

2.5.2.4 Galvanic Corrosion

Galvanic corrosion occurs due to differences in potential between metals when they are submerged within a conductive solution; this typically occurs if bone plates/screws are made of different alloys. The potential difference is the driving force of the reaction, which leads to a flow of electrons between the metals, leading to corrosion of the more susceptible alloy [25]. This leads the alloy to act as an anode while the more corrosion resistant acts as a cathode and is therefore further protected. The extent of galvanic corrosion is affected

by the distance between the acting electrodes as well as their respective areas and the environment they are exposed to [84]. As passive materials have a protective oxide film on the surface of the metal, the presence of galvanic corrosion is hindered dramatically compared to the coupling of active metals [92].

2.5.2.5 Intergranular Corrosion

A corrosive attack that preferentially occurs on/adjacent to the grain boundaries of an alloy. The process for this differs between metals, although at a microscopic level, is quite similar. For CoCrMo alloys, there can be chromium carbides precipitated along the grain boundaries causing areas with reduced chromium in the vicinity of the boundary [25]. These reduced chromium zone possess dissimilar potentials to that of the alloy, leading to a galvanic circuit and therefore degradation of the alloy. [25].

2.5.3 Tribocorrosion

Tribocorrosion is the process of degradation of material from the simultaneous action of both mechanical processes and corrosion. The use of passive materials in tribological environments can lead to the removal of the protective oxide film, this is highly dependent on the contact mechanics and any present lubrication. Oxidation of the substrate then takes place, resulting in the loss of metallic ions from the alloy. A schematic displaying this particular process is shown in Figure 2.16 below.

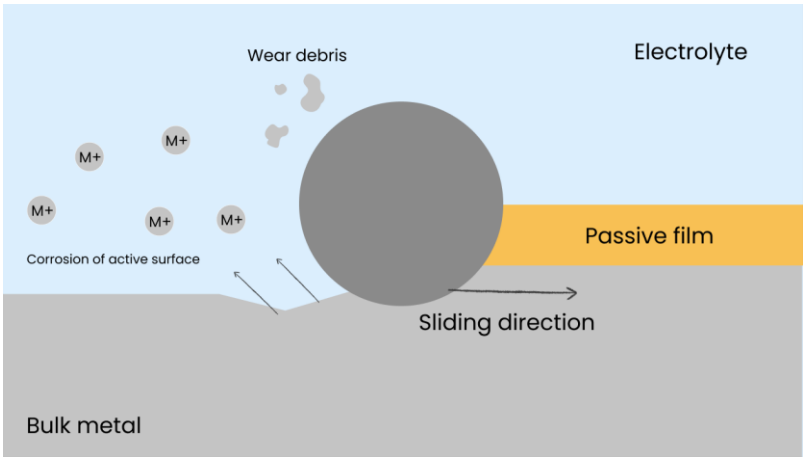

Figure 2.16 Schematic of the tribocorrosion process

Uhlig et al. [94] were one of the first to observe the role of both corrosion and wear within fretting contacts. He went on to prove that the deterioration of

material stems from two distinctive mechanisms: mechanical wear and wear-accelerated corrosion. This leads to Equation 2.11 being deduced, where V_{mech} is the volume of material lost via mechanical wear and V_{chem} represents the volume of material lost via wear accelerated corrosion.

Equation 2.11 Total volume of material loss from a tribological system [94]

$$V_{total} = V_{mech} + V_{chem}$$

However, this model doesn't take into consideration that passive corrosion occurs outside of said contacts, the material being in a de/re-passivation state or any variations within the mechanics of said contacts. Therefore a synergetic approach needed to be considered; according to ASTM G119, the total tribocorrosion material lost is described by Equation 2.12, with W being material lost due only to wear, C is material lost due only to corrosion and S is the synergy due to the combined wear and corrosion [95].

Equation 2.12 Systematic view of material loss from a tribological system [95]

$$T = W + C + S$$

$$S = \Delta S_w + \Delta S_c$$

2.5.4 Factors affecting the rate of corrosion

Within the body, metal implants are usually exposed to a corrosive environment for long periods of time. The rate at which corrosion occurs is heavily affected by this surrounding environment, with the following section all playing a key role.

2.5.4.1 Composition of the environment

The composition of the surrounding environment plays a major role in determining the corrosion rate of the metal. The addition of oxidising agents to a solution leads the corrosion potential to shift in the anodic direction; the amount is dependent on its redox potential and kinetic parameters [91]. The concentration of oxidising agents needs to equal or be greater than the minimum amount necessary to induce passivation so as not to cause damage to the alloy [91]. The presence of aggressive species in the environment, such

as Cl^- can increase the rate of corrosion due to faster formation of pit growth [92].

2.5.4.2 The pH of the environment

The pH is defined as the measure of the concentration of hydrogen ions in a specific solution. At acidic pH, an excess of H^+ ions are present, whilst for an alkaline pH, an excess of OH^- is present. Under an acidic pH, the rate of corrosion increases due to the redox potential of the aqueous solution being raised from the presence of extra H^+ ions [96]. Sun et al. [97] investigated the effect of pH on CoCrMo alloys determining that acidic pH conditions can increase the corrosion current by as high as 67% (Figure 2.17) therefore increasing the number of metal ions released.

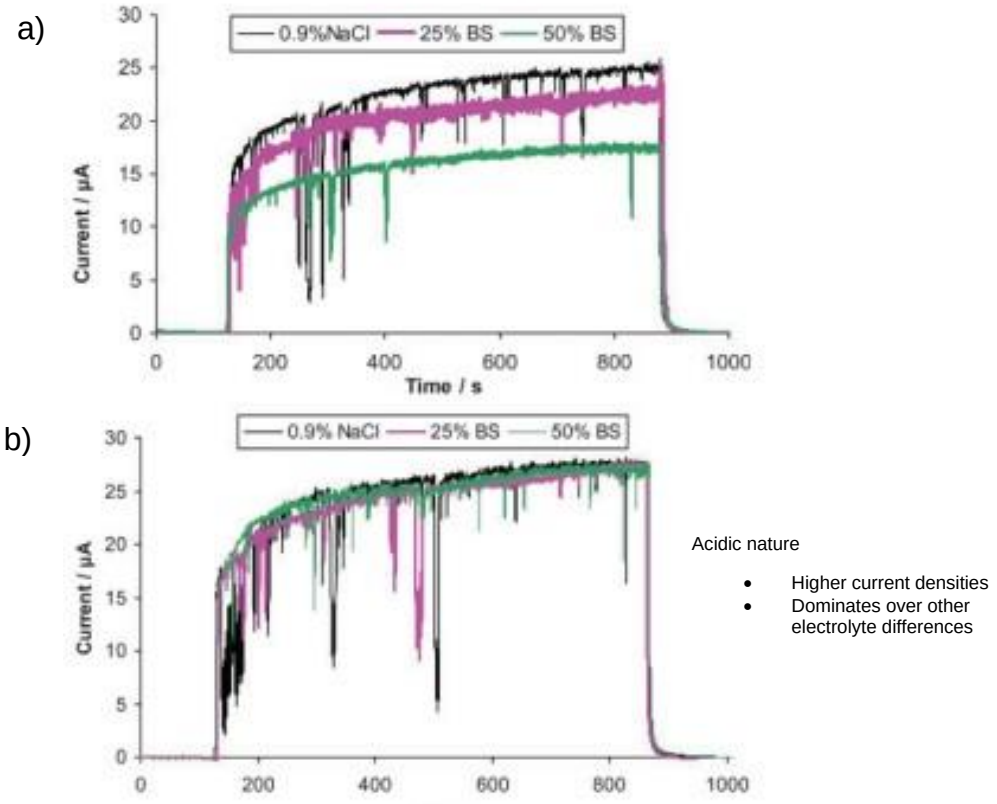

Figure 2.17 Current comparisons under abrasive wear corrosion for CoCrMo in various simulated bodily solutions (a) pH 7.4 (b) pH 4.0 [97]

2.5.4.3 Temperature

The rate of corrosion increases as the temperature does due to more of the molecules having the desired activation energy for the chemical and

electrochemical reactions, which in turn increases diffusion rates in the electrolyte [96]. This causes the transport of ions and electrons through the electrolyte or environment to increase across the passive film that forms on the metal surface, leading to an increase in corrosion rate. At higher temperatures, the rate has been seen to decrease due to reduction of oxygen stability, lowering the external cathodic reaction rate and hence the rate of corrosion [81].

2.5.5 Protein effects on Corrosion

The existence of an adsorbed species at the metal/environment interface can cause alterations to the electrochemical processes that govern corrosion. The presence of proteins has been known to strongly influence the corrosion behaviour of materials, the extent to which is controlled by multiple factors including the alloy composition, the adsorption properties of the protein, and the interactions of the protein with the surrounding electrolyte [75].

The electrochemical behaviour of CoCrMo alloys with albumin has thoroughly been examined in recent years; for investigational purposes, bovine serum albumin (BSA) is utilised seeing as it's a model protein of HSA. Yan et al. [80] noted that the effects of BSA on CoCrMo is twofold: it can enhance the dissolution of the metal via binding to the metal species but can also inhibit mass loss by the formation of a biofilm. The prevention of corrosion of alloys due to protein presence is down to inhibiting the release of metallic ions by blocking key mechanisms such as electrochemical dissolution, thus slowing the rate of corrosion [75]. This can also result in oxide film growth due to the biofilm inhibiting charge transfer due to diminished transport of corrosive ions and soluble products [98]. Protein is known to inhibit the cathodic half-reaction by physically blocking the active sites where oxygen reduction occurs, hence lowering the ion release rates and improving corrosion resistance [99]. Munoz et al. [100] showed this by investigating the protein changes in the electrochemical behaviour of the alloy by altering the passive film characteristics. By undertaking potentiodynamic polarization scans, it showed that albumin moves the potential in the cathodic direction whilst also increasing the passive current density in both saline and PBS environments [100]. The results are indicated in Figure 2.18 (further explanation on potentiodymanic polarisation in section 2.5.7.2).

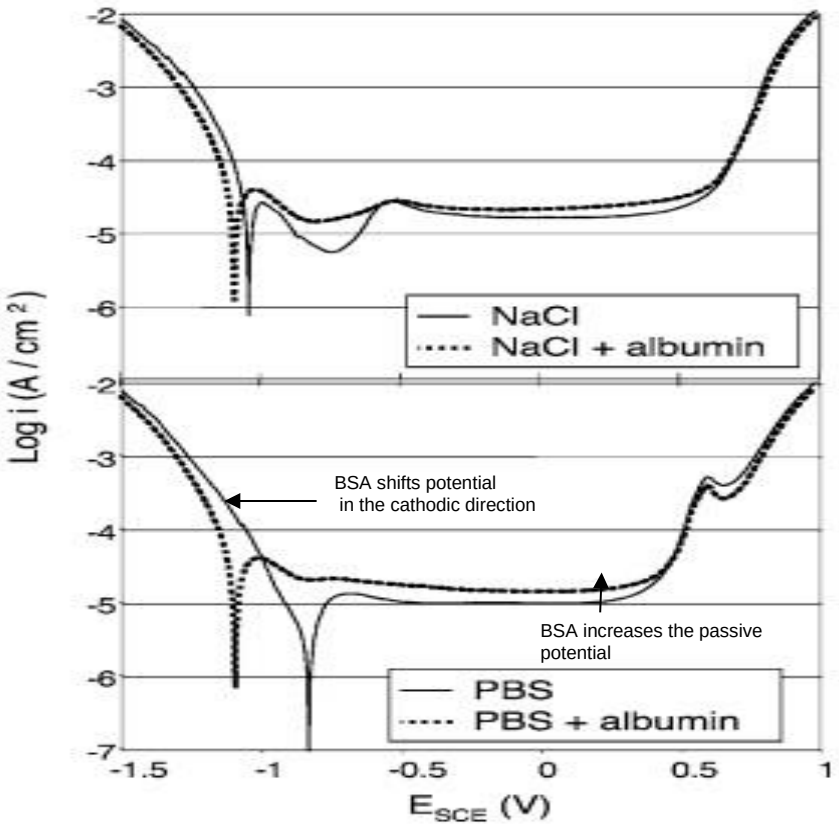

Figure 2.18 Potentiodynamic curves depicting the effects of albumin on the corrosion potential of CoCrMo in NaCl and PBS solutions [100].

However, the presence of proteins has also been shown to enhance the rate of corrosion. The adsorption of the species onto the surface can lead to oxygen deficiency, resulting in a weaker oxide film enhancing corrosion [75]. Y.Yan [101] observed using AFM (Figure 2.19) that the potential of BSA is lower than that of the CoCrMo, meaning that BSA can promote the electron transfer reaction on the alloy's surface, resulting in a higher rate of corrosion. The formation of chelates can occur as the protein complexes with metallic ions, these compounds can then be transported away into the bulk solution increasing dissolution of the alloy and weakening the integrity of the alloy. Espallargas et al. [102] observed an increase in molybdenum dissolution when BSA was present within a range of different domains when investigating the effects on CoCrMo. The availability of any protein-metal interaction depends on the characteristics of the surface of the alloy. Williams et al. [103] conducted in-vitro wear tests on various alloys (effects when the oxide film is cleaved and the bare metal exposed) and found that alongside protein forming

the metal chloride complexes, the protein altered the repassivated oxide film affecting the future performance of the alloy.

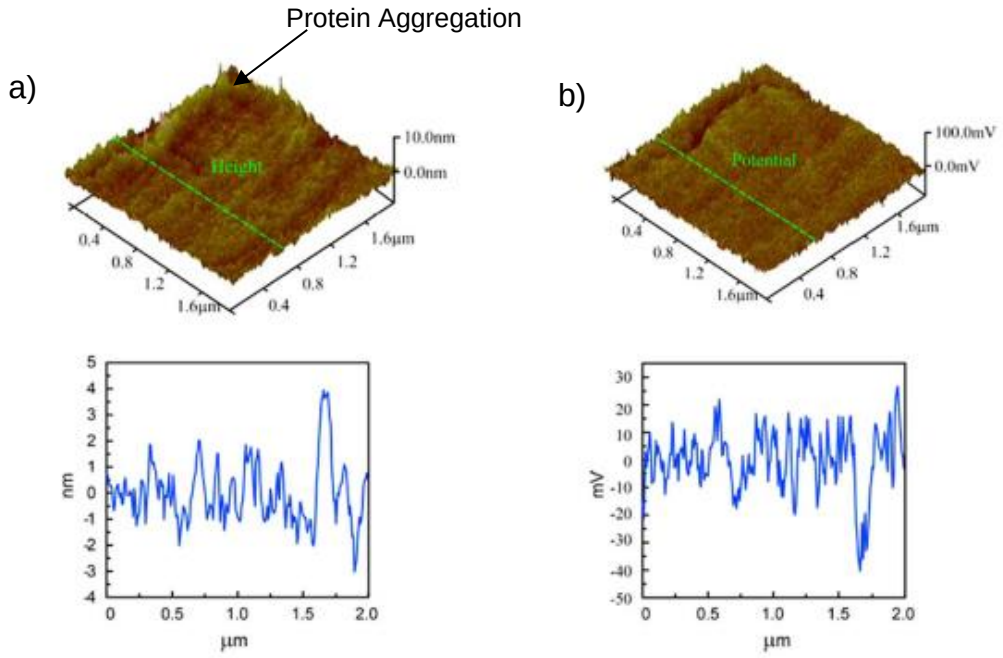

Figure 2.19 AFM images of CoCrMo with BSA adsorbed on the surface (a) Topography (b) Potential [101]

2.5.6 The Products of Corrosion

The rate of corrosion is affected greatly by the physical nature of the products from corrosion. These can be defined into three basic types [84]:

- Dissolved ions
- Porous films
- Passive films

Hydrated cations or complexes that can diffuse away into the bulk solution are the product of corrosion of metallic alloys in acidic conditions [84]. More often than not, they play no role in the rate of corrosion.

Under basic or neutral environments, the products of corrosion are only slightly soluble. This causes them to precipitate along the surface of the alloy as either metal salts or hydroxides covering the alloy in a porous film. These films do not protect the alloy from corrosion itself; they only hinder the rate at which it takes place [86]. An example of this is rust formed on a stainless steel surface.

On certain metals, there is the formation of a compact film that acts as a barrier to the environment shielding the alloy from corrosion. This leads to a highly diminished rate of corrosion. These films are formed of metal oxides that occur spontaneously on the surface of the metal when exposed to air. Even some metals have shown compact film formation in humid or liquid environments.

2.5.7 Techniques to measure corrosion

The use of a potentiostat and a cell (typically three-electrode) are required to determine the corrosion behaviour of an alloy. A standard three-cell electrode is comprised of a working electrode (WE), a counter electrode (CE), and a reference electrode (RE) (Figure 2.20). The potential of the WE is measured against the RE, which is usually an individual cell with a metal submerged in its respective metal ion electrolyte, providing a stable potential.

The potentiostat measures the potential difference between the WE and RE and can apply an overpotential to the WE, enabling electrochemical conditions to be investigated. To undertake this, a current is enforced between the WE and CE either by applying/withdrawing electrons. This alters the potential of the WE, with its direction determining if it is anodically or cathodically polarized. This circuit is complete due to the flow of an ionic current through the electrolyte between the WE and CE.

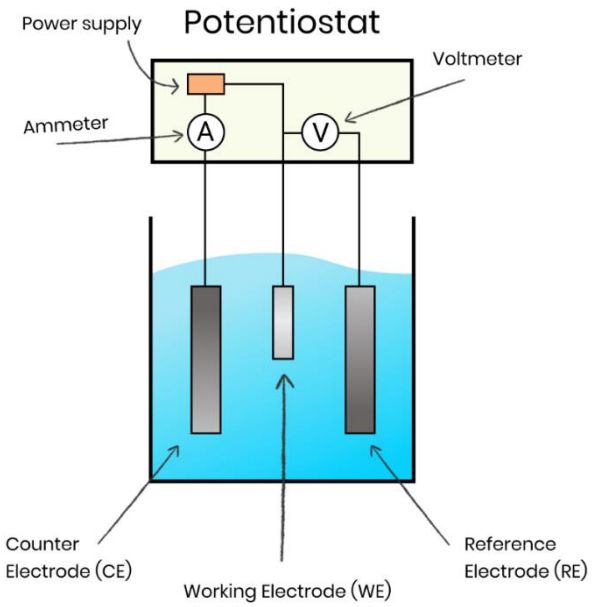

Figure 2.20 Schematic of the three-electrode cell setup. Adapted from [51]

2.5.7.1 Open Circuit Potential

The OCP, also known as the free corrosion potential, is the difference in potential between a working and a reference electrode when there is no current present. Therefore, the cathodic and anodic reactions occur simultaneously at the same rate. By examining the OCP as a function of time, information about when the system is at a steady state can be identified. This measurement can also represent information about possible chemical reactions that can occur on the surface of the WE.

The direction of the change in the potential is determined by how the EDL adapts to the electrolyte present; if the potential tends towards the anodic region, then typically, a passive film is formed on the surface, which protects the alloy [83]. Whereas if the potential tends towards the cathodic region, then typically, the surface forms a porous hydroxide layer, which only slows the rate of corrosion [83].

2.5.7.2 Potendiodynamic

Passive metals (e.g. CoCrMo) are known to exhibit active-passive behaviour, which can be manipulated by the conditions the alloy is under and measured by utilising electrochemical techniques. A current against applied potential is shown for a typically passive metal in Figure 2.21. This is undertaken by continuously increasing the potential difference at a constant rate between the WE and RE. This is known as a Tafel or Evans plot, which is useful at accessing the corrosion behaviour of an alloy.

The rate of corrosion (i_{corr}) can be determined by extrapolating the linear sections of the graph back to the place where they intersected, this is where the rate of the anodic and cathodic reactions are equal. This intersection point is known as E_{corr}. At potentials below that of the corrosion potential (E_{corr}), the alloy is a net cathode. Once the potential rises past the E_{corr}, the alloy becomes a net anode and undergoes corrosion; this is known as the active state. The alloy remains in this state until the potential rises sufficiently to induce passivation (E_{pp}), resulting in a drop in current from i_{crit} to i_{pass} as a passive film has fully developed on the surface, protecting the alloy from the environment; this is known as the passive state of the alloy. It's important to note that corrosion does still occur but just at a highly reduced rate. The passive film will breakdown if the potential is raised to a certain value (E_b) which is highly dependent on the alloy and the environment it is exposed to,

this is known as the transpassive region, and the material will continue to corrode until the potential is dropped and repassivation occurs (E_r).

Key corrosion properties that can be determined from an Evans graph are as follows [25]:

- The rate of corrosion (i_{corr}) is proportional to the rate of corrosion when under active conditions.
- The oxide layer has higher stability with a greater breakdown potential (E_b).
- The resistance of the alloy to pitting and crevice corrosion increases as the difference between the corrosion potential (E_{corr}) and breakdown potential (E_b) increases.
- The resistance of the alloy to localised corrosion increases the closer in potential the breakdown (E_b) and repassivation potentials (E_r) are.

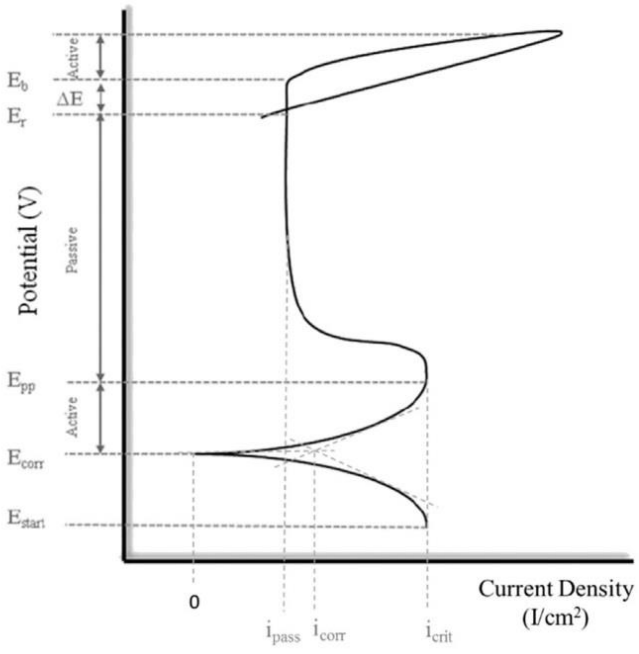

Figure 2.21 Typical anodic dissolution behaviour of an active-passive metal [25]

In regards to CoCrMo alloys, there have been multiple studies in recent years investigating the passive nature of the alloy. The electrolyte is known to have a drastic impact on the electrochemical behaviour of the alloy, being affected by the presence of inorganic ions, i.e. phosphates, as well as the presence of

organic matter. Munoz et al. [100] observed that the presence of phosphates lowers the corrosion rate of the alloy in comparison to saline conditions, as they act as anodic inhibitors shifting the corrosion potential to higher values. Whereas BSA was seen to act as a cathodic inhibitor, increasing the corrosion rate of the alloy by shifting the corrosion potential to lower values and increasing the passivation current (Figure 2.18).

2.5.7.3 Electrochemical Impedance Spectroscopy (EIS)

EIS is a procedure in which the characterisation of the metal/electrolyte interface can be determined in terms of the potential applied and the influence of external factors such as the composition of the electrolyte, the pH of the solution, and the oxygen content. When CoCrMo is investigated under OCP/Passive conditions, it displays typical passive behaviour characterised via a semi-circle arc (capacitive behaviour) and high values of impedance [100,104,105]. Munoz et al. [100] observed that phosphates increase the corrosion resistance of CoCrMo under both OCP and passive conditions, whereas BSA was seen to shift the phase angle to lower frequencies under passive conditions but decrease the resistance of the film at OCP (lower R_{out}). This would be due to the different rates of film formation that occur at these two potentials; as BSA is a relatively large molecule, it's more likely to interfere with a slow growth process such as OCP.

This method measures the response of an electrode to a small amplitude (10 mV) of sinusoidal potential at various frequencies, with impedance being the tendency of the circuit to resist the flow of alternating current. The mathematical expressions are shown below:

Equation 2.13 Relationship between the Impedance, applied potential, and the resulting intensity [104,106]

$$Z = \frac{E(t)}{I(t)} = \frac{E_0.\cos(\omega f)}{I_0.\cos(\omega f - \varphi)} = Z_0 \frac{\cos(\omega t)}{\cos(\omega f - \varphi)}$$

Where the sinusoidal potential is represented as $E(t)$, with E_0 being the amplitude of the wave (V), and the radial frequency is defined as $\omega = 2\pi f$. This potential induces a sinusoidal current $I(t)$, which is present in a shifted phase (φ) with an altered amplitude. The correlation between the potential

applied and the resulting current is known as the electrochemical impedance (Z).

The use of Euler's relationship allows the representation of these functions in the complex plane. Therefore the impedance is represented by the vector total of both the real and imaginary parts [104].

Equation 2.14 Application of Eulers Relationship with Equation 2.13 [104,106]

$$Z_0 e^{(j\varphi)} = Z_0(cos\varphi + jsin\varphi)$$

Where $j^2 = -1$ is the imaginary number

To characterise impedance, the magnitude must be specified along with the frequency and phase angle at which it is measured. These parameters are plotted on Bode and Nyquist plots, which are commonly used to display EIS data. For the Bode plot, the modulus of the impedance and the phase shift are both on the y-axis as a function of the logarithmic frequency. The Nyquist plot is where the impedance is on the complex plane, so on the x-axis is the real part and the imaginary part is on the y-axis for different frequencies, examples of these plots are shown in Figure 2.22.

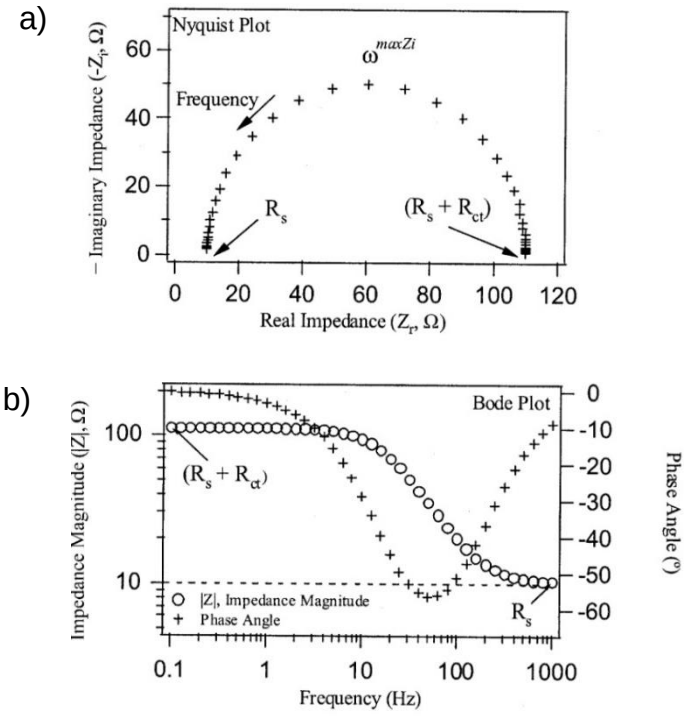

Figure 2.22 Examples of EIS spectra a) Nyquist plot b) Bode plot [104]

2.5.7.3.1 Interpretation of EIS data

To interpret the impedance data obtained, an electric model of a combination of electrical elements must be applied to the experimental data with a suitable fit. The most common electrical elements are listed in Table 2.3. Mektikos et al. [107] defined three guidelines for obtaining a good data fit:

1. Utilise the minimum amount of electrical elements to define a cell
2. Obtain a suitable value of chi-squared error ($X^2<10^{-4}$)
3. Errors associated with each individual electrical element should be less than 5%

Table 2.3 Typical components of an electrical system

Element	Physical Representation
Resistance (R)	Equates to charge transfer across a particular interface (i.e. metal/electrolyte)
Capacitance (C)	Ability of a system to store electric charge (EDL)
Inductance (L)	Resistance to oppose a change in the electric current
Warburg (W)	Represents linear diffusion whilst exposed to semi-infinite conditions

The simplest circuit to describe a corrosion process is the Randles circuit (Figure 2.23). It is formed of solution resistance (R_s), a double layer capacitance (C_{dl}), and charge transfer resistance (R_{ct}). This circuit is used as the starting point for other more complicated systems which are dependent on the applied conditions and environment [104,106].

Figure 2.23 Example of the Randles circuit

When fitting a cell, a constant phase angle element (CPE) is used in the place of a capacitor seeing as it accounts for the non-ideal behaviour of the capacitive elements. This arises due to physical phenomena that occur in real-

life situations such as the heterogeneity of the surface which is a consequence of surface roughness, impurities, dislocations, and the existence of grain boundaries [104]. This application seems to be commonplace within the recent literature [100, 104, 105].

Equation 2.15 Electrical expression of the CPE

$$Z(\omega) = Z_0(i\omega)^{-n}$$

Where Z_0 is the constant of the CPE, and n is its exponent. Depending on the quantity of n, CPE can either represent resistance $(n = 0, Z_0 = R)$, a capacitor $(n = 1, Z_0 = C)$ or warburg impedance $(n = 0.5, Z_0 = W)$ [104]. If the value of n is between 0.5 and 1, then the CPE defines the allocation of dielectric relaxation times within the frequency space.

Helsen [108] was one of the first to relate the obtained capacitance to the thickness of the film, with the following expression being determined:

Equation 2.16 Relation of capacitance to film thickness [108]

$$C = \varepsilon\varepsilon_0 \frac{A}{d}$$

With ε representing the relative dielectric of the film, ε_0 is the permittivity of the vacuum, with A being the area exposed to the electrolyte (cm^2) and d being the thickness of the film (cm). Namus et al. [105] utilised this expression alongside EIS and determined the thickness of the passive film under OCP conditions to be between 0.7 - 0.9 nm, increasing with the time the condition was applied. This obtained value is concordant with other research, Munoz et al. [100] obtained a thickness of between 0.8 - 1.0 nm for the thickness of the CoCrMo film at OCP conditions from AES depth profiling.

2.6 The Passive Film

Passivation is the creation of a protective layer on the surface of a metal/alloy due to the spontaneous oxidation in the presence of air. Passive films consist of metal oxides and hydroxides, the composition of these films varies with the metal and the surrounding environment [84,91].

Equation 2.17 General pathways for the formation of metal oxides and hydroxides

$$M_{(s)} + O_{2(g)} \rightarrow M_x O_{y(s)}$$
$$M_x O_y + H_2 O_{(l)} \rightarrow M_x(OH)_{y+1(s)}$$

The hydroxyl groups are usually located at the outer surface of the film indicating that the oxide surface is hydrated; within XPS data, this is depicted as broadening of the oxygen peak [84]. This is due to the difference in chemical shifts between metal oxides and hydroxides. Typically during a growth phase of an oxide film, anions can become trapped from the electrolyte: PO^{3-}_4, Cl^-, these anions can then occupy the lattice sites of O_2^- ions or they are located as defects [84].

The biomedical alloy, CoCrMo is known to have a passive film that is mainly comprised of chromium (III) oxide with small influences of cobalt and molybdenum oxides [30,80]. The film acts as a barrier that separates the metal from the corrosive environment, minimising the loss of metal ions to the environment and corrosion of the metal. P. Zeng [109] showed the film to possess an amorphous and porous structure that was not crystalline by the use of EELS and TEM. With the film being extremely thin, usually just being a few nanometres thick, electrons can still transfer through via quantum electron tunnelling [84]. L.Wang [110] utilised Mott-Schottky analysis to determine that CoCrMo behaves as an n-type semiconductor (donor defects) at OCP but with potential increase tends towards a p-type (acceptor defects). As the film has low ionic conductivity, it is resistant to corrosion but is highly unstable when exposed to high levels of chloride [84].

The thickness and structure of the film are dependent on the pH, temperature, the potential applied, and time exposed to the environment [84, 91]. Vidal [111] observed an increase in CoCrMo oxide thickness with an increase of temperature from room to 37°C at 0.35$V_{Ag/AgCl}$ with EQCM (0.3 – 0.4 nm) and XPS (0.1 - 0.12 nm). Corresponding potentiostatic data from these results indicated that although the film was thicker, it was not as protective as the oxide film formed at room temperature [111]. Milosev [30] monitored the thickness of the CoCrMo passive film as a function of potential using angle-resolved XPS. Under higher passive potentials, the presence of cobalt and molybdenum within the film increases as well as the thickness of the film [30].

This thickness increase could be due to the greater size of molybdenum atoms in comparison to chromium.

2.6.1 Growth of the Passive Film

There are two prevailing theories within the literature in regards to the growth of a passive film, the High Field Model (HFM) and the Point Defect Model (PDM). The key differences are that the HFM states that whilst under potentiostatic conditions, the strength of the electric field within the oxide film decreases as the film gets thicker, whereas within the PDM, the electric field strength remains constant throughout [112,113].

2.6.1.1 High Field Model

The HFM was originally put forward in 1935 by Verwey, with modifications coming later on, first by Cabrera and Mott and then by Fehlner and Mott. The base model states that growth of the oxide film exclusively occurs at the film/electrolyte interface with no dissolution of the alloy occurring. This model assumed that the strength of the electric field has no upper limit but decreases as the oxide film is grown, shown in Equation 2.17.

Equation 2.17 Passive film growth expressed as a function of time [112]

$$\frac{dL}{dt} = Ae^{(b\varepsilon)}$$

Where L is the thickness of the film, A and b are constants that vary depending on the properties of the alloy, and ε is the electric field within the film. By taking into account the potential drop occurring across the film, Equation 2.18 then becomes:

Equation 2.18 Passive film growth accounting for the potential drop [112]

$$\frac{dL}{dt} = Ae^{(\frac{bV}{L})}$$

Where V is constant for potentiostatic conditions, this equation states that as time tends to infinity, then so does the thickness. As the length increases, then the dL/dt tends to zero, as this rate is proportional to the ionic current as time tends to infinity, then the current tends to zero. Aligizaki et al. [112]

experimentally determined that the film thickness reaches a true steady-state with the current reaching a constant value but never being zero.

The modifications of this model were undertaken to include dissolution at the interface, enabling analytical relationships to be derived between the maximum film thickness and passive current density as well as the potential applied and the pH of the environment. However, the newfound dependency of the current on the voltage was later found to be in disagreement for systems that conform with the initial assumptions.

2.6.1.2 Point Defect Model

In 1981, the PDM was put forward by Macdonald and built upon later on to account for film dissolution. This model describes the growth of a film alongside the processes that form/deform vacancies within the interfaces. Just like with the HFM, this model implies that the occurring reactions at the metal/film interfaced are rate controlling. Although PDM attributes the current drop to the decrease of the potential drop at the metal/film interface as thickening of the oxide film takes place instead of the decrease of field strength with oxide film growth [113]. This is indicated within their equation for film growth:

Equation 2.19 Rate of film growth under potentiostatic conditions [112]

$$\frac{dL}{dt} = ae^{-bL} - c$$

Where a and b are constants depending on the kinetic parameters of the interfacial reactions, with c being the dissolution rate which is dependant on the electrolyte properties. When under steady-state conditions with no alterations to the oxidation state upon loss of cations from the film, Equation 2.20 yields for the steady-state film thickness L_{ss}:

Equation 2.20 Steady-state thickness L_{ss} [112]

$$L_{ss} = \left(\frac{1-\alpha}{\varepsilon}\right)V + \left(\frac{2.303n}{\alpha_2 K} - \frac{\beta}{\varepsilon}\right)pH + \frac{1}{\alpha_2 K}\ln\left(\frac{k_2^0}{k_s^0}\right)$$

Where $K = \gamma\varepsilon$

The transfer coefficient and standard rate constant for the generation of oxygen vacancies at the interface are represented by k_2^0 and α_2 respectively, n represents the kinetic order of the rate of the dissolution reaction for H^+, the dependence of the drop in potential across the interface of the film/solution on pH is represented via β and k_s^0 is the standard rate constant for dissolution of the film. Integration of this equation with the limits (L_0, t=0, V) to (L,t, V+∆V), enables the transient in film thickness to be expressed; indicated in Equation 2.21.

Equation 2.21 Expression for the current transient in film thickness [112]

$$L(t) = L_0 + \left(\frac{1}{b}\right)\ln[1 + \frac{a'}{c}e^{-bL_0(e^{bct}-1)}] - ct$$

Where $a' = \alpha e^{\alpha\alpha 2\chi\gamma\Delta V}$ and $\gamma = \frac{F}{RT}$

Where χ is the stoichiometry of the oxide ($MO_{\chi/2}$), and α is the polarizability of the interface between the film/electrolyte.

2.6.2 Breakdown of the Passive Film

At transpassive/break potentials or mechanical disruption, alterations to the properties of the passive film and an increase in corrosion rate are observed. This can be the direct result of film oxidation at this potential, the presence of certain anions, or interactions with external bodies. The types of dissolution behaviour are discussed in the following sections.

2.6.2.1 Dissolution by Oxidation

Uniform dissolution of the film occurs when the passive film is oxidised, producing species that have a higher solubility. This is common for metals in column VI, such as chromium, molybdenum, and tungsten, which form soluble oxyanions in the +6 valence state [84].

For chromium, Cr_2O_3 is formed upon passivation, providing a protective barrier against the environment. Within transpassive potentials, the metal is oxidised into the hexavalent form, which possesses superior solubility in aqueous media, forming either CrO_4^{2-} (basic conditions) or $Cr_2O_7^{2-}$ (acidic conditions).

2.6.2.2 Dissolution via Localised Pitting

When the alloys are in the presence of particular anions, such as chloride, they lose their passivity above a certain potential, known as the pitting potential. This leads to metal dissolution from localised sites when a

breakdown has occurred and is responsible for pitting corrosion. There are three main mechanisms for the film dissolution and pit initiation, which are: anion penetration, anion adsorption, and dissolution through defects

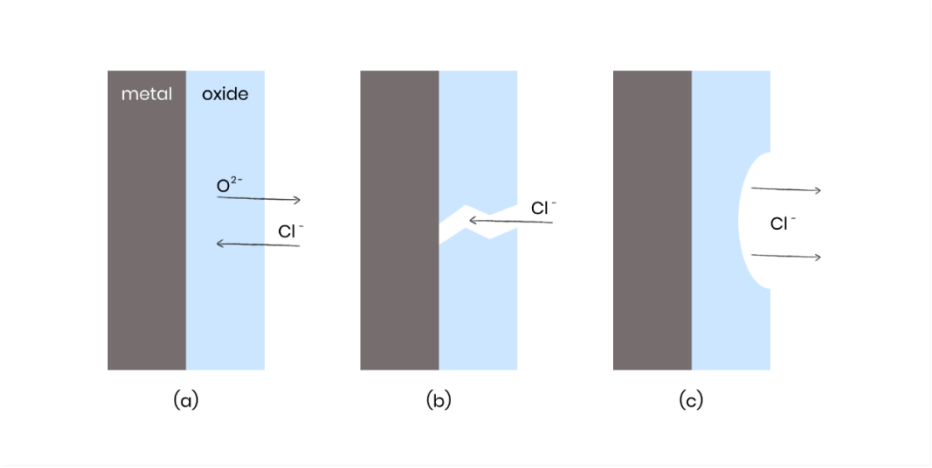

Figure 2.24 The proposed anodic dissolution mechanisms in the presence of aggressive anions such as chloride (a) Anion penetration (b) Dissolution through defects (c) Anion adsorption. Adapted from [84]

Anion penetration - Chloride or other aggressive anions present penetrate the passive film where they interchange with O^{2-} ions in the crystal lattice. This alters the film's properties, increasing its conductivity and aiding dissolution as vacancies occur due to size differences between the divalent and monovalent species [84]. This specific process is aided by the induction time which becomes smaller at higher potentials with increasing concentrations of chloride ions [114].

Anion adsorption - This theory is built upon the adsorption of aggressive species on the surface of the alloy, which displaces the outer hydroxy layer. The adsorption of these ions leads to thinning of the film, eventually leading to a breakdown in a localised site [84]. Evidence for this mechanism has been provided via experiments using a rotating ring-disk electrode [115].

Dissolution through defects - Several authors have attributed anodic depassivation to dissolution through defects, where aggressive anions migrate towards pre-existing defects in the film, such as cracks or pores [84,91]. These defects form in brittle oxide films due to the plastic deformation owed to the metal underneath. At these defects, there could be direct contact with the metal and the electrolyte, leading to localised rapid dissolution and pit growth. This process occurs like crevice corrosion which was explained earlier on.

2.6.2.3 Dissolution via Wear Accelerated Corrosion

Wear can drastically increase the corrosion rate by leading to local thinning and even removal of a passive film. Models have been used to describe this phenomenon which assumes that plastic deformity occurs at the point of contact between the asperity and the alloy and follows Archard's approach [116]. Local breakdown of the film and corrosion of the fresh surface is implied by the plastic deformation of the asperity junction, with new asperities being formed as a result of sliding [117].

Mischler [117] described a continuous local depassivation/repassivation process of a passive metal in terms of accelerated corrosion current I; this is demonstrated in Equation 2.22. Where k is the proportionality factor which is dependent on the total number of asperities in contact with the alloy, v_s is the velocity at which sliding occurs, Q is the charge density of passivation, F_n is the normal force, H is the hardness of metal indentation, and exponent b is a function of the contact geometry.

Equation 2.22 Wear accelerated corrosion describing the process of continuous local depassivation/repassivation of a passive metal [117]

$$I = kv_sQ(\frac{F_n}{H})^b$$

2.6.3 Repassivation Process

The process in which an oxide film re-establishes itself due to oxidation of an exposed surface is known as repassivation; this can occur when a passive film has been compromised/removed. Once the film has been compromised/removed from a passive alloy, the metal is exposed to the environment, so the rate at which repassivation occurs is vital to minimise corrosion. The metal elements can also oxidize into the environment alongside interacting with oxidants to re-establish the oxide layer. The potential pathways are shown in Equations 2.23.

Equation 2.23 The passivation and dissolution pathways for an active-passive metal

$$M_{(s)} \rightarrow M^{n+}_{(aq)} + ne^-$$

$$M_{(s)} + O_{2_{(g)}} \rightarrow MO_{2_{(s)}}$$

$$M_{(s)} + \frac{n}{2} H_2O_{(l)} \rightarrow MO_{n/2_{(s)}} + nH^+_{(aq)} + ne^-$$

Both the dissolution and passivation pathways generate free electrons, these can be detected as current transients. This implies that the formed transient is formed of the sum of dissolution and oxide film growth currents. Ambrose [118] noted that as an oxide layer is developing, the fraction of area protected by oxide (θ) increases with time. By assuming the height of the film is constant, then the relationship with current is as follows:

Equation 2.24 Shows the current formed from the growth of the oxide film [118,119]

$$i_{film} = \frac{nF\rho v}{M_w} \frac{d\theta}{dt}$$

By applying the kinetics, the film growth rate, i_{film} is dependant on Faradays Law as well as the regrowth rate of the passive layer. Where ρ is the film's density, v is the total volume of oxide to grow, M_w is the molecular weight, and n is the overall transferred charge.

For the pathway of ionic dissolution, Tafel-like behaviour of the exposed alloy must be assumed to enable the current formed to be expressed as:

Equation 2.25 Shows the current formed from ionic dissolution [118,119]

$$i_{diss} = i_0^{diss}(1-\theta)e^{\frac{V-V^{eq}}{\beta}}$$

An exponential time decay of the total current when a fixed potential is applied to the surface is formed from the differential equation. Where i_0^{diss} represents current density due to dissolution across the surface of the exposed alloy, V is the voltage change due to dissolution of the alloy, and β is the Tafel constant. While there are many assumptions with these models, they give good interpretations of the repassivation process and have been used throughout research [118].

The total anodic current produced is, therefore:

Equation 2.26 Shows the total anodic current produced from repassivation [118,119]

$$i = i_{film} + i_{diss} = \frac{nF\rho v}{M_w}\frac{d\theta}{dt} + i_0^{diss}(1-\theta)e^{\frac{V-V^{eq}}{\beta}}$$

$$\text{Where } \theta(t) = 1 - e^{(\frac{-t}{\tau})}$$

Goldberg et al. [120] noted that this differential equation resulted in an exponential time decay for the overall current and recommended fitting a first-order decay curve to the data. This enables the repassivation kinetics in numerous electrolytes during corrosion to be determined, with the findings displaying the applied potential and environment drastically influence the repassivation of a CoCrMo alloy [120]. Sun [121] expanded on this initial model, determining that a second-order decay curve gives a better representation of the data seeing as it reflects on the complex nature of the reforming film, this is dependent on the oxygen diffusion rate to reach the surface of the alloy. As it accounts for both the coverage of the surface with oxide and then it's thickening to its maximum state, which isn't taking into account for the first-order decay model [121,122].

The second-order equation is shown in Equation 2.27, with a comparison of the first and second-order fit for repassivation of CoCrMo in Figure 2.25.

Equation 2.27 Depicts the second-order decay fit [122,123]

$$I(t) = I_1 e^{(\frac{-t}{\tau_1})} + I_2 e^{(\frac{-t}{\tau_2})} + I_3$$

Where $I(t)$ represents the overall current formed in regards to time, t is the time period of the process, I_1 and I_2 correspond to the maximum currents of the exponential curves, τ_1 and τ_2 correspond to the time constants of the formed decay curves with I_3 being the final steady-state current achieved.

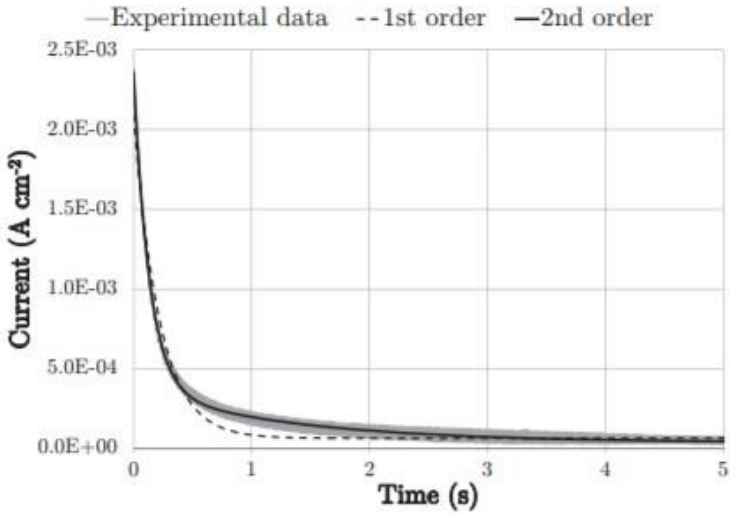

Figure 2.25 Comparison of a first and second-order fit for CoCrMo in simulated bodily fluids [123]

2.7 Summary of Reviewed Literature

Corrosion, hip replacements, the passive nature of metallic alloys, and the biological environment has been reviewed in this chapter. Although there has been much research done into this field in recent years, there are still numerous questions that need answering. Such as the surface interactions of the protein with the alloy for any condition the implant might experience and, more importantly, how these interactions occur.

Up to now, there has not been a comprehensive review of CoCrMo from a purely electrochemical viewpoint. This enables a foundation to be built in which the interactions with the alloy and electrolyte are fully understood in the absence of wear. In this thesis, particular focus will be placed on the role of BSA on the passive film pre and post oxide removal to assess how the corrosion resistance of the implant varies over time and the potential adverse health effects this brings. Studies have shown that molybdenum has a clear affinity for BSA. However, the reason for this affinity and why it is prioritised over cobalt and chromium is unknown. To address this, focus will be placed on the binding interactions of metal ions with BSA, this data will then be related to the formation of the protective biofilm. This will enable a deeper understanding of the mechanisms in play and developing the future performance of these implants.

Chapter 3
Experimental Methodology and Techniques Utilised

3.1 Introduction

The following chapter summarizes the experimental procedures utilised throughout this project and gives a detailed outline of the workings of all of the techniques. This includes sample preparation, electrochemical measurements, surface chemistry analysis, and electrolyte analysis.

3.2 Experimental Setup

3.2.1 Metal and Electrolytes under Investigation

The alloy under investigation was low carbon (LC) CoCrMo (ASTM 1537-94). Plates with a thickness of 3 mm (Ø = 6 mm) were cut from rods which gave a face surface area of 0.28 cm^2. Table 3.1 indicates the composition of the alloy under investigation according to ASTM [124].

Table 3.1 The weight composition of LC CoCrMo (ASTM 1537-94). Published previously within [125]

	Co %	Cr %	Ni %	Mo %	C %	Other Elements
LC CoCrMo	66	27	0.2	5.5	<0.04	-

Corrosion of CoCrMo was simulated in 100 mL of the following environments: saline (0.9%) and phosphate-buffered saline (PBS), with varying amounts of bovine serum albumin powder (BSA, 96%, Fischer Scientific) present which ranged from 0 to 4 g/L. The composition of PBS is shown in Table 3.2.

The saline solution signifies basic bodily fluids seeing as it contains a comparable level of chloride ions to a person. The impact of phosphates on the alloy was evaluated using PBS solution, which was made from PBS powder (98.9 g forms 10 L of solution, Fischer Scientific). BSA was used to simulate a more natural environment, due to it being a model protein of human serum albumin (HSA) as it possesses similarities within its shape (spheroid, 3.8 nm x 3.8 nm x 15 nm), composition (583 amino acid residues, overall negative charge), binding sites and molecular weight (66.5 kDa) [88,126]. The

use of BSA for all forms of research allows for standardisation between different research whilst also being easily accessible [126]. Albumin was investigated due to its low relative weight and high concentration within the serum; therefore, due to the laws of mass transportation arrives first at the implant and plays a key role in initial adsorption [62,75,88]. The experiments enable the effects of protein to be observed and how changes in its concentration affect the corrosion behaviour of CoCrMo and any possible mechanisms that take place.

Table 3.2 Indicates the individual components of PBS solution. Published previously within [125]

Compound	Concentration (mmol/l)	Concentration (g/l)
NaCl	137	8.00
KCl	2.70	0.20
Na_2HPO_4	10.0	1.44
KH_2PO_4	1.80	0.24

3.2.1 Sample Preparation

The metal samples were mechanically polished utilising a Grinder Polisher (Buehler, DE) to attain a surface roughness (R_a) of ~10 nm. Firstly, wet grinding of the sample using SiC paper with a coarseness of 120 was undertaken followed by 320,600,800 and 1200. Then the sample was polished using a diamond suspension of 6 microns followed by 3 microns to obtain a mirror-like finish to the surface of the sample, which will undergo testing. The freshly polished sample was then washed with deionised water and dried using compressed air; this procedure was done immediately before the samples were used.

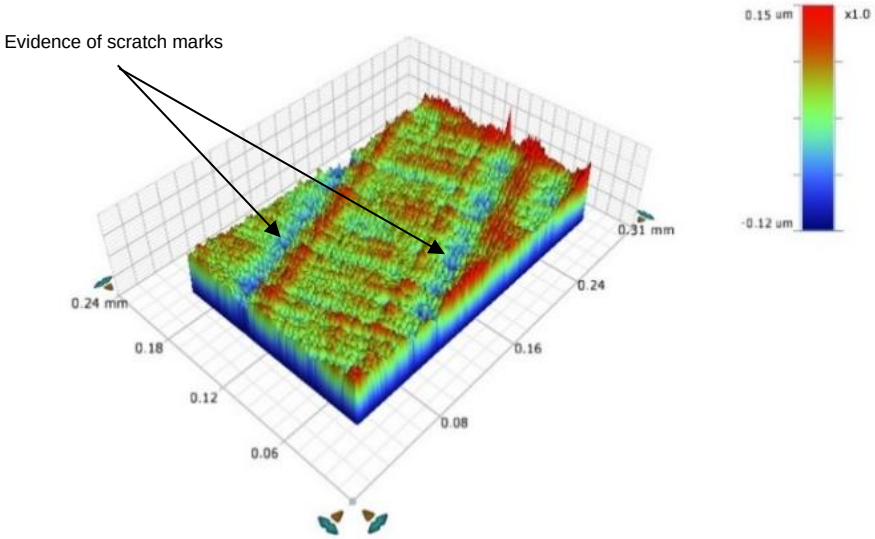

Figure 3.1 Surface of the freshly polished CoCrMo surface via White light interferometry (R_a~10 nm)

3.3 Electrochemical Techniques

Throughout this research, electrochemical techniques have been used to assess corrosion, passivity, and the role of the lubricant on the electrochemical properties of CoCrMo surfaces. A post-test assessment was used to determine any mechanisms that have taken place. This meant a custom electrochemical cell had to be developed, enabling samples to be easily transferred to the different analytical instruments indicated within Figure 3.2.

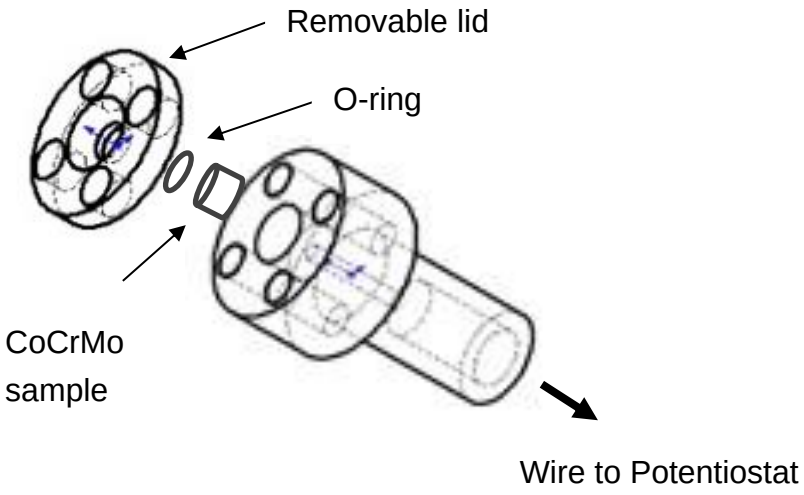

Figure 3.2 The designed sample holder used for the electrochemical tests (acts as the working electrode). Published previously within [125]

The sample is linked to the potentiostat as it rests upon a copper plate within the holder, which was soldered to a wire enabling a connection to be made. A quality connection of the sample/copper plate was ensured via a detachable lid and an O-ring which is held tightly in place with screws. The use of the O-ring also helps prevent any solution from getting through to the copper plate. The total surface area of the sample exposed to the environment was 0.13 cm^2. Utilising this holder also meant that after electrochemical testing was complete, the sample could simply be withdrawn for surface analysis.

The electrochemical behaviour was analysed using a potentiostat (Princeton Applied Research potentiostat/galvanostat Model 263A) which was controlled via a computer. The electrical impedance was measured using the Multi Autolab (Metrohm M204), which utilises the FRA32M module, as this measurement was not possible to undertake on the Princeton. For all of the electrochemical experiments, a three-electrode cell was utilised, which consists of a working electrode (WE), and a combination reference/counter electrode which consists of an Ag-AgCl reference electrode (3M KCl) and a platinum counter electrode (CE). This reference electrode (RE) has an offset of 0.222 V_{SHE} [127].

All of the electrochemical tests undertaken were completed at least three times to provide reliable data. An example of the reproducible data is shown

in Figure 3.3; the data is for a potentiodynamic scan of CoCrMo within a saline solution.

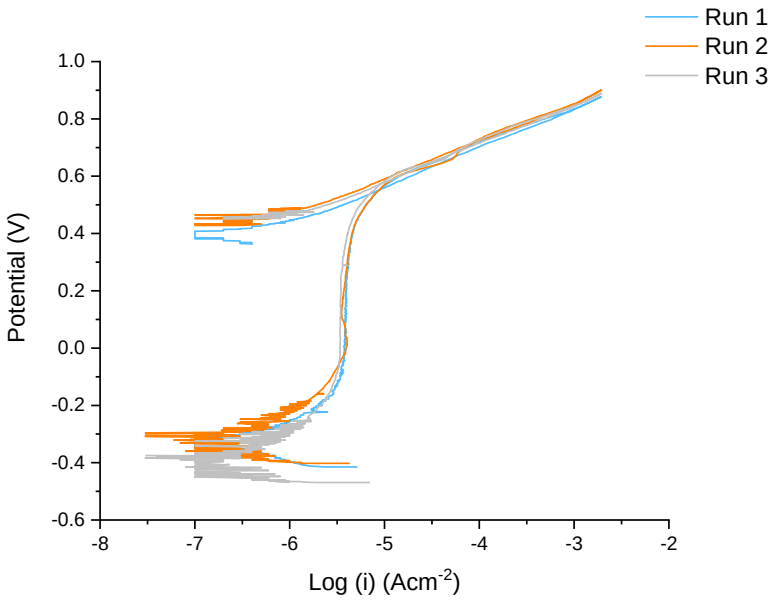

Figure 3.3 An example of reproducibility for the electrochemical experiments conducted, potentiodynamic scan for CoCrMo in a saline environment

3.3.1 Open Circuit Potential (OCP)

As detailed previously, the OCP is the difference in potential between the WE and RE when there is no current present. As such, the rates of the anodic and cathodic reactions are the same. The OCP for all conducted tests was observed for 1 hour to let stabilisation occur, with the rate of data collection being at 1 point per second.

3.3.2 Potentiodynamic Polarization

The overall corrosion behaviour of CoCrMo was assessed by undertaking both anodic and cathodic polarization curves within the different electrolytes. For these experiments, the potential is continuously scanned either in the anodic or cathodic direction with respect to OCP; the corresponding current is recorded throughout the scan. Separate scans were undertaken to avoid unnecessary damage to the surface due to drastically shifting the potential from cathodic to anodic. Munoz et al. [100] observed this phenomenon in conducted electrochemical tests with CoCrMo in differences of up to 0.65V between the OCP and E_{corr} when tests were done in one complete scan.

Polarization of samples was conducted by stepping voltage either up to $1V_{RE}$ for the anodic tests and down to $-1V_{RE}$ for the cathodic ones with a step height of 0.167 mV/s. This is the standard ASTM scan rate, with faster scan rates often leading to distorted data due to the sample able to stabilise at each potential resulting in more active noise and key values (passivation potential, breakdown potential) occurring at more positive values [127]. For the anodic scan, a backward scan was also included (500 $\mu A/cm^2$) for the anodic potentiodynamic experiments so that the repassivation behaviour of the material could be investigated. This gave a deeper insight into understanding the corrosion mechanisms of localised corrosion via comparing the current density of the forward and backward conditions. An example of an annotated anodic potentiodynamic graph for CoCrMo in PBS is shown in Figure 3.4. Key data that was extracted from the graph was the corrosion potential (E_{corr}), the passivation current (i_p), the breakdown potential (E_b), and the repassivation potential (E_r).

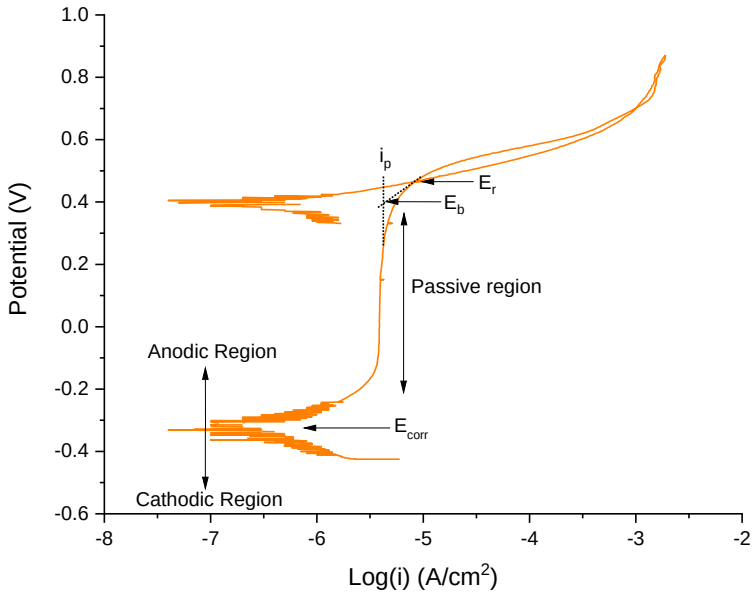

Figure 3.4 Annotated anodic potentiodynamic graph for CoCrMo in PBS

Tafel analysis was used to analyse the polarization graphs occurring at the E_{corr} by identifying the linear portions of the anodic (β_a) and cathodic (β_c) slopes. These slopes were established within the linear region 100 mV above/below the OCP, with extrapolation being undertaken to the point at which these lines intersect; the potential of this intersection is the corrosion potential (E_{corr}) with the current corresponding to (i_{corr}) [83].

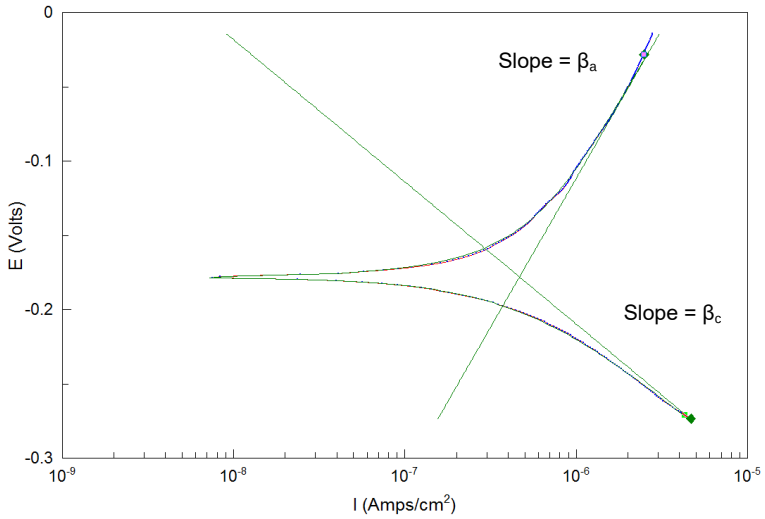

Figure 3.5 Example of Tafel extrapolation process for CoCrMo in PBS solution. Published previously within [125]

The passivation current (i_p) was taken from the potentiodynamic scan when the current became stable due to passivation. Breakdown of the passive film was taken from the point at which extrapolated passive and trans-passive lines intersected (Figure 3.4) [83]. Repassivation occurs at the point in which the forward and backward scans cross one another.

3.3.3 Potentiostatic Polarization

Potentiostatic polarization involves measuring the current density when a specific potential difference is imposed on the system (i.e. between WE and RE). These experiments were undertaken to investigate the effects of potential on the corrosion kinetics and properties of the alloy; thus, for this study, three voltage regions were studied based to observe this, which were based on the potentiodynamic polarization observations:

- Cathodic (-1 V_{RE})
- Passive (+0.1 V_{RE})
- Transpassive (+1 V_{RE})

The cathodic potential was chosen to observe metal/environment interactions as the applied potential is more negative than that of the standard reduction potential of $Cr/Cr^{2+,}$ enabling the removal of the oxide film, yet sufficiently noble to not produce hydrogen [128]. This passive potential was used seeing as it is well defined within the passive region for all of the conditions investigated, with OCP being used as a comparison that the effect of potential has on the passive film. A transpassive potential was chosen to see how active corrosion affects the surface of the alloy and how this alters interactions with the environment.

Each potential was applied to the sample for one hour, with the resulting currents being samples at a rate of 100 Hz.

3.3.3.1 Charge of Dissolution

The total measured charge (Q_T) at anodic potentials can be determined by integrating the current-time graph obtained, assuming only anodic oxidation occurs. An example of this is depicted within Figure 3.6; the integration is equivalent to the area underneath the current-time data obtained. The use of ICP-MS alongside this enables the comparison of charge contributions from all of the different factors in place.

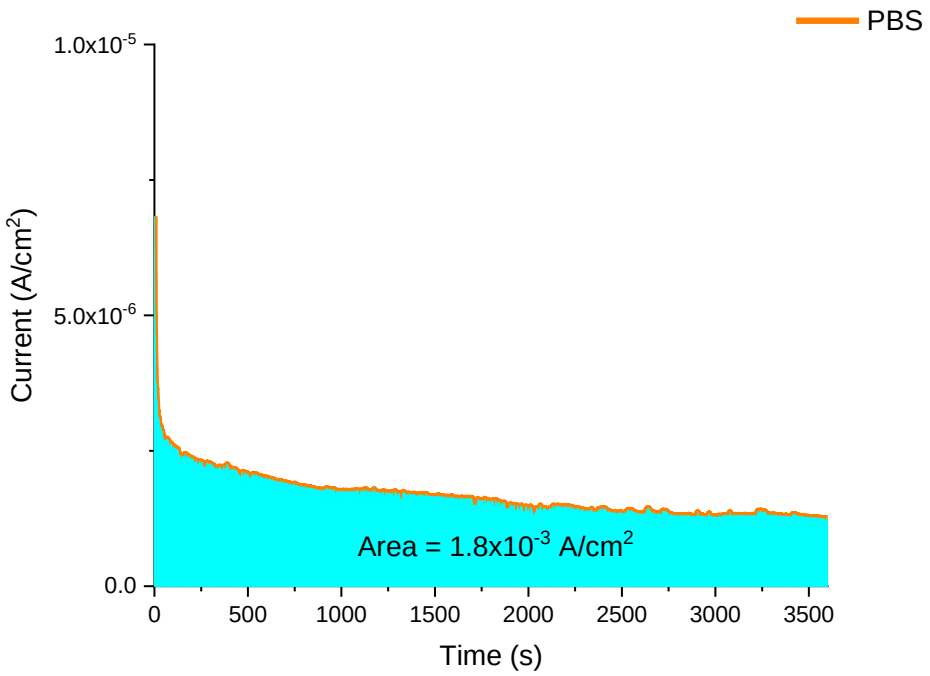

Figure 3.6 Integration of the current-time graph obtained for passively polarizing (+0.1V_{RE}) a CoCrMo sample in PBS solution

For certain conditions (OCP and Passive), the total measured charge is equal to the growth of the oxide (Q_{film}) and the number of ions lost to the solution (Q_{diss}). As all conducted tests were undertaken in aerated conditions, a contribution from the reduction of oxygen (Q_{O_2}) is possible. Therefore it is possible to deduce that the total measured charge (Q_t) can be represented by the following:

Equation 3.1 Contributors to the total measured charge for OCP and Passive conditions [102]

$$Q_t = Q_{film} + Q_{diss} + Q_{O_2}$$

By taking into account that the oxide film is mainly comprised of chromium (III) oxide (M_w = 152 $gmol^{-1}$), which has a density (ρ) of 5.22 gcm^{-3}. Utilising the literature, we can assume a thickness of 2 nm when polarized at passive conditions, the charge of film formation (Ccm^{-2}) can be determined by using Equation 3.2 [100,102,105].

Equation 3.2 Determination of the charge contribution towards film growth

$$Q_{film} = \frac{2d\rho n_{Cr}F}{M_w}$$

The stoichiometric factor of Cr within Cr_2O_3 is represented by the two times multiplication factor (2 Cr atoms in each molecule of Cr_2O_3), d is the thickness of the film formed (m), n_{Cr} is the valence oxidation of chromium, and F being the Faraday constant.

The use of Faraday's law allows for the conversion of the quantities of metallic ions from ICP-MS analysis into the total charge lost (Equation 3.3).

Equation 3.3 Determination of the charge contribution towards ion dissolution

$$Q_{diss} = \sum \frac{|M|_i n_i VF}{PM_i}$$

Where $|M|_i$ is the concentration of each ion present in the solution, n_i is the valency of oxidation (Co(II), Cr(III), Mo(IV)), V is the volume of electrolyte used

(100 mL), F is the Faradays constant with PM_i is the atomic mass of each metal.

3.3.3.2 Repassivation Investigation

To investigate the kinetics of repassivation, potentiostatic polarization was used. A sufficient cathodic potential was first applied to the WE to remove the passive film (-1V_{RE} for 30 mins) before shifting to a passive potential (+0.1V_{RE} for 30 mins) and monitoring the current transient formed. These times were chosen as it provides the system more than enough time to reach steady-state for each section whilst keeping the total time under potential consistent, enabling post-assessment comparisons to be able to be drawn up against the standard potentiostatic tests. The resultant currents were sampled at a rate of 100 Hz. An example of the current transient formed is shown in Figure 3.7.

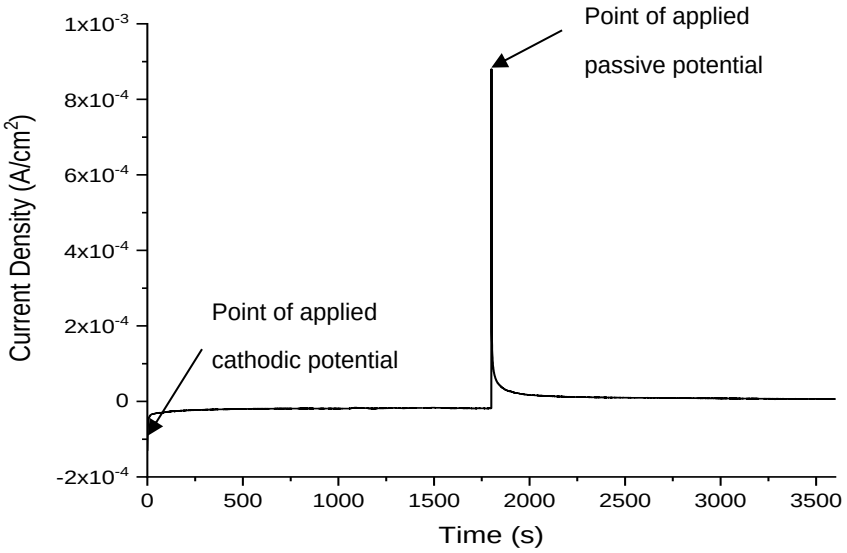

Figure 3.7 Repassivation investigation for CoCrMo in PBS, repassivated at +0.1V_{RE}

Analysis of this transient was then undertaken by fitting to a second-order decay curve (theory explained in Section 2.6.3) to obtain the kinetics of the reaction as it accounts for the complexity of the film growth [83-86]. This fit was applied by the use of Origin Pro and shown in Figure 3.8; for clarity, the difference between the first-order fit is also indicated.

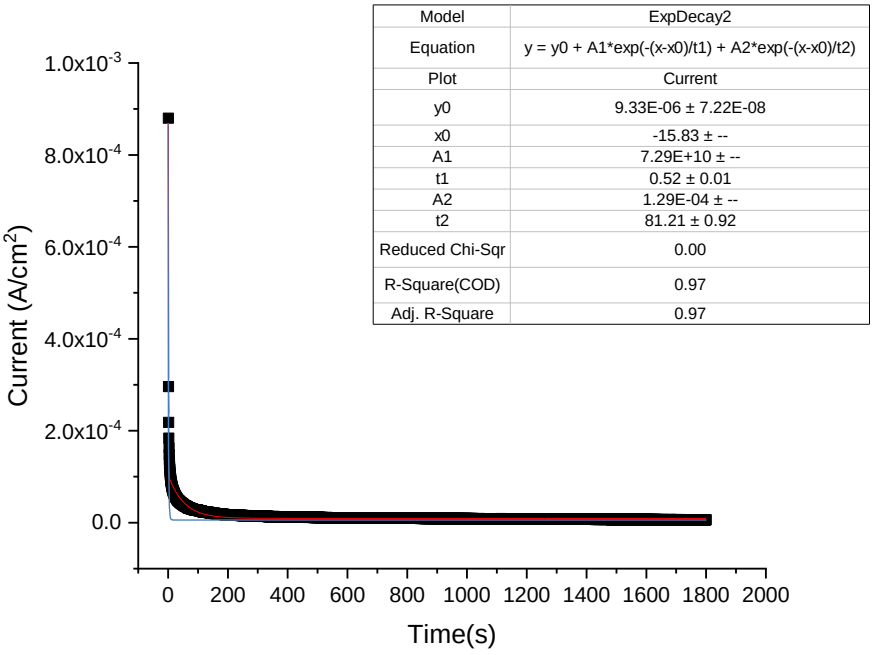

Figure 3.8 An example of the differences between the first order (blue line) and second-order (red line) exponential fits for CoCrMo repassivated at +0.1V_{RE} in PBS. Published previously within [125]

3.3.4 Electrochemical Impedance Spectroscopy (EIS)

In this study, the Cathodic (-1 V_{RE}), OCP, Passive (+0.1 V_{RE}), Transpassive (+1 V_{RE}) were investigated to determine differences in the properties of the surface.

The samples were polarized for 10 frequency decades from 1 mHz to 10^5 Hz with an amplitude of ±10 mV. To investigate the mechanisms behind the data obtained, an equivalent circuit was applied to the data; this can be applied as electrochemical systems often behave as simple electric cells. For all analysis undertaken, the Randles circuit was used as the starting point with more complex features adding depending on the features present [104,107]. This analysis was undertaken by using the Nova 2.1 software, strictly following the guidelines set out by Mektikos [107].

Examples of EIS results for passive conditions are shown in Figure 3.9a; there are high values of impedance present (~40 KΩcm^2) with capacitive behaviour indicated via the semicircle shape obtained; this could be caused via two superposed semicircles. The first time constant relates to the oxide resistance (R_{in}/C_{in}), whilst the second corresponds to the resistance of charge transfer (R_{out}/C_{out}). As always, there is also the resistance of the solution (R_s). A constant phase element was utilised instead of a capacitor seeing as it

accounts for the non-ideal behaviour of the capacitive elements which arise due to a variety of different physical phenomena such as the heterogeneity of the surface, this is a direct result of surface roughness, impurities, dislocations, and the occurrence of grain boundaries. This cell (Figure 3.9a) shows a good fit with the raw data obtained and has been used to model CoCrMo alloys throughout the literature [89,100,104]. The data obtained for OCP conditions were similar, resulting in the same cell being used to fit the data; this would be due to both conditions possessing a passive film on the surface of the alloy.

For the cathodic conditions examined, in Figure 3.9b, the obtained plot is comprised of a small-semi circle located at high frequency, which is followed by an increasing line at lower frequencies. This implies the existence of a diffusion-controlled reaction which is characterised via Warburg impedance (W). The data was fitted to the equivalent circuit presented in Figure 3.9b and shows a good fit. Vidal et al. [104] also found this circuit to be the best fit for these conditions

The spectrum obtained under trans-passive conditions is characterised by the high frequency capacitive, which reflects the high field-assisted migration of defects in the alloy [104]. There is then an inductive loop (L/R) at medium frequency due to the relaxation of the corrosion product charge formed at the interface formed by the number of cation vacancies [104]. At the lowest frequencies, Faradaic pseudocapacitance is detected, indicating the presence of an inner layer (CPE_{in}/R_{in}) which originates due to electroporation of oxidants present onto the electrode [104,129]. A good description of this cell was found indicated in Figure 3.9c.

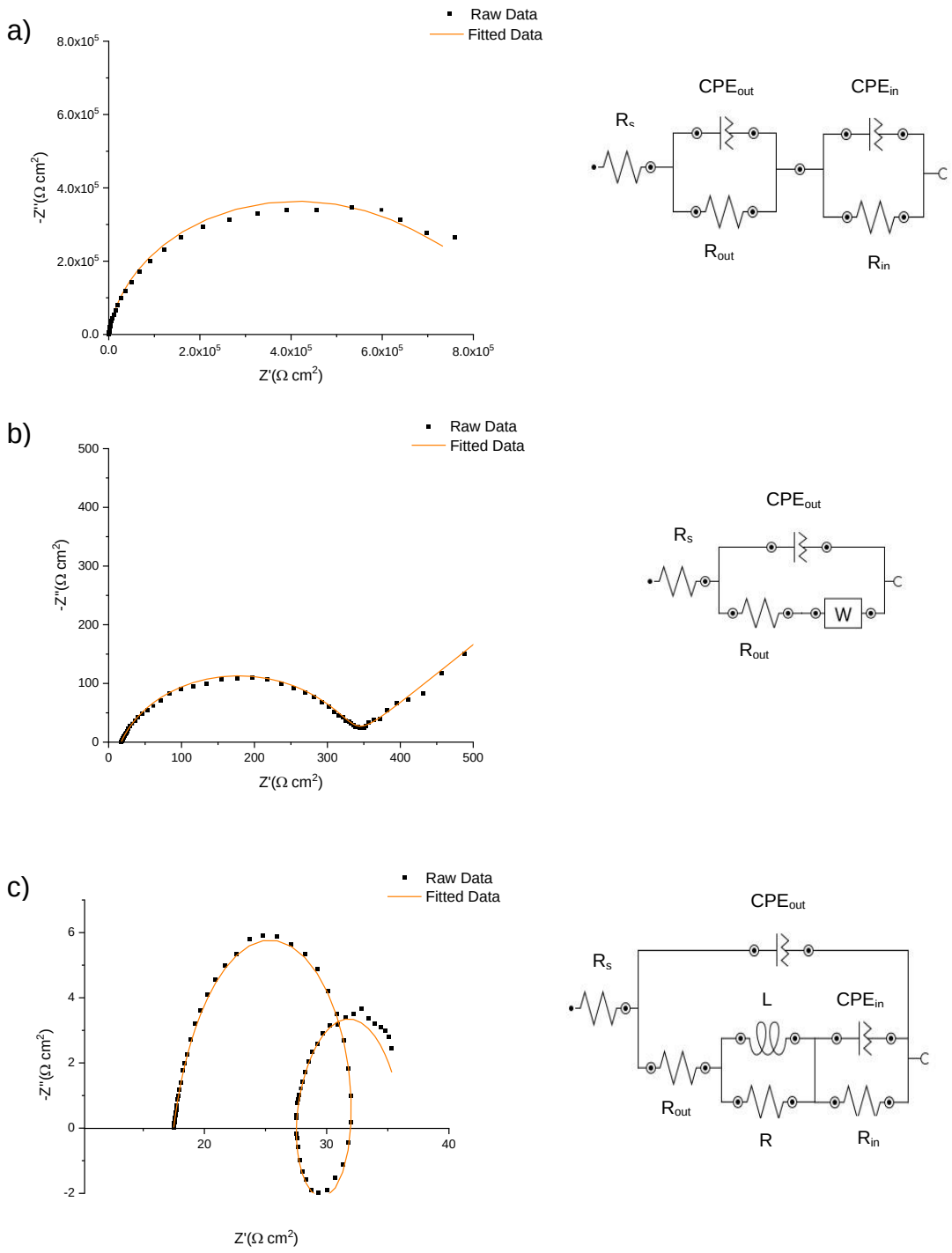

Figure 3.9 EIS data obtained for CoCrMo in PBS for the various conditions, showing a suitable fit with their respective equivalent circuits (a) Passive (+0.1V_{RE}) (b) Cathodic (-1V_{RE}) (c) Trans-passive (+1V_{RE})

3.4 Surface and Chemical Analysis Techniques

A range of surface characterisation techniques were employed to obtain a deeper sense of how the surface is affected by the potential applied and the surrounding environment. Techniques have also been utilised to analyse changes in the environment due to the corrosion of the alloy.

3.4.1 Optical Microscopy

A Leica DM6000M Microscope was used for the physical observation of the changes in the surface of the alloy post-test. LAS V3.8 software was used to capture high-definition images on a variety of lenses (x5, x10, x50). This microscope uses light and a variety of lenses which the power of magnification is dependent on, to view enhanced images of a sample. This enables a quick insight into the structures of corrosion produces.

3.4.2 White Light Interferometry (WLI)

The Bruker NPFlex was utilised to acquire a 3D image of the CoCrMo samples investigated. This is a non-contact technique that uses white light to form the image of the surface; the 3D profile is built up due to the differences in path lengths of the white light and the sample surface. The software used to take key measurements such as surface roughness from a CoCrMo sample was Bruker Vison 64.

3.4.3 Scanning Electron Microscopy (SEM)

SEM uses a highly focused beam of electrons to generate a high-resolution image on the nanometre scale due to the use of electrons which have much shorter wavelengths than the wavelength of light used in optical microscopes. The images were obtained by using the Hitachi TM3030Plus benchtop microscope in secondary electron mode, with an operating voltage of 15 keV. Three areas (25 μm x 25 μm) of each analysed sample were undertaken to ensure reliable results were obtained.

After the sample is mounted in the machine, the chambers are evacuated by the use of a vacuum so that there is no disruption to the electron path. The image is formed due to the scanning of a focused beam of electrons over the surface of the sample. Due to the supplied electrons possessing kinetic energy, it causes the emission of electrons from the outer shell of the sample. The relaxation of electrons within the sample to account for this change then leads to the emission of X-rays which possess specific characteristics of that particular element. The presence of elastic scattering can cause some of the

electrons supplied to be reflected off the sample; these are known as backscattered electrons. These secondary electrons, backscattered electrons, and X-Rays produced from the sample due to the interactions of the sample and electron beam are collected and formed into images.

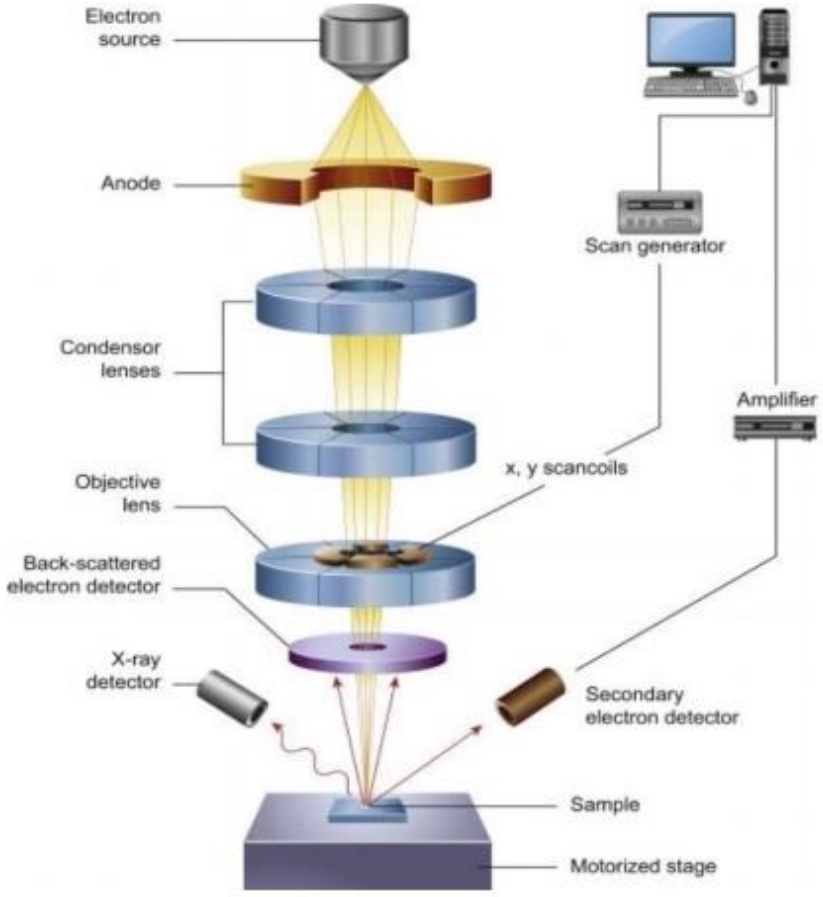

Figure 3.10 Schematic of a SEM [130]

3.4.4 Energy Dispersive X-Ray Spectroscopy (EDX)

EDX is an analytical method for the identification of the elemental composition of a sample; this is used in conjunction with the SEM. The experiments are also being conducted upon the Hitachi TM3030Plus as it possesses an EDX mode. This is a non-destructive technique that detects emitted x-rays from the sample due to the bombardment of the sample with an electron beam. These X-Rays are used to characterise the elemental composition of the surface due to the differences in their energy values.

3.4.5 Focused Ion Beam (FIB)

This process, alongside Transmission Electron Microscopy (TEM), was used to determine the thickness, composition, and morphology of the alloy's surface after being exposed to an electrolyte on the nanoscale.

To undertake this, an area of interest on the sample was identified (Figure 3.11a), with that section then being prepared for TEM by use of the FEI Helios G4 CX DualBeam. To safeguard the alloys surface during this preparation phase, a layer of Pt was deposited upon the surface (Figure 3.11b). Either side of this layer was then milled away to around a depth of 10 μm by use of the ion beam (Figure 3.11c). The sample was then attached to a micromanipulator and cut free from the alloy by severing the remaining attached side using the ion beam (Figure 3.11d). This sample was then attached to the stage with the micromanipulator, then being severed from the sample (Figure 3.11e). Further thinning of the sample was achieved with milling using Ga+ ions with an energy of approximately 5 kV to give a final thickness of between 50 - 100 nm so that the sample was electron transparent (Figure 3.11g).

a)

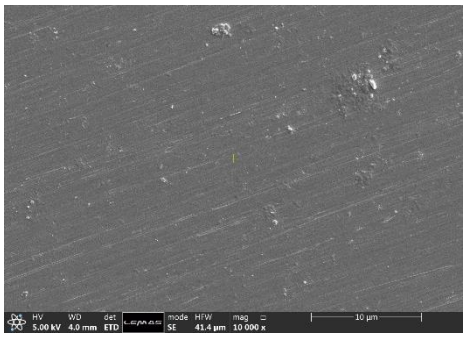

b)

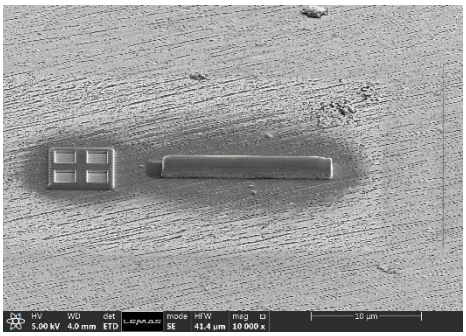

c)

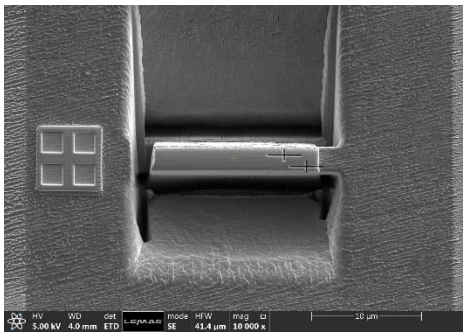

d)

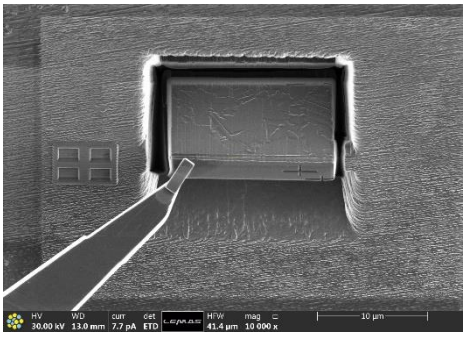

e)

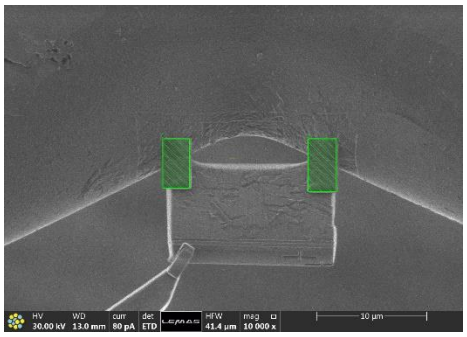

f)

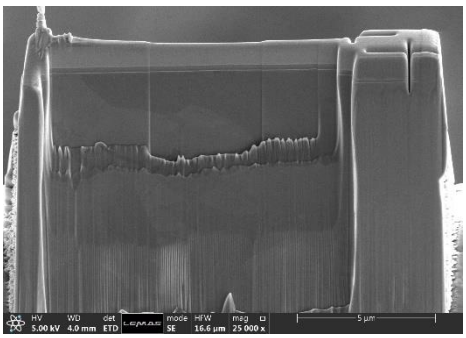

g)

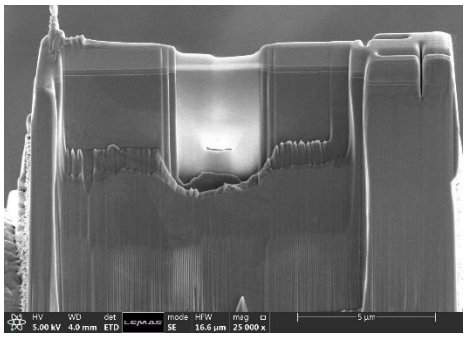

h)

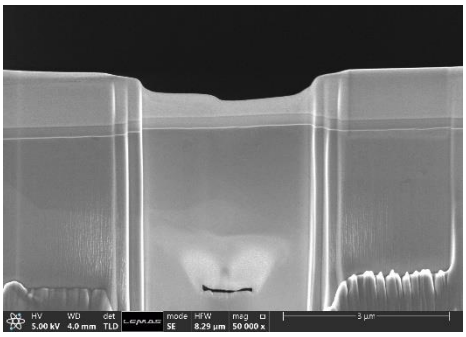

Figure 3.11 The preparation process of FIB-SEM of the TEM section (a) Surface pre-treatment (b) After deposition of the Pt layer (c) Removal of material either side of the Pt layer (d) Removal of sample from bulk material (e) Attachment of sample to the stage (f) Sample prior to thinning (g) Sample after thinning to 50 - 100 nm (h) Close up of the examined section

3.4.6 Transmission Electron Microscopy (TEM)

TEM is another microscopy technique that utilises electrons to form an image. In this case, a high energy beam of electrons is aimed across an extremely-thin sample (<100 nm), with the interactions between the electrons and the sample being used to form an image. This thickness of the sample is key as the electrons must be able to transmit through the sample. This formed image is then amplified and focused onto an imaging device which enables extremely fine details of the inner structures (dislocations and grain boundaries) of the sample to be observed and analysed.

The analysis was undertaken using the FEI Titan3 Themis 300, which also has other built-in analysis tools which were utilised, including EDX, Selective Area Electron Diffraction (SAED), and Electron energy loss spectroscopy (EELS). In this specific case, the electrons are treated as waves and not particles due to the mass and velocity of the emitted electrons. Due to the

differences between the wavenumbers of the electrons and the atomic spacing, the electrons are diffracted. This occurs via elastic scattering as they lose no energy, so they remain at the same wavelength

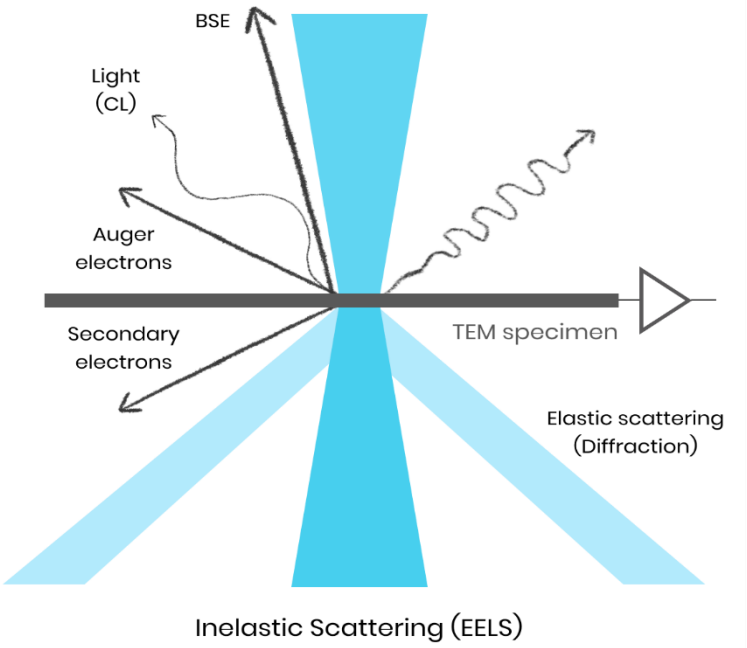

Figure 3.12 Schematic indicating the different scattering's possible and the techniques that take advantage of them. Adapted from [131]

3.4.6.1 Selective Area Electron Diffraction

SAED is used to determine the orientation of the atomic planes within a crystal, where a parallel beam of high-energy electrons is fired at the sample. These electrons possess energy between 100 – 400 keV, enabling them to pass through the ultra-thin sample with ease.

Analysis of the diffraction patterns was undertaken by the use of Digital Micrograph to obtain the d spacings, which can be related to a crystallography database to determine the phase [132].

3.4.6.2 Electron Energy Loss Spectroscopy

EELS can determine the chemical and structural nature of the sample from sub-nanometer areas of interest within the sample. This is due to the differences in the kinetic energy of the electrons within the beam after undergoing inelastic interactions with the material, as these interactions may cause the electrons to lose energy. The core state excitations are labelled according to the type of core state that was excited; Table 3.3 lists the most

common peaks observed. An example of the EELS spectrum standard of an amorphous carbon spectrum is shown in Figure 3.13

Table 3.3 The naming convention for core excitations which are dependent on the quantum numbers of the core states [133]

Label	Core State
K	$1s_{1/2}$
L_1	$2s_{1/2}$
L_2	$2p_{1/2}$
L_3	$2p_{3/2}$
M_1	$3s_{1/2}$
M_2	$3p_{1/2}$
M_3	$3p_{3/2}$
M_4	$3d_{3/2}$
M_5	$3d_{5/2}$

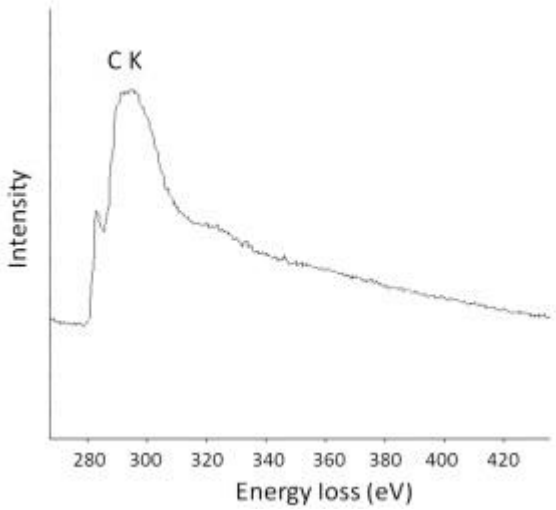

Figure 3.13 EELS spectra for the standard amorphous carbon spectrum [109]

Spectral areas around the known elements within the alloy (Co, Cr, Mo) alongside other key elements (C, O) were undertaken. Subtraction of the

background and noise reduction was utilised before the assignment of the peaks was undertaken by contrasting against EELS databases [134,135].

3.4.7 X-Ray Photoelectron Spectroscopy (XPS)

XPS is a surface sensitive technique that utilises the photoelectric effect to identify elements present within the top few nanometers of the surface, alongside their chemical state. The low-energy X-rays are either emitted from an aluminium or magnesium source (Mg-Kα 1253.6 eV, Al- Kα 1486.6 eV) [106]. These incoming photons lead to the emission of electrons after direct energy transfer from the photon; these emitted electrons are then separated and counted according to their energies. It's this energy that can be related to the atomic and molecular environment, with the number of electrons corresponding to the concentration of the species present.

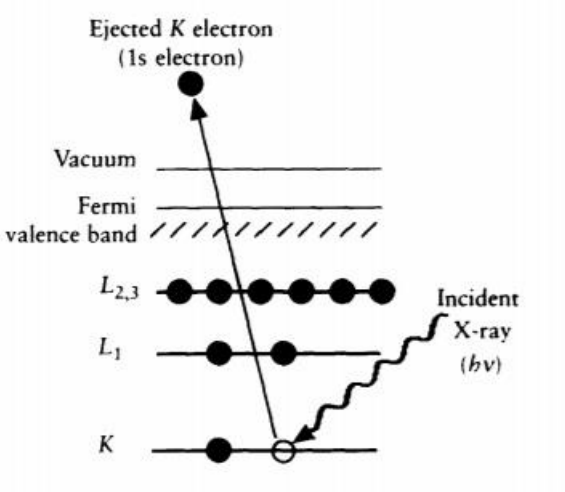

Figure 3.14 Schematic of the XPS process [136]

XPS analysis was undertaken using a monochromatic aluminium K-α X-Ray source with the Thermo Escalab 250. The samples were mounted using carbon table to make sure that no movement of the sample occurred during analysis. The area of the sample under investigation was 500 μm, utilising a power of 150W. Individual peaks of interest were analysed in detail using step size of 0.1 eV along with an energy of 20 eV. The number of scans for each peak was optimized to obtain a good signal/noise ratio. Etching of samples was performed by using monoatomic argon ions from an ion gun attached to the XPS.

CasaXPS fitting software was used to analyse the obtained data sets. For calibration of the binding energy, the carbon 1s peak was set to 285 eV, with this eV change being applying to all spectra of the set. The peaks were then applied a Linear or Shirley baseline fit, which was dependant on the initial

baseline of the peak. Then the peaks were identified, fitted, and deconvoluted following the literature [136].

3.4.8 Atomic Force Microscopy (AFM)

AFM, also known as scanning probe microscopy (SPM), generates a 3D nanoscale image of the surface of a material. This is obtained by measuring any vertical deflection of a cantilever that is run over the surface of the material; these deflections are due to repulsive interactions, which are monitored with high accuracy. A schematic of the AFM is shown in Figure 3.15.

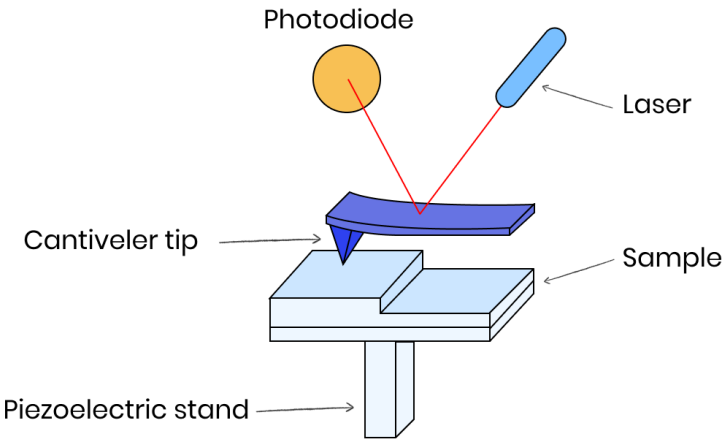

Figure 3.15 Schematic of the AFM

The bend of the lever is monitored via the use of a laser and a photodiode to form the image of the sample. The quantity of this force (F) is dependent on the spring constant of the cantilever (K) and the distance between the tip and sample (x), which is described via Hooke's Law.

Equation 3.4 Hooke's Law

$$F = Kx$$

The topography of CoCrMo was investigated using an AXS SAS (Bruker, USA) a scan size of 10 µm x 10 µm was used as a control going down to smaller areas for particular regions of interest. The AFM was used in Peakforce Quantitative Nanomechanical tapping mode with a silicon tip at a scan rate of 0.528 Hz.

3.4.9 Raman Spectroscopy

Raman is a non-destructive analysis that provides details about the chemical structure, molecular interactions, and polymorphism of a substance. A high-intensity laser source is used, the light is then scattered via the molecules present. Most of the light is scattered at the same wavelength as the source of the laser (Rayleigh Scatter), with a small percentage being scattered at different wavelengths depending on the chemical structure (Raman Scatter). When Raman scattering occurs, the system exchanges energy with the incoming photons, exciting the system, which then decays to vibrational energy levels either above/below the initial state [137]. A frequency shift is then caused due to the energy difference between the scattered and incident photon (Raman shift), which is relative to the up/downshift of the photon.

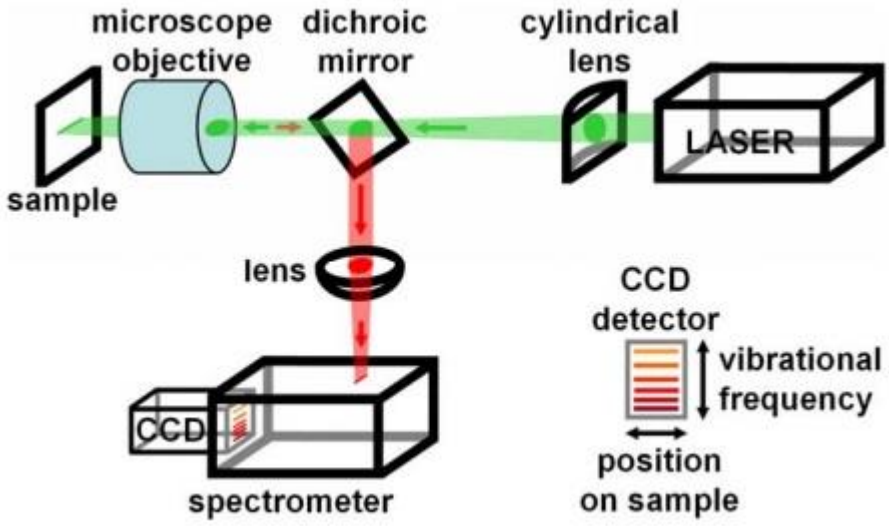

Figure 3.16 Schematic of a Raman spectrometer [138]

Raman was conducted on an InVia spectrometer system (Renishaw, UK). Before the start of any testing, the machine was calibrated to ensure that the laser was working correctly; the machine has a built-in auto-calibration system where the laser focuses onto a silicon sample with a corresponding shift of 520 cm^{-1}. Any offset in the laser was adjusted accordingly. The samples were fixed onto the motorized stage and focused by the use of objective lenses (x5, x20, x50), with the single spot analysis method being used. Spectra were collected using a 785 nm laser with 100% power, 20 seconds exposure time, and 4 accumulations per acquisition to obtain crisp/clean data over a range of 100 - 4000 nm. To ensure that the laser didn't damange the protein different spots were analysed after each run. Peak analysis was undertaken by using

Renishaw's Wire 3.4 software. In the case of peak deconvolution, the peaks were fitted with mixed Gaussian/Lorentzian curves to determine the peak position, intensity, and full width half maximum.

3.4.7.1 Analysis of BSA

As explained previously, BSA is a small globular protein found within Synovial fluid that is comprised of 585 amino chain residues linked together by 17 disulphide bridges. This molecule is folded via the polypeptide chain, which separates the molecule into three different α-helical domains. It is well known throughout the literature that most of the mammalian albumins, including HSA and BSA, contain four different active sites in which metal ions can bind. These active sites all vary in size, structure, and specificity [66].

The specific structure of the secondary (how the amino acids are arranged) and tertiary (three dimensional arrangement of its polypeptide chain in space) structure of BSA has been determined from Raman spectroscopy via analysis of the fingerprint region. The spectra obtained from BSA powder is shown in Figure 3.17, with key features being highlighted upon the spectra. There are multiple bands present, including the Amide I band at 1658 cm^{-1} with Amide III at 1258 cm^{-1}. The C-C vibrations are located within the region of 900 – 950 cm^{-1}, with a strong peak of phenylalanine occurring at 1000 cm^{-1} [139,140].

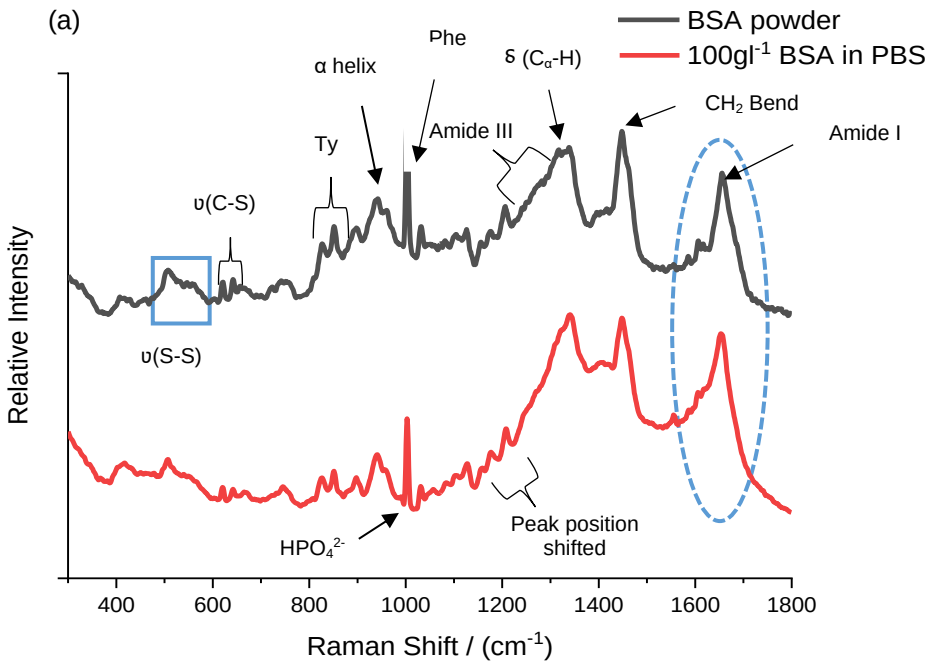

Figure 3.17 Comparison of the Raman fingerprint region of BSA powder and 100 g/L BSA in PBS (300 – 1800 cm^{-1})

Information about the disulphide bonds that hold the molecule together can also be extracted from the spectra. The S-S bond of the cysteine residues are present between 500 – 600 cm^{-1}; this bond can exist in three different conformations which have defined peak positions [140,141]. The peak obtained from the spectra is shown in Figure 3.18, with the structure percentages/indications in Table 3.4.

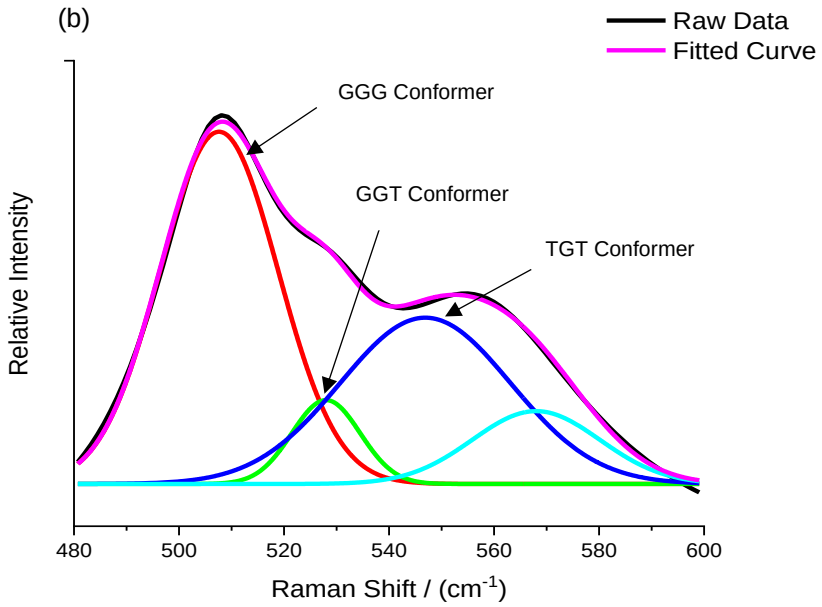

Figure 3.18 Dissection of the disulphide bond of BSA powder (480 – 600 cm^{-1})

Table 3.4 Contributions of the Raman spectra for the S-S peak in BSA powder

Peak	Position / cm^{-1}	Percentage Area / %	Structure Indication
Cystine, S-S	500-510	55	GGG Conformer
	515-525	8	GGT Conformer
	530-550	37	TGT Conformer

These three different conformations are possible due to the different formations that the Cα, Cβ and disulphide bridge can adopt in relation to each other (gauche 90º, trans 180º) to give the molecule its most favourable

thermodynamic configuration depending on steric effects [140,141]. Newman projections depicting this are shown in Figure 3.19.

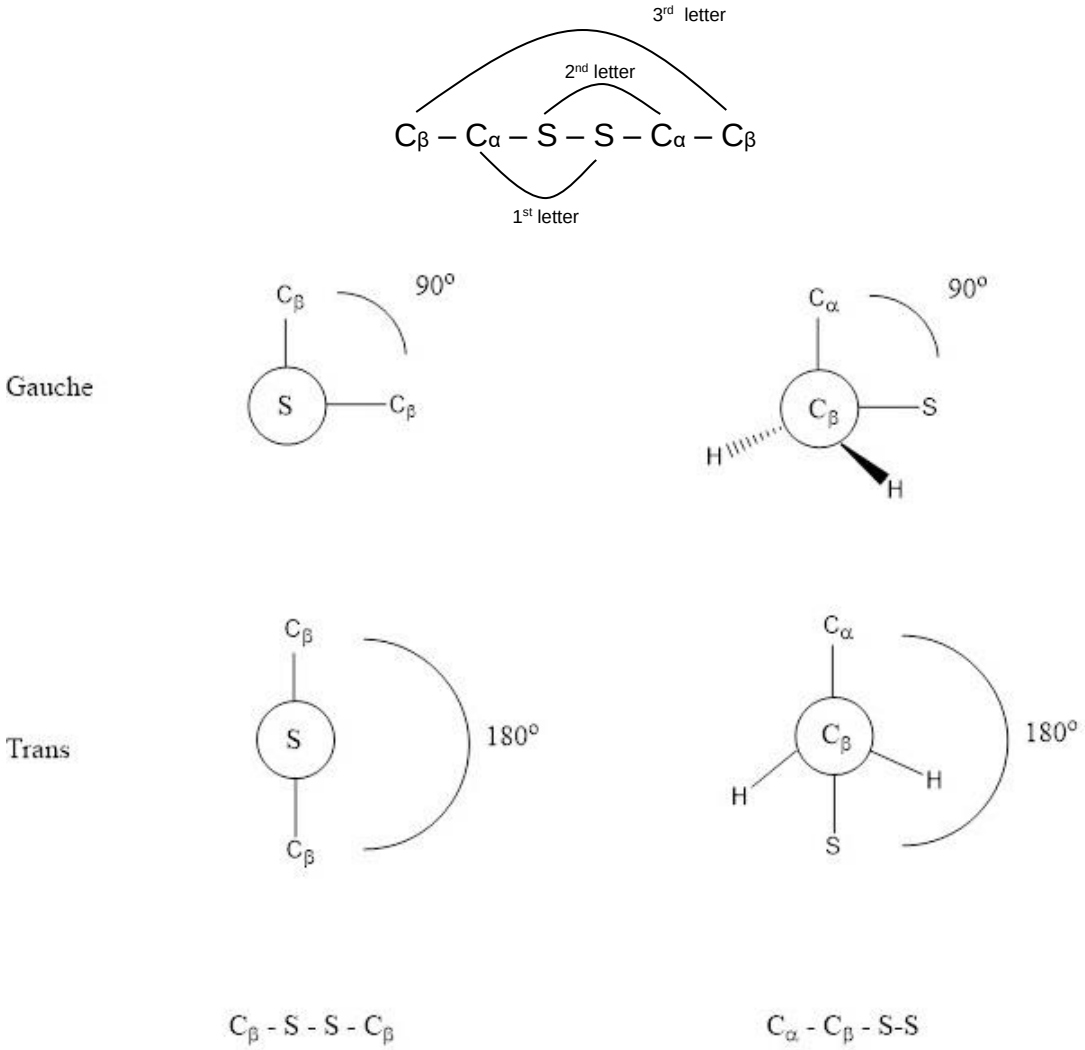

Figure 3.19 Newman projections of both the trans and gauche configurations of the C_β-S-S-C_β and the C_α-C_β-S-S chains

When the BSA powder is present in a solution, slight changes are seen in the spectra. A comparison of the fingerprint region between BSA powder and BSA in PBS solution was shown in Figure 3.17. It can be seen that they consist of basically the same secondary and skeletal structure due to the positions of both Amide I and III. A new peak is produced in the presence of phosphates; this is seen just below 1000 cm^{-1} and corresponds to HPO_4^{2-} [140]. The broadness of the Amide I is due to the protein now being hydrated. The presence of the species also causes changes in the conformation of the S-S bond, with it now being favoured in the TGT conformer over the GGG that was previously favoured for powdered BSA.

3.4.7.2 Structure of the metal salts under investigation

The Raman spectra of the metal salts used are shown in Figure 3.20; these were used as controls. The spectra mainly consist of low Raman shift wavenumbers as the metal ions are bound to an electronegative atom with a high coordination number.

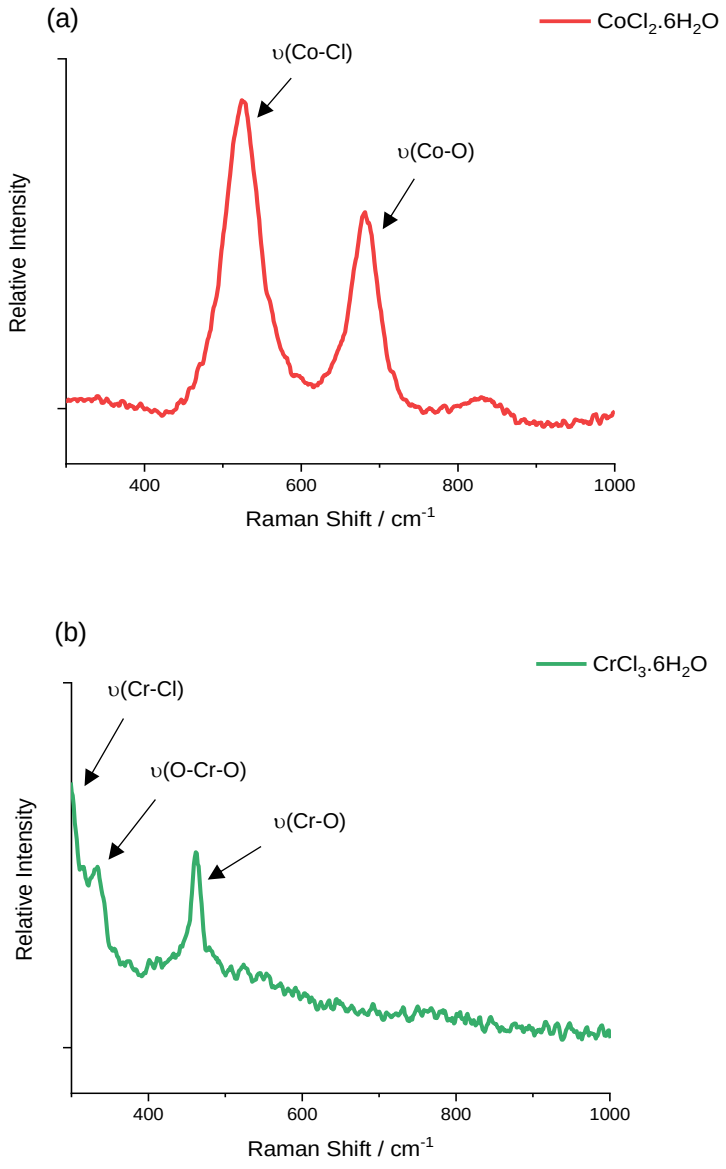

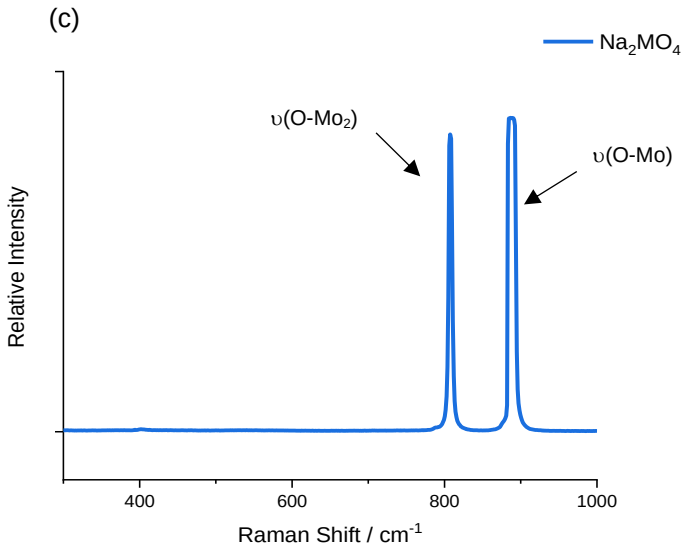

Figure 3.20 Raman spectra of the metal salts used throughout the investigation (300 – 1000 cm^{-1}) (a) Cobalt (II) Hexahydrate (b) Chromium (III) Hexahydrate (c) Sodium Molybdate

3.4.10 Circular Dichroism (CD)

CD is another absorption spectroscopy technique; it is based on the differences of left and right-handed polarized light of optically active molecules, which can be measured and interpreted. This is a rapid, non-destructive technique that gives details about the stability, structure and mechanisms of proteins and nucleic acids. Figure 3.21 shows the three commonly seen forms of the secondary structure of BSA. The α helix is formed of a positive band at 194 nm along with 2 negative bands at 210 and 222 nm, β sheets are defined by a less intense positive band at 197 nm with only one negative band at 217 nm while the irregular structure has just one negative band at 197 nm [142].

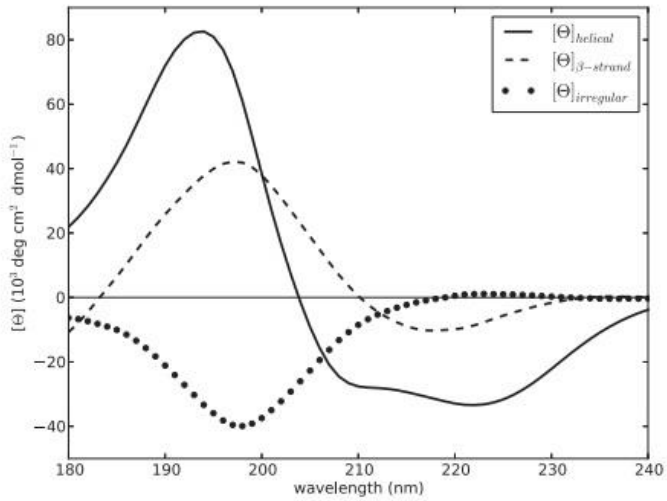

Figure 3.21 Obtained CD spectra for a 100% content of α-helix (-), β-strand (--) and irregular (..) [142]

Experiments were conducted using a Chirascan Plus spectropolarimeter (Applied Photophysics, UK). The Far-UV (190 – 260 nm) CD spectroscopy was obtained with a 1 mm path length cuvette at room temperature, using a constant concentration of BSA (0.2 mg/ml) and respective metallic salt (500 uM).

3.4.11 Inductively Coupled Plasma-Mass Spectrometry (ICP-MS)

ICP-MS is a form of elemental analysis technology that can detect almost all elements at trace levels in fluids. The fluid is put through a plasma source where they become ionized; this enables the ions to easily be sorted by their mass/charge ratio due to the use of the mass spectrometer.

Analysis was undertaken using the Perkin Elmer ELAN DRE-e ICP-MS with the TotalQuant method, which uses specific TotalQuant calibration solutions. To account for this, the solutions for analysis were prepared to contain 2% nitric acid to correct for matrix effects; in the case of protein-containing solutions, a precipitate was formed, which needed to be centrifuged off as not to interfere with ICP-MS analysis. This was done via the CPS Disc Centrifuge DC24000, which was set to 12000 RPM for 2h at room temperature, with the solution then being decanted for ICP-MS analysis. Samples were then matrix-matched against the standards and blank for identification and quantification. Throughout this whole process, the ICP-MS samples were always stored in the refrigerator throughout this process to preserve the specimen in its original condition.

The electrolytes of three repetitions of all the potentiostatic electrochemical tests were analysed, the isotopes of metal ions that were of specific interest were Co 59, Cr 52 and Mo 98.

3.5 Summary

The experimental procedures outlined within the chapter enabled a comprehensive investigation into the corrosion behaviour of CoCrMo in simulated biological fluids. By covering a range of electrochemical conditions, all aspects of an implanted alloy have been covered. The post-test surface analysis made it possible to account for both the physical and chemical changes that the alloy underwent. Analysis of the electrolyte made it possible to quantify metal ion dissolution and determine why some ions are favoured by BSA.

Chapter 4
The Electrochemical Characterisation of CoCrMo Under Simulated Bodily Fluids

4.1 Introduction

The biocorrosion of CoCrMo alloys within the body is one of the main issues associated with the implant due to the release of metal ions which can lead to immunological effects and genotoxicity. The composition of the environment has been seen to have a vital role on the behaviour of the alloy alongside the differences in the galvanic coupling that can occur within the human body. By undertaking a complete electrochemical study of the alloy, properties of the electrolyte/interface can be obtained, which leads to a greater understanding of how the alloy interacts with the environment.

The purpose of the following chapter is to undertake a complete electrochemical study on the alloy in a variety of simulated bodily fluids. This enables corrosion mechanisms to be deduced as well as the effects that each component within the fluid has on the corrosion behaviour. The following measurements have been made to achieve this aim: open circuit potential (OCP), potentiodynamic polarisation, potentiostatic measurements and electrochemical impedance (EIS).

As explained in the experimental section, every test was replicated at least three times to ensure reproducibility. For ease of depicting trends between the electrolyte compositions, only one repeat is shown.

4.2 Electrochemical Results

4.2.1 OCP

The evolution of the OCP as a function of time for the various simulated bodily fluids is indicated in Figure 4.1a. The extracted average final values of OCP are depicted in Figure 4.1b. The voltage was monitored at a rate of 5 Hz for 1 hour to ensure that steady-state had been achieved.

The value of potential tends towards the positive direction for all conditions. This feature indicates the ennoblement (change in the oxide chemistry) formation of a passive film; the more positive the overall value is, the more protective the formed filmed is indicated to be [80]. It takes time for this film to

be formed as when the alloy is submerged within the electrolyte, the air oxide film is converted into a metal-electrolyte interface [83].

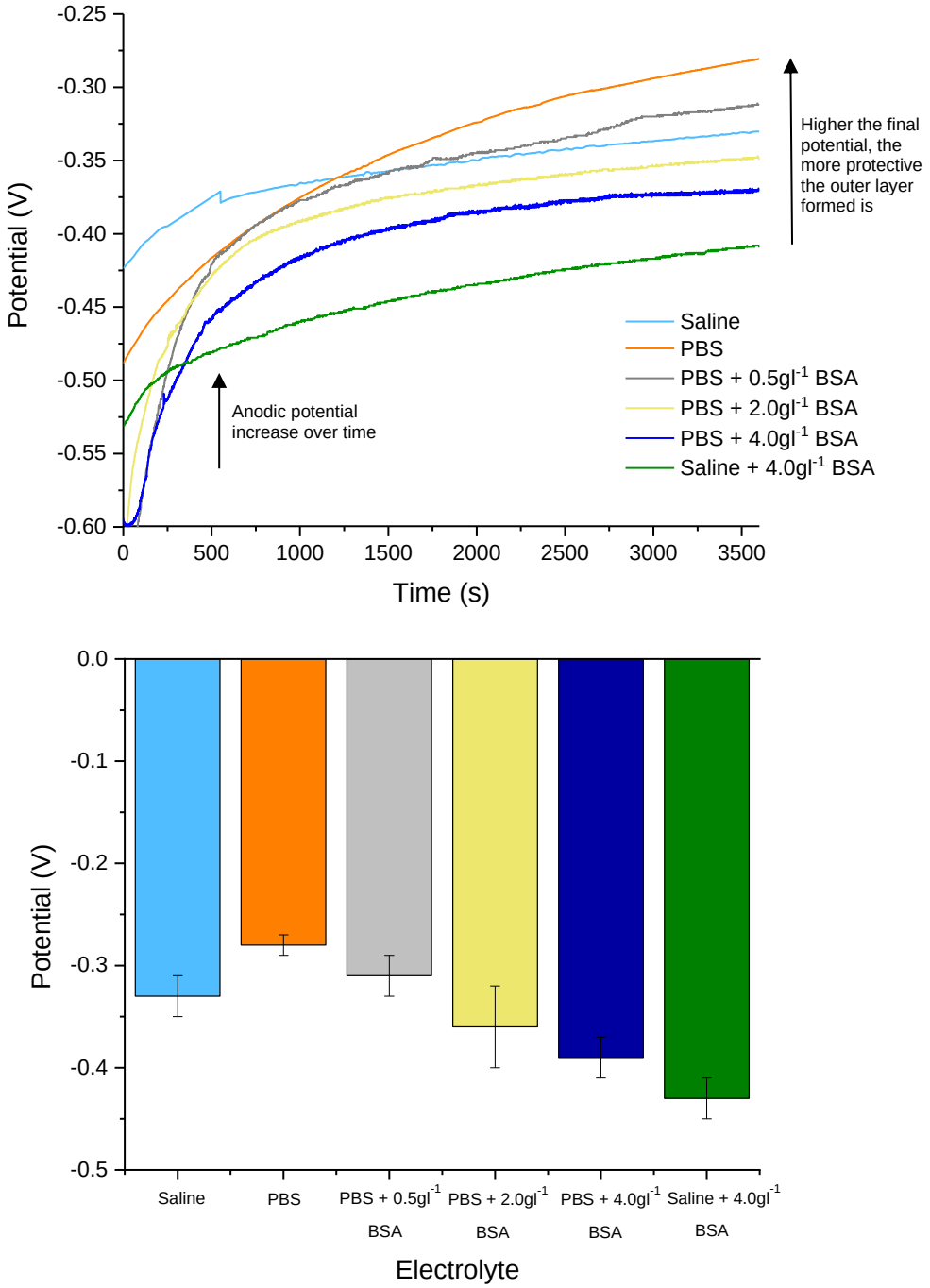

Figure 4.1 The OCP data obtained for CoCrMo in simulated bodily fluids over an hour (a) potential - time curve (Published previously within [125]) (b) average OCP values

From the different levels of steady-state obtained for the various conditions, it can be seen that the composition of the electrolyte plays a key part in the

corrosion behaviour. By using saline as a control, it is seen that phosphates lead to OCP value increases as they act as an anodic inhibitor. BSA has the opposite effect decreasing OCP values by acting as a cathodic inhibitor. When phosphates are present alongside BSA in the environment, the effects of BSA dominate the behaviour of the alloy. The higher the concentration of BSA in the electrolyte, the greater the observed effect.

The time needed to reach a fairly steady state is also affected by the electrolyte chemistry. Steady-state occurs when the metal-electrolyte interface is stable and doesn't significantly change with time. For these experiments, this is achieved quickest in just a saline environment. The inclusion of inorganic/organic species causes steady-state to be reached at a slower rate due to influencing the formation of the EDL; this could occur via adsorption of species or inhibiting the flow of oxidants.

4.2.2 Potentiodynamic Polarization

To determine the overall corrosion behaviour of CoCrMo in a range of different simulated bodily fluids, potentiodynamic polarization was undertaken. The potentiodynamic scans were undertaken right after 1hr of OCP stabilisation. As stated previously, individual tests were done for the anodic and cathodic scans to prevent the previous polarisation test affecting the current density.

4.2.2.1 Anodic Polarization

The anodic potentiodynamic curves for CoCrMo are shown in Figure 4.2 below, with the extracted values depicted in Table 4.1. These values were obtained as previously detailed in Section 3.3.2.

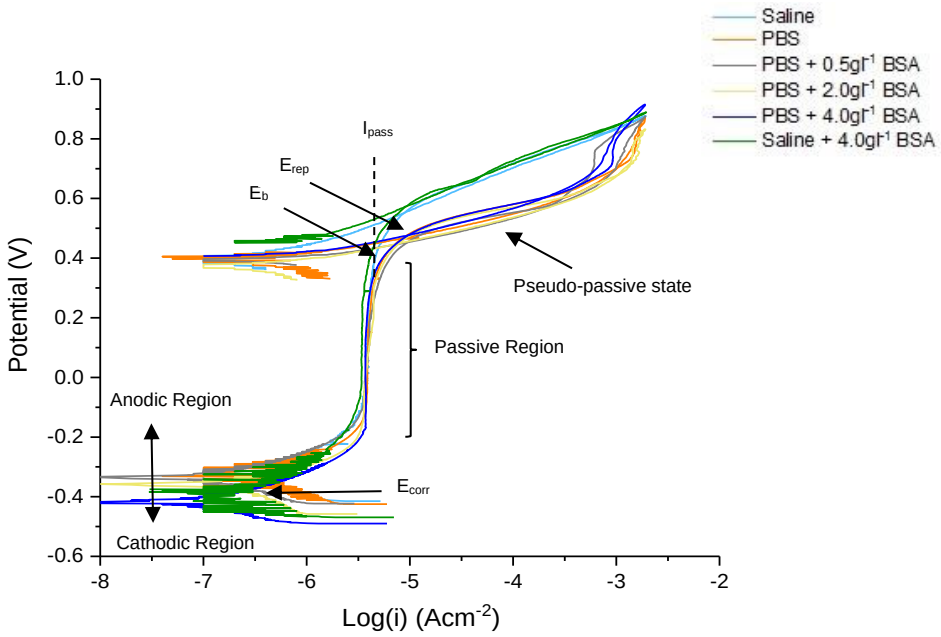

Figure 4.2 The anodic potentiodynamic curves obtained for CoCrMo in simulated bodily fluids. Published previously within [125]

Table 4.1 The extracted values obtained from the anodic scans. Published previously within [125]

Electrolyte	OCP/E_{corr} (V)	I_{corr} (μA/cm²)	I_{passs} (μA/cm²)	E_b (V)	E_r (V)	$E_b - E_r$ (V)	β_a (mV)	β_c (mV)
Saline	-0.33 ± 0.02	0.18 ± 0.05	3.82 ± 0.04	0.52 ± 0.02	0.56 ± 0.03	0.04 ± 0.05	148 ± 24	-75 ± 7
PBS	-0.28 ± 0.01	0.12 ± 0.04	3.42 ± 0.06	0.46 ± 0.04	0.47 ± 0.02	0.01 ± 0.06	114 ± 18	-98 ± 11
PBS + 0.5gl^{-1} BSA	-0.31 ± 0.02	0.24 ± 0.03	3.53 ± 0.05	0.45 ± 0.01	0.46 ± 0.03	0.01 ± 0.04	121 ± 16	-102 ± 10
PBS + 2.0gl^{-1} BSA	-0.36 ± 0.04	0.28 ± 0.03	3.59 ± 0.07	0.48 ± 0.03	0.47 ± 0.01	0.01 ± 0.04	122 ± 13	-97 ± 6
PBS + 4.0gl^{-1} BSA	-0.39 ± 0.02	0.29 ± 0.02	3.74 ± 0.03	0.46 ± 0.03	0.48 ± 0.02	0.02 ± 0.05	112 ± 19	-111 ± 14
Saline + 4.0gl^{-1} BSA	-0.43 ± 0.02	0.39 ± 0.04	3.91 ± 0.06	0.54 ± 0.03	0.57 ± 0.02	0.02 ± 0.05	130 ± 11	-86 ± 8

The anodic region of the curve is at potentials higher than that of the $E_{corr.}$ Past this potential, the WE becomes the anode, and hence there is a net anodic current. Possible anodic reactions that take place are indicated below in Equation 4.1.

Equation 4.1 Anodic reactions that can occur for CoCrMo in simulated biological fluids

$$Co_{(m)} \rightarrow Co^{2+}_{(aq)} + 2e^-$$

$$Cr_{(m)} \rightarrow Cr^{3+}_{(aq)} + 3e^-$$

$$Mo_{(m)} \rightarrow Mo^{4+}_{(aq)} + 4e^-$$

$$2OH^-_{(aq)} \rightarrow \frac{1}{2}O_{2_{(aq)}} + H_2O + 2e^-$$

Within a saline environment, the active domain lies between -0.30V_{RE} and -0.1V_{RE}, with the passive domain existing between -0.10V_{RE} and 0.52V_{RE}. These parameters are well defined within the literature for CoCrMo in a saline environment [24,143].

By using the saline environment as a control, it can be seen that E_{corr} tends to more noble values, with i_{corr} decreasing in the presence of phosphates. The opposite effect is observed in a BSA environment. This indicates that phosphates enhance the corrosion resistance of the alloy, whereas BSA weakens the alloy's corrosion resistance. For these effects, BSA is observed to be dominant over PBS when they are both present in the environment. The higher the concentration of BSA, the greater the observed effect.

Similar trends are observed for i_{pass}. The presence of phosphates leads to a lower value obtained in comparison to a saline environment. This means that passivation of the surface occurs much more readily, thus giving the alloy a greater corrosion resistance. This is in line with the effects of E_{corr} and I_{corr} seen. In the presence of BSA, the value of i_{pass} is seen to increase; the higher the concentration of BSA, the greater the observed effect. Again BSA is seen to be dominant over phosphates when they are both within the electrolyte.

The presence of phosphates leads to reduced values of E_b compared to the value achieved within a saline environment. This phenomenon could be due to the production of phosphate chromium ion complexes (Equation 4.2). Authors have stated that these complexes can activate trans-passive

dissolution, which is accelerating the breakdown of the passive film and localised corrosion [143]. BSA is seen to not lead to any alterations in the E_b, with all values obtained being within experimental error of the environments without BSA.

Equation 4.2 Formation of phosphate chromium ion complexes [144]

$$Cr_2O_3 + 4H_2O \rightarrow Cr_2O_7^{2-} + 8H^+ + 6e^-$$

Both phosphates and BSA lead to reductions in the difference between the values of E_b and E_r. This indicates that with the species present, the alloy's resistance to localised corrosion is increased [25]. Due to the more negative value of E_{corr} for BSA containing environments, the difference between the E_{corr} and E_b is enhanced, resulting in the alloy having a greater resistance to pitting and crevice corrosion [25].

The values of the β_a are relatively consistent for all environments, whereas the presence of phosphates and BSA lead to higher values of β_c. This suggests that the cathodic reaction is more favoured in the presence of these species.

The hysteresis of the scan was obtained by conducting a reverse scan alongside the initial one and is indicative of any repassivation or pitting process post passive film breakdown. The appearance of the hysteresis alters in the presence of phosphates compared to the saline environment. A close up of the hysteresis obtained for CoCrMo in a phosphate environment is shown in Figure 4.3 to analyse the specific effects phosphates have within this region. It is seen that there are two hysteresis loops, one positive and one negative. The negative loop (1) occurs between 0.68-0.86V_{RE} and is deduced as the reversed current density is smaller than that of the original scan; this indicates either that a protective film is present on the surface or some other anodic reactions occurring on the surface were slower during the backward scan [144,145]. This is a sign that the current recorded past 0.68V_{RE} is not due to metal dissolution but to other redox reactions occurring on the surface.

The positive loop (2) occurs between 0.46-0.68V_{RE}, indicating that dissolution of the film has occurred [144,145].

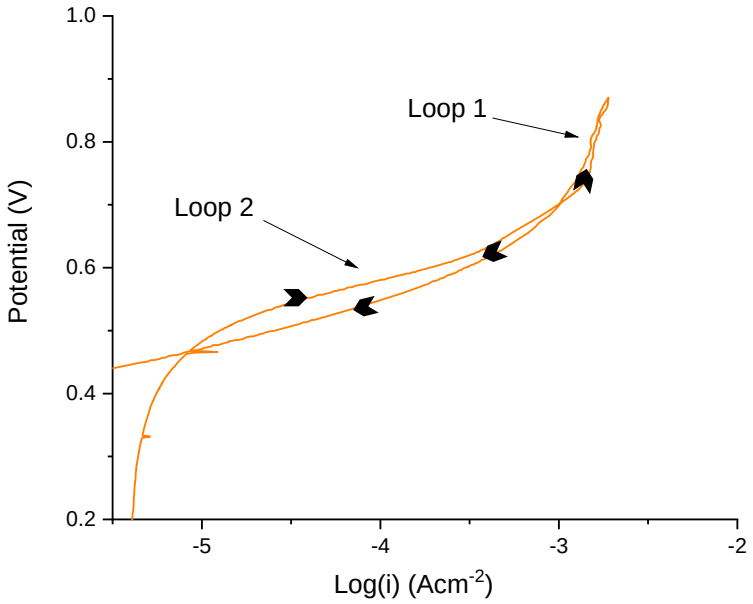

Figure 4.3 The hysteresis of the anodic scan for CoCrMo in PBS

4.2.2.2 Cathodic Polarization

The cathodic scans for CoCrMo within the various electrolytes are displayed in Figure 4.4. The values obtained for the E_{corr} we consistent with the anodic experiments.

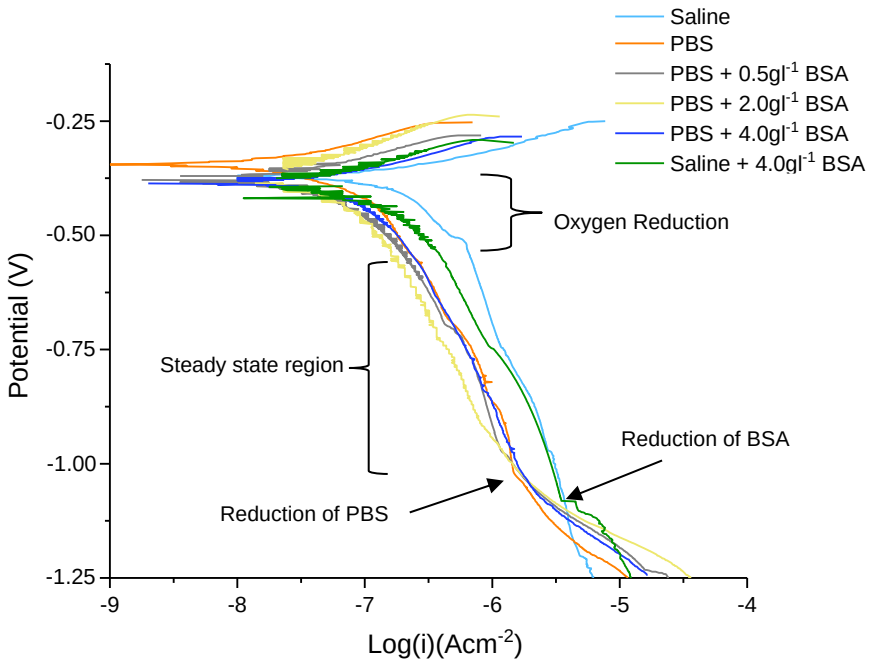

Figure 4.4 The cathodic potentiodynamic curves obtained for CoCrMo in simulated bodily fluids. Published previously within [125]

The cathodic domain is located at all potentials below that of the E_{corr} for the alloy, as the WE acts as a cathode, there is a net cathodic current. Within this region, the current is primarily determined by the reduction of oxygen as well as the reduction of other species (PBS, BSA, Hydrogen) if there is a sufficient thermodynamic driving force.

From Figure 4.4, at potentials just below the $E_{corr,}$ there is an initial increase of current due to the reduction of oxygen taking place (from OCP to -0.55V_{RE}). This is limited by the rate of molecule diffusion into the solution (activation controlled), followed by a region of a fairly steady state. This region of steady-state is non-ideal, as the current is slightly increasing over this region; this is common for stagnant experiments due to slow EAS transport to the surface of the alloy [83]. Once there is a sufficient thermodynamic driving force, the current density is seen to increase again as other species are reduced.

Equation 4.3 The reactions that typically dominate in the cathodic domain

Oxygen Reduction	$O_2 + 4H^+ + 4e^- \rightarrow H_2O$	Acidic Conditions
	$O_2 + H_2O + 4e^- \rightarrow 4OH^-$	Alkali Conditions
Hydrogen Evolution	$2H^+ + 2e^- \rightarrow H_2$	

In a saline environment, only reduction of oxygen can be seen, indicating that hydrogen evolution doesn't occur during this potential range. In the presence of phosphates, the current is diminished, with a current increase being observed at -1.05$V_{RE,}$ which is owed to the reduction of phosphates. BSA also leads to a diminished current but not to the same extent of phosphates, reduction of BSA leading to a current increase at around -1.10V_{RE}. The reduction of these extra species increases the current densities of these environments, giving them the highest current densities by the end of the experiment. These observations correlate with the previously seen increase in β_c for phosphate and albumin species. Throughout all of the steady-state regions obtained, the rate of current increase is the same for all environments indicating that at these potentials, no interactions occur with phosphates or protein.

4.2.2.3 Determination of binding energies

By utilising the polarisation curves of CoCrMo, it is possible to determine the activation energies for the corrosion process, enabling the adsorption mechanism to be investigated. The corrosion processes activation energy was obtained from the linear variation of the metal dissolution rate assigned as the corrosion current density, which follows the Arrhenius equation. This method was discussed in detail in Section 2.5.1.1.

An example of the obtained Tafel regions for CoCrMo whilst in a PBS environment for a range of temperatures is shown in Figure 4.5. All extracted values from the investigated Tafel regions are depicted in Table 4.2. As expected, the E_{corr} and I_{corr} increase with temperature due to the increased energy of the molecules. Temperature changes seem to have little/no effect on the values of β_a and β_c.

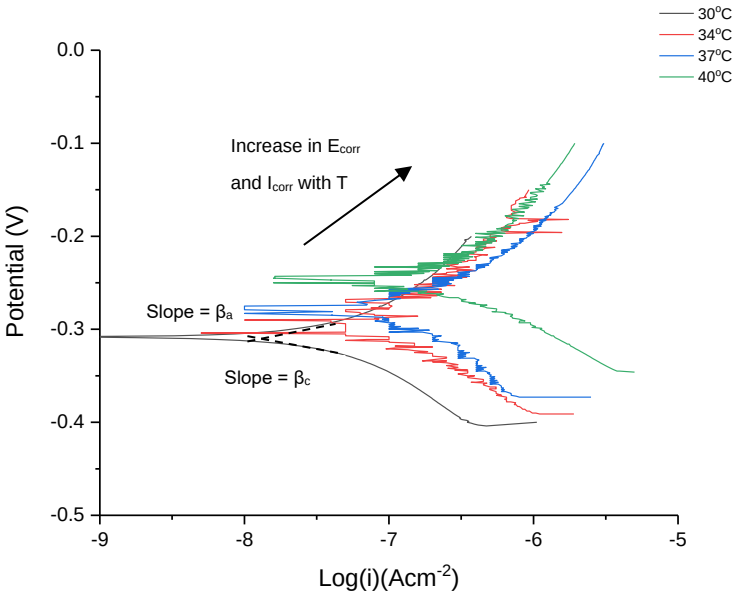

Figure 4.5 The Tafel regions for CoCrMo in PBS at a range of different temperatures

Table 4.2 Extracted values from the Tafel regions investigated at a range of temperatures for CoCrMo (a) Saline (b) PBS (c) PBS + 0.5 gl^{-1} BSA (d) PBS + 2.0 gl^{-1} BSA (e) PBS + 4.0gl^{-1} BSA (f) Saline + 4.0 gl^{-1} BSA

a)

Saline				
Temperature (K)	E_{corr} (V)	I_{corr} (µA/cm^2)	B_a (mV)	B_c (mV)
303.15	-0.37 ± 0.03	0.12 ± 0.02	136 ± 15	-76 ± 12
307.15	-0.35 ± 0.01	0.15 ± 0.02	130 ± 20	-72 ± 11
310.15	-0.33 ± 0.02	0.18 ± 0.05	148 ± 24	-78 ± 7
313.15	-0.29 ± 0.03	0.22 ± 0.03	143 ± 21	-81 ± 6

b)

PBS				
Temperature (K)	E_{corr} (V)	I_{corr} (µA/cm^2)	B_a (mV)	B_c (mV)
303.15	-0.32 ± 0.01	0.09 ± 0.02	106 ± 17	-93 ± 17
307.15	-0.31 ± 0.02	0.11 ± 0.01	117 ± 22	-86 ± 10
310.15	-0.28 ± 0.01	0.12 ± 0.04	114 ± 18	-98 ± 11
313.15	-0.25 ± 0.02	0.14 ± 0.03	111 ± 16	-95 ± 16

c)

PBS + 0.5gl^{-1} BSA				
Temperature (K)	E_{corr} (V)	I_{corr} (µA/cm^2)	B_a (mV)	B_c (mV)
303.15	-0.36 ± 0.01	0.21 ± 0.02	128 ± 22	-99 ± 12
307.15	-0.34 ± 0.03	0.22 ± 0.01	123 ± 14	-95 ± 9
310.15	-0.31 ± 0.02	0.25 ± 0.03	121 ± 16	-102 ± 10
313.15	-0.27 ± 0.02	0.26 ± 0.01	123 ± 15	-100 ± 13

d)

PBS + 2.0gl^{-1} BSA				
Temperature (K)	E_{corr} (V)	I_{corr} (µA/cm^2)	B_a (mV)	B_c (mV)
303.15	-0.39 ± 0.02	0.24 ± 0.01	116 ± 17	-106 ± 15
307.15	-0.38 ± 0.03	0.26 ± 0.02	125 ± 14	-99 ± 11
310.15	-0.36 ± 0.04	0.28 ± 0.03	122 ± 13	-97 ± 6
313.15	-0.32 ± 0.02	0.30 ± 0.02	131 ± 22	-104 ± 14

e)

PBS + 4.0gl^{-1} BSA				
Temperature (K)	E_{corr} (V)	I_{corr} (µA/cm^2)	B_a (mV)	B_c (mV)
303.15	-0.44 ± 0.02	0.25 ± 0.04	121 ± 15	-104 ± 15
307.15	-0.41 ± 0.03	0.29 ± 0.02	105 ± 24	-97 ± 12
310.15	-0.39 ± 0.02	0.29 ± 0.02	112 ± 19	-111 ± 14
313.15	-0.38 ± 0.01	0.33 ± 0.03	118 ± 15	-106 ± 10

f)

NaCl + 4.0gl^{-1} BSA				
Temperature (K)	E_{corr} (V)	I_{corr} (µA/cm^2)	B_a (mV)	B_c (mV)
303.15	-0.49 ± 0.02	0.30 ± 0.06	124 ± 17	-82 ± 12
307.15	-0.45 ± 0.04	0.37 ± 0.01	123 ± 14	-94 ± 13
310.15	-0.43 ± 0.02	0.39 ± 0.04	130 ± 11	-86 ± 8
313.15	-0.40 ± 0.03	0.45 ± 0.02	136 ± 16	-88 ± 4

The linear versions of the plots were obtained by plotting the logarithmic values of the corrosion current density against the inverse of temperature. This is shown in Figure 4.6, with the extracted activation energies for the environments over the temperature range of 30 - 40^{o}C indicated in Table 4.2.

The highest activation energy can be seen in a saline environment, with the presence of phosphates causing the energy for corrosion activation to decrease, indicating the alloy has a higher susceptibility to corrosion [88]. The same effects are observed with albumin, but to a greater extent, the concentration of BSA seemed to have little effect on the E_a. Vidal [88] found similar trends to these, obtaining activation energy for a saline environment to be 49.4 kJmol^{-1}. Lower values of E_a indicate the adsorption of species onto the surface of the alloy (physisorption/chemisorption) [146].

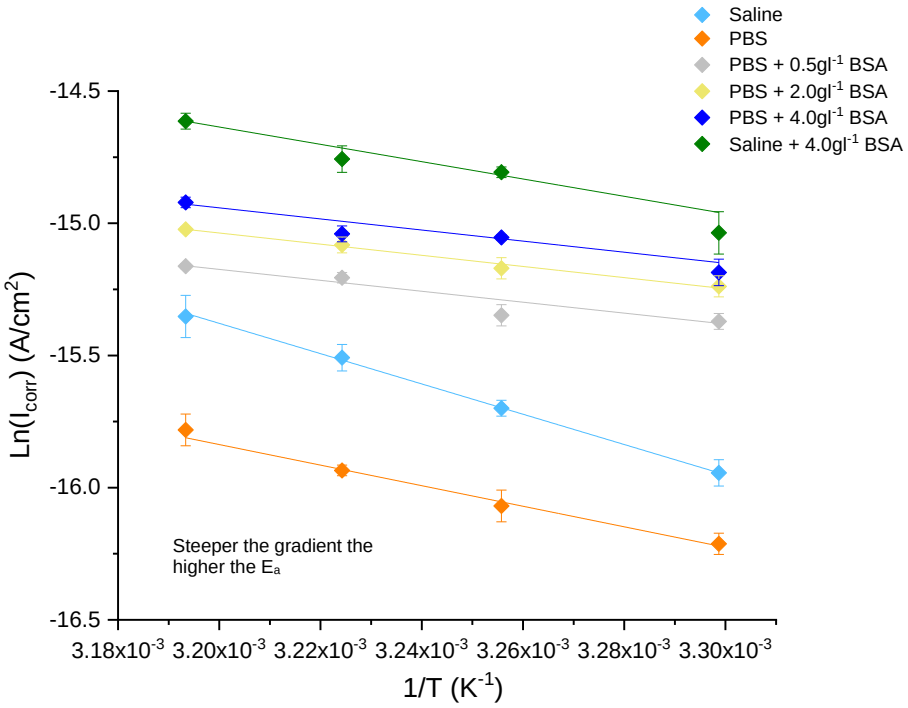

Figure 4.6 Arrhenius plot to determine the E_a by variation of the temperature for CoCrMo in simulated bodily fluids

The use of the transition state theory, as explained in Section 2.5.1.1, enables the parameters of transition state activation to be determined. This is obtained from plotting $\ln\left(\frac{i_{corr}}{T}\right)$ against $\frac{1}{T}$ which gives a straight line with the slope being equal to $\left(-\frac{\Delta H^{\ddagger}}{R}\right)$ and the intercept being $\left(ln\frac{R}{Nh}+\frac{\Delta S^{\ddagger}}{R}\right)$. The obtained graph is shown in Figure 4.7, with the extracted values within Table 4.3. The positive values of enthalpy indicate that that the absorption of these organic species to the alloy is an endothermic process (system absorbs heat from the surroundings) [145,146]. The negative values of ΔS_a suggest that this process is driven by the enthalpy changes [89]. Due to the negative nature of the ΔS_a, it is possible to conclude that the activated complex in the rate-determining step represents association with no significant changes to the internal structure of the species [89,90]. This is due to the total disorder of the system decreasing, so no internal bonds have been broken.

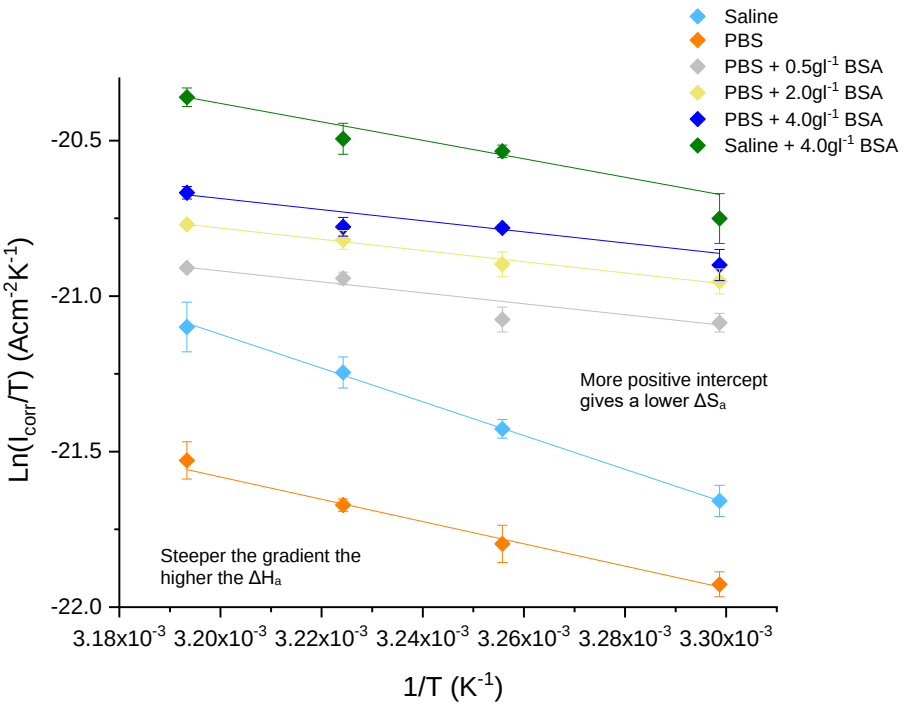

Figure 4.7 Transition state theory plot to determine the ΔH_a and ΔS_a for CoCrMo in simulated bodily fluids

Table 4.3 Thermodynamic parameters obtained for the reactions of CoCrMo in a variety of electrolytes

Solution	E_a (KJ/mol)	ΔH_a (KJ/mol)	ΔS_a (J/Kmol)
Saline	47.5	44.5	- 230.6
PBS	33.9	31.3	- 276.5
PBS + 0.5gl^{-1} BSA	18.0	15.5	- 321.9
PBS + 2.0gl^{-1} BSA	17.5	14.9	- 322.5
PBS + 4.0gl^{-1} BSA	19.4	16.8	- 315.5
Saline + 4.0gl^{-1} BSA	31.8	29.3	- 273.2

4.2.2.4 Mixed Potential Theory

A qualitative explanation of the effects of both phosphates and albumin on the corrosion behaviour of CoCrMo can be gained by the use of mixed potential theory. The diagram of mixed potential constructed from utilising the Tafel slopes of anodic dissolution and the cathodic reactions from the potentiodynamic experiments is shown in Figure 4.8.

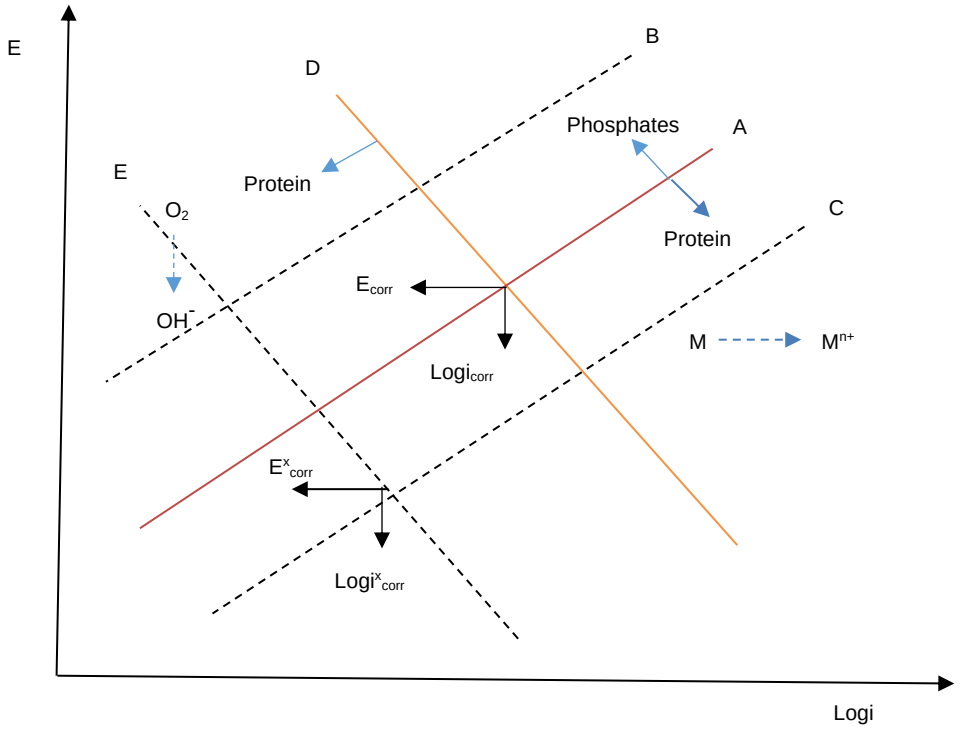

Figure 4.8 Mixed potential theory applied to the effects of phosphates and BSA on the potential and current density of CoCrMo (anodic branch depicted in red, cathodic branch depicted in orange)

When phosphates are present, they adsorb onto the surface of the alloy, decreasing the rate of the anodic reaction (A→B). The effect of BSA is two-fold; it causes an increase in the rate of dissolution from the alloy (A→C) but also reduces the cathodic current (D→E). At potentials around E_{corr}, these opposite effects cancel each other out to some degree; when the potential is shifted to anodic, the presence of BSA accelerates dissolution, with its effect on the cathodic current being negligible.

The effect of temperature can also be investigated by using the data obtained from analysing the Tafel regions over 304 - 314K. The constructed diagram is shown in Figure 4.9.

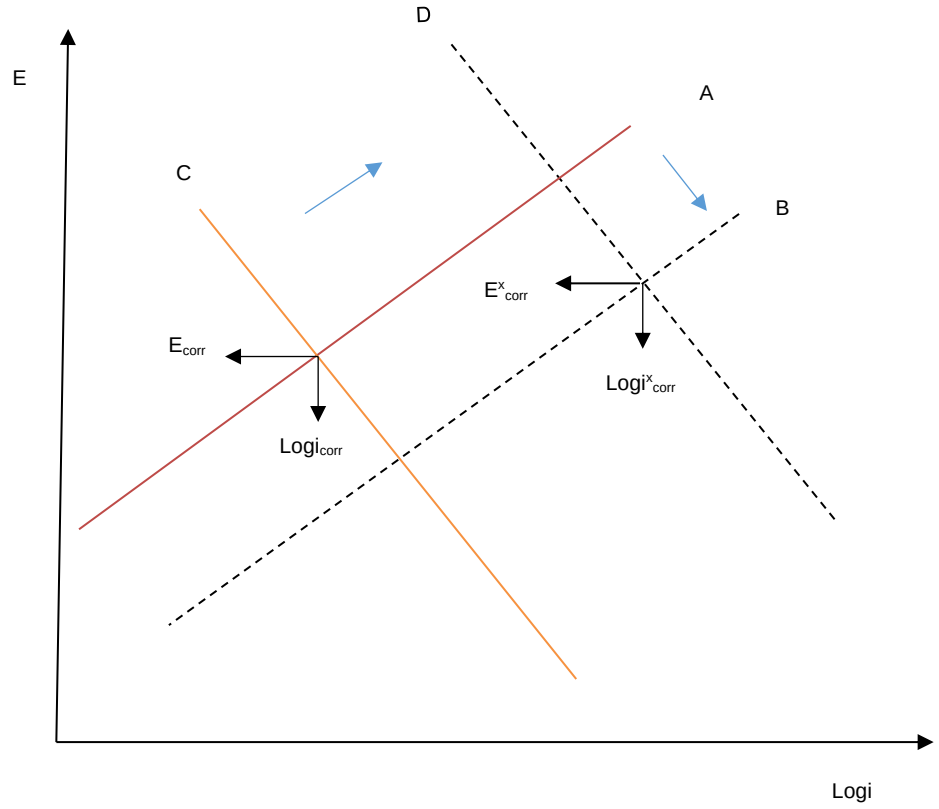

Figure 4.9 Mixed potential theory applied to the effects of temperate on the potential and current density of CoCrMo (anodic branch depicted in red, cathodic branch depicted in orange)

This representation indicates that temperature increases the rate of metal ion dissolution from CoCrMo (A→B) and leads to increases within the cathodic reaction rates (C→D). Overall, an increase in temperature causes increases in both the corrosion potential and passive current density due to the system possessing higher energy levels.

4.2.3 Effects of Electrochemical Potential on Metal – Protein Interactions

Specific regions of interest have been identified from the previously conducted potentiodynamic experiments. The identified domains are as follows:

- The cathodic domain (-1V_{RE})
- At OCP
- The passive domain (+0.1V_{RE})
- The transpassive domain (+1V_{RE})

Potentiostatic measurements were conducted from the different regions to further understand the kinetics of corrosion alongside determining the level of dissolution from the alloy under these conditions. Electrochemical Impedance Spectroscopy was undertaken to understand the properties of the alloy under different conditions and investigate the effects of potential and environment on the interface of the alloy. The fits for each applied potential were discussed previously in Section 3.3.4.

4.2.3.1 Cathodic Domain

When polarized at -1$V_{RE,}$ the current is determined from the cathodic reaction of the reduction oxygen alongside other species. This in turn, leads the current to be negative from the start of the test. Similar behaviour has been seen under these conditions for CoCrMo by Espallargas [102]. The electrochemical data obtained can be seen in Figure 4.10.

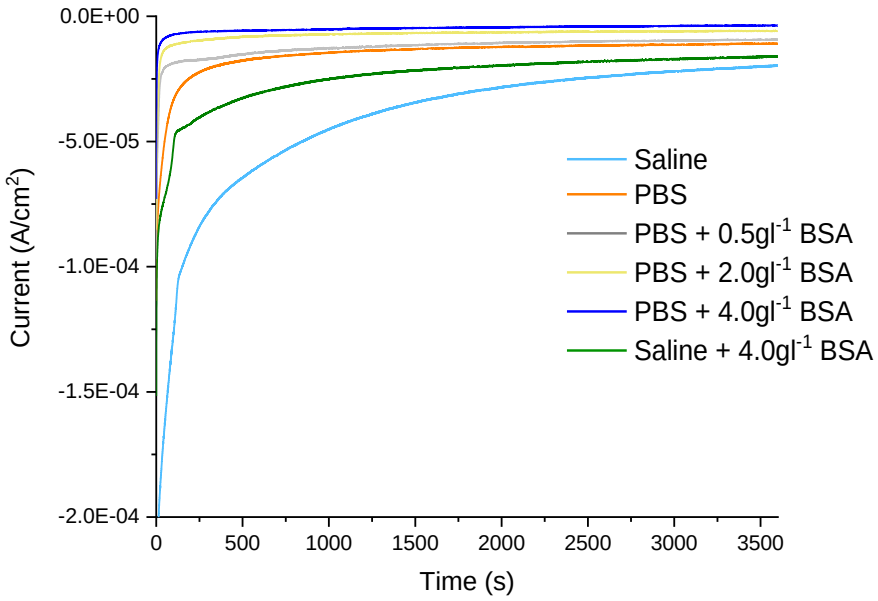

Figure 4.10 Current evolution over an hour for CoCrMo alloy in various bodily conditions under -1V_{RE}

The current values for saline containing conditions are observed to have the highest overall negative charge density, and this indicates that the reduction reaction is highly favoured. The presence of phosphates and albumin both reduce the current density in comparison to a saline environment as they adsorb onto the surface. The highest recorded current is in a PBS and BSA containing environment due to giving the alloy a more complete coverage. The more BSA is in the electrolyte, the greater the observed effect seen is. This is

in concordance with the data obtained via the potentiodynamic tests seen in Section 4.2.2.2

The impedance spectra for CoCrMo under cathodic potential of -1.0V_{RE} is displayed within Figure 4.11, the corresponding electrical circuit for the data is shown in Figure 4.12 alongside the extracted values in Table 4.4. This circuit was also found to be the best fit for these conditions by Vidal [105].

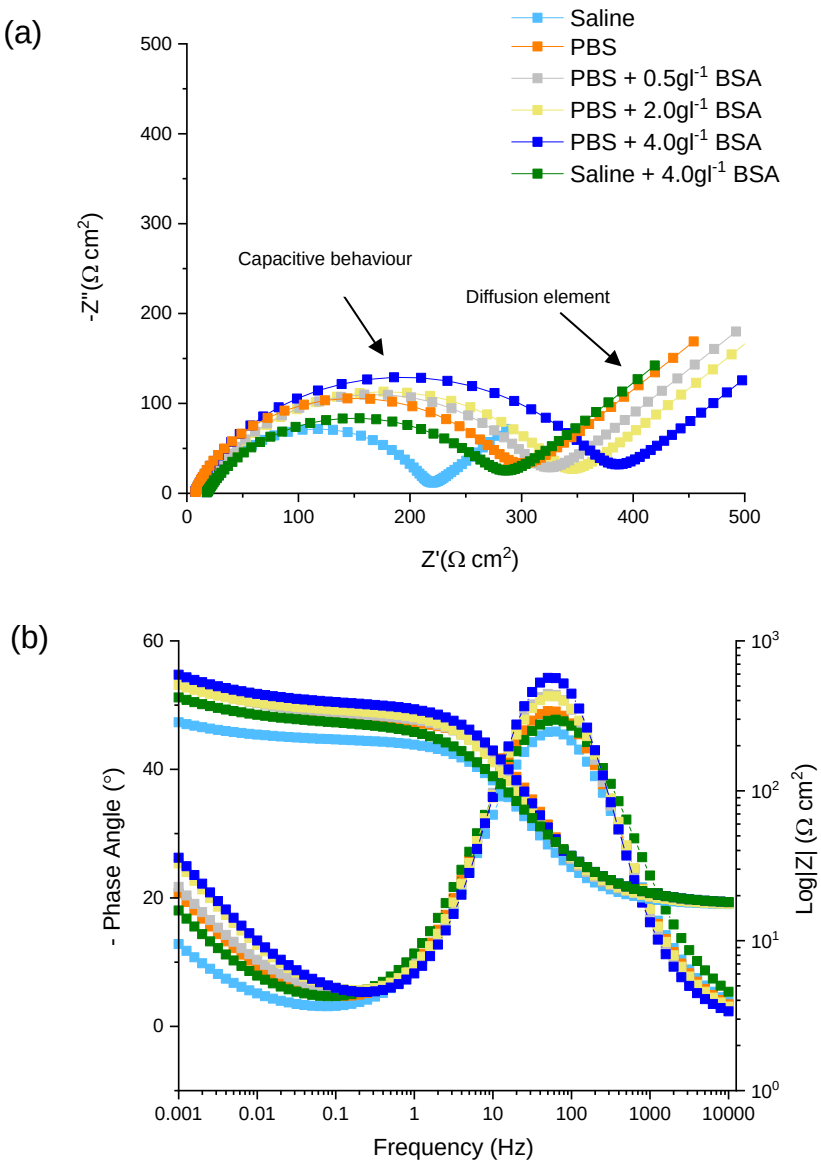

Figure 4.11 Nyquist (a) and bode plots (b) of CoCrMo alloys under cathodic conditions (-1V_{RE}) in simulated bodily fluids. Published previously within [125]

The Nyquist plots are comprised of a small semi-circle at high frequency followed by a line at lower frequencies, this implies that a diffusion-controlled reaction occurs which is characterised via Warburg impedance.

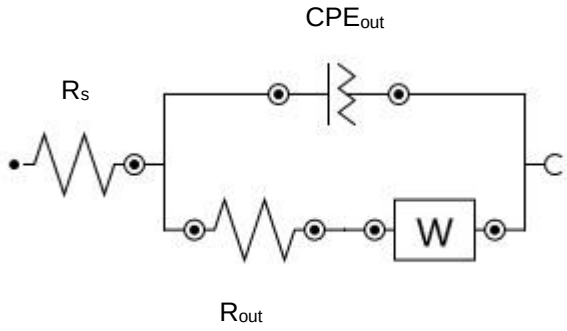

Figure 4.12 Equivalent circuit used to analyse the impedance spectra obtained under passive conditions. R_s (solution resistance), R_{out} (outer layer resistance), CPE_{out} (CPE of the outer layer), W (Warburg diffusion). Published previously within [125]

Table 4.4 The extracted values obtained from the electrochemical fitted circuit for cathodic conditions. Published previously within [125]

Electrolyte	R_s (Ω cm^2)	R_{out} (Ω cm^2)	CPE_{out} (μF/cm^2)	n_{out}	W (mMhos$^{1/2}$)
Saline	16.4 ± 0.9	110 ± 16	14.1 ± 0.9	0.80 ± 0.03	12.8 ± 0.6
PBS	14.8 ± 0.4	213 ± 25	13.5 ± 0.4	0.83 ± 0.02	10.9 ± 0.4
PBS + 0.5gl^{-1} BSA	17.4 ± 0.6	298 ± 21	10.2 ± 0.7	0.82 ± 0.01	10.1 ± 0.7
PBS + 2.0gl^{-1} BSA	18.1 ± 1.0	321 ± 29	8.4 ± 0.5	0.80 ± 0.03	8.9 ± 0.8
PBS + 4.0gl^{-1} BSA	19.3 ± 0.8	342 ± 37	5.8 ± 0.7	0.83 ± 0.01	7.38 ± 0.9
Saline + 4.0gl^{-1} BSA	16.8 ± 0.4	227 ± 17	9.2 ± 1.1	0.80 ± 0.02	11.1 ± 1.6

The low values of R_{out} obtained alongside a high value of CPE_{out} (compared to OCP/Passive data) indicate that oxide film has been thinned/weakened and possibly even fully reduced. The presence of diffusion indicates that the interface is porous, allowing the dissolution of the oxide, which is limited by the rate of diffusion.

When phosphates were present in solution, the values of R_{out} increase, indicating the alloy is more corrosion resistant, this correlates with the potentiodynamic data in which a decrease in current density is observed. The lower value of CPE_{out} observed indicates an increase in thickness of the interface, this is further supported by the well-known fact that phosphates adsorb on the alloy's surface [104,105]. The lower level of diffusion from the alloy also consolidates that the molecules adsorb onto the surface.

From the potentiodynamic data, it was seen that albumin acts as a cathodic inhibitor due to lower values of current density observed at $-1V_{RE}$. The EIS data is in good agreement with this due to the much higher values of R_p obtained alongside reduced values of CPE_{out} and W. This enables us to conclude that BSA adsorbs onto the alloy, hindering the reduction reaction, therefore acting as a cathodic inhibitor.

4.2.3.2 OCP

The impedance spectra for alloy at OCP in the various electrolytes are shown in Figure 4.13, the corresponding electrical circuit is shown in Figure 4.14 alongside the extracted values in Table 4.5.

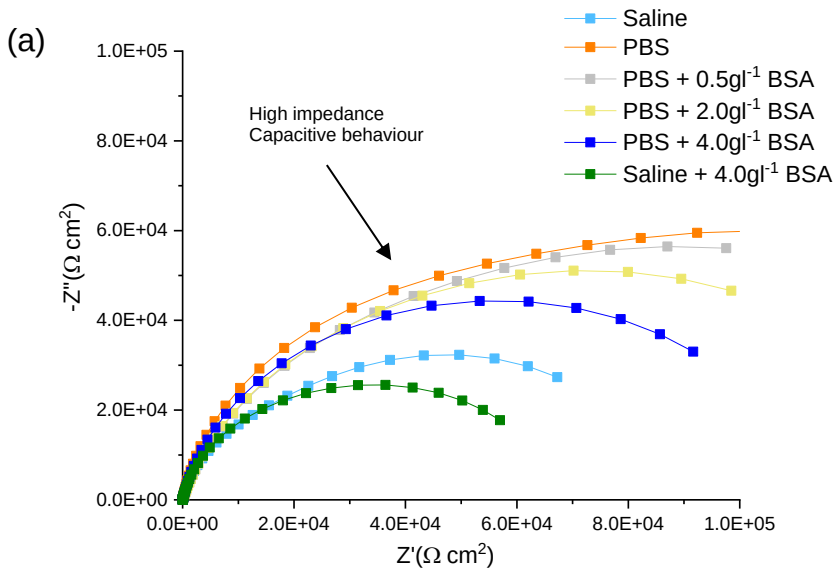

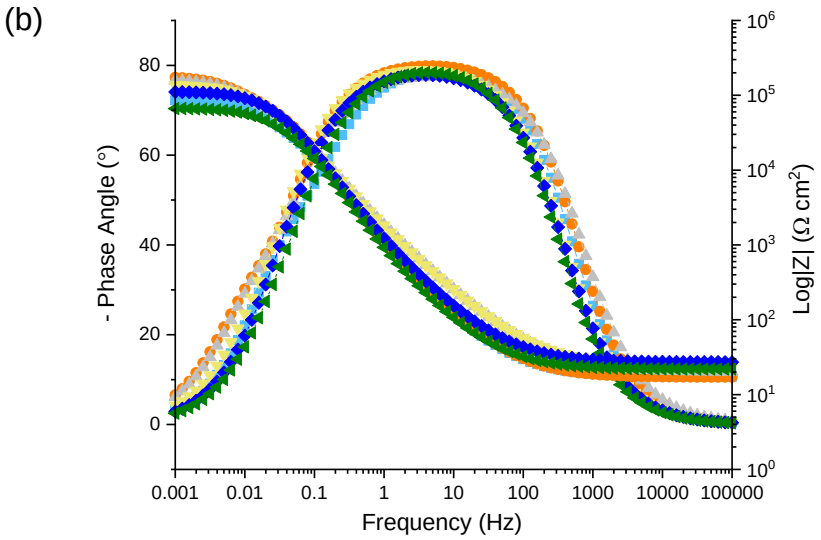

Figure 4.13 Nyquist (a) and bode plots (b) of CoCrMo alloys under OCP conditions in simulated bodily fluids

The data obtained displays typical passive behaviour characterised via high impedance values whilst also exhibiting capacitive behaviour, this is signalled due to the semicircle shape. Seeing as there are two points of inflexion within the Bode plot, it implies that the cell is comprised of two separate time constants. The first of these relates to the oxide resistance (R_{in}/C_{in}), whilst the second corresponds to the resistance of charge transfer (R_{out}/C_{out}).

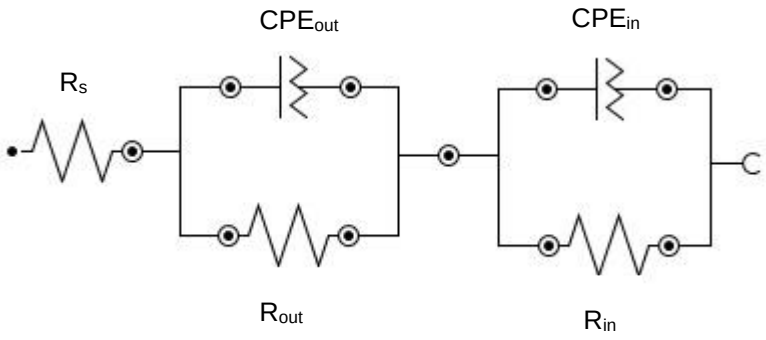

Figure 4.14 Equivalent circuit used to analyse the impedance spectra obtained under passive conditions. R_s (solution resistance), R_{out} (outer layer resistance), CPE_{out} (CPE of the outer layer), R_{in} (inner layer resistance), CPE_{in} (CPE of the inner layer)

Table 4.5 The extracted values obtained from the electrochemical fitted circuit for OCP conditions

Electrolyte	R_s (Ω cm^2)	R_{out} (MΩ cm^2)	CPE_{out} (μF/cm^2)	n_{out}	CPE_{in} (μF/cm^2)	n_{in}	R_{in} (MΩ cm^2)
Saline	17.4 ± 0.5	0.07 ± 0.01	7.39 ± 0.44	0.89 ± 0.02	5.85 ± 0.96	0.90 ± 0.03	0.02 ± 0.01
PBS	17.1 ± 0.3	0.11 ± 0.02	11.20 ± 1.32	0.89 ± 0.03	3.56 ± 0.56	0.90 ± 0.01	0.07 ± 0.01
PBS + 0.5gl^{-1} BSA	20.2 ± 0.7	0.10 ± 0.02	9.81 ± 0.55	0.87 ± 0.01	3.94 ± 0.42	0.88 ± 0.02	0.06 ± 0.01
PBS + 2.0gl^{-1} BSA	24.1 ± 1.1	0.08 ± 0.01	8.45 ± 1.21	0.87 ± 0.04	4.29 ± 0.67	0.91 ± 0.03	0.06 ± 0.02
PBS + 4.0gl^{-1} BSA	27.1 ± 0.4	0.06 ± 0.01	9.24 ± 0.39	0.90 ± 0.03	4.54 ± 0.31	0.88 ± 0.02	0.06 ± 0.01
Saline + 4.0gl^{-1} BSA	21.8 ± 0.8	0.04 ± 0.01	10.2 ± 0.62	0.89 ± 0.02	6.13 ± 0.70	0.90 ± 0.01	0.03 ± 0.01

The high values of R_{in} obtained alongside the CPE_{in} values indicate that an oxide layer is present for all conditions examined [100]. As seen previously, phosphates increase the impedance of CoCrMo, the vales of R_{in} and R_{out} are

both seen to increase, suggesting absorption of an organic layer as well as affecting the composition of the passive film.

Albumin is seen to reduce the value of R_{in} and R_{out} obtained; this is in agreement with the slight increases in corrosion current seen from the potentiodynamic work conducted. This could be due to the albumin molecules interfering with film growth due to inhibiting of oxidant. The higher the concentration of albumin in the electrolyte, the greater the effect.

4.2.3.3 Passive Domain

CoCrMo samples were polarized at passive conditions upon submersion (+0.1V_{RE}) to induce electrochemical passive film formation. This passive potential was well defined for the conditions investigated. The experimental data obtained is shown in Figure 4.15. Upon application of the potential, the current for all conditions is seen to reduce until a steady state is obtained. This is due to the formation of the electrochemical oxide film, which takes a finite amount of time to form on the surface of the alloy, depending on the electrolyte.

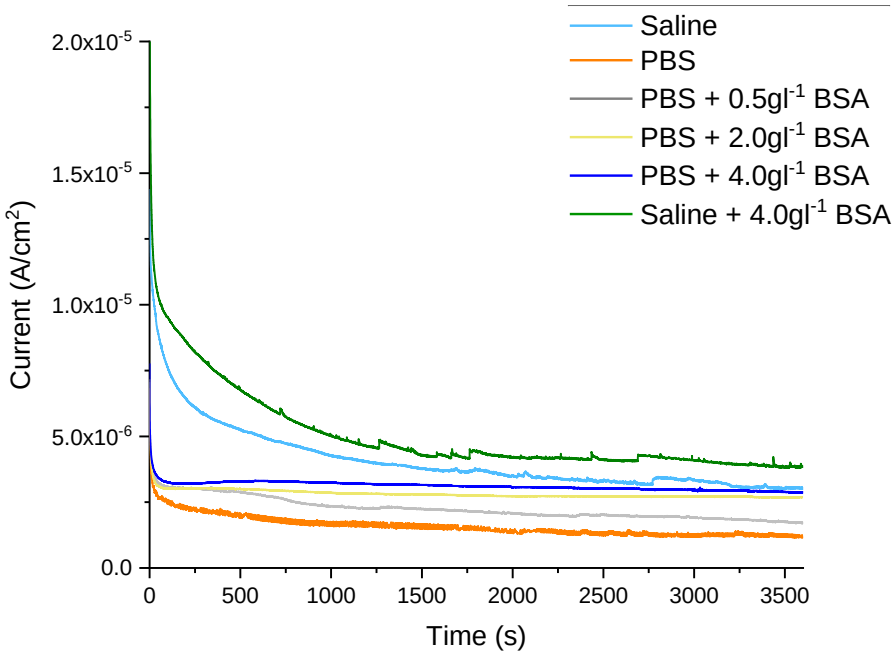

Figure 4.15 Current evolution over an hour for CoCrMo alloy in various bodily conditions under +0.1V_{RE}

When phosphates are present, the current density is reduced, indicating a more corrosion resistance interface which could be due to adsorption of the species. BSA had the opposite effect to phosphates increasing the current

density and is seen to be the more dominant species when both are present. This could be due to the size of the molecule, which restricts access of oxidant to the surface as well as competing to adsorb against phosphates leading to an un-uniform organic layer that is less protective.

The impedance spectra for the passive potential of +0.1V_{RE} is displayed within Figure 4.16, with the extracted values in Table 4.6. The spectra possess the same characteristics (high levels of impedance, two-time constants) as the ones obtained under OCP conditions. Therefore the data was fitted to the same equivalent circuit (Figure 4.16).

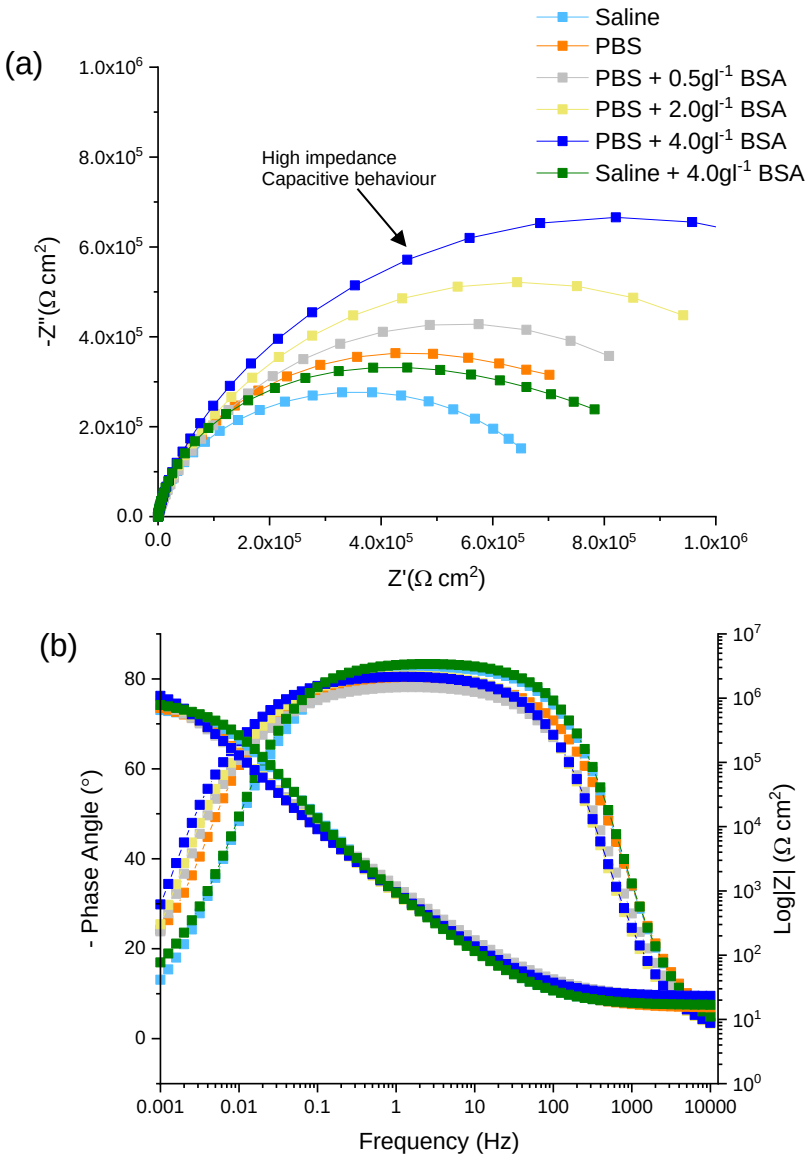

Figure 4.16 Nyquist (a) and bode plots (b) of CoCrMo alloys under passive conditions in simulated bodily fluids. Published previously within [125]

Table 4.6 The extracted values obtained from the electrochemical fitted circuit for passive conditions. Published previously within [125]

Electrolyte	R_s (Ω cm^2)	R_{out} (MΩ cm^2)	CPE_{out} (μF/cm^2)	n_{out}	CPE_{in} (μF/cm^2)	n_{in}	R_{in} (MΩ cm^2)
Saline	13.4 ± 0.9	0.42 ± 0.05	1.90 ± 0.13	0.90 ± 0.02	2.29 ± 0.23	0.85 ± 0.03	0.26 ± 0.04
PBS	15.3 ± 0.4	0.76 ± 0.03	1.02 ± 0.09	0.92 ± 0.03	1.75 ± 0.15	0.88 ± 0.01	0.46 ± 0.02
PBS + 0.5gl^{-1} BSA	22.4 ± 1.4	0.84 ± 0.06	0.88 ± 0.10	0.91 ± 0.03	1.97 ± 0.14	0.88 ± 0.02	0.49 ± 0.04
PBS + 2.0gl^{-1} BSA	22.6 ± 0.8	0.98 ± 0.12	0.75 ± 0.04	0.93 ± 0.02	2.05 ± 0.06	0.88 ± 0.02	0.46 ± 0.03
PBS + 4.0gl^{-1} BSA	23.0 ± 1.8	1.15 ± 0.09	0.72 ± 0.05	0.92 ± 0.01	2.13 ± 0.10	0.88 ± 0.01	0.48 ± 0.02
Saline + 4.0gl^{-1} BSA	16.7 ± 0.3	0.64 ± 0.05	1.55 ± 0.09	0.93 ± 0.03	2.90 ± 0.16	0.87 ± 0.03	0.42 ± 0.03

From the data obtain, it can be seen that the environment in which passivation takes place has a clear effect on the properties of CoCrMo. When phosphates are present in the environment, the resistance of the alloy increases substantially, as seen by the values of R_{out} and R_{in} almost doubling compared to just a saline condition. This effect suggests that as well as adsorbing onto the surface acting as a barrier to the environment (increasing the charge resistance), the phosphates must have an interaction with the passive film to

increase its overall resistance (increase in R_{in}). The data obtained from both the potentiostatic and potentiodynamic is in good agreement as the presence of phosphates lead to the overall lowest values of i_p. Alongside, enhancing the corrosion resistance of the alloy, the thickness of the oxide layer was noted to increase indicated via to a lower value of CPE_{in} obtained.

Albumin leads to a higher value of R_{out} and lower CPE_{out} values indicating that the molecules adsorb on oxide film further shielding the alloy; due to the size of these molecules, the layer is thicker when also in the presence of phosphates (lower CPE_{out} for phosphates and BSA than for just BSA). The presence of BSA also causes differing characteristics to the Bode plot, shifting the phase angle obtained towards lower frequencies indicating the system is less likely to corrode [148].

4.2.3.4 Transpassive Domain

A potential of $+1V_{RE}$ was chosen as an upper limit to polarise CoCrMo to mimic trans-passive conditions. As expected, much higher current densities are obtained for all of the conditions in comparison to the other domains investigated; this suggests that transpassive oxidation occurs. The data is depicted in Figure 4.17.

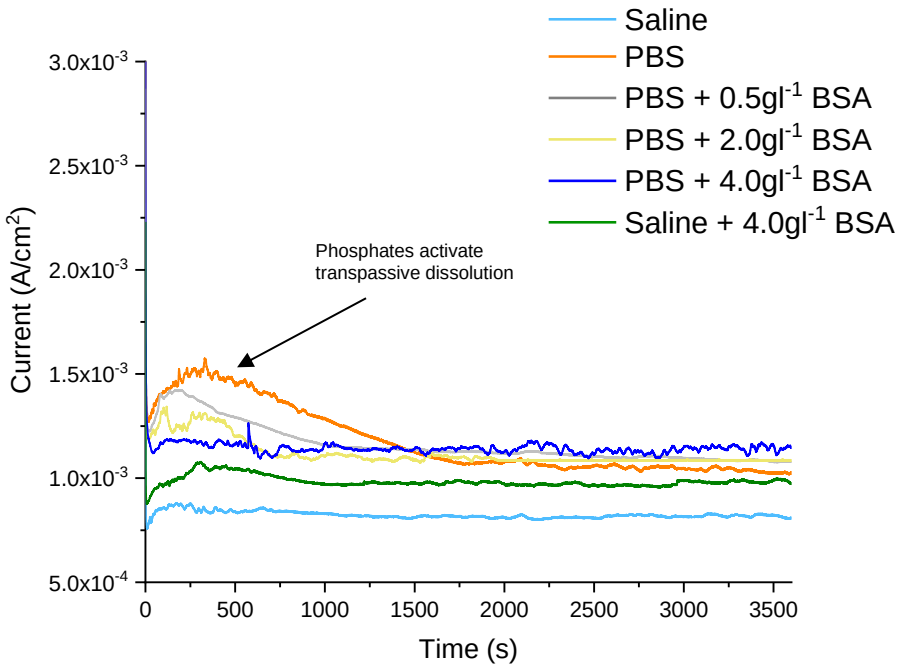

Figure 4.17 Current evolution over an hour for CoCrMo alloy in various bodily conditions under $+1V_{RE}$

In a phosphate environment, there is an initial peak before stabilization due to phosphates activating transpassive oxidation leading to a faster rate of oxide dissolution accounted for by the current spike. The presence of albumin seems to slow the oxide film dissolution due to competitive absorption but leads to an overall greater current detected.

From the current time graphs alongside the impedance spectra (Figure 4.18), it suggests that the oxide film has been dissolved due to the high values of current density obtained, which indicate that there is a non-barrier layer as there is little/no resistance to current.

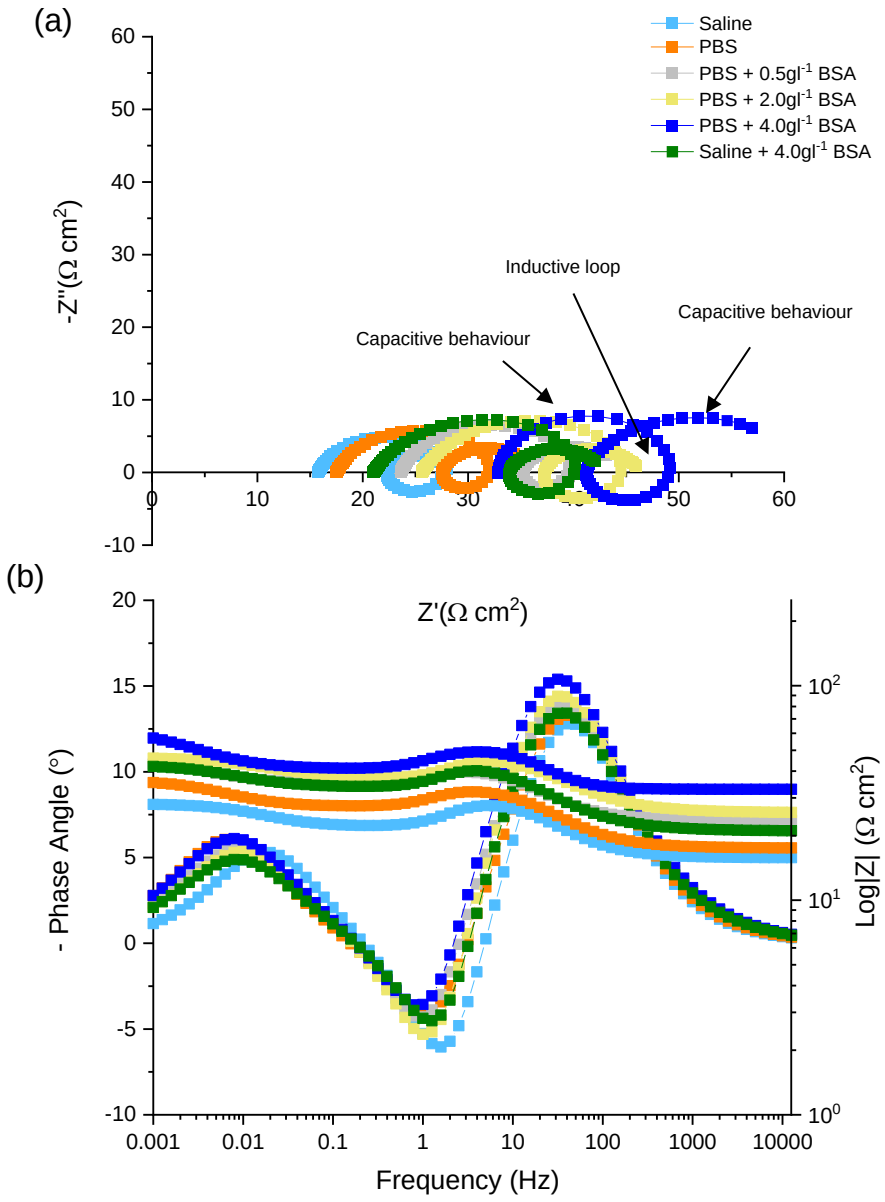

Figure 4.18 Nyquist (a) and bode plots (b) of CoCrMo alloys under transpassive conditions in simulated bodily fluids

The spectrum obtained under transpassive conditions are characterised by the high frequency capacitive, which reflects the high field-assisted migration of defects in the alloy [104]. There is then an inductive loop at the medium frequency (~1 Hz) due to the relaxation of the corrosion product charge formed at the interface formed by the quantity of cation vacancies [149]. At the lowest frequencies ($1x10^{-2}$ – $1x10^{-3}$ Hz), Faradaic pseudocapacitance is detected, indicating the presence of an inner layer that originates due to electroporation of oxidants present onto the electrode [104,149].

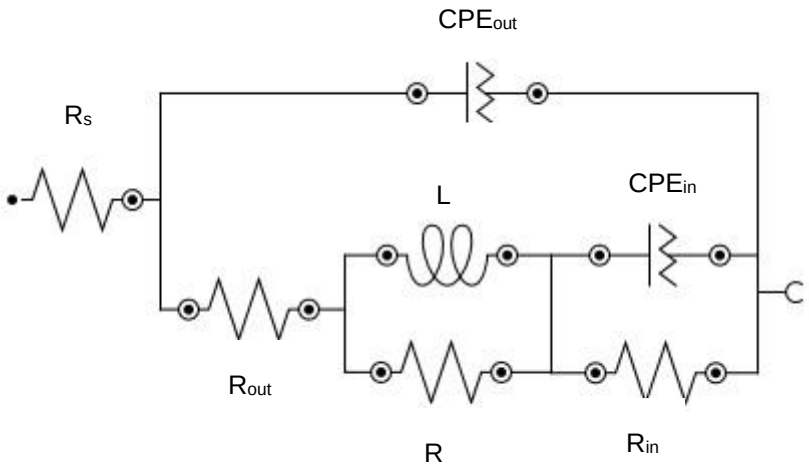

Figure 4.19 Equivalent circuit used to analyse the impedance spectra obtained under passive conditions. R_s (solution resistance), R_{out} (outer layer resistance), CPE_{out} (CPE of the outer layer), L (inductance), R (resistance), R_{in} (inner layer resistance), CPE_{in} (CPE of the inner layer)

Table 4.7 The extracted values obtained from the electrochemical fitted circuit for trans-passive conditions

Electrolyte	R_s (Ω cm^2)	R_{out} (Ω cm^2)	CPE_{out} (μF/cm^2)	n_{out}	L (H)	R (Ω cm^2)	CPE_{in} (mF/cm^2)	n_{in}	R_{in} (Ω cm^2)
Saline	15.7 ± 0.7	6.24 ± 0.48	84.0 ± 3.1	0.81 ± 0.04	1.80 ± 0.12	6.9 ± 0.9	87.1 ± 6.3	0.75 ± 0.02	6.16 ± 0.78
PBS	17.5 ± 0.5	9.80 ± 0.93	81.2 ± 1.9	0.80 ± 0.02	2.40 ± 0.29	9.0 ± 0.4	132.2 ± 11.6	0.76 ± 0.01	8.93 ± 0.62
PBS + 0.5gl^{-1} BSA	23.6 ± 0.4	11.2 ± 0.77	73.1 ± 5.3	0.82 ± 0.01	3.12 ± 0.19	10.3 ± 0.7	138.9 ± 17.2	0.75 ± 0.03	9.91 ± 0.87
PBS + 2.0gl^{-1} BSA	25.6 ± 0.8	11.0 ± 0.81	72.3 ± 4.2	0.82 ± 0.03	3.41 ± 0.25	10.8 ± 0.6	136.5 ± 13.2	0.76 ± 0.02	10.1 ± 1.21
PBS + 4.0gl^{-1} BSA	32.8 ± 1.2	12.6 ± 1.1	68.5 ± 3.4	0.81 ± 0.02	4.18 ± 0.37	9.8 ± 0.3	139.3 ± 9.5	0.78 ± 0.03	11.7 ± 0.97
Saline + 4.0gl^{-1} BSA	21.0 ± 0.4	11.5 ± 0.5	78.2 ± 2.6	0.79 ± 0.02	2.88 ± 0.32	9.8 ± 0.4	90.7 ± 8.3	0.78 ± 0.03	9.32 ± 0.54

The extremely low values of resistance obtained consolidate that the oxide film has broken down; the high value of CPE_{in} is due to the presence of vacancies on the surface of the alloy with phosphates leading to higher values as they activate trans passive dissolution [149]. The presence of albumin seems to have little effect on this. The values of R_{in} are seen to increase when both phosphates and albumin are present as they adsorb onto the electrode creating a more resistant inner layer.

By looking at the Point defect model, it is determined that the cation vacancies are formed due to the ejection of cations via oxidative means from the passive film into the electrolyte/barrier layer [150]. As the oxide film mainly consists of chromium, then the main product formed is chromic oxide (+6 oxidation state); this is formed from Equation 4.4. The Kroger-Vink notation is utilised in the equation, with Cr_{Cr} signifying a Cr(III) cation within a normal site of the oxide film and V_{Cr} being the vacancy in the lattice after oxidation [150]. These produced ions form a layer close to the alloy; the higher the inductance, the more ions are present [149]. In the presence of organic species, the values are higher due to either a higher dissolution or just more of the species becoming trapped near the interface.

Equation 4.4 The formation of chromium vacancies from the oxide film [150]

$$Cr_{(Cr)} + 4H_2O \rightarrow CrO_4^{2-} + V_{Cr}^{3\prime} + 8H^+ + 3e^-$$

Under these conditions, the presence of phosphates and albumin adsorbed onto the surface of the alloy lead to a higher R_{out} due to these species leading to a higher defect migration of metal species. The corresponding capacitance is seen to decrease, indicating a more compact layer is also formed.

4.2.4 Repassivation Kinetics

The kinetics of repassivation were investigated by first polarising the samples at $-1V_{RE}$ for 30 minutes to strip the alloy of the oxide film before shifting to a passive potential of $+0.1V_{RE}$ to induce passive film formation. These potentials were defined from the potentiodynamic data obtained (Section 4.2.2) as well as the EIS experiments (Section 4.2.3).

The current transient formed when the potential is shifted from cathodic to passive conditions is shown in Figure 4.20.

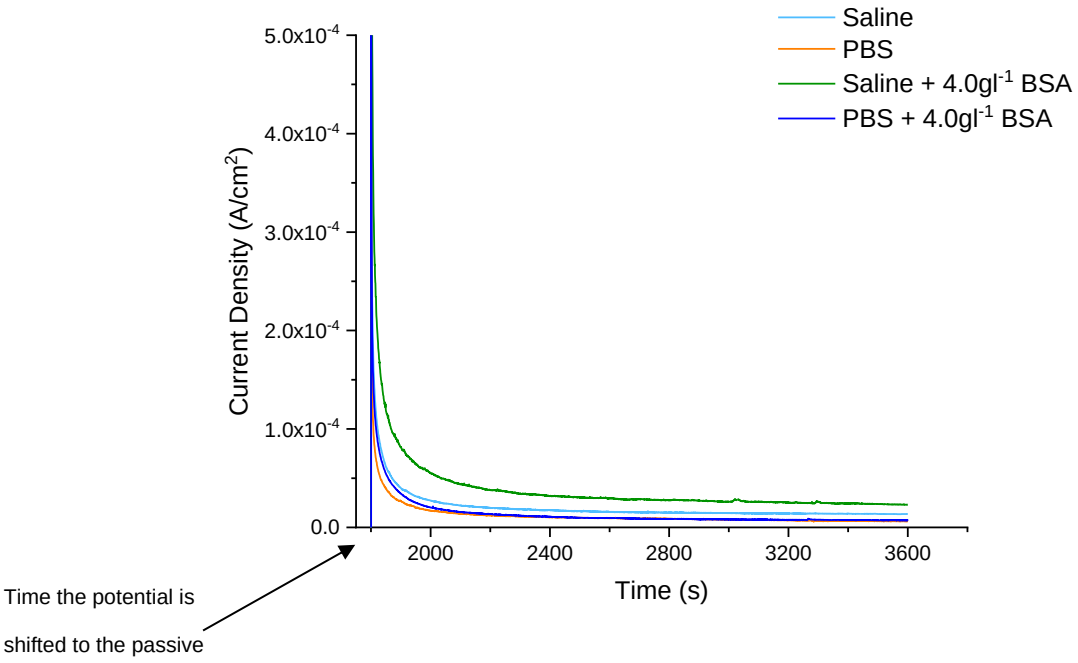

Figure 4.20 The current transients formed from investigating the repassivation for CoCrMo in simulated biological environments. Published previously within [125]

When the sample is initially passivated, the current increases as corrosion is taking place on the surface in the form of anodic oxidation, producing metal ions and electrons. The current then decreases rapidly as the passive film is formed; from the graph it can be seen that the rate of repassivation is considerably affected by its environment alongside the stability of the overall passive film produced indicated by the distinct steady-state potentials achieved.

These current transients can then be modelled on a second-order decay curve to obtain the kinetics of repassivation (See Section 3.3.3.2). This fitting enables us to account for both the coverage and growth phases of passive film formation. Firstly it defines the lateral growth of the oxide to encompass the surface and then increasing the thickness of the oxide to its maximum state. Figure 4.20 indicates that the coverage phase (τ_1) is dominant indicated by the rapid current drop from the peak towards steady-state. The current is then observed to gradually descend until the steady-state current has been achieved, which is indicative of the thickening phase (τ_2).

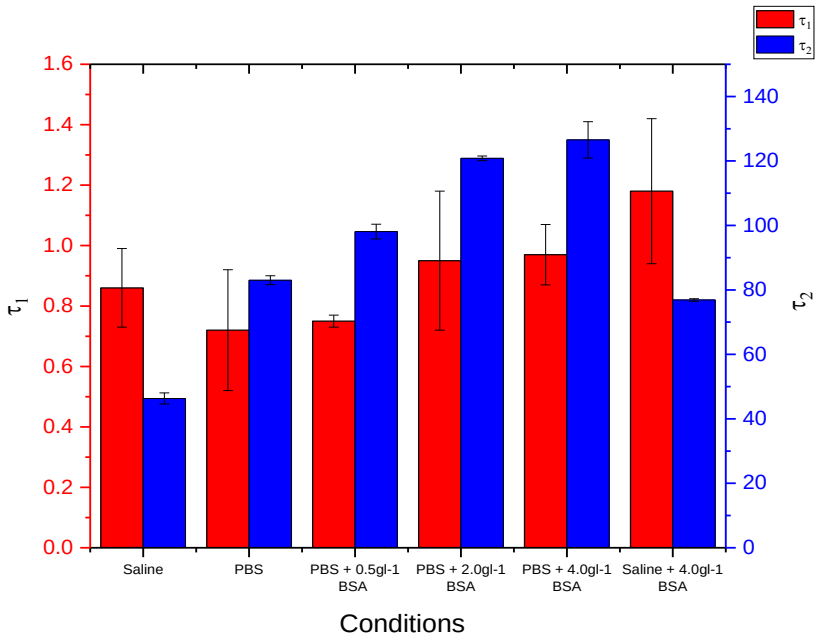

Figure 4.21 Shows the values of the exponential fits for τ_1 and τ_2 determined from the current transients. Published previously within [125]

Figure 4.21 shows the time constants obtained from the second-order fit. It is clear to see that repassivation occurs quickest within a phosphate environment, with albumin hindering the development of both the growth and thickening phases.

As τ_1 is shown to be the dominant time constant out of the phases, a longer τ_1 leads the alloy to undergo a longer period of corrosion as the time for the alloys protective film to form is increased, which would lead to an increase in metal ions released into the solution. From the values of τ_2 obtained, it is seen that the thickening phase of oxide growth occurs fastest in just a saline environment, with the presence of phosphates and albumin slowing down the rate. As anticipated, the final steady-state currents achieved are smallest in a phosphate environment as these molecules adsorb onto the surface of the film, further protecting the alloy hence the lower current density.

The integrity of the film formed can be obtained from the current transients by plotting the data onto a Log-Log scale, this enables the repassivation index to be acquired [122,151]. The empirical form and Log-Log scale equations are shown below. If the oxide formed is extremely ordered and compact, then n=1 with the porosity of the film increasing the closer n tends to zero [122].

Equation 4.5 The Log-Log Equation to determine the index of repassivation [122,150]

$$i(t) = At^{-n}$$

$$Log(i) = Log(A) - nLog(t)$$

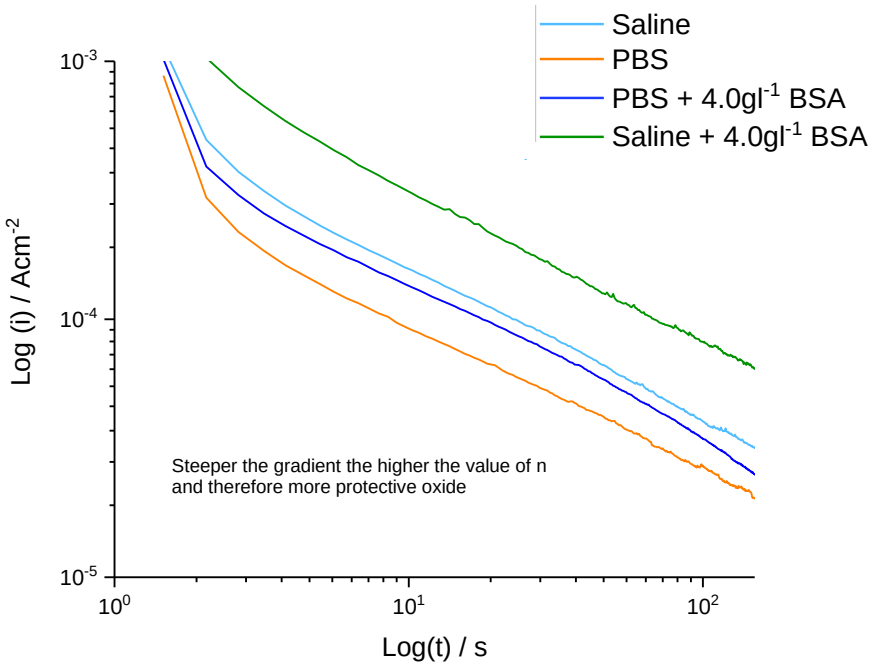

Figure 4.22 Shows the Log-Log plots of the current transients obtained. Published previously within [125].

Table 4.8 The obtained values of the repassivation Index determined from the slope of the Log-Log plot. Published previously within [125]

Electrolyte Used	Repassivation Index
Saline	-0.41 ± 0.01
PBS	-0.52 ± 0.02
PBS + 0.5gl^{-1} BSA	-0.50 ± 0.01
PBS + 2.0gl^{-1} BSA	-0.46 ± 0.02
PBS + 4.0gl^{-1} BSA	-0.44 ± 0.02
Saline + 4.0gl^{-1} BSA	-0.39 ± 0.01

From Table 4.8, it can be seen that the oxide film established in a phosphate environment is the most protective, with the presence of BSA slowly weakening the oxide layer due to increased levels of porosity; the higher the concentration of BSA, the greater the effect. This is due to competitive binding with the oxidant to the surface of the alloy.

4.2.4.1 Effect of potential on repassivation rate

The applied potential to carry out repassivation was investigated to determine the effects on the rate of repassivation. Applied voltages of $0V_{RE}$ and $+0.2V_{RE}$ were undertaken, which are also well defined within the passive region for all of the different electrolyte compositions. The comparisons of the extracted τ_1 and τ_2 values are shown in Figure 4.23.

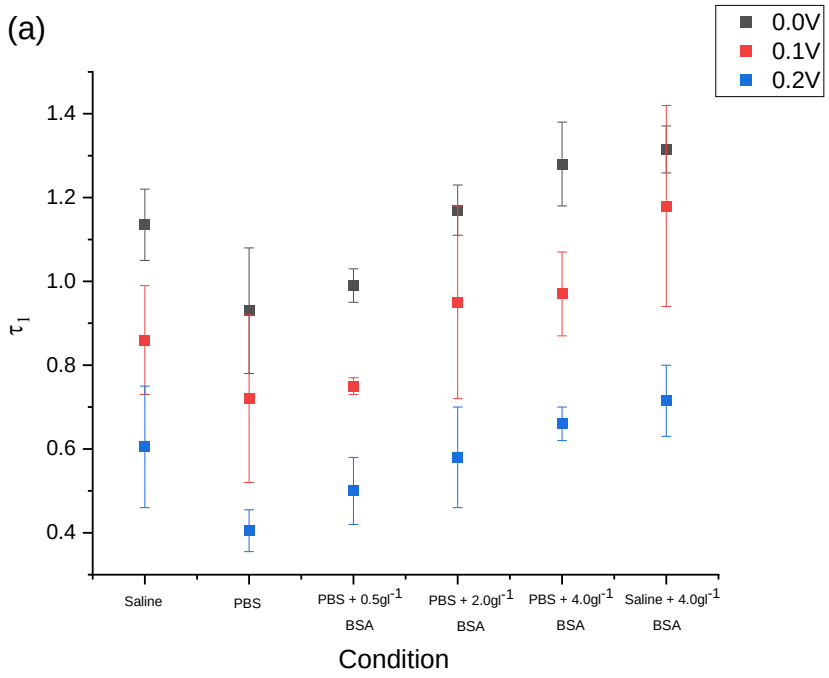

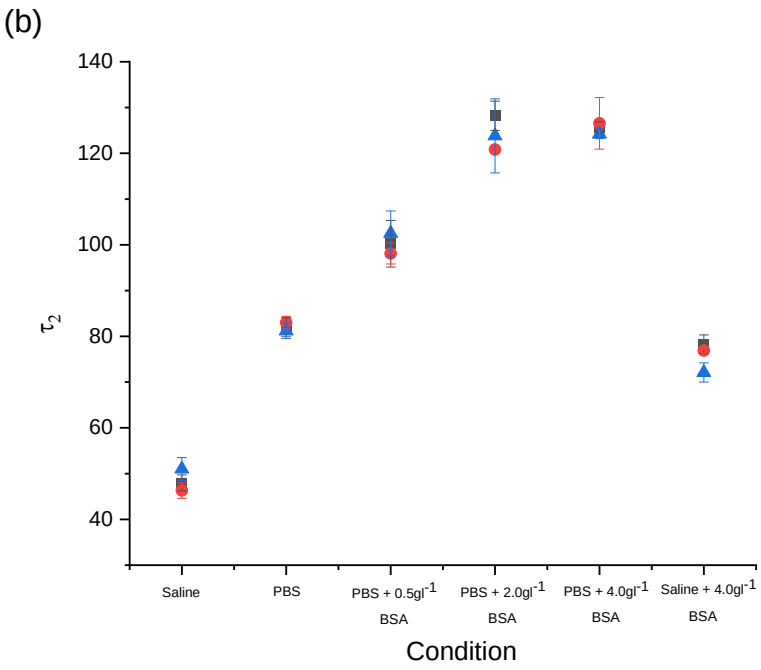

Figure 4.23 Shows the effects of potential on the exponential fits for τ_1 (a) and τ_2 (b) determined from the current transients

From Figure 4.23, it can be seen that the potential at which repassivation occurs affects the rate of repassivation. The value τ_1 tends to lower values when a higher passive potential is applied, characterised via a faster current drop towards a steady state. The higher reactivity at higher potentials leads to a faster repassivation rate. In regards to τ_2 it would appear that the potential has little/no effect on the rate of growth of the film, indicating that it is limited by just the surrounding environment. However, the conductivity of the media neither has a strong effect due to diminished currents after the surface of the alloy is initially covered [123]. The same trends for both τ_1 and τ_2 are shown across the potential range for the different compositions the alloy is exposed to.

The peak currents for the potentials are indicated in Figure 4.24. Observations indicate that higher potentials also leads to higher peak currents suggesting that more corrosion occurs on the surface of the alloy. This is due to the higher reactivity under higher potentials leading to the enhanced reformation of the film but also enhanced dissolution of the alloy [123]. The lowest peak currents are seen in albumin containing conditions as they suppress the cathodic

reaction as they are a cathodic inhibitor. As expected, the overall steady-state current achieved is lower with a higher passive potential.

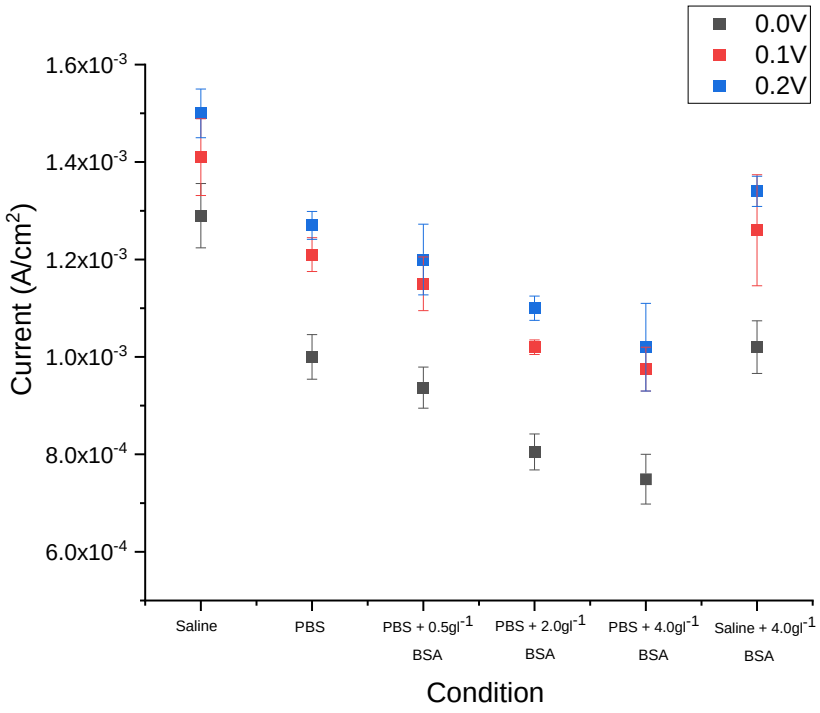

Figure 4.24 Indicates the peak currents obtained for the repassivation of CoCrMo under different potentials

4.3 Discussion

From the electrochemical measurements undertaken, it has been indicated that the composition of the electrolyte and the applied potential play key roles in determining the metal's resistance to corrosion. This section will give a detailed explanation and critique of the observations that have been noted throughout this chapter.

4.3.1 Effect of the electrolyte

The addition of phosphates to the system is shown to enhance the alloy's resistance to corrosion as indicated by more positive values of OCP, more noble values of E_{corr} and i_{corr} as well as giving lower values of i_p. These findings indicate that the species absorb onto the alloys surface and act as a barrier to corrosion, restricting the anodic reaction, i.e. acting as an anodic inhibitor. Results from the cathodic potentiodynamic experiments also consolidate this as the current is diminished in a phosphate environment. However,

phosphates have been shown to activate transpassive dissolution, as indicated in Figure 4.3. A study of the potential on the film composition of CoCrMo was carried out by Milosev [30]; it was determined that the passive film of CoCrMo was mainly composed of Cr_2O_3 and $Cr(OH)_{3,}$ but the percentage of CoO within the film increases with potential, and between 0.47-0.68V_{RE} the ratios are equal. Therefore it can be suggested that the increase in current from 0.47V_{RE} onwards is due to the formation of phosphate chromium complexes which alter the composition of the film, making it more susceptible to corrosion as it consists of more CoO. The point at which transpassive dissolution occurs for CoCrMo in PBS is from 0.68V_{RE} onwards, indicated by the start of the second loop (Figure 4.3), which is also in concordance with the breakdown potential of the alloy in saline environments. At this potential complete breakdown of the passive film occurs, and corrosion of the surface readily occurs.

The presence of BSA is seen to have differing effects to phosphates, as they shift the E_{corr} in the cathodic direction. This suggests that BSA inhibits access of oxidant towards the alloy, weakening the passive film, increasing the rate of corrosion. The passivation current is seen to increase with BSA, indicating that its presence can accelerate the anodic reaction leading to further dissolution of the passive film. These effects indicate that BSA has the opposite effect to phosphates, adsorbing onto the surface acting as a cathodic inhibitor [143].

The experiments undertaken have indicated that both phosphates and BSA adsorb onto the surface of the alloy via chemisorption; this was determined from substantial decreases to the E_a when these species are present individually or together. In this process, the phosphate/BSA undergoes charge sharing/charge transfer with the alloy surface, which forms a co-ordinate type bond [146]. This process is enabled as a donation of electrons into the unoccupied d orbitals of the metal is thermodynamically favoured, as chromium is the main constituent of the film, its vacancies are the dominant point defects utilised by the species [88,147].

4.3.2 Comparison of the applied domain on the alloy

By undertaking EIS on the four different regions for CoCrMo in a variety of electrolytes, a complete picture of how the environment acts with the alloy under the different conditions can be made by comparing the datasets.

The polarization resistance of the alloy is the sum of all the resistance values obtained from the resistors within the fitted equivalent circuits determined from EIS. A comparison of these values is depicted within Figure 4.25; due to the scale of R_p obtained, these have been grouped into Cathodic-Transpassive and OCP-Passive.

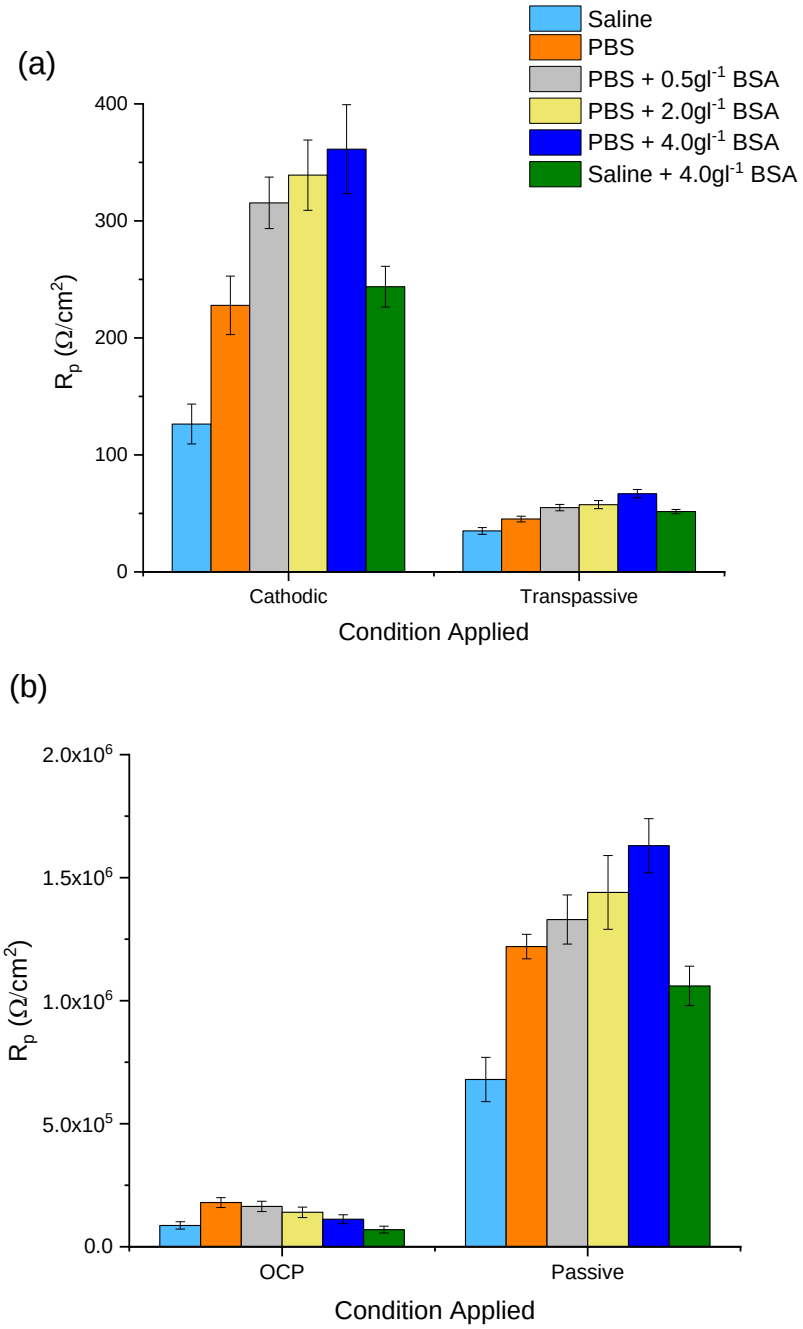

Figure 4.25 Shows the overall polarization resistance (R_p) for all of the different conditions applied to CoCrMo (a) Cathodic/Trans-passive (b) OCP/Passive.

The corrosion resistance of the alloy is seen to increase under all of the potentials in a phosphate environment, depicted by increased polarization resistances of the different conditions applied. This is achieved via adsorbing onto the surface of the alloy via chemisorption, protecting the surface from corrosion. In the cases of the OCP and passive conditions, phosphates were shown to increase the resistance of the film itself, which could be due to leading to a differing favoured composition. This will be explored in more detail within the following chapter.

BSA has different effects on the resistance depending on the electrochemical conditions; under OCP, it decreases the resistance, whereas for cathodic, passive and trans-passive, it is enhanced. Therefore adsorption of BSA is twofold; it can inhibit the access of oxidants to the alloy leading the adsorbed organic layer/passive film to be weaker, increasing the corrosion rate but can alter the passive film due to the molecule being a cathodic inhibitor increasing the resistance of corrosion in the passive domain [100]. These effects were also noted by Munoz [143]; he suggested that it could be down to the rate of oxide formation as albumin is a relatively large molecule, so it would interfere more with the growth process during slow processes such as at OCP. In conditions where there was little/no oxide film (cathodic/trans-passive), the effect of cathodic inhibition is the only factor that occurs, being the dominant force into why albumin presence is beneficial for these conditions.

A part of the difference in polarisation resistance values between the OCP and passive domain can be explained via the differences in the estimated oxide thickness produced. This is possible due to the same ECC being used to fit the data and the clear presence of a passive film, which doesn't apply to the cathodic and trans-passive domain. This is determined by utilising the values of C_{in}, within Equation 2.16F shown within the Literature review. The obtained data is shown in Figure 4.26.

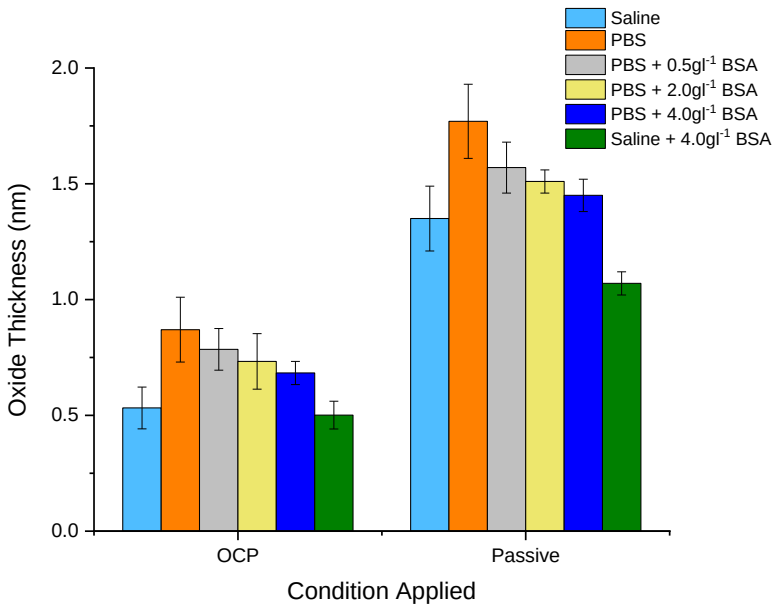

Figure 4.26 Comparison of the oxide thickness between OCP and Passive conditions

From the data shown, it is clear that the thickness of the passive film is much greater under passive conditions than OCP. According to extrapolated results obtained by Milosev [30] and Hodgson [127], it is noted that with an increase in potential, the thickness of the film increases for potentials between the OCP and $0.3V_{RE}$. There have been reports of an OCP formed film having a thickness of between 0.8 – 1 nm, which is concordant with the data obtained [100]. In both conditions, the presence of phosphates leads to a thicker oxide film formed; this could be due to phosphates being an oxidant themselves contributing to film formation. Whereas albumin is seen to reduce the thickness of the film as the large molecule would inhibit access of oxidant to the surface of the alloy as well as blocking active sites. The formation of film at OCP is slow in comparison to passive potentials and with albumin being a relatively large molecule has a higher chance to interfere with film growth.

Another difference noted between OCP, and passive conditions is the effect of albumin on the R_{out}. It is seen that under OCP, the presence of BSA causes values of R_{out} to decrease both with and without phosphates, whereas under passive conditions, the values of R_{out} are seen to increase. Munoz [100] also noted these different effects on R_{out} for OCP and Passive conditions, suggesting that this could be due to the applied conditions having different effects on both the orientation and conformation of the adsorbed layer.

The impedance values obtained under passive conditions consist of high values of 10^5 Ωcm^2, this is a typical value for a CoCrMo passive film [100,104]. When contrasted against the data obtained in the cathodic domain, it can be seen that those under cathodic conditions are highly diminished alongside a capacitance over a factor of magnitude higher, indicating that oxide film has greatly been reduced seeing as the cathodic reaction is highly favoured [102]. These findings are in accordance with the literature in that if the potential becomes sufficiently negative then little/no oxide will form (less than -0.5V_{RE} vs Ag/AgCl). [127,143,152]

The obtained values of impedance for the transpassive region are lower than those for the cathodic tests. Under trans-passive conditions, it is well known that the oxide film breaks down, and localised corrosion occurs. It is hard to compare the bare surfaces for cathodic and trans-passive conditions due to the occurrence of vacancies on the surface of the alloy under trans-passive conditions, which would drastically affect the impedance values by underestimating the resistance of the non-barrier layer.

4.3.3 Repassivation Process

The kinetics of repassivation was undertaken from investigating the current transients obtained. The quickest repassivation rate occurred in a phosphate environment, as they are an oxidising agent that can aid the coverage phase (τ_1) of the oxide. However, they are seen to hinder the growth phase (τ_2) of the oxide, as the oxidant now needs to also diffuse through the adsorbed layer alongside the freshly formed passive film to get to the alloys surface and be reduced, leading to a slower growth rate of the film to its maximum state. The presence of BSA has been shown to inhibit both the growth and coverage phases. In regards to the growth phase, the rate is reduced due to the molecules inhibiting the oxygen reduction reaction by hindering access to active sites of the surface of the alloy [127,153]. At the same time, the coverage phase is hindered due to the same reason as for phosphates, although the rate is even slower due to the size of the BSA molecules in comparison to phosphate complexes. D.Sun [154] also observed an increased repassivation time for proteinaceous environments when the oxide was cleaved via a scratch test. It was indicated that that the gradual re-establishment of the electrical double layer contributes to the slow recovery of current [154]. The data obtained from the potentiodynamic tests back up these theories as BSA was shown to act as a cathodic inhibitor.

In regards to the effect of applied passive potential on the rate of repassivation, it was observed that a higher passive potential gives a faster rate of repassivation as the rate of coverage is increased due to the enhanced reactivity of the condition. Pyun et al. [155] explored the effect of potential on the repassivation rate of aluminium, and alongside determining that the speed of passivation was increased with passive potential, the films become less porous (higher value of n obtained).

4.3.3.1 Limitations

The methods used to investigate the repassivation kinetics are desirable when it comes to predicting the behaviour of the CoCrMo under a variety of conditions, but multiple factors need to be taken into consideration that can influence/affect the data sets obtained, which range from the response time of the equipment used to the rate at which the oxide is removed [156].

Specific limitations with this data obtained are due to ohmic limitations alongside the potentiostat response time, which didn't have the ability to collect data on the nanosecond time scale [156,157]. With response time of the potentiostat being slow, it fails to substantially increase the current fast enough to maintain the potential which is essential due to the drastic difference between the cathodic and passive potentials, this results in a percentage of the charge being lost within the early transition [156]. This profound change in conditions causes an ohmic drop which alters the early form of the current transient [156,157]. These limitations make the data obtained only instructive with respect to environment analysed.

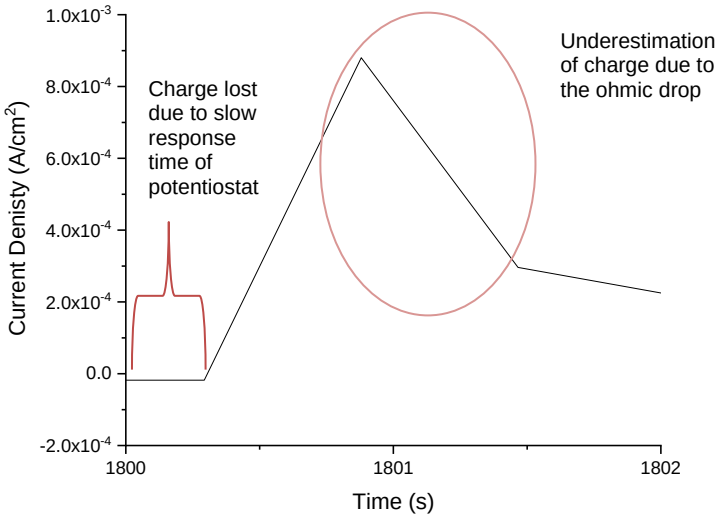

Figure 4.27 A close up of the transition time of CoCrMo in PBS, repassivated at +0.1V_{RE} (Figure 3.6)

4.4 Conclusion

An in-depth study on the electrochemical corrosion behaviour of CoCrMo alloys in various simulated bodily fluids was undertaken, this enabled the following conclusions to be reached.

1. The effects and properties of the surface of a CoCrMo alloy are highly influenced by the composition of the surrounding electrolyte, the applied potential as well as temperature.
2. Phosphates reduce the rate of corrosion as they adsorb onto the surface of the alloy via chemisorption acting as a barrier between the alloy and the environment
3. The effects of albumin are two-fold: it can inhibit the access of oxidants to the alloy leading the adsorbed organic layer/passive film to be weaker, increasing the corrosion rate but can alter the passive film due to the molecule being a cathodic inhibitor increasing the resistance of corrosion in the passive domain. The molecule also adsorbs onto the surface via chemisorption
4. The domain to which the alloy is exposed has a drastic effect on the properties of CoCrMo
    - Cathodic domain (-1.0V_{RE}), the current is determined from the reduction oxygen reaction, which leads to major/complete reduction of the oxide film

- OCP, there is an oxide film formed that protects the alloy. The thickness of the film is between 0.5 - 1.0 nm for the environments analysed
- Passive domain (+0.1V_{RE}), a thicker oxide film is formed, which enhances the corrosion resistance of the alloy. The thicknesses obtained were between 1.0 - 1.8 nm.
- Transpassive domain (+1.0V_{RE}), there is a presence of a non-barrier layer, the oxide film is broken down under these conditions with localised corrosion occurring on the surface

5. The rate of repassivation has been noted to vary with the environment in which it occurs, the fastest repassivation rate was observed in a phosphate-containing environment, whereas the presence of BSA, leads to slower repassivation rates seeing as the oxidant is being inhibited due to the proteins size which blocks the active sites on the surface. Repassivation under a higher passive potential leads to a higher rate of coverage but has little/no effect on the growth phase.
6. An increase in temperature increases the rate of the corrosion rate of CoCrMo alongside increasing the cathodic reaction rates.

Chapter 5
The Effects of the Environment and Applied Electrochemical Conditions of the Surface of CoCrMo

5.1 Introduction

The surface chemistry of CoCrMo is affected by the environment it is exposed to and the applied conditions; these slight changes can lead to changes in the corrosion resistance of the alloy. By building up a profile of the surface at different conditions, it enables a deeper insight into any prevailing mechanisms that occur. Key emphasis was placed upon any changes to the composition and structure of the passive film, which gives the alloy its corrosion resistance.

The following chapter aims to explore any chemical or physical changes in the surface under a range of simulated bodily fluids at specific electrochemical potentials. To undertake this surface characterisation, tests were conducted on post-test samples, with a polished CoCrMo sample being used as a control. The following analysis was undertaken to achieve these aims: Optical Microscopy (OM), Scanning Electron Microscopy (SEM), Transmission Electron Microscopy (TEM), X-Ray Photoelectron Spectroscopy (XPS), Electron Energy Loss Spectroscopy (EELS), Energy-Dispersive X-ray Spectroscopy (EDX) and Atomic Force Microscopy (AFM).

5.2 CoCrMo Alloy

A polished wrought Low Carbon CoCrMo sample was examined to determine the surface properties of the alloy when just exposed to air; this then can be used as a control for comparisons. As stated before, the roughness of each sample was ~10 nm after the polishing phase discussed in Section 3.2.1. The surface of the sample as observed by Optical Microscopy is shown in Figure 5.1.

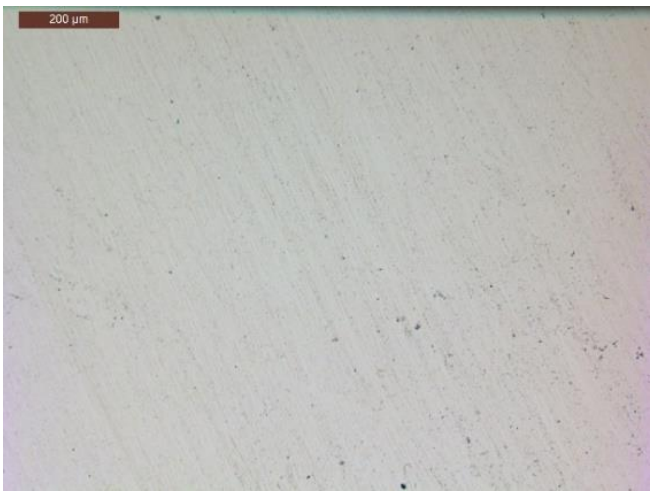

Figure 5.1 Surface of the polished CoCrMo sample via optical microscopy

5.2.1 SEM/EDX Analysis

The composition of the freshly polished surface was initially analysed by SEM/EDX; the data obtained is shown in Figure 5.2. The contributions from the metal elements are as expected (Co 72wt%, Cr 21wt%, Mo 8wt%) and in concordance with the specifications of the alloy, The SEM/EDX analysis indicated the presence of carbon-rich areas, the AFM and XPS data shown later on also consolidates the presence of carbide peaks. The imaging revealed these carbon-rich areas as dark areas, which are distributed randomly and are generally around 1 µm.

a)

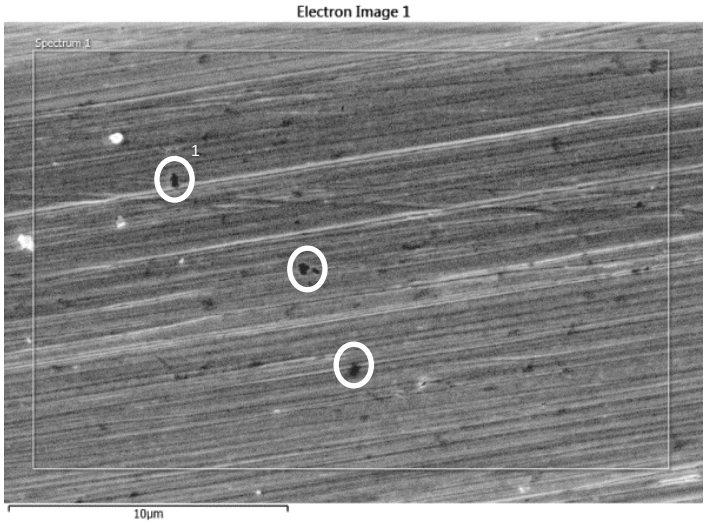

b)

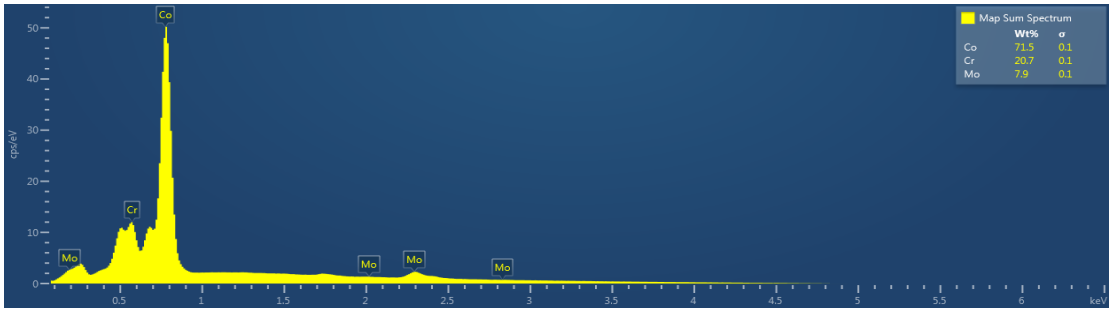

c)

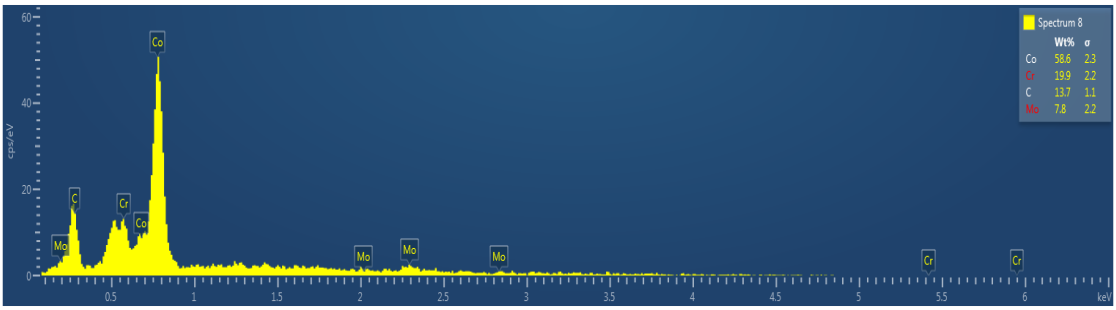

Figure 5.2 (a) SEM image of the polished CoCrMo surface (b) EDX analysis of spectrum 1 from the SEM (c) EDX analysis of white circle[1], indicating a high carbon presence

5.2.2 Crystalline Structure Analysis

TEM was utilised to assess the crystalline structure of the alloy. Figure 5.3a indicates the high angle annular dark field obtained from the surface of Ir-CoCrMo, with the areas analysed via diffraction analysis indicated. The upper 50 nm of the alloy has indications of deformation due to the crystals in this region possessing a finer structure compared to the bulk alloy. Individual grains of the alloy can easily be distinguished, with some segregation of Cr and Mo being seen in places as indicated within Figure 5.3b. There looks to be a presence of an interface between the Ir layer and alloy; this couldn't be identified by the use of EDX at these magnifications but is believed to be an oxide layer.

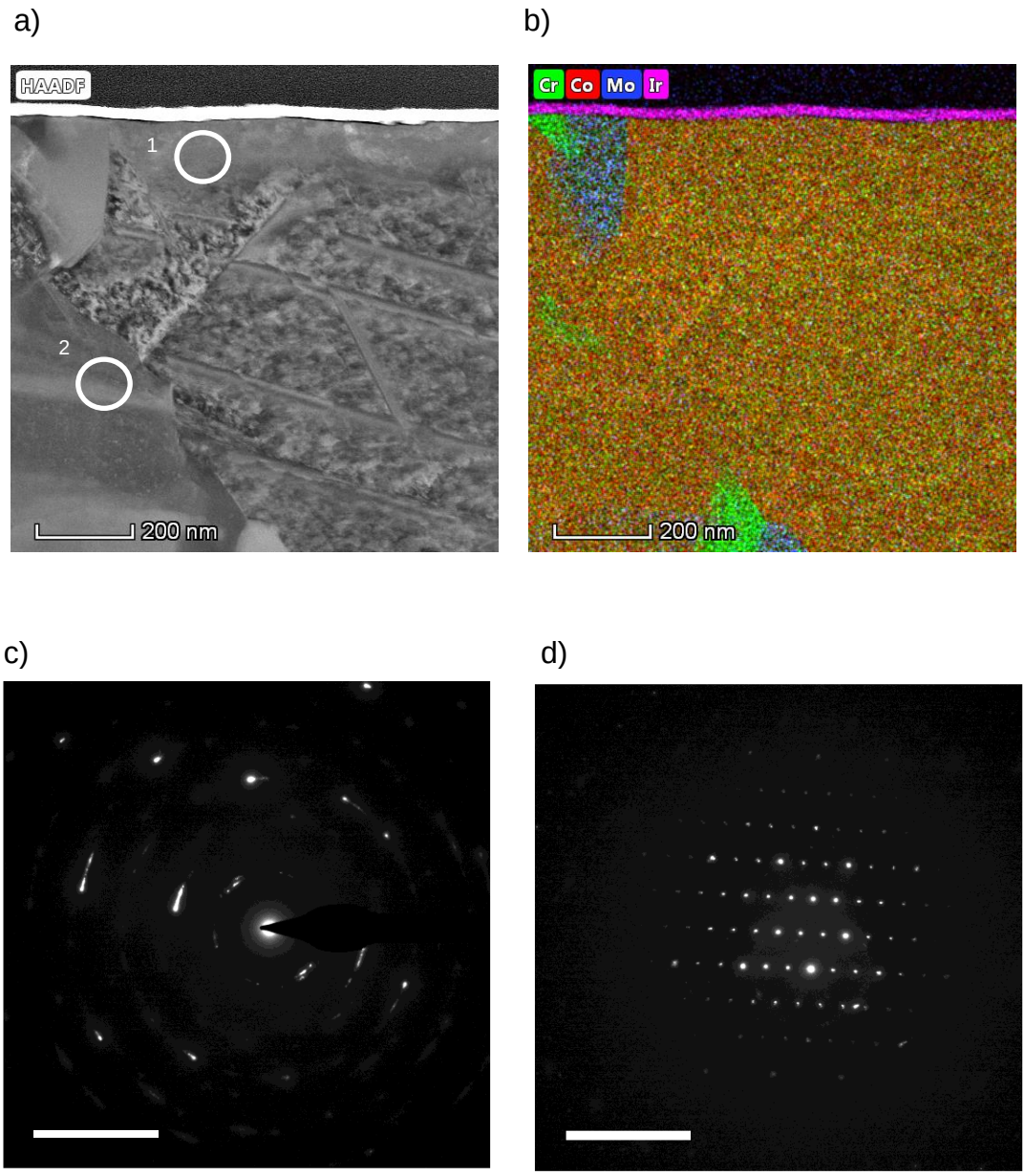

Figure 5.3 High angle annular dark field TEM image of a polished CoCrMo cross section (b) Elemental X-Ray map of the TEM image (c) SAED of the upper region (1) within the TEM image (d) SAED of bulk material (2) within the TEM image

Selected Area Electron Diffraction (SAED) patterns were acquired from the finer crystals near the surface as well as the bulk material. These obtained images further support and consolidate that the upper region has a finer structure as Figure 5.3c, possessing a ringed diffraction pattern. This pattern is nano-crystalline due to a large number of crystals that are orientated in different ways induced by strain from the polishing procedure [158]. This

structure demonstrates hexagonal structure d-spacing, which is a characteristic of ε – cobalt [159]. This is different to the bulk material, which appears to have a rigid linear structure. These findings are in correlation with the structure expected for a polished CoCrMo sample, with high levels of strain being able to convert the metastable FCC structure into an HCP phase [158].

5.2.3 Surface Chemistry Analysis

The composition of the surface of a polished CoCrMo sample in the absence of etching was investigated by the use of X-Ray Photoelectron Spectroscopy, with an overall survey spectrum being shown in Figure 5.4. Analysis of the surface revealed the following elements: Carbon (C 1s), Oxygen (O 1s), Chromium (Cr 2p), Cobalt (Co 2p), Molybdenum (Mo 3d).

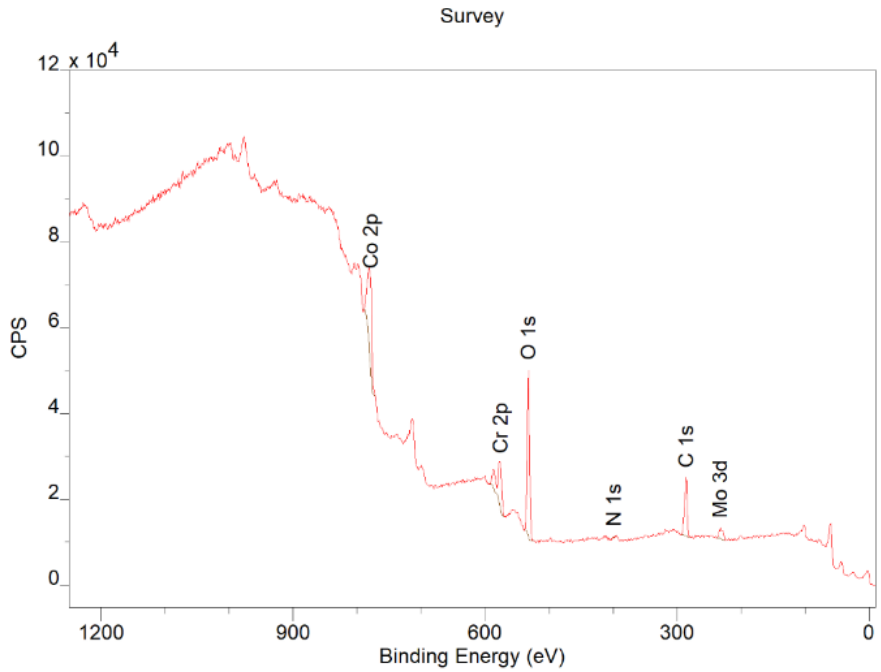

Figure 5.4 XPS survey spectrum of the polished CoCrMo surface

Table 5.1 Data extracted from the spectrum depicting peak position and atomic percentage

Elemental Species	Binding Energy (eV)	Atomic Percentage %
Mo 3d	231.38	0.56
C 1s	285.38	56.22
N 1s	398.38	0.19
O 1s	531.38	34.38
Cr 2p	575.38	4.72
Co 2p	780.38	3.37

The deconvoluted elements detected from the spectra are shown in Figure 5.5. Elemental carbon is shown (Figure 5.5a), the peak typically consists of C-C at 285 eV, C-O at 287 eV and C=O at 289 eV, but there is also evidence for metal carbides due to the presence of a peak at around ~283 eV. The oxygen peak (Figure 5.5b) is characterised via a peak around 533 eV. The metal oxide peak appears at significantly lower binding energy enabling it to easily be differentiated from the species; in this case, ~530 eV accounts for the oxides that make up the passive film. This peak is dwarfed by the quantity of oxygen that exists as hydroxide, possibly due to the surface being hydrated from the polishing process.

The metal peaks are characterized by a well-defined peak with the level of oxidation leading to increases to the binding energy slightly. The cobalt and chromium peaks are formed of two states ($\frac{3}{2}$ spin, $\frac{1}{2}$ spin) as the atoms contain unpaired electrons, coupling between the unpaired electrons in the core and outer layer leads to the production of another state [155]. For both of the deconvolutions involving Co and Cr, only the peak corresponding to the $\frac{3}{2}$ spin-state is analysed this is due to this spin state producing satellite features that overlap the $\frac{1}{2}$ spin-state [160,162].

The cobalt peak (Figure 5.5c) is seen to primarily exist in the hydroxide form with a small contribution for cobalt oxide. The chromium peak (Figure 5.5d) primarily exists as Cr(III) oxide and hydroxide, with the Cr(III) oxide peak having many multiplet-split components. By fitting each component, it prevents false identification of any of the chemical states [162]. Molybdenum

(Figure 5.5e) is known to be able to adopt multiple oxidation states (IV, V, VI). It is seen that molybdenum VI is favoured out of the states available, with the element preferring to exist as an oxide within the surface over its elemental form.

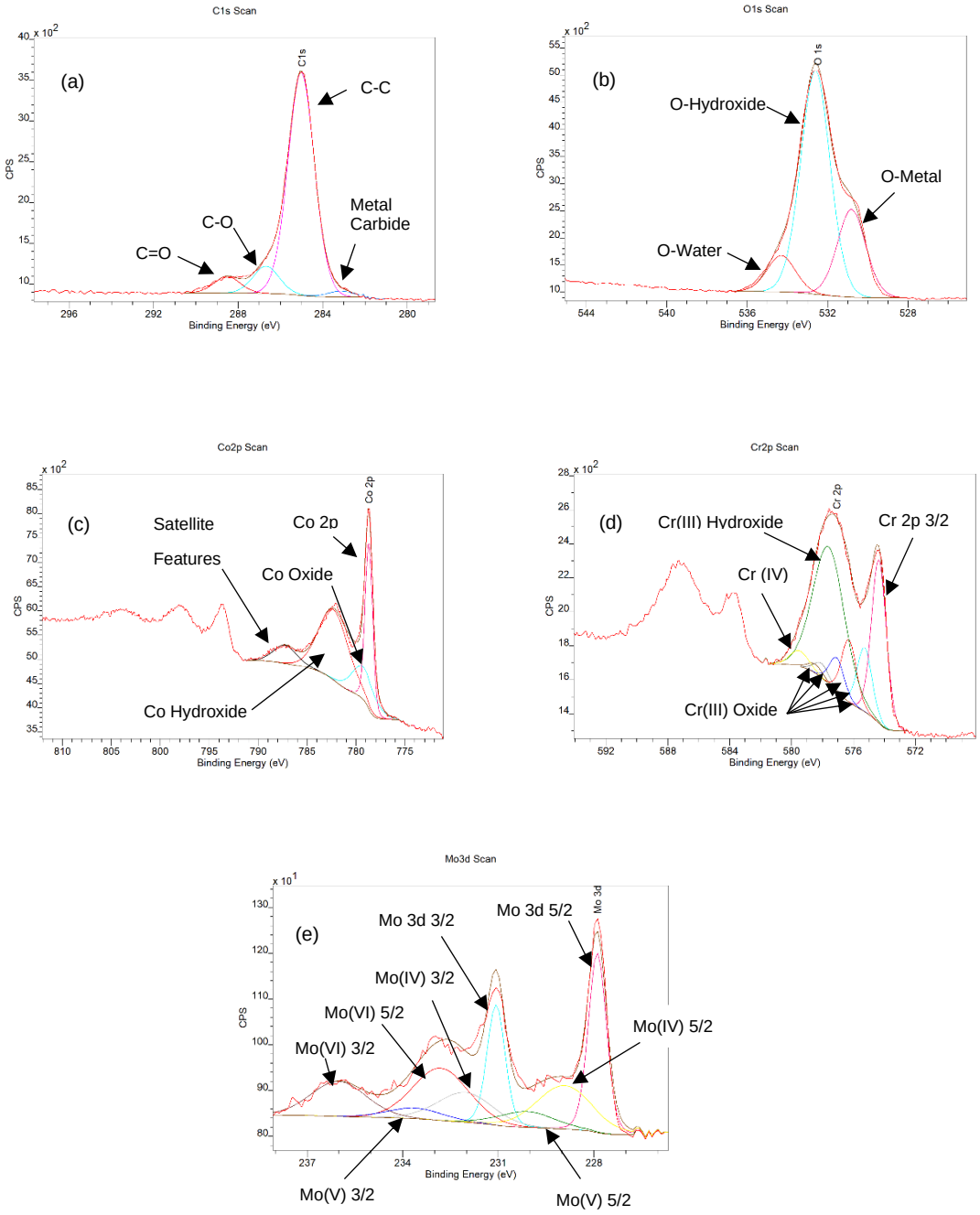

Figure 5.5 Fitting of XPS peaks on a polished CoCrMo surface: (a) Carbon, (b) Oxygen, (c) Cobalt, (d) Chromium and (e) Molybdenum

5.2.4 Morphology of the Surface

The morphology of the sample was further examined by the use of AFM; Figure 5.6a shows the surface of a polished CoCrMo sample. The surface is seen to be relatively smooth except for a few trenches. These can stem from polishing, and even though they are easily visible, the maximum depth they exist at is ~30 nm. Some carbides (lighter regions) are distributed randomly over the surface, being around 20 nm higher than the substrate. Overall the roughness of the samples is concordant with the NPFlex measurements of around ~10 ± 2 nm.

A dissipation profile of the same area (Figure 5.6b) shows more detail about the surface energy of the CoCrMo sample. Upon closer inspection of some of the deformities (peaks and valleys), it is seen that they are due to carbide formation as they readily form at grain boundaries when the energy free barrier is low enough [134]. The surface energy of these carbides is much higher than that of the alloy matrix (white regions); this indicates that carbides have a higher resistance to corrosion than the bulk alloy [101].

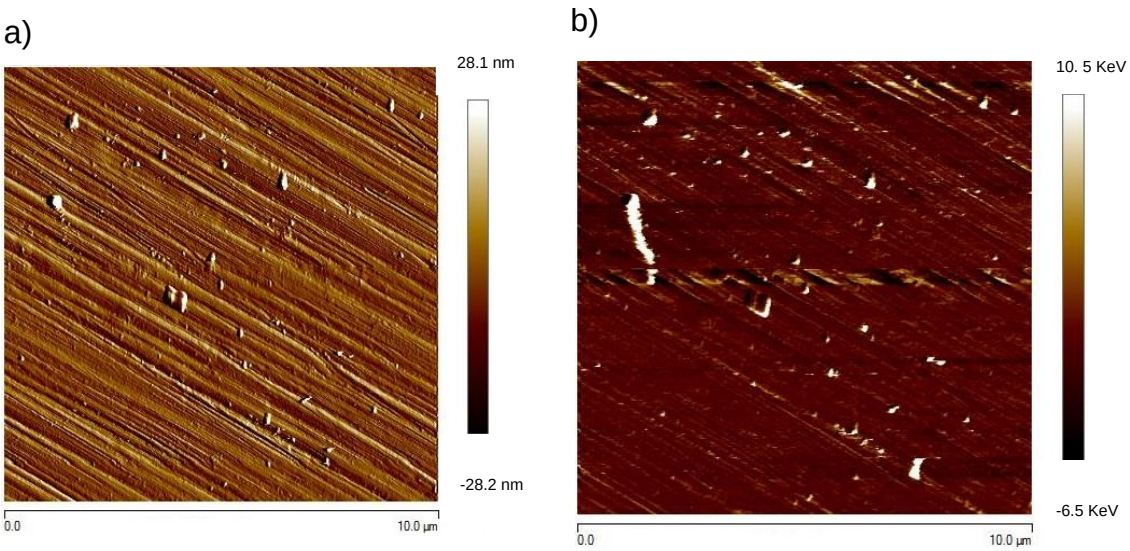

Figure 5.6 AFM images taken from a polished CoCrMo sample (a) Height profile (b) Dissipation profile (surface energy)

5.3 Effects of simulated bodily fluids on the surface of CoCrMo

The addition of inorganic salts and organic molecules has been shown to have drastic effects on the corrosion behaviour of CoCrMo; the use of surface analysis was used to further understand the electrochemical observations. All samples within this section were passivated at +0.1V_{RE} within the selected electrolyte upon submersion. This corresponds to the electrochemical data obtained within Section 4.2.3.3.

5.3.1 Observable effects on the surface

Figure 5.7 depicts a CoCrMo surface passivated (+0.1V_{RE}) within a PBS solution. By comparing the image with Figure 5.2a, it appears that there is a deposition of inorganic salts due to the surface appearing smoother. The use of C Kα (Figure 5.7b) indicates the presence of carbides on the surface, with other species on the surface assumed to be salts (white circles). The use of EDX to determine these species was, however, not possible; this could be due to the area of the sample that was investigated. The O Kα (Figure 5.7c) indicates that oxygen is consistently present on the surface of the alloy, which would correlate with the formation of a passive film.

a)

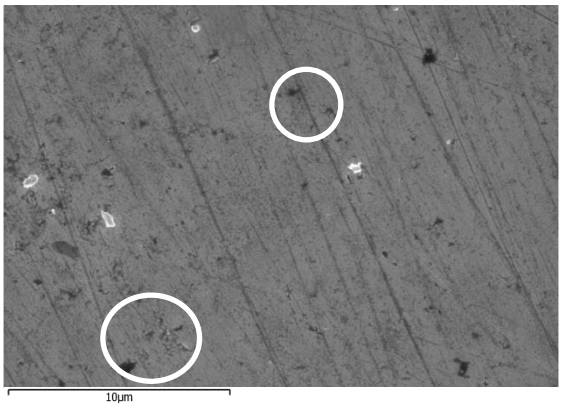

b)

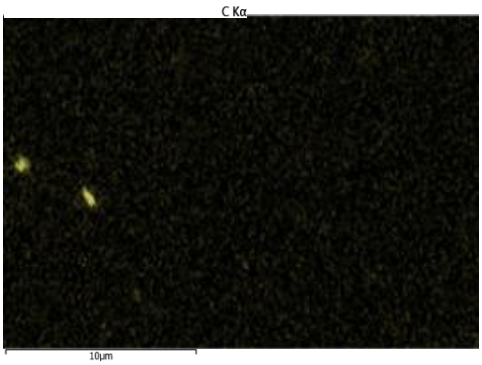

c)

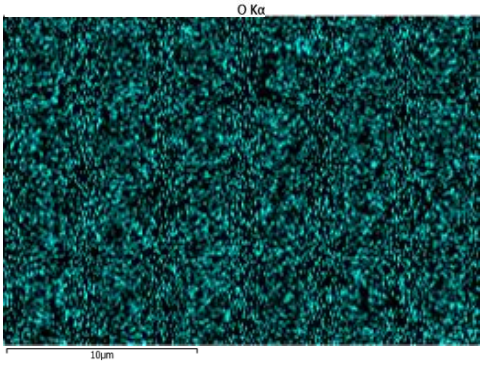

Figure 5.7 SEM image taken of a passivated (+0.1V_{RE}) CoCrMo sample within a PBS solution (b) Elemental X-Ray map of C Kα (c) Elemental X-Ray map of O Kα

Figure 5.8a depicts a cross-sectional view of the same sample with the use of TEM. Just as seen previously, there appears to be an interface present at the surface of the alloy; an EDX profile of this region (Figure 5.8b) enables the thin oxide film (~2 nm) to be visible. This film is uniformly present across the surface of the alloy. The bulk alloy is a combination of all the metallic elements present, consolidating that the previously seen Cr/Mo affinity occurs only in localised sites.

a)

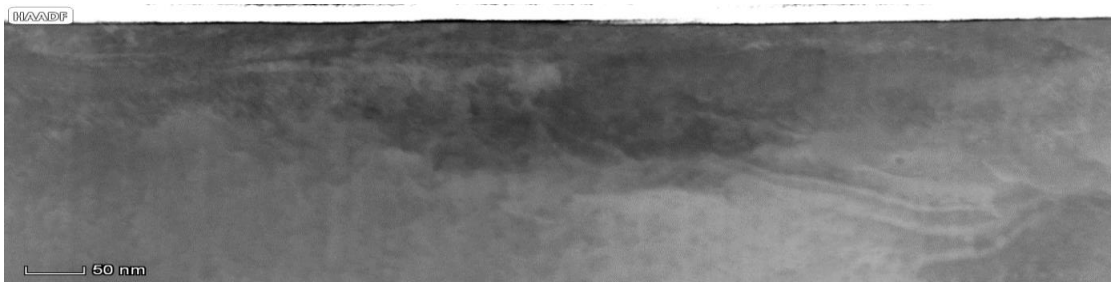

b)

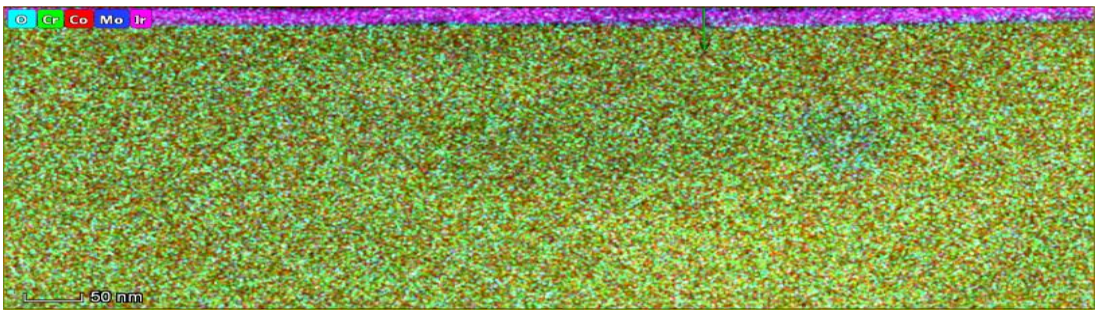

Figure 5.8 TEM side view of a passivated (+0.1V_{RE}) CoCrMo sample within a PBS solution (b) Elemental X-Ray map

Figure 5.9a depicts CoCrMo passivated within PBS and 4gl^{-1} BSA solution; this leads to a build-up of BSA on the surface, which seems to build up as aggregates. C Kα and O Kα are used to determine the presence of BSA on the surface of the alloy as these are the two main elements that BSA is composed of. The C Kα and O Kα spectra depict areas of high protein concentration in random areas on the surface. The overall surface of the alloy seems to have inorganic deposition, too, due to the less visible presence of the surface structure, as seen before with a polished sample in Figure 5.2a. From these images, we can conclude that both the inorganic and organic species can adsorb onto the surface of the alloy.

a)

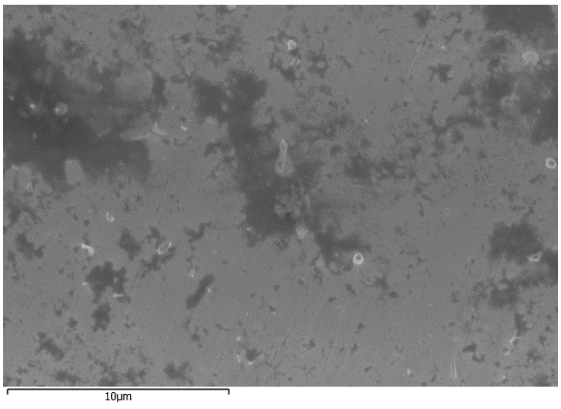

b)

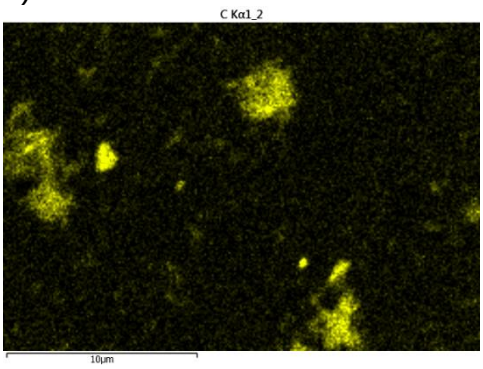

c)

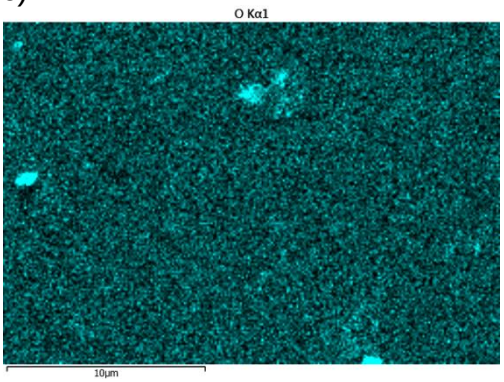

Figure 5.9 SEM image taken of a passivated ($0.1V_{RE}$) CoCrMo sample within a PBS and $4gl^{-1}$ BSA solution (b) Elemental X-Ray map of C Kα (c) Elemental X-Ray map of O Kα

By utilising FIB alongside TEM, it was possible to observe a side view of the passivated CoCrMo sample. An example of the CoCrMo passivated with PBS, and $4gl^{-1}$ BSA is shown in Figure 5.10a, with the EDX image in Figure 5.10b. The oxide film (blue) and protein layer (yellow) on the surface are easily distinguishable by the use of EDX; for ease of viewing the adsorbed layers, only cobalt out of the metal elements is shown. This oxide film had a varying thickness of between 1.5 – 2 nm, with the protein layer being slightly thicker at around 4 nm.

a)

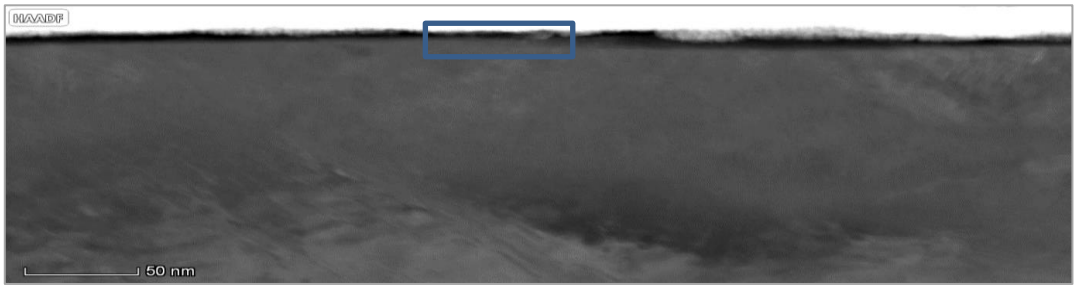

b)

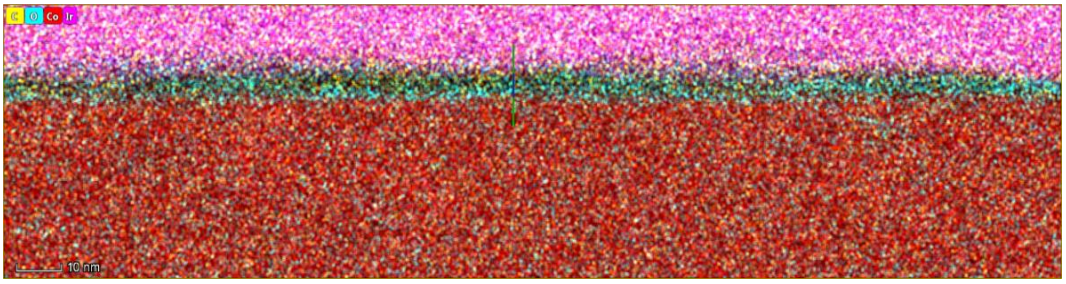

Figure 5.10 TEM side view of a passivated (+0.1V_{RE}) CoCrMo sample within a PBS and 4gl^{-1} BSA solution (b) Elemental X-Ray map

5.3.2 Effects of electrolyte on passive film composition

5.3.2.1 EELS Analysis

The use of EELS was undertaken alongside TEM imaging to determine changes within the interfaces from the cross-sections investigated. EELS possesses a much higher energy resolution than EDX, enabling different forms of the same element to be identified. The assignment of EELS peaks was done by contrasting against EELS databases [136,137].

The image of a CoCrMo sample passivated (+0.1V_{RE}) within PBS and the spectrum obtained is shown in Figure 5.11. From the analysis of the oxide film (~2 nm), it can be seen that there is a slight presence of C K, which occurs at 300 eV; this is most likely due to contamination on the surface [136,137]. The presence of O K at 540 eV confirms that this is an oxide layer which is comprised of both Cr L 3,2 (600 eV) and Co L 3,2 (780 eV), the quantities of these elements within the oxide film appear to be similar from the data obtained [136,137]. When comparing to the bulk layer, there are just the metal elements present. The ratio of Co L 3,2: Cr L 3,2 has increased as expected due to the stoichiometry of the alloy. Molybdenum edges are not seen due to it having high binding energy (2520 eV) on the EELS spectra [136].

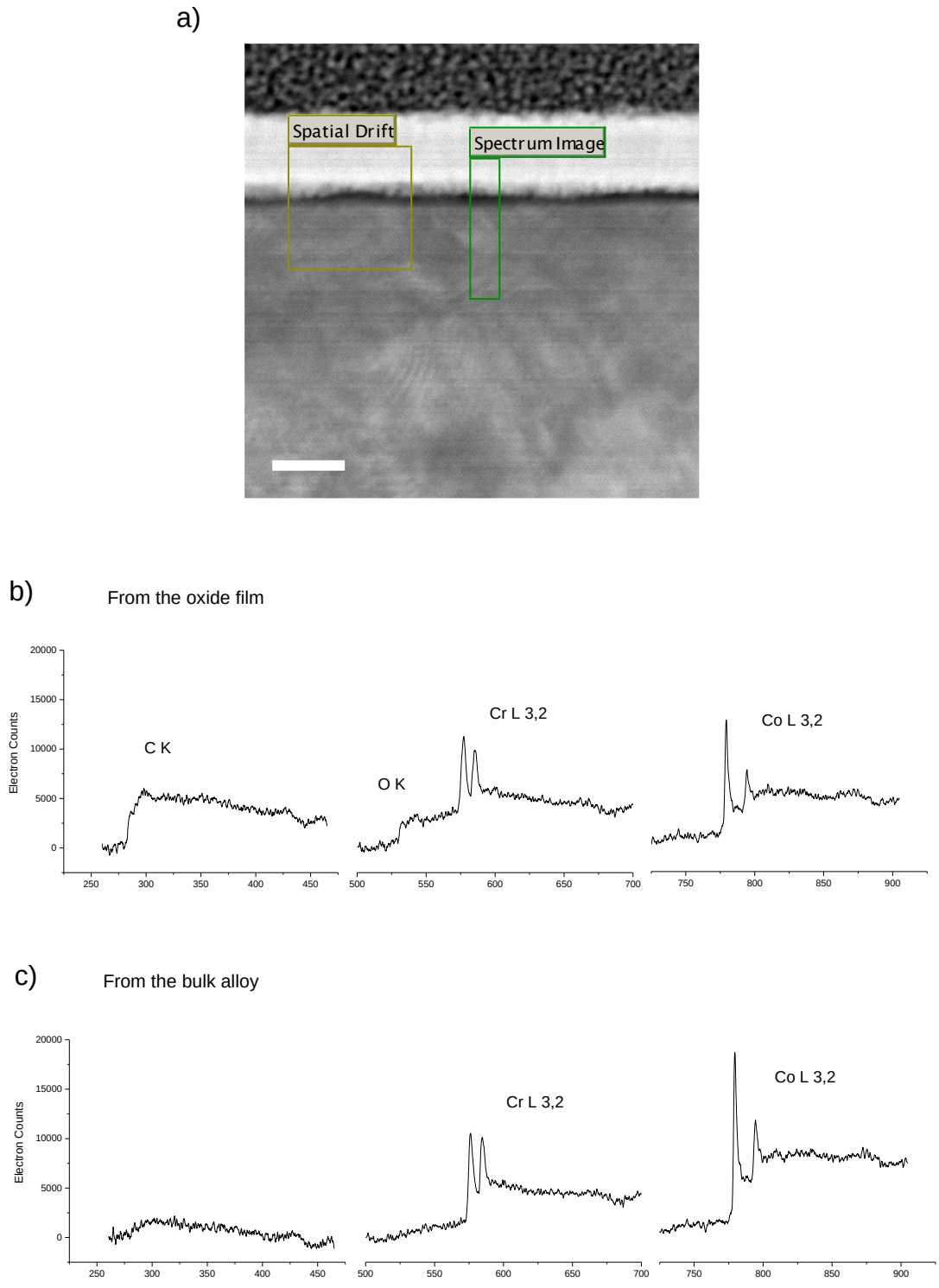

Figure 5.11 EELS of CoCrMo passivated (+0.1V_{RE}) within PBS covering the areas of interest (a) TEM image of area taken (b) EELS spectra of the oxide film (c) EELS spectra of the bulk alloy

The image of a CoCrMo sample passivated at 0.1V_{RE} in PBS, and 4gl^{-1} BSA and the spectrum obtained is shown in Figure 5.12. Due to the presence of BSA within the electrolyte, an outer carbonaceous layer (~ 4 nm) on the surface was observed. EELS analysis confirms this due to the strong C K peak; this possesses a very similar fine structure to that of amorphous carbon (Figure 5.12b). This presence of carbon is not seen within the oxide film or bulk alloy, possessing similar characteristics to a purely PBS environment. As seen previously, the oxide film is comprised of both Cr L 3,2 and Co L 3,2. However, the ratio seems to shift in favour of Cr L 3,2 now. As expected, the bulk alloy is just comprised of identifiable metal elements.

a)

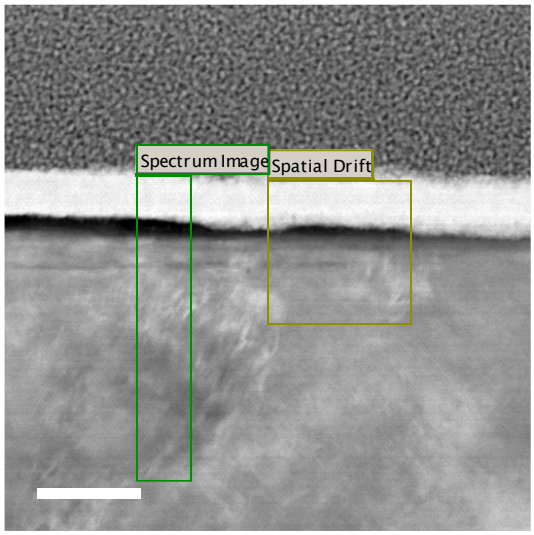

b)

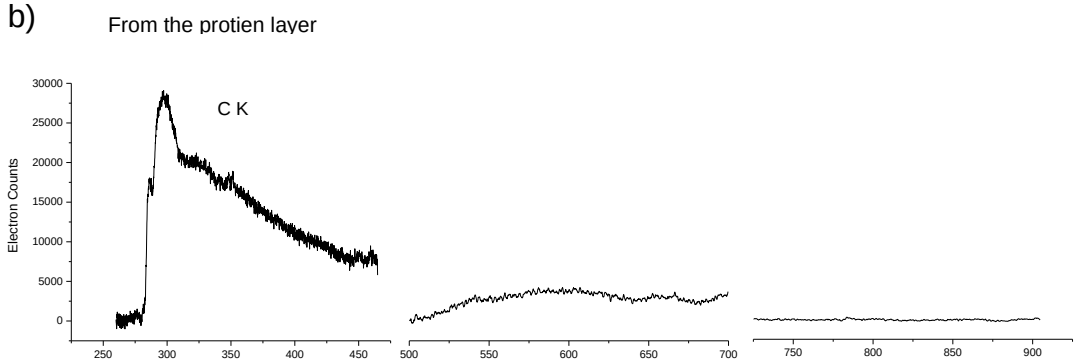

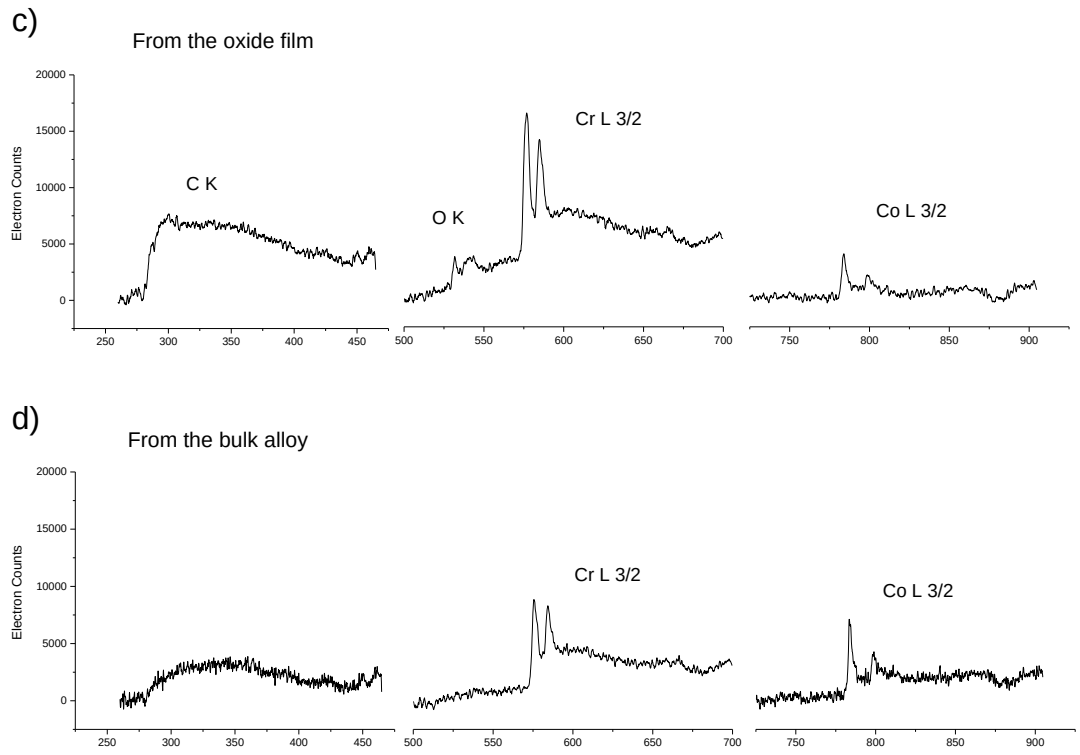

Figure 5.12 EELS of CoCrMo passivated (+0.1V_{RE}) within PBS and 4gl^{-1} BSA covering the areas of interest (a) TEM image of area taken (b) EELS spectra of the protein layer (c) EELS spectra of the oxide film (d) EELS spectra of the bulk alloy

5.3.2.2 XPS Analysis

XPS analysis of the CoCrMo samples after passivation (+0.1V_{RE}) under simulated bodily fluids signalled the following elements: carbon (C 1s), oxygen (O 1s), chromium (Cr 2p), cobalt (Co 2p), molybdenum (Mo 3d). When immersed in a PBS environment, phosphorous (P 2p) was also identified , the presence of BSA lead to the detection of nitrogen (N 1s) and traces of sulfur (S 2p). For BSA containing environments, etching was done until the metal peaks became visible, which varied from sample to sample. Deconvolution was undertaken for all environments; however, just the PBS and PBS with 4.0gl^{-1} BSA are depicted in Figure 5.13 for clarity (the peak for sulfur has not been deconvoluted due to the lack of a clear peak due to its extremely low quantity within the protein).

PBS Environment

PBS + 4.0gl^{-1} BSA Environment

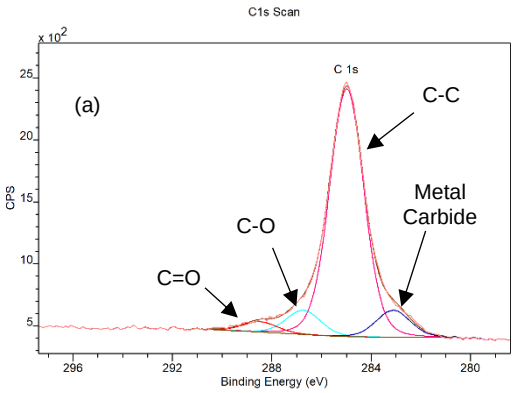

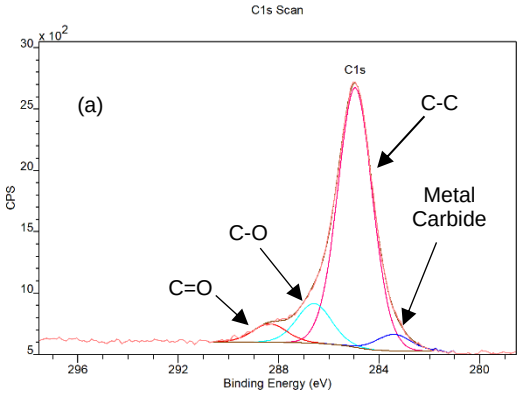

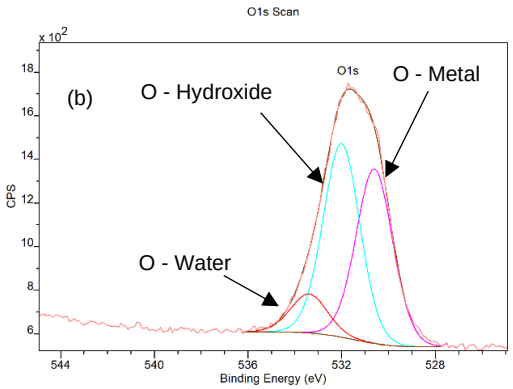

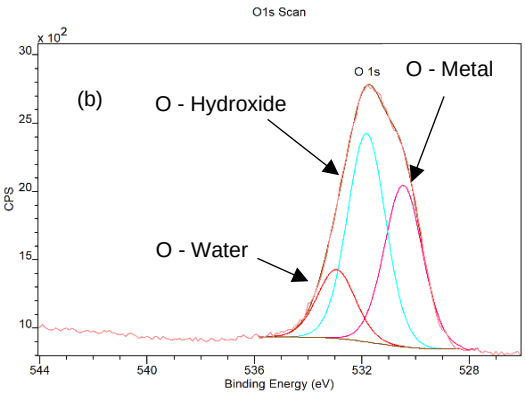

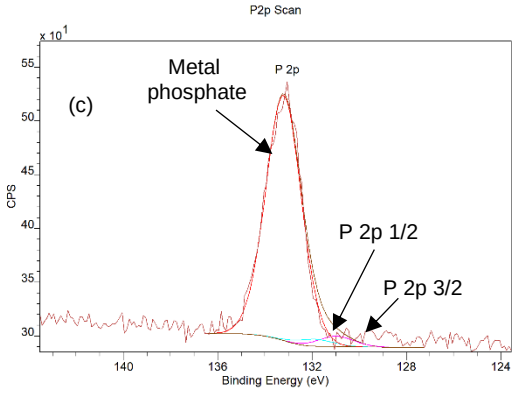

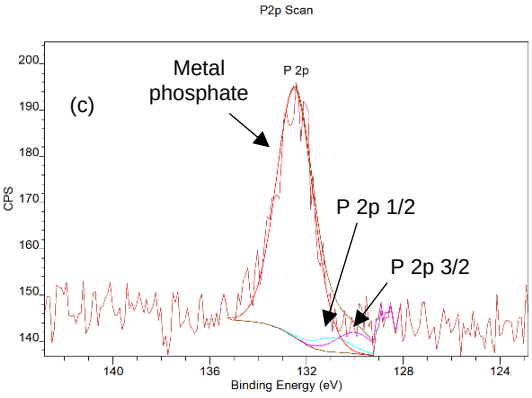

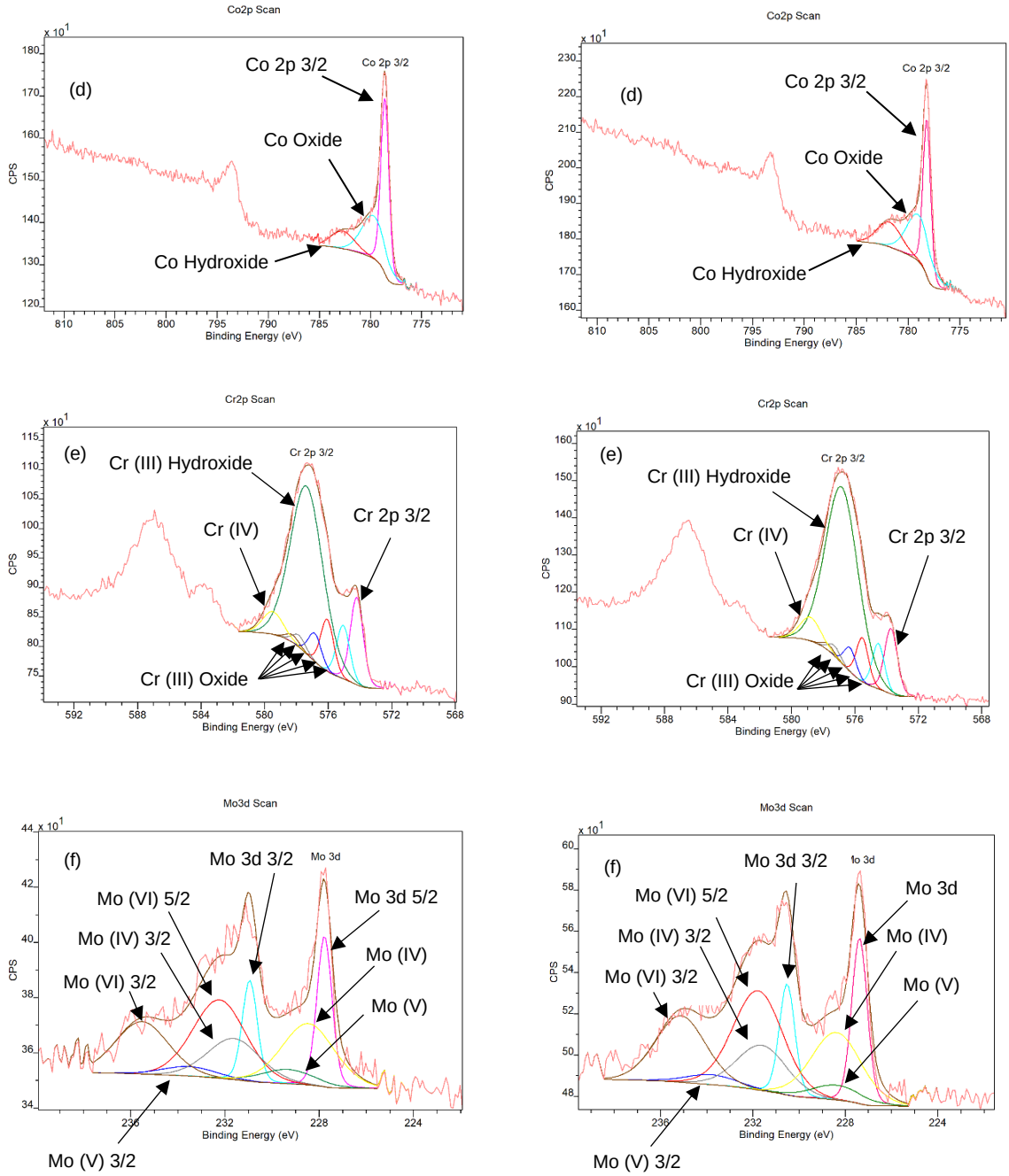

Figure 5.13 Fitting of XPS peaks on passivated (+0.1V_{RE}) CoCrMo in PBS and PBS with 4.0gl^{-1} BSA after 1hr: (a) Carbon, (b) Oxygen, (c) Phosphorus (d) Cobalt, (e) Chromium and (f) Molybdenum

When comparing a polished CoCrMo sample with a passivated one, it can be seen that the percentage of oxygen that exists as a metal oxide when passivated has dramatically increased (Figure 5.5b: Figure 5.13b). This is further highlighted within the cobalt and chromium spectra's (Figure 5.5c,5.5d: Figure 5.13d,5.13e). The peaks representing elemental chromium (Cr 2p 3/2)

and molybdenum (Mo 3d 5/2 and Mo 3d 3/2) are visibly reduced within the passivated samples, with more of this metal existing as an oxide or hydroxide.

The phosphorus peaks (Figure 5.13c) indicate that the absorbed layer on the surface of the alloy is bound to the metal. This is consistent in an environment with/without the presence of BSA. F

When BSA is present, the carbon spectra (Figure 5.13a) of the alloy is altered, giving a higher proportion of the carbon being present either in the C-O or C=O form. The peak is also observed to be broader; this indicates that BSA is adsorbs onto the surface of the alloy; this is further consolidated by the development of a strong N 1s peak seen when BSA is present [100]. The deconvoluted peak is shown in Figure 5.14. The nitrogen peak is characterised via a peak corresponding to C-NH_2 around 400 eV. The presence of metal nitrates seen at lower binding energies (~ 394 eV) suggests that bonding of the protein to the alloy can occur through the nitrogen group.

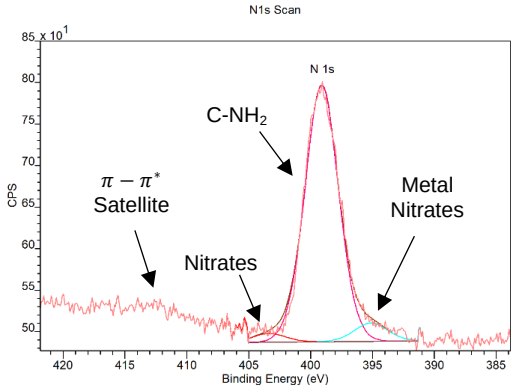

Figure 5.14 Nitrogen (N 1s) XPS peak of a passivated CoCrMo sample in PBS + 4.0gl^{-1} BSA

The presence of BSA also leads to changes within the deconvoluted metal peaks. There are slight increases in the percentage of hydroxide formed within the Co 2p, although it still mainly exists in the metal form. As expected, chromium exists mainly as either Cr(III) oxide and hydroxide, with the proportions of both $Cr_{metal/oxide}$ and $Cr_{metal/hydroxide}$ increasing when the protein was present (Figure 5.13e). Mo(VI) is still the favoured form for molybdenum, but there is a substantial percentage increase in Mo(IV) when in the presence

of albumin, this could be credited to molybdenum being bound to the protein on the alloy's surface (Figure 5.13f).

The percentage of metallic elements (Co, Cr, Mo) within the oxide layer of the alloy determined from XPS is depicted in Figure 5.15. This was undertaken via analysis of the individual spectra obtained and then deducing the quantities of metal in the oxide state. This enables further understanding about the composition of the oxide layer under various simulated bodily fluids.

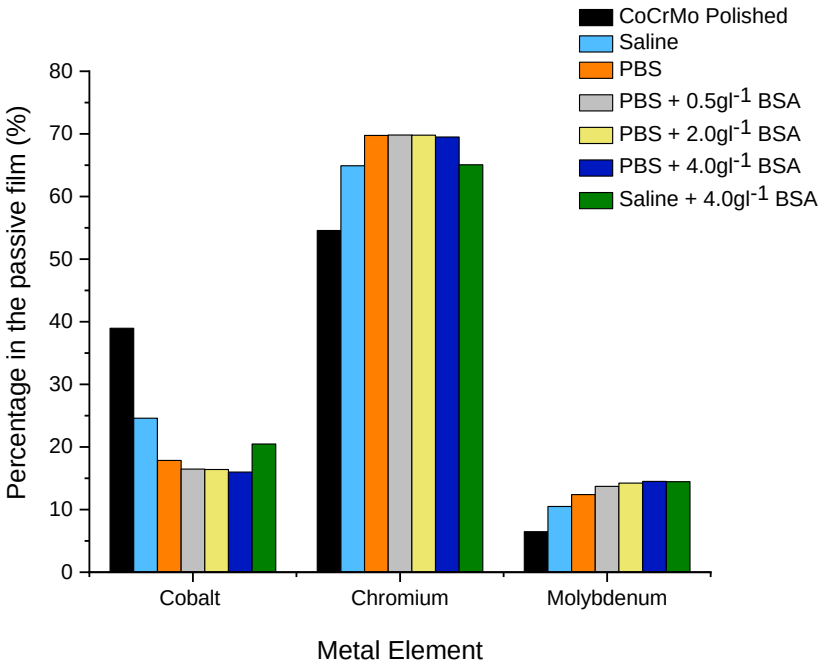

Figure 5.15 Percentage of metallic elements present in the oxide state of passivated (+0.1V_{RE}) CoCrMo from XPS analysis

From the data within Figure 5.15, it can be seen that the composition of the passive film is highly affected by its surrounding environment. Cobalt is the main constituent of the alloy (~66%) but is seen not to be the dominant metallic element within the film. When the film is electrochemically formed in saline conditions, the level of cobalt within the film is drastically reduced in comparison to the oxide film formed in air and this effect is further enhanced when exposed to phosphates and albumin. Chromium is seen to possess the highest presence within the passive film, composing of over 65% in all passivated samples analysed. Even in an air oxide formed film, molybdenum exceeds its stoichiometry in the alloy, with the content being seen to increase in the presence of inorganic and organic species, reaching a high of 15%. This could be due to the supposed high affinity the BSA molecule has with molybdenum.

5.3.3 Effects of Repassivation on the Surface Properties

Analysis of the passive film after an electrochemical repassivation phase was undertaken to examine if there were any alterations to the film formation (Section 4.2.4). CoCrMo samples were submerged within the electrolyte and polarized at cathodic conditions (-1.0V_{RE}) for 30 minutes, followed by passive conditions for 30 minutes (+0.1V_{RE}).

The comparison of the TEM/EDX cross-sections for a passivated/repassivated CoCrMo sample in a PBS and 4gl^{-1} BSA solution was intriguing (Figure 5.10:Figure 5.16). The upper surface region (Figure 5.16a) appears to be composed of nano-crystalline material; this seems to delve deeper into the alloy than previously seen, which could have been due to the cathodic potential applied to remove the oxide layer and the different reactions that occur (O_2 reduction). With regards to the EDX data (Figure 5.16b), the oxide film (blue) and protein layer (yellow) on the surface are easily distinguishable, as done previously for ease of viewing the adsorbed layers, only cobalt out of the metal elements is shown. However, the layer of protein deposited on the surface is overall thicker under repassivation conditions when compared to the passivated sample (Figure 5.10b), typically being ~6 nm but as high as 12 nm. The thickness of the oxide is consistent with the passivated sample being in the region of 2 nm.

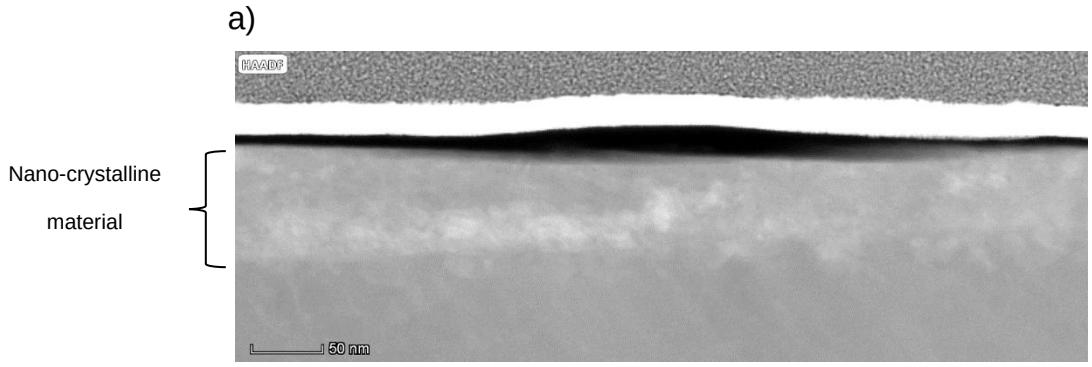

b)

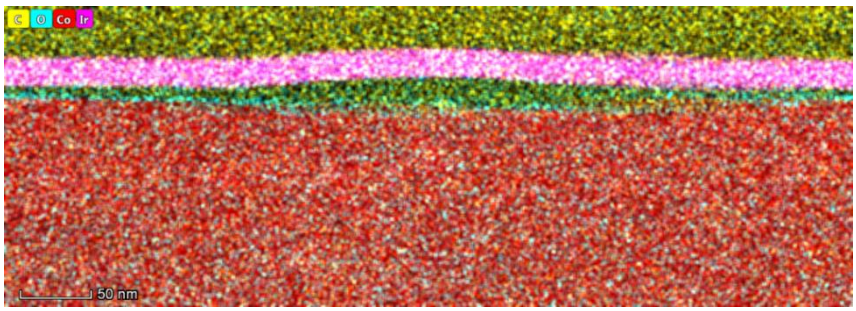

Figure 5.16 TEM cross-section of a repassivated CoCrMo sample within a PBS and 4gl^{-1} BSA solution (b) Elemental X-Ray map

An EDX line profile through the thickest part of the protein layer is shown in Figure 5.17a, with its corresponding weight fraction along the line in Figure 5.17b starting from inside the Ir layer to the bulk alloy. As expected, the protein layer is formed of primarily carbon and oxygen ions; there is the presence of some metal ions within this film. This phenomenon could be due to protein molecules complexing with the metal ions lost to the solution when the metal was active upon the potential change. The oxide film is mainly shown to be formed of chromium oxide. However, there is a substantial carbon peak within the film, which could be due to inhibited oxide by the adsorbed protein molecules.

a)

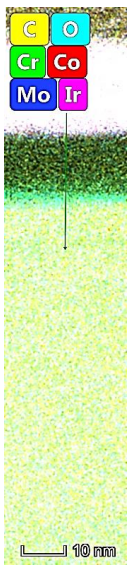

b)

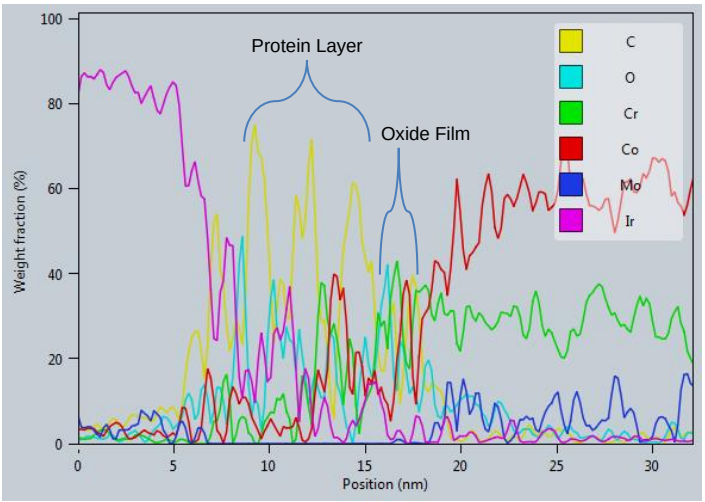

Figure 5.17 Close up EDX profile of the TEM side view of a repassivated CoCrMo sample in PBS and 4.0gl^{-1} BSA (b) Weight fraction percentage of the line profile

5.3.3.1 EELS Analysis

EELS was used to further examine this observation of protein within the passive film by looking at the different layers separately. The obtained results are shown in Figure 5.18. Within the protein film on the surface (Figure 5.18a), there is a very strong C K edge which corresponds to amorphous carbon. In the oxide film (Figure 5.18b), the O K and Cr L 3/2 edges are highly prominent with some contribution from the Co L 3/2; this is in concordance with the XPS findings. There is also a strong C K presence within the oxide which has not been seen before; this could indicate that the presence of protein interferes with the repassivaiton phase. In the bulk metal (Figure 5.18c), there is no presence of a C K or O K edge, with the spectrum just being formed of strong Cr L 3/2 and Co L 3/2.

. a)

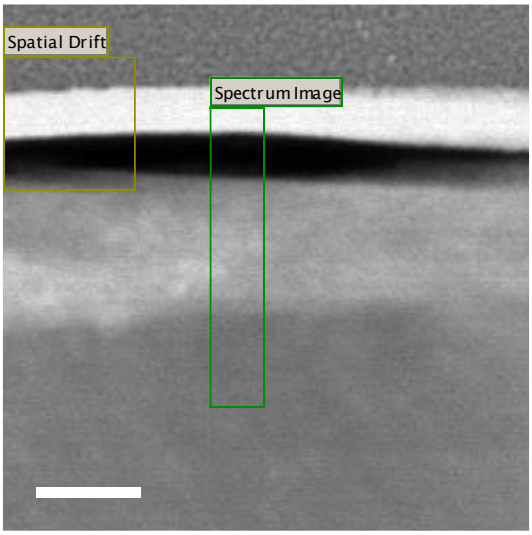

b)

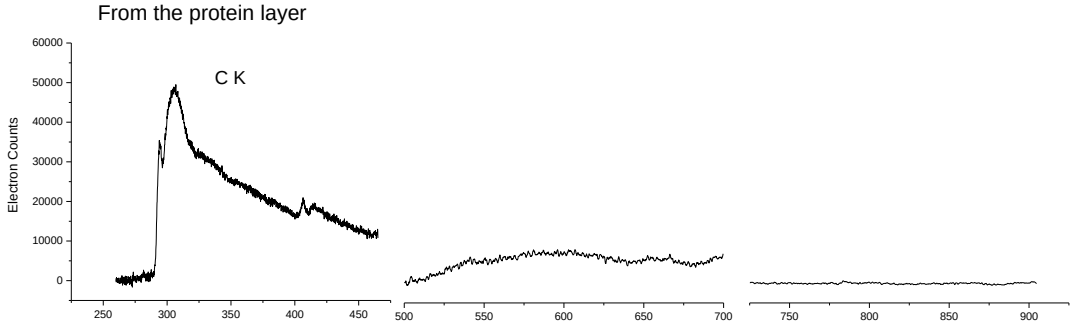

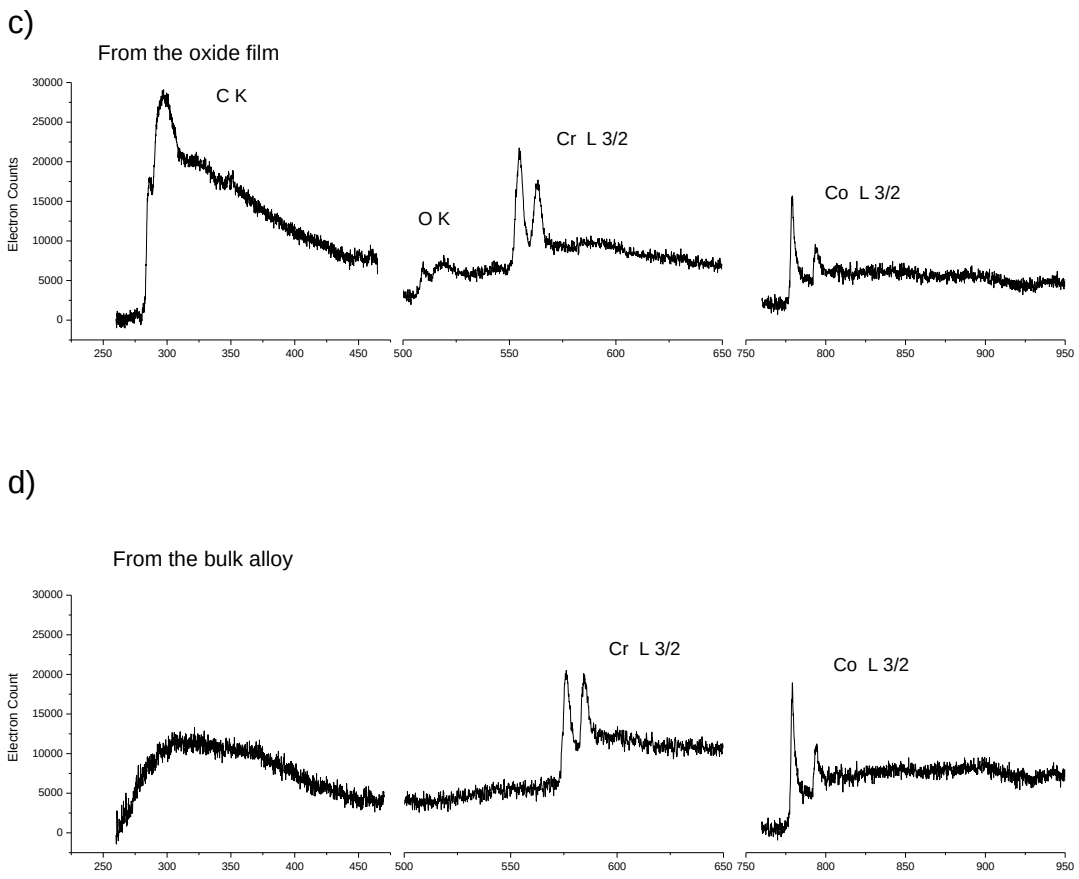

Figure 5.18 EELS of repassivated CoCrMo within PBS and 4gl^{-1} BSA covering the areas of interest (a) TEM image of area taken (b) EELS spectra of the protein layer (c) EELS spectra of the oxide film (d) EELS spectra of the bulk alloy

5.3.3.2 XPS Analysis

XPS analysis of the CoCrMo samples after repassivation (+0.1V_{RE}) under simulated bodily fluids signalled the following elements: carbon (C 1s), oxygen (O 1s), chromium (Cr 2p), cobalt (Co 2p), molybdenum (Mo 3d). As expected, phosphorous (P 2p) was detected in a PBS environment, with nitrogen (N 1s) and traces of sulphur (S 2p) being observed in the presence of BSA. As done previously for BSA containing environments, etching was done until the metal peaks became visible, which varied from sample to sample. Deconvolution was undertaken for all environments; however, just the PBS and PBS with 4.0gl^{-1} BSA are depicted in Figure 5.19 for clarity.

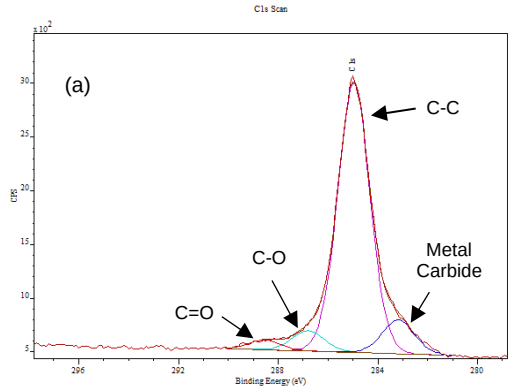
C1s Scan
(a)
C-C
C-O
C=O
Metal
Carbide
CPS
Binding Energy (eV)

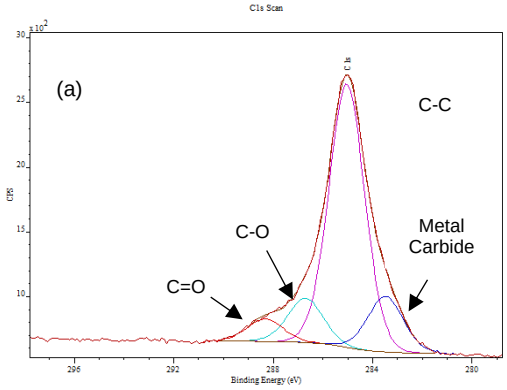
C1s Scan
(a)
C-C
C-O
C=O
Metal
Carbide
CPS
Binding Energy (eV)

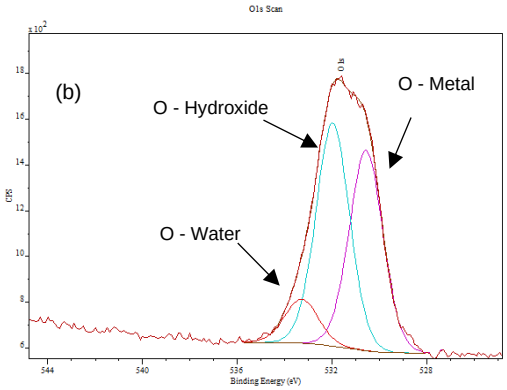
O1s Scan
(b)
O - Hydroxide
O - Metal
O - Water
CPS
Binding Energy (eV)

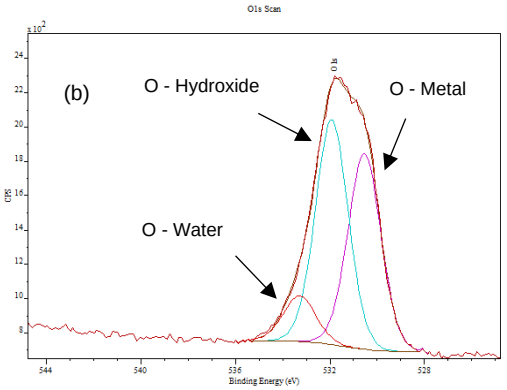
O1s Scan
(b)
O - Hydroxide
O - Metal
O - Water
CPS
Binding Energy (eV)

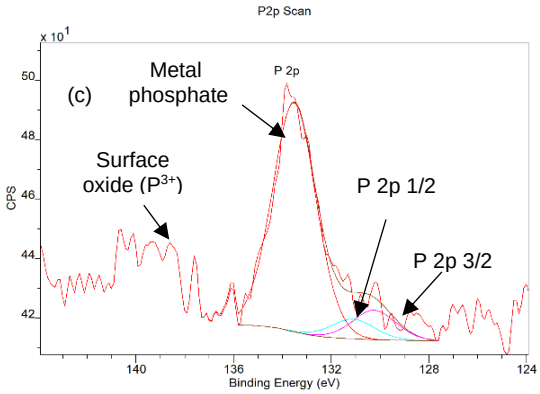
P2p Scan
(c)
Metal
phosphate
P 2p
Surface
oxide (P3+)
P 2p 1/2
P 2p 3/2
CPS
Binding Energy (eV)

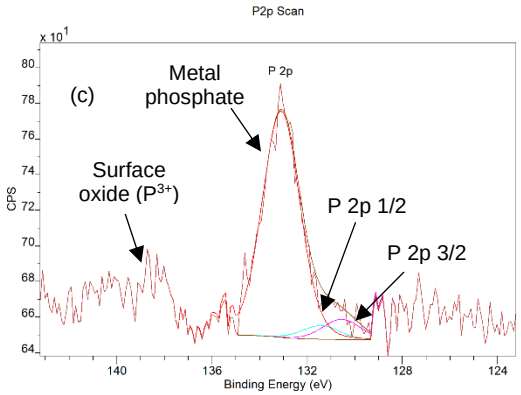
P2p Scan
(c)
Metal
phosphate
P 2p
Surface
oxide (P3+)
P 2p 1/2
P 2p 3/2
CPS
Binding Energy (eV)

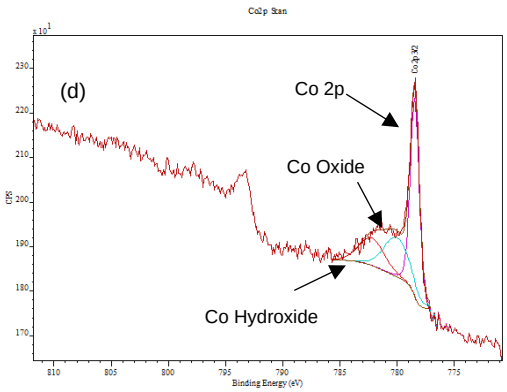
Co2p Scan
(d)
Co 2p
Co Oxide
Co Hydroxide
CPS
Binding Energy (eV)

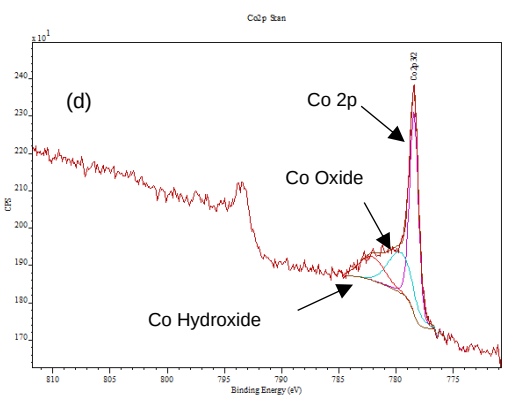
Co2p Scan
(d)
Co 2p
Co Oxide
Co Hydroxide
CPS
Binding Energy (eV)

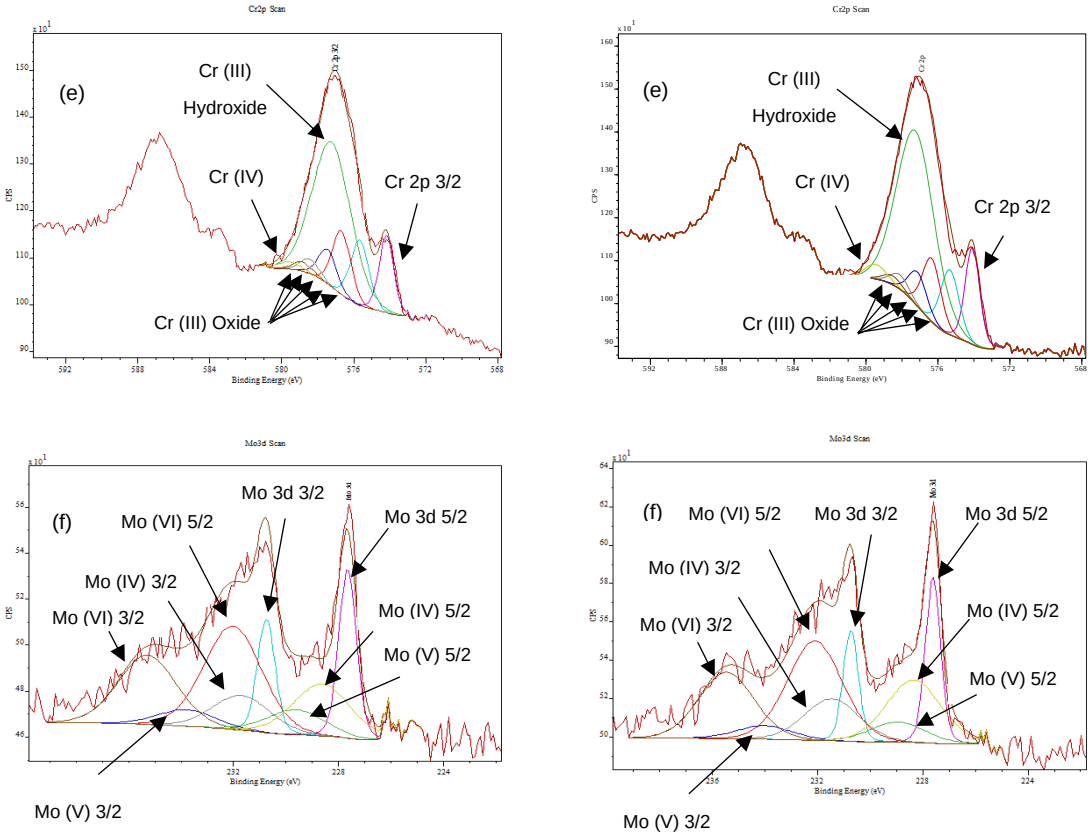

Figure 5.19 Fitting of XPS peaks after a repassivation phase for CoCrMo in PBS and PBS with 4.0gl-1 BSA after 1hr: (a) Carbon, (b) Oxygen, (c) Phosphorus (d) Cobalt, (e) Chromium and (f) Molybdenum. Published previously within [125]

The species and trends obtained from deconvolution were primarilyF consistent with the peaks obtained from a passivated sample (+0.1V_{RE}). The observed effects of BSA again depicting higher proportions of carbon in the C-O or C=O form alongside an overall broader peak (Figure 5.19a). There is the appearance of phosphate surface oxides within the phosphorous spectra (Figure 5.19c). In regards to the Co and Cr peaks (Figure 5.19d, Figure 5.19e), there are increases in the levels of the metal present in the hydroxide form. Again there are increases in the Mo(IV) state when exposed to albumin (Figure 5.19e).

The percentage of metallic elements (Co, Cr, Mo) in the repassivated oxide film of CoCrMo from XPS are depicted in Figure 5.20. Again this was determined via deconvolution of the individual XPS spectra and determining the quantity of metal present in the oxide state. As before, even though cobalt is the primary constituent of the alloy, its content is highly reduced when

electrochemically repassivated and even further when exposed to phosphates or molybdenum. As expected, chromium makes up the majority of the passive film, reaching as high as 75% of the film when in a saline 4gl^{-1} BSA environment. The presence of molybdenum in the oxide film increases in a phosphate environment but decreases with the addition of albumin. From the data obtained, the percentage of molybdenum decreases to ~9% and ~10% when albumin is present in saline and PBS solutions, respectively, whereas for passivated samples, molybdenum accounted for ~15% of the film for these solutions with albumin.

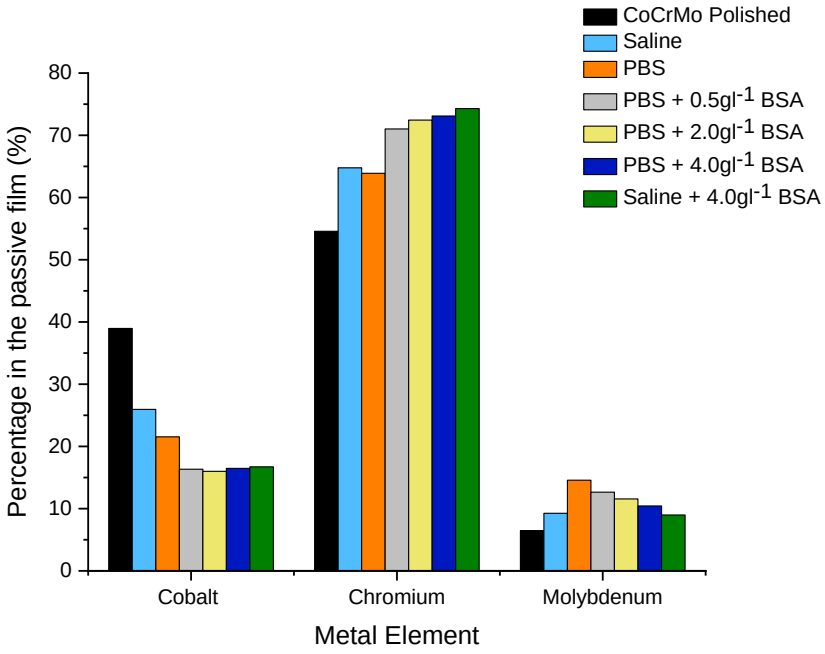

Figure 5.20 Percentage of metallic elements present in the oxide state of CoCrMo after a repassivation phase. Published previously within [125]

5.4 Effects of simulated bodily fluids on the morphology of the surface

AFM was utilised to investigate the changes to the morphology of the surface CoCrMo in a variety of simulated bodily fluids. The surface of a CoCrMo sample passivated within the saline solution (Figure 5.21a); this leads the topography of the surface to alter in comparison to a freshly polished sample (Figure 5.6). The surface is now covered with small and large domes, which are known to be oxides [163]. If phosphates are present in the solution (Figure 5.21b), the visibility of these domes is hindered. Upon closer inspection, it is

seen that there is an inorganic layer on the surface of the alloy due to the alteration of appearance; this would be due to the adsorption of phosphates.

a)

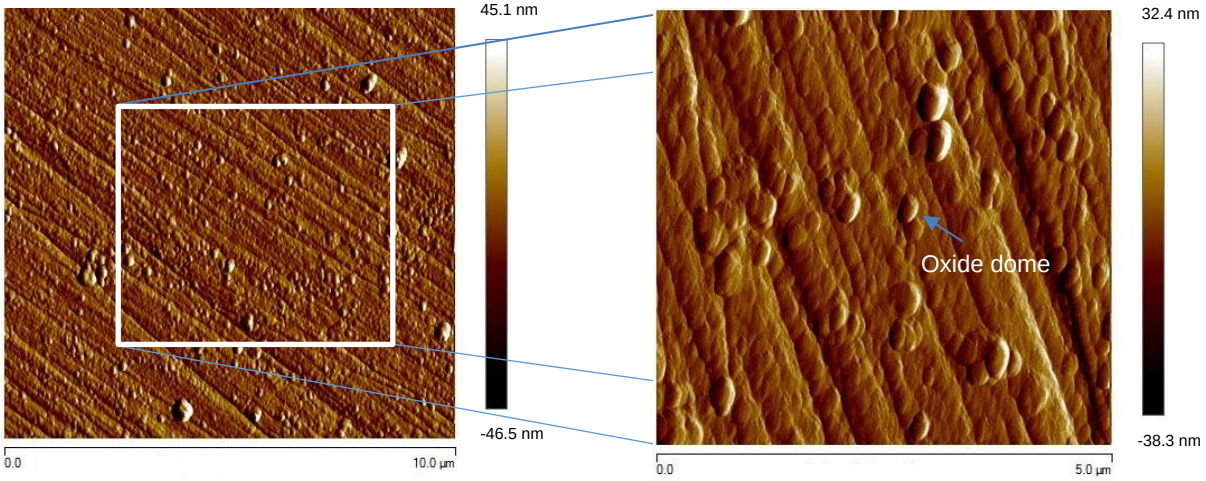

b)

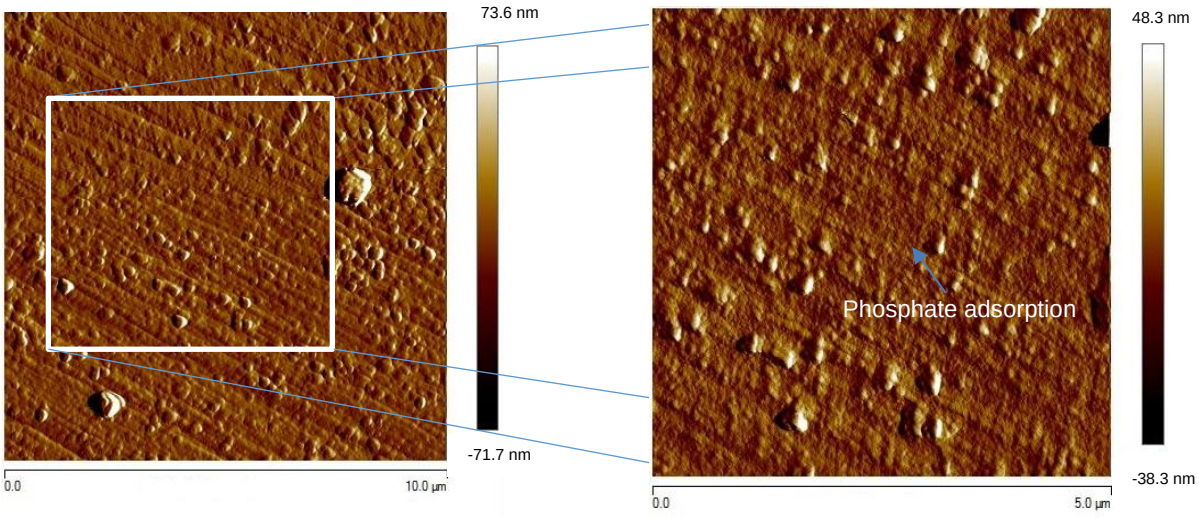

Figure 5.21 AFM profile of the surface of CoCrMo (a) Passivated (+0.1V_{RE}) in a saline solution (b) Passivated (+0.1V_{RE}) within a PBS solution

The surface of a passivated CoCrMo sample within saline with 4gl^{-1} BSA is shown in Figure 5.22. This was undertaken to solely observe the interactions of BSA with the surface. The surface (Figure 5.22a) is now shown to have organic matter adsorbed, which are characterised via nodal features [101]. Only the deep scratches can be seen on the surface now due to the adsorption of albumin. By closely looking at the surface, using adhesion (Figure 5.22b), it is possible to see the individual BSA molecules adsorbed onto the surface. A height profile indicates that the molecules possess a height of around 4 nm.

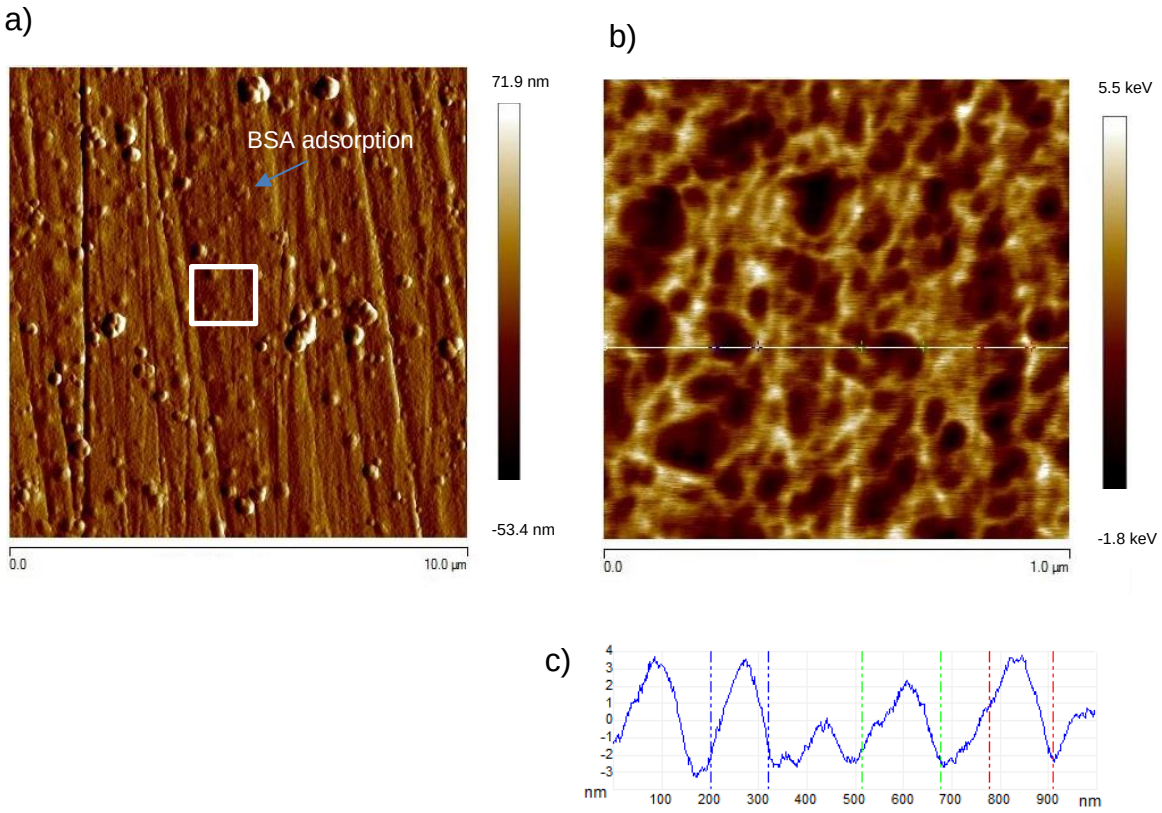

Figure 5.22 AFM profile of the surface of CoCrMo passivated (+0.1V_{RE}) in a saline solution with 4gl^{-1} BSA (b) Energy profile of the surface (c) Height profile of the marked line

The surface of a CoCrMo sample passivated under PBS and 4gl^{-1} BSA is shown in Figure 5.23. At first glance (Figure 5.23a), it appears that there is more organic deposition for this sample when compared with the saline protein environment; this could be due to the phosphates helping to facilitate adsorption of BSA onto the surface. On closer inspection (Figure 5.23b), there is the presence of nodal features once more. The energy of the surface is generally more positive than before, suggesting that the protein adsorbs first onto the surface with phosphates. From the height profile (Figure 5.23c), it's hard to determine the exact dimensions of the molecule due to phosphate presence.

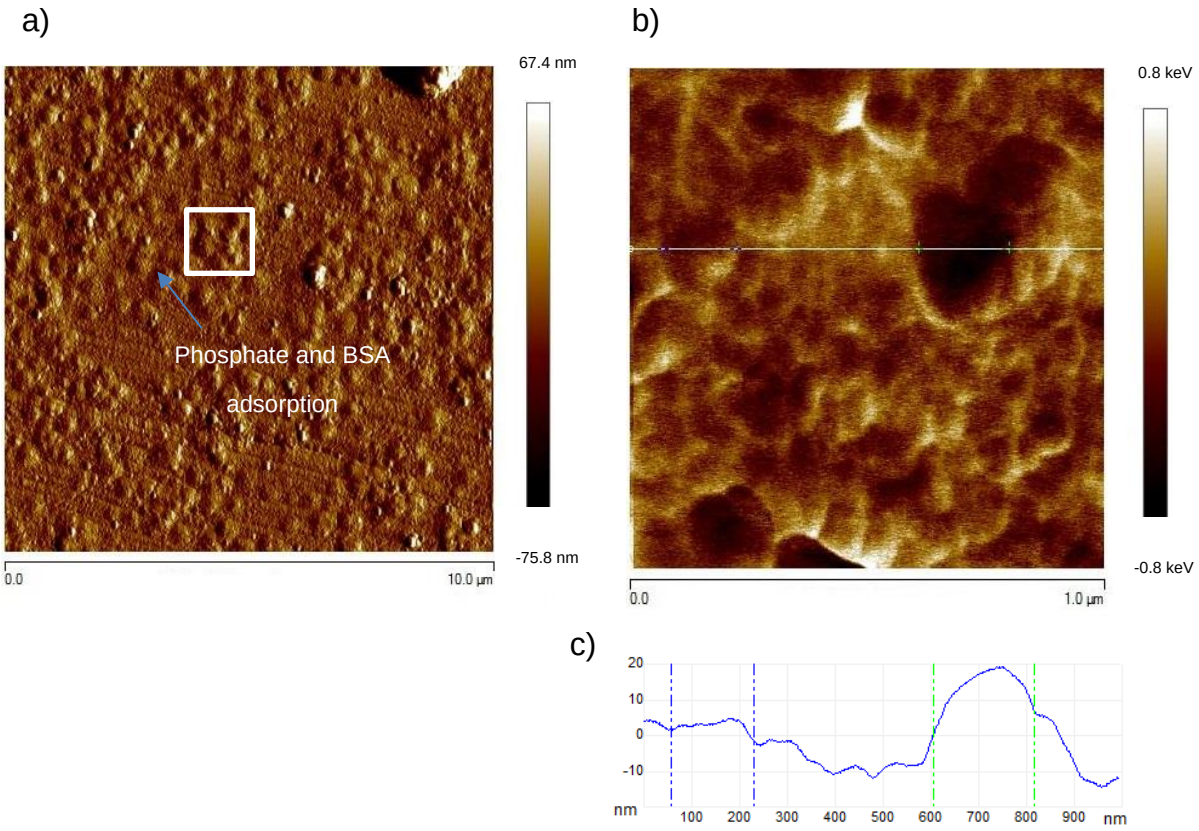

Figure 5.23 AFM profile of the surface of CoCrMo passivated in a PBS solution with $4gl^{-1}$ BSA (b) Energy profile of the surface (c) Height profile of the marked line

5.4.1 Effects of applied electrochemical condition on the morphology

By investigating the surfaces of CoCrMo in a protein containing environment under different conditions, it gives an idea of how the condition affects protein adsorption.

A comparison of AFM images for CoCrMo samples polarized at cathodic (-$1V_{RE}$), passive (+$0.1V_{RE}$) and transpassive (+$1V_{RE}$) conditions are shown within Figure 5.24. It is clear to see that there is a higher protein deposition for cathodic when compared to the other conditions. The use of the potential profile helps to confirm this as the isoelectric point of BSA is 4.7, and so for all of the conditions (~7 pH), the overall charge of the molecule is negative (dark areas indicate BSA adsorption). For the passive conditions, the coverage is not as consistent as at cathodic conditions. It has been noted previously that at passive potentials, protein adsorption only occurs onto a small fraction of

the alloy but with an increase in passive potential, the coverage increases [101]. At transpassive conditions, there are only slight areas of coverage which could be due to the protein preferring to bind to the metal ions that are released into solution.

Height Profile

a)

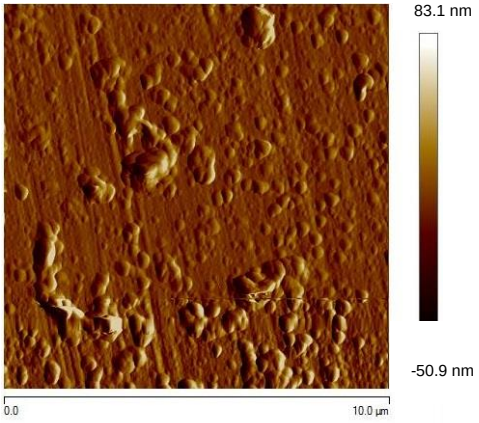

b)

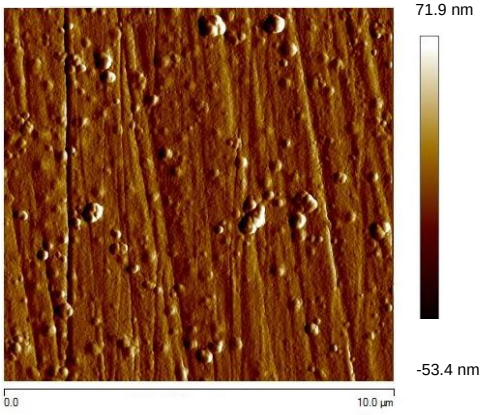

Potential Profile

a)

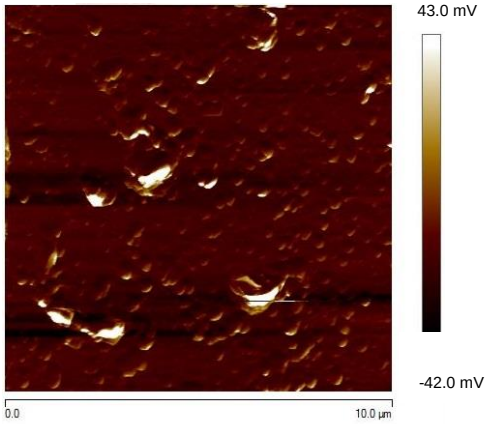

b)

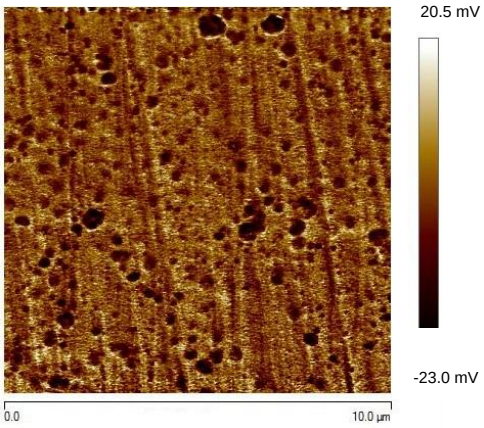

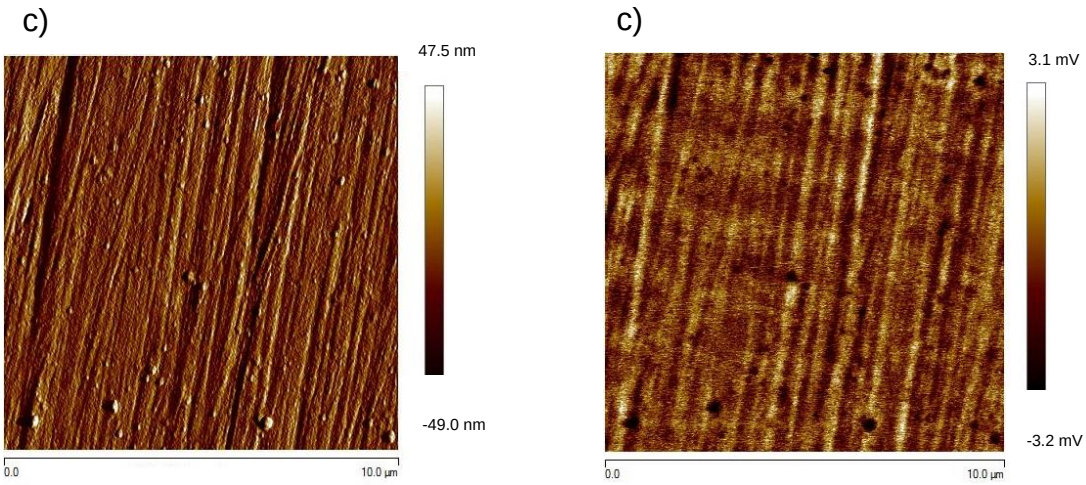

Figure 5.24 AFM profile of the surface of CoCrMo polarized at different conditions in PBS with 4gl^{-1} BSA (a) Cathodic -1V_{RE} (b) Passive +0.1V_{RE} (c) Transpassive +1.0V_{RE}

The surface roughness of the samples was also determined from the AFM; the R_a was taken from analysing 3 sections of 2 x 2 um from each of the samples. The data obtained is depicted in Table 5.2. The R_a of cathodic and passive conditions are roughly the same, with transpassive conditions being the roughest due to corrosion/pitting taking place on the surface of the alloy.

Table 5.2 Surface roughness of CoCrMo polarized under different conditions determined via AFM

Condition	Potential Applied	Average Ra (nm)
Polished	-	8.44 ± 0.03
NaCl	Cathodic	7.99 ± 0.03
	Passive	7.94 ± 0.04
	Transpassive	9.59 ± 0.07
PBS	Cathodic	7.54 ± 0.02
	Passive	7.42 ± 0.05
	Transpassive	8.44 ± 0.06
PBS + 4.0gl^{-1} BSA	Cathodic	7.08 ± 0.03
	Passive	7.03 ± 0.01
	Transpassive	7.46 ± 0.04
NaCl + 4.0gl^{-1} BSA	Cathodic	7.60 ± 0.02
	Passive	7.53 ± 0.02
	Transpassive	7.93 ± 0.03

5.4.2 Effects of repassivation on the morphology

The surfaces of repassivated CoCrMo within saline/PBS and 4gl^{-1} BSA are shown in Figure 5.25. There appears to be a fuller coverage of BSA on the surface, which is characterised by finer and more distributed deposits of BSA, similar to that seen at a cathodic potential (Figure 5.24a), which would indicate that the binding of BSA is irreversible at this potential (-1.0V_{RE}). This is concordant with the TEM data, where thicker BSA layers were observed after electrochemical repassivation. The presence of agglomerates are starting to appear, which wasn't seen to this extent on just a passivated sample (Figure 5.24b).

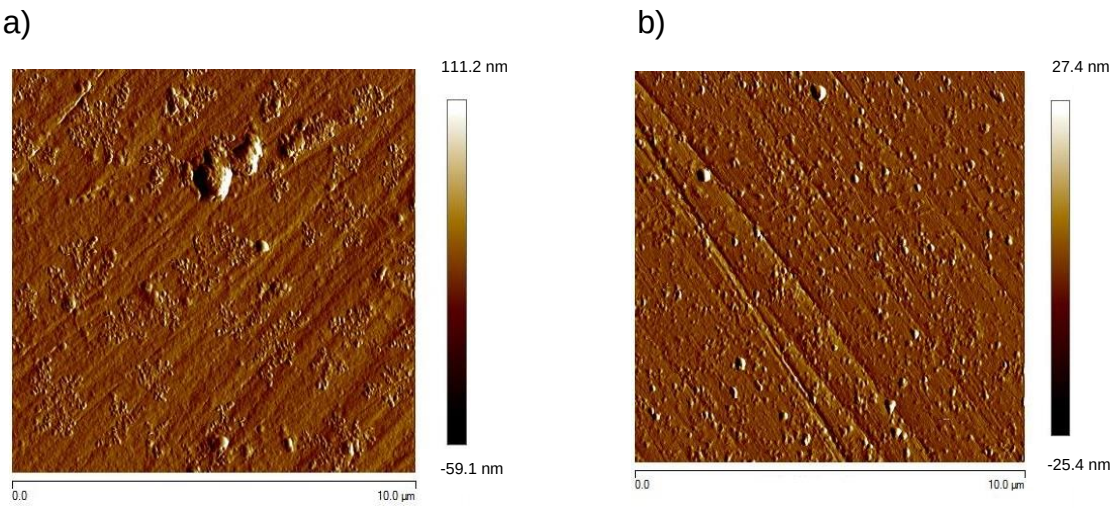

Figure 5.25 AFM profile of the surface of CoCrMo repassivated under different conditions (a) Saline and 4gl^{-1} BSA (b) PBS and 4gl^{-1} BSA

Discussion

From the surface analysis measurements undertaken, it has been indicated that the composition of the electrolyte leads to changes within the passive film alongside adsorbing onto the surface. These effects have been seen to vary depending on the electrochemical condition that the alloy is under. This section will give a detailed explanation and critique of the observations that have been noted throughout this chapter.

5.5.1 The Passive Film

It is well known within the literature that CoCrMo spontaneously forms an oxide film when exposed to air. The use of various surface analysis techniques has enabled a detailed profile of this oxide to be determined and how it is affected depending on the environment, it is exposed to. For all passivated conditions investigated, the oxide has been seen to exist uniformly across the surface of the alloy, taking the form of domes that range in size. The overall thickness of this film from cross-sectional TEM-EDX analysis was determined to be between 1.5 - 2.0 nm which is in concordance with other research [30,100,164]. This was also in line with the EIS data, where the oxide film for passivated conditions was calculated to be between 1.0 -1.8 nm.

The composition of the passive film is intriguing as even though cobalt is the main constituent of the alloy, it is not the most prominent metal detected, with

the oxide primarily being comprised of chromium. Munoz et al. [100] stated that that the concentration of cobalt within the film is typically around 25%. This is due to chromium having the lowest standard reduction potential out of the metals present and is, therefore, the most favoured to be oxidised. It is important to note that there are contributions to the oxide layer from both cobalt and molybdenum though. Milosev et al. [30] noted oxidised cobalt within the oxide film and primarily within the interface of the metal/oxide.

The presence of phosphates within the surrounding electrolyte leads to an adsorbed inorganic layer on the surface of the alloy, which involves the formation of a phosphate metal bond. The absorbing layer provides effective coverage of the oxide, protecting it from the environment and leads to a lower R_a. The interactions of the alloy with phosphates lead to alterations within the passive film, promoting chromium and molybdenum presence at the expense of cobalt.

Albumin is also seen to adsorb onto the surface of the alloy and form large aggregates, which are possible due to their ability to easily form intermolecular bridges. From the TEM cross-sections and AFM height profiles, it was seen that the thickness of this layer was 4 nm. Due to the dimensions of a BSA molecule being roughly 4 x 4 x 14 nm that exists in an ellipsoidal shape, we can determine that the layer is only one molecule thick. According to the molecular feature, there are two different ways in which a monolayer of albumin can adsorb onto a surface: side-on or end-on [165]. From the data obtained, the corresponding model is side-on. Tencer et al. [166] investigated BSA adsorption on strips of Au and determined that BSA formed a monolayer of around 2 nm thick, indicating that the side-on model was favoured. Y.Yan [101] observed a 4 nm monolayer of BSA adsorbed onto CoCrMo, also putting forward the favoured side-on model; suggesting that the difference in thickness found between techniques is down to proteins being naturally soft and therefore easily deformed by an AFM probe. AFM analysis also depicts the potential of the BSA molecules is lower than the alloy, which indicates that adsorbed BSA can promote the electron transfer process on the sample's surface, enhancing the rate of corrosion [101]. As expected, the surface roughness is smoother in the presence of albumin, which is in concordance with M. Gisperts work [167].

5.5.2 The effect of repassivation

After the oxide has been electrochemically cleaved, the composition of the reformed oxide is seen to be reliant on the surrounding environment. Li et al. [168] observed that the composition of the passive film was altered when examining the effects of wear, noting decreased levels of chromium within the oxide after a repassivation phase.

As expected with chromium-containing alloys, the reformed film primarily consists of Cr(III) oxide and Cr(III) hydroxide. From analysis via TEM/EDX, the thickness of the film is consistent before and after the repassivation phase being around 2 nm. It is interesting to note the formation of phosphate surface oxides which could appear to the anions (PO^{3-}_4) being trapped during the oxide growth phase where they can occupy the lattice sites of O^{2-} [84]. Figure 5.26 depicts the differences in compositions of an oxide film formed by electrochemical passivation (Figure 5.15) and via electrochemical repassivation (Figure 5.19). The comparison of the molybdenum content is intriguing within Figure 5.26, as in a protein containing environment, the percentage present within the reformed film is drastically reduced (considering the overall percentage in the film). There would be a decrease in the content of molybdenum when the passive film is compromised as now the reactive bare metal is exposed, leading to enhanced electronic interactions, causing stronger interactions and dissolution of the favoured molybdenum ion. This isn't possible when a film is present, as the alloy is protected from interactions with the protein. It's well-known that protein molecules interacted weakly and reversibly with the passive layer seeing as it's relatively unreactive and an apolar surface [103,169]. The increase in chromium content observed can be attributed to its tendency to form solid oxide over the other constituent of the film, cobalt.

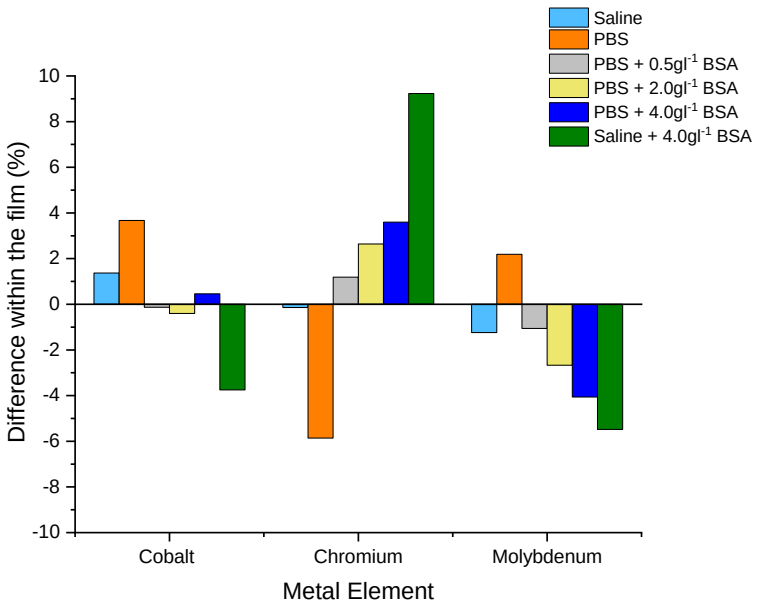

Figure 5.26 Graph depicting the metal percentage differences between a CoCrMo electrochemically formed passive film (+0.1V_{RE}) and a reformed film after electrochemical cleavage

For BSA containing conditions, the adsorbed protein layer is much thicker than seen previously, generally existing at 6 nm but reaching a high of 12 nm. This phenomenon could be due to stronger protein adsorption when the alloy is cathodically polarized, with multiple reports stating that there is a higher binding affinity under these conditions [101,105,170]. The protein layer was seen to contain a high quantity of metal ions, which would occur due to complexing with the dissolved metal ions. This process could cause the protein to undergo structural changes, which could account for the varying thickness of the film [170]. A high presence of BSA within the passive film suggests that the molecules interfere with the passivation process, which could lead the layer to become irregular and more susceptible to corrosive attack.

5.5.3 Effect of the applied electrochemical condition

BSA deposition has been seen to vary with the electrochemical condition that the alloy is placed under. A complete level of deposition was seen under cathodic potentials; this could be due to BSA being a cathodic inhibitor therefore it adsorbs onto the surface more favourably; the condition could also lead to the reduction of BSA that leads to the formation of an insoluble product on the surface, which would account for the difference in appearance [101]. The three possible ways of interaction that the metal could interact with the

protein are hydrophobic, electrostatic and hydrogen bonding [170-173]. As there is more deposition at cathodic potentials, it would suggest that hydrophobic interactions are the main way in which BSA binds to the metal seeing as the electrostatic interactions are unfavourable under these conditions. Hydrophobic interactions produce a net entropy gain resulting from dehydration of the protein, which decreases the surface area of the protein exposed to water reducing the undesired interactions with the water molecules. For the passive conditions, the coverage is not as consistent as at cathodic conditions (oxide film between the BSA and the alloy). It has been noted previously that at passive potentials, protein adsorption only occurs onto a small fraction of the alloy, but with an increase in passive potential, the coverage increases [101]. At transpassive conditions, there are only slight areas of coverage which could be due to the protein preferring to bind to the metal ions that are released into solution.

Conclusion

A thorough investigation of the effects that simulated bodily fluids have on the surface of CoCrMo has been conducted. Determination of these effects will help explain the changes in corrosion behaviour seen and provide a complete picture of how these species interact with the alloy. The following conclusions have therefore been reached.

- The passive film of CoCrMo was measured to be between 1 – 2 nm thick and is primarily formed of Cr(III) oxide and hydroxide, with small contributions from cobalt and molybdenum oxide.
- The species present can have a drastic effect on the surface of the alloy.
    - Phosphates can adsorb onto the surface of the alloy, altering the composition of the film by increasing the quantity of chromium and molybdenum within the oxide film at the expense of cobalt. Its presence leads to a higher level of BSA adsorption.
    - BSA adsorbs onto the surface of the alloy via the side-on model; the layer is typically 4 nm thick, suggesting it is only one monolayer thick. This adsorption enhances the rate of corrosion by promoting the electron transfer process. Alterations to the composition of the passive film are also observed, increasing the quantity of molybdenum within the film due to supposed high affinity.

- The effect of repassivation can alter the reformation of the passive film, depending on the contents of the electrolyte.
    - Phosphates lead to an increase of chromium and molybdenum within the passive film and the formation of phosphate surface oxides.
    - BSA increases the quantity of chromium within the film even further but leads to a decrease in molybdenum content as the protein can extract the ion into the solution. It appears to also interfere with the consistency of the film.
- By applying different potential domains to the alloy, different effects are observed with BSA adsorption.
    - Cathodic (-1V_{RE}) – Observe the highest level of BSA deposition, indicating that the adsorption process is dominated via hydrophobic interactions.
    - Passive (+0.1V_{RE}) – Deposition of BSA occurs agglomerates on small fractions of the alloy.
    - Transpassive (+1V_{RE}) – Only small levels of BSA deposition suggests the BSA prefers to bind to metal ions that are released into the solution.

Chapter 6
The Effect of Applied Potential and Electrolyte on Metal Ion Dissolution

6.1 Introduction

Although there has been a great deal of investigation into the electrochemical behaviour of biomedical alloys, the complimentary ion release is not well investigated. The effect of the environment on the release of metallic ions from the implant is of great importance due to these ions leading to adverse effects within the human body. As serum albumin is the most abundant protein present within the synovial cavity, its direct effect on metal ion release is of great importance, as it could affect the performance of the biomaterial. By undertaking a post-assessment study of the electrolyte after electrochemical polarisation was conducted, the quantification of metal ions could be achieved.

The purpose of the following chapter is to quantify the amount of metal ion released into the electrolyte under specific electrochemical potentials, relating the charge given off to that of the electrochemical process conducted. The following measurements have been made to achieve these aims: Potentiostatic polarisation and Inductively Coupled Mass Spectroscopy (ICP-MS).

6.2 Metal Ion Dissolution

Metal ion dissolution has been determined by analysing the electrolyte from the potentiostatic experiments conducted within Section 4.2.3. The conditions analysed were Cathodic (-1V_{RE}), OCP, Passive (+0.1V_{RE}) and Transpassive (+1V_{RE}). Each of these tests were conducted for one hour with varying simulated bodily fluids to determine the effects of potential and environment on ion release. The data obtained is shown in Table 6.1 and shown graphically in Figure 6.1. A comparison of the total percentage of ion dissolution for three conditions where ion release was seen throughout is shown in Figure 6.2.

Table 6.1 ICP-MS values obtained for the potentiostatic experiments conducted

Electrolyte	Electrochemical Condition											
	Cathodic (-1V$_{ref}$)			OCP			Passive (+0.1V$_{ref}$)			Transpassive(+1.0V$_{ref}$)		
	Co (µg/L)	Cr (µg/L)	Mo (µg/L)	Co (µg/L)	Cr (µg/L)	Mo (µg/L)	Co (µg/L)	Cr (µg/L)	Mo (µg/L)	Co (µg/L)	Cr (µg/L)	Mo (µg/L)
Saline	0.03 ± 0.02	0.01 ± 5x10^{-3}	-	0.53 ± 0.05	0.18 ± 0.03	0.01 ± 7x10^{-3}	0.46 ± 0.04	0.11 ± 0.01	0.01 ± 3x10^{-3}	72.22 ± 5.33	22.59 ± 1.47	2.45 ± 0.23
PBS	-	-	-	0.26 ± 0.02	0.07 ± 0.01	0.01 ± 3x10^{-3}	0.17 ± 0.02	0.06 ± 0.01	-	62.31 ± 4.12	30.55 ± 2.12	4.61 ± 0.31
PBS + 0.5gl^{-1} BSA	0.02 ± 8x10^{-3}	-	-	0.21 ± 0.01	0.09 ± 0.02	0.02 ± 5x10^{-3}	0.14 ± 0.01	0.06 ± 9x10^{-3}	0.03 ± 5x10^{-3}	59.50 ± 3.22	26.51 ± 1.25	4.95 ± 0.52
PBS + 2.0gl^{-1} BSA	0.01 ± 6x10^{-3}	-	-	0.23 ± 0.02	0.07 ± 0.02	0.09 ± 0.01	0.19 ± 0.02	0.05 ± 5x10^{-3}	0.05 ± 0.01	58.55 ± 5.60	23.53 ± 1.88	5.32 ± 0.14
PBS + 4.0gl^{-1} BSA	-	-	-	0.24 ± 0.02	0.09 ± 0.01	0.12 ± 0.01	0.21 ± 0.02	0.06 ± 0.01	0.07 ± 0.02	58.84 ± 4.55	22.61 ± 2.45	5.90 ± 0.15
Saline + 4.0gl^{-1} BSA	0.02 ± 0.01	-	-	0.35 ± 0.03	0.12 ± 0.01	0.19 ± 0.03	0.31 ± 0.01	0.13 ± 0.01	0.11 ± 0.01	62.17 ± 2.09	16.78 ± 1.99	4.45 ± 0.43

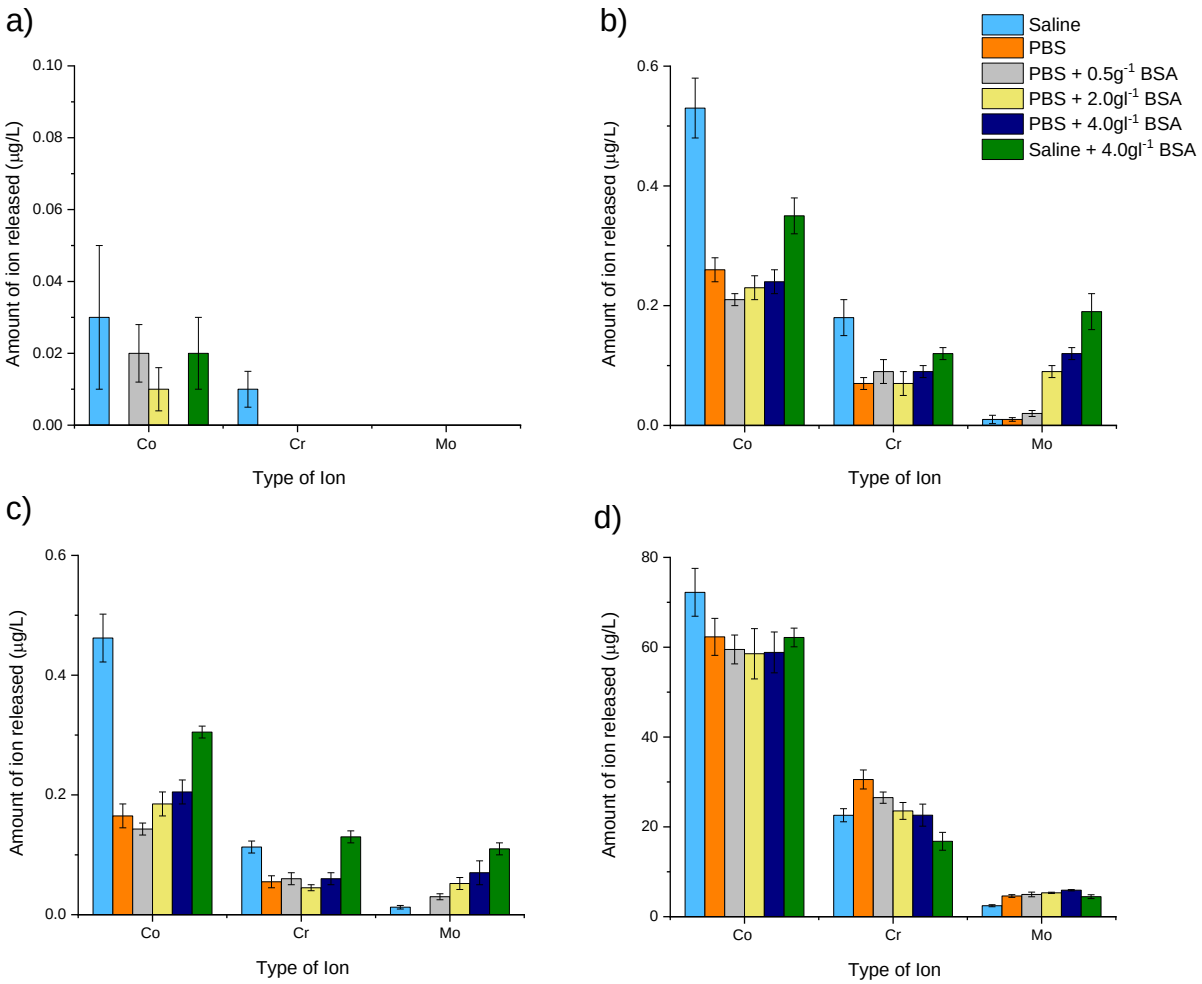

Figure 6.1 ICP-MS values obtained for the potentiostatic experiments conducted (a) Cathodic (-1V_{RE}) (b) OCP (c) Passive (+0.1V_{RE}) (d) Trans-passive (+1V_{RE})

a)

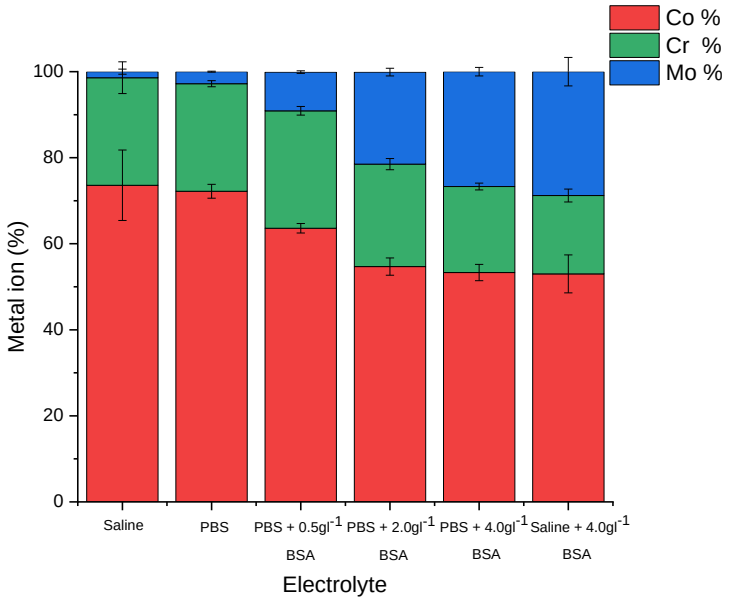
Co %
Cr %
Mo %
Metal ion (%)
0
20
40
60
80
100
Saline
PBS
PBS + 0.5gl-1 BSA
PBS + 2.0gl-1 BSA
PBS + 4.0gl-1 BSA
Saline + 4.0gl-1 BSA
Electrolyte

b)

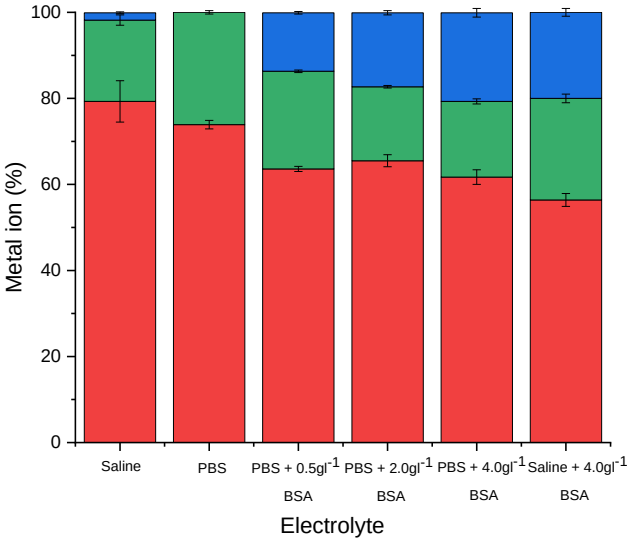
Metal ion (%)
0
20
40
60
80
100
Saline
PBS
PBS + 0.5gl-1 BSA
PBS + 2.0gl-1 BSA
PBS + 4.0gl-1 BSA
Saline + 4.0gl-1 BSA
Electrolyte

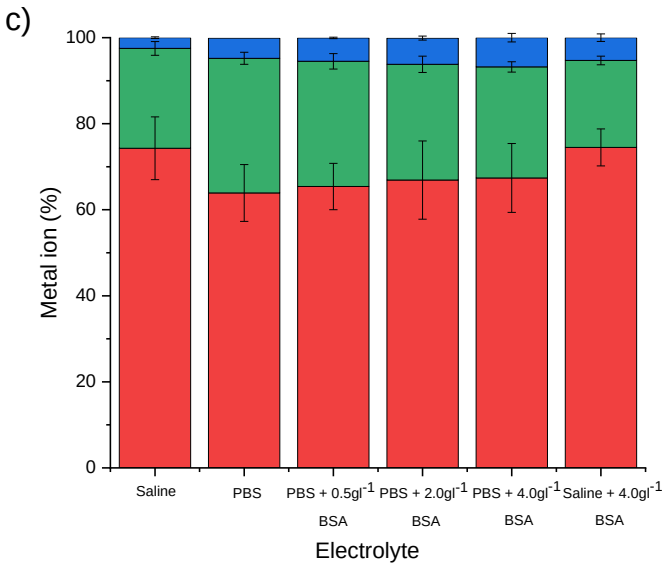

Figure 6.2 The total quantities of metal ion released expressed as percentages, quantified via ICP-MS (a) OCP (b) Passive (+0.1V_{RE}) (c) Trans-passive (+1V_{RE})

Generally, the majority of ions released by polarized samples of CoCrMo are cobalt and its even seen to exceed the stoichiometry of the alloy in some places (saline and PBS environments). From the data obtained, it is clear to see that the presence of BSA tends to increase the dissolution contribution of molybdenum from the alloy; this is seen in Figure 6.2. This will be explored in further detail later on in the next Chapter.

The quantity of metal ion release is quite similar for OCP and passive conditions, displaying the same trends of ion release with similar quantities. The metal ion release is highest under transpassive conditions (+1V_{RE}); the electrolyte is shown not to possess the same effect as seen in OCP and passive conditions with the type of ion lost keeping in order with the stoichiometry of the alloy. Cathodic conditions (-1V_{RE}) lead to minimal loss of ions to the environment, with only slight dissolutions of Co(II) ions seen.

6.2.1 Charge of Dissolution

For investigating charge contributions for OCP and passive conditions, the following equation can be used. The theory and justification for this method were discussed within Section 3.3.3.1.

Equation 6.1 Contributors to the total measured charge for OCP and Passive conditions

$$Q_t = Q_{film} + Q_{diss} + Q_{O_2}$$

The total measured charge (Q_T) was determined from the integration of the current time graphs obtained, as seen before in Section 3.3.3.1. The Q_{film} was determined from Equation 3.2, for passive conditions it was calculated to be 0.75 mC when the area of the specimen was taken into account and assuming a thickness of 2 nm. For OCP conditions, the passive film was considered to thinner at 1 nm thick, giving a charge needed for film formation to be 0.38 mC. Q_{diss} was calculated from the ICP-MS analysis and use of Equation 3.3. All calculated values are depicted in Table 6.2.

Table 6.2 Comparisons between OCP and Passive charge values for the total reaction and for dissolution (Q_{film} OCP = 0.38 mC, Q_{film} passive = 0.75 mC)

Condition	Q_{Diss} (mC)		Q_T (mC)	
	OCP	Passive	OCP	Passive
Saline	2.77 ± 0.22	2.19 ± 0.12	1.01 ± 0.10	1.95 ± 0.17
PBS	1.88 ± 0.13	1.24 ± 0.09	0.23 ± 0.02	0.78 ± 0.13
PBS + 0.5gl^{-1} BSA	1.95 ± 0.07	1.25 ± 0.14	0.29 ± 0.06	1.04 ± 0.06
PBS + 2.0gl^{-1} BSA	2.11 ± 0.14	1.56 ± 0.06	0.44 ± 0.07	1.31 ± 0.08
PBS + 4.0gl^{-1} BSA	2.44 ± 0.11	1.84 ± 0.10	0.51 ± 0.04	1.43 ± 0.11
Saline + 4.0gl^{-1} BSA	3.62 ± 0.17	3.03 ± 0.16	1.33 ± 0.06	2.34 ± 0.14

The Q_T values obtained follow the same trends for both OCP and passive conditions, with the presence of phosphates heavily reducing the values as they adsorb on the surface of the alloy restricting ion flow. Albumin is seen to increase the total value of charge as they inhibit the flow of oxidants to alloy, inhibiting film growth and form organometallic complexes.

In terms of the charge contributions for Q_{Diss} and Q_{Film} (OCP and Passive), it's clear to see that the bulk total charge is due to loss of metallic ions, which is

validated throughout the literature [102,129,130]. Generally for passive condtions, the vales of Q_{Diss} and Q_T present a relatively close agreement with respect to the experimental error. The use of Equation 6.1 enables the Q_{O2} to be determined by taking into account the charge balance. The contribution of Q_{O2} is seen to be greater for OCP conditions over passive as there is a greater value of Q_{Diss} with a lower value of Q_T; this is to be expected as lower potentials favour the cathodic reaction.

6.3 Effect of Repassivation on Metal Ion Dissolution

Metal ion dissolution was determined from analysis of the electrolyte after an electrochemical repassivation phase was applied (Section 4.2.4). For consistency, the sample was submerged for a total of one hour within the selected simulated bodily fluids. The ICP-MS data obtained CoCrMo after an electrochemical repassivation phase is depicted in Table 6.3, with its corresponding graph for ease of view being displayed in Figure 6.3.

Table 6.3 ICP-MS values obtained for CoCrMo after an electrochemical repassivation phase

Electrolyte	Repassivaiton Phase		
	Co (µg/L)	Cr (µg/L)	Mo (µg/L)
Saline	0.91 ± 0.05	0.07 ± 0.02	0.02 ± 0.01
PBS	0.37 ± 0.05	0.16 ± 0.03	0.02 ± 0.01
PBS + 0.5gl^{-1} BSA	0.18 ± 0.03	0.08 ± 0.02	0.06 ± 0.01
PBS + 2.0gl^{-1} BSA	0.17 ± 0.02	0.08 ± 0.02	0.12 ± 0.02
PBS + 4.0gl^{-1} BSA	0.15 ± 0.03	0.10 ± 0.02	0.37 ± 0.03
Saline + 4.0gl^{-1} BSA	0.21 ± 0.05	0.04 ± 0.02	0.45 ± 0.04

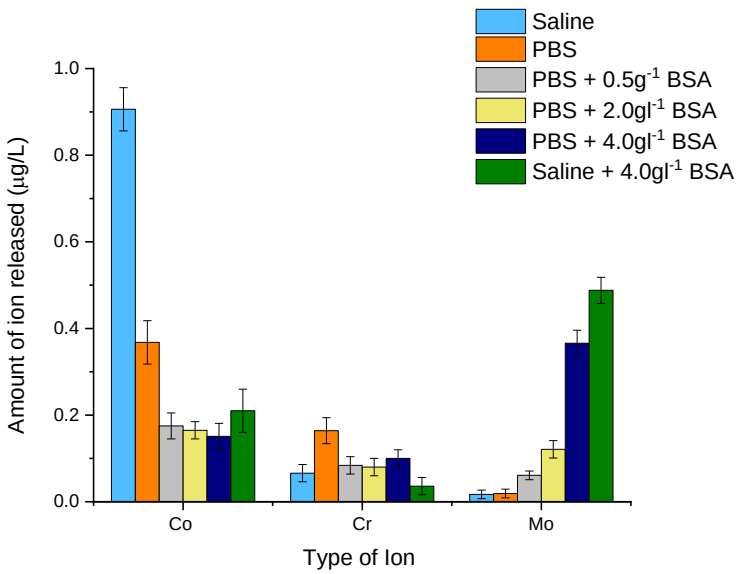

Figure 6.3 Quantity of metal ions released from the alloy after an electrochemical repassivation phase, determined from ICP-MS

A comparison of the total percentage of ion dissolution for the electrochemical repassivation phase is depicted in Figure 6.4.

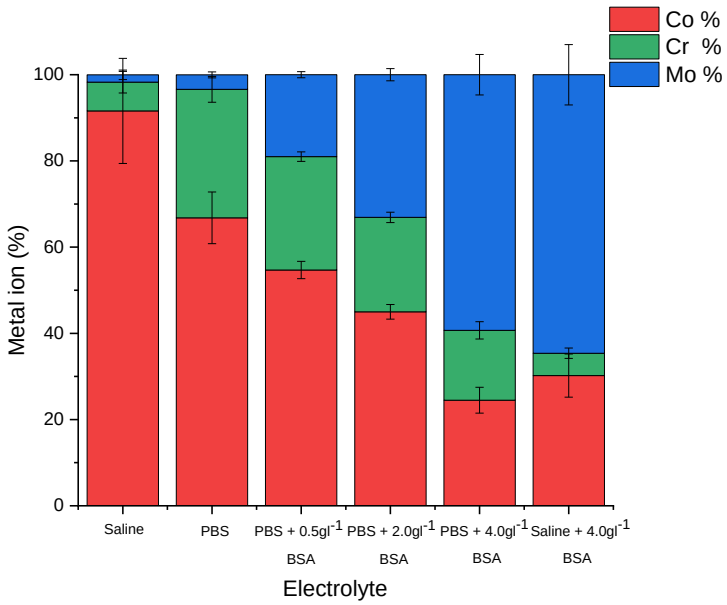

Figure 6.4 The total quantities of metal ion after an electrochemical repassivation phase released expressed as percentages, quantified via ICP-MS

As seen previously, cobalt is readily lost in a saline solution. Phosphates are seen to reduce the overall number of ions lost. However, it leads to an increase of chromium ions released; this could be due to phosphate ions

having a known affinity for chromium enabling this species to be lost to the solution when the potential is shifted, and corrosion initiated. Albumin is seen to increase the release of molybdenum from the alloy whilst lowering the quantities of cobalt and chromium ions lost to the solution; the more protein is present, the higher the effect.

6.3.1 Effect of Repassivation on the Charge of Dissolution

The extracted charge data from the current transients formed from repassivation is shown in Table 6.4.

Table 6.4 The total charge and charge of dissolution after an electrochemical repassivation phase. Published previously within [125]

Condition	Q_{Diss} (mC)	Q_T (mC)
Saline	3.40 ± 0.32	2.18 ± 0.15
PBS	2.19 ± 0.37	1.15 ± 0.09
PBS + 0.5gl^{-1} BSA	1.29 ± 0.25	1.22 ± 0.16
PBS + 2.0gl^{-1} BSA	1.47 ± 0.26	1.53 ± 0.11
PBS + 4.0gl^{-1} BSA	2.52 ± 0.33	2.09 ± 0.13
Saline + 4.0gl^{-1} BSA	2.85 ± 0.29	3.02 ± 0.22

As seen before, the Q_{Diss} is seen to account for the majority of the overall total charge for the environments. As expected, Q_{Diss} and Q_T are both diminished in a phosphate environment seeing as the passive film is reformed at a faster rate, with the ratio of ion charge remaining relatively consistent. Albumin leads to elevated levels of Q_T due to slower repassivation rates along with the reduction of BSA molecules, enabling them to adsorb onto the surface.

A comparison of the charge contributions for the passive potentiostatic experiment (+0.1V_{RE}) and after an electrochemical repassivation phase are shown in Figure 6.5. The ratios of charge owed to dissolution for a reformed film is altered to favour molybdenum ions indicating that the albumin extracts the ion into the environment; the electrochemical reactions between these species could also account for the increased levels of total charge observed. In comparison to a passive film, the Q_{Diss} and Q_T for a repassivation phase are

both increased as the alloy was fully exposed upon shifting the potentials leading to enhanced corrosion and a spike in current density.

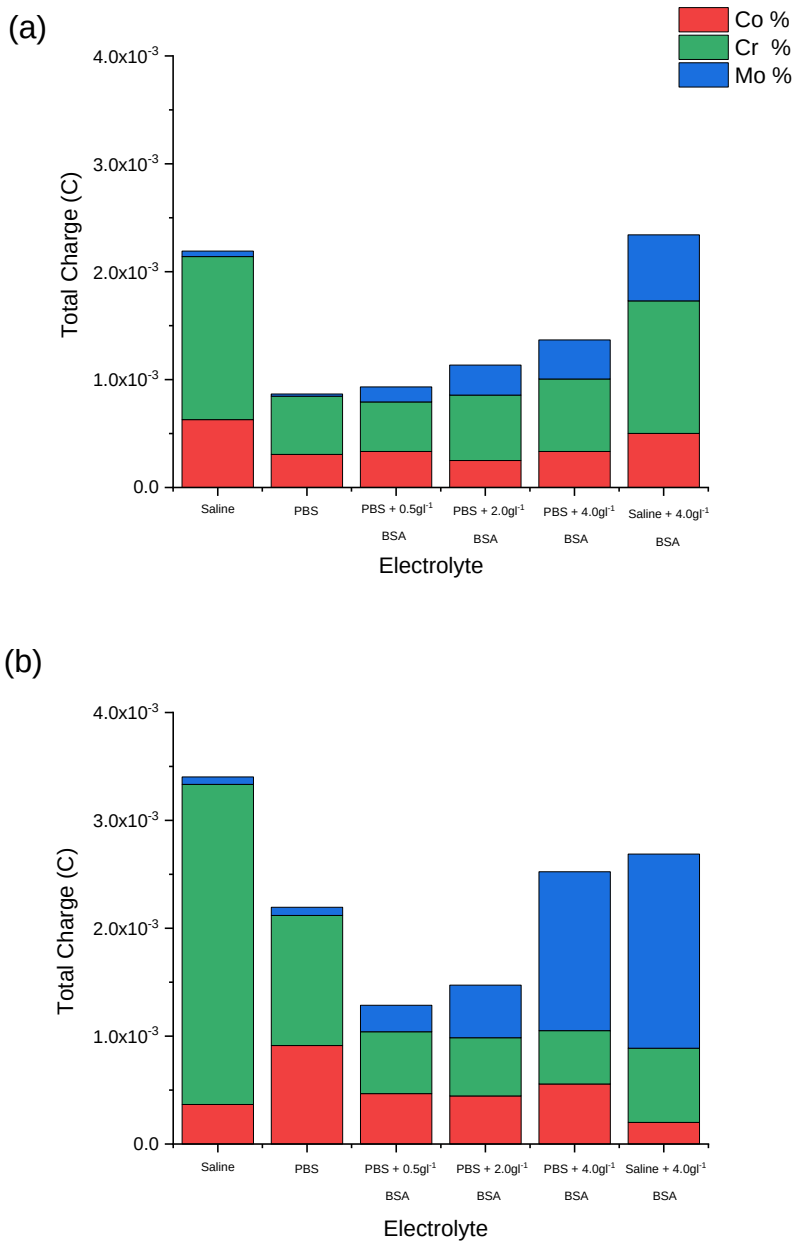

Figure 6.5 Ratio of charges for each of the metal ions lost to the solution after (a) Passivation (+0.1V_{RE}) (b) Electrochemical repassivation

There are two notable differences between the charge contributions from a passivated and a repassivated system. In a phosphate environment, the quantity of chromium ions lost is enhanced when the alloy undergoes repassivation. It is also clear to see that albumin presence leads to a much greater molybdenum release, accounting for over 50% when added in the

highest quantity. The interactions that govern this affinity will be discussed in the next chapter.

6.4 Discussion

From the ICP-MS data obtained for a variety of bodily fluids, it is clear the presence of BSA can drastically affect the type of metal species that are lost to the environment. By investigating how each metal ion binds with the BSA, a deeper insight into explaining the observed trends can be deducted. This section will give a detailed explanation and critique of the observations that have been noted throughout this chapter.

6.4.1 Dissolution of CoCrMo

The ICP-MS data gives a clear insight into the species of the alloy which are readily dissolved into the electrolyte and how the composition of the electrolyte affects the ratios of the species dissolved. For all conditions examined, cobalt was the main metal element released into the solution; this is attributed to the fact that cobalt readily forms dissolved ions as it easily complexes to water molecules present [102]. The presence of phosphates lead to a reduction of ions lost as it adsorbs onto the surface, restricting ion flow. However, the amount of chromium released is seen to increase, which could be due to favourable interaction to form phosphate complexes. BSA is seen to increase the amount of molybdenum that is lost to the environment. This trend has been noted before in the literature and is said to be due to the high affinity between the two molecules [102,125,167]. The determination of the binding sites will help further explain this phenomenon.

There are slightly more ions released during OCP (Figure 6.1b) than there is for passive conditions (Figure 6.1c) due to being polarized at a lower potential which leads to slower formed and more porous passive film. Transpassive conditions (Figure 6.1d) lead to high volumes of metal loss as corrosion of the alloy is readily occurring; the electrolyte is shown to have very little effect on the type of ion that is lost to the solution keeping in order with the stoichiometry of the alloy. Whereas under cathodic conditions (Figure 6.1a), a negative charge is imposed on the metal due to the flow of the electrons. This inhibits metal ion loss, with only small magnitudes of cobalt ions being detected in some cases.

6.4.2 Effects of repassivation on CoCrMo Dissolution

When a passive film is electrochemical stripped and reformed, the quantity of metal ions is increased due to the surface becoming active. However, the ratio of metallic elements lost is altered; this shows the protective nature of the passive film, which shields the active surface from environmental interactions.

In a PBS environment, there is enhanced loss of chromium ions which could again be due to favourable interactions with phosphate molecules. The stripping of the film allows these complexes to easily diffuse away into the solution. BSA is seen to drastically increase the quantities of molybdenum lost to the solution. Within the electrolyte, the overall globular charge of the protein is negative, this is due to the protein having an isoelectric point of 4.7 which leads to deprotonation of functional groups with the protein [88,104,174].These negative groups can bind with the metal ions, forming an irreversible bond with the ion and leading it to be extracted into solution. The effect is enhanced due to the metal being exposed; the presence of the passive film restricts the loss due to the protein having weak and reversible interactions with the apolar surface [103,168].

6.5 Conclusion

A detailed study on the metal ion release of CoCrMo under various electrochemical conditions has been carried out, determining the effect of applied potential and electrolyte of metal ion dissolution. The following conclusions have therefore been achieved.

1) The domain in which the alloy is polarized has a drastic effect on the number of metal ions given off.
    - Cathodic domain (-1.0V_{RE}) almost halts any dissolution of the alloy by negatively polarising the metal.
    - OCP and Passive domain (+0.1V_{RE}) get reduced metal ion release due to passive film formation, which protects the alloy
    - Transpassive domain (+1.0V_{RE}) gives a high number of metallic ions due to no protective film being present, so corrosion readily occurs.
2) Phosphates tend to reduce the number of metal ions released as they adsorb onto the surface inhibiting ion flow.

3) The presence of albumin leads to increased dissolution of molybdenum from the alloy. The higher the concentration of albumin, the greater the effect.
4) The higher the rate of repassivation, the less ion dissolution occurs as the alloy is exposed less to the environment. In the presence of phosphates, the overall dissolution is lower, although there is an increased percentage of chromium lost due to these ions being drawn to the surface when the cathodic-passive transition occurs. Albumin is seen to increase the over dissolution, with massive increases seen in the quantity of molybdenum released as they complex favourably over the other metallic ions present.

Chapter 7
The interactions of BSA with the individual metal ions produced from CoCrMo

7.1 Introduction

It has been seen that the presence of BSA can have a drastic impact on the corrosion behaviour of CoCrMo alongside the quantity/ratio of metal ions lost to the environment. As serum albumin is a versatile molecule in regards to its binding sites, it can interact with the metal ions in a variety of different ways. Analysis of metal/protein solutions will give a deeper insight into how the alloy and its ions interact with a protein containing environment.

The purpose of the following chapter is to determine which binding sites of the protein the metal ions interact with, relating the information to a real-world environment and possible adverse effects on the patient. The following measurements have been made to achieve these aims: Raman spectroscopy and Circular Dichroism.

As explained in the experimental section, each test was repeated at least three times to ensure reproducibility. For ease of depicting trends between the electrolyte compositions, only one repeat is shown.

7.2 Binding interactions between Metal ions and BSA

The effects of the metal ion interactions (Co(II), Cr(III), Mo(IV)) with BSA has been investigated by the use of Raman spectroscopy and Circular Dichroism to help explain the different metallic ion dissolution quantities seen within this chapter. The structures of both BSA and the metal salts have been discussed previously in Section 3.4.7.2 and have been utilised as a control against which the combined species could be compared

.

7.2.1 Effect of Cobalt ions on BSA

The fingerprint region for BSA in the presence of cobalt ions is shown in Figure 7.1. From initial observations of the comparisons, an increased broadness of Amide I and around the deformations of the C-H is noted. There are no new peaks formed in the presence of cobalt ions, with the position of the existing peaks remaining consistent throughout.

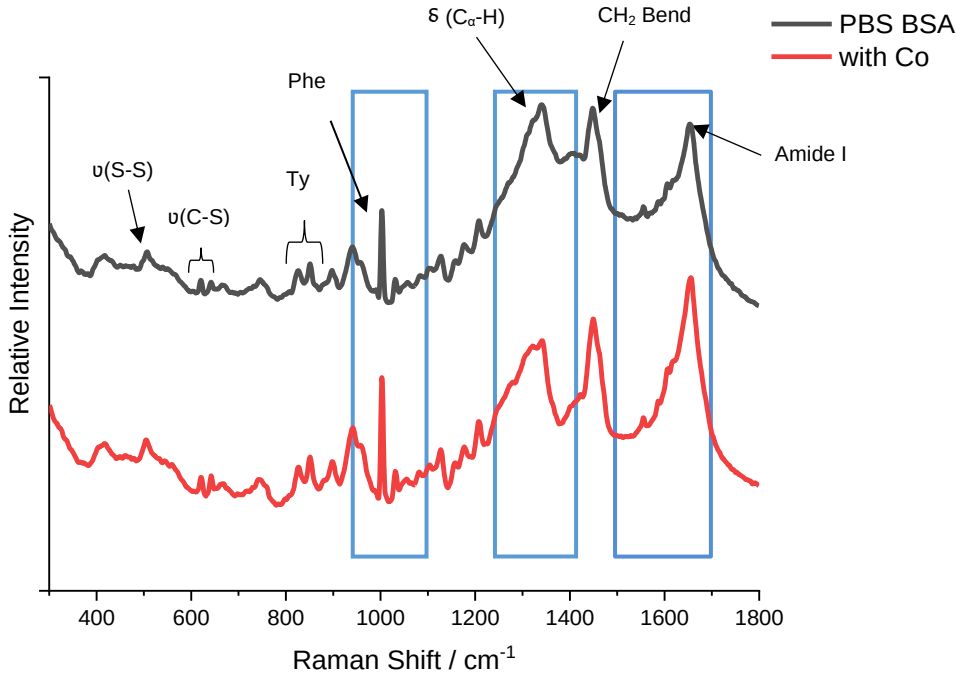

Figure 7.1 Comparison of the Raman fingerprint region between 100g/L BSA with/without cobalt ions (300 – 1800 cm^{-1})

A close-up comparison of the Amide I peaks for BSA in PBS solution, and the presence of cobalt ions is shown in Figure 7.2. The main peaks are as follows: Amine I (1655 cm^{-1}), Phe/Tyr/Trp (1616 cm^{-1}), Phe (1606 cm^{-1}) and Aromatics, Amide II (1550 – 1585 cm^{-1}) [142,143].

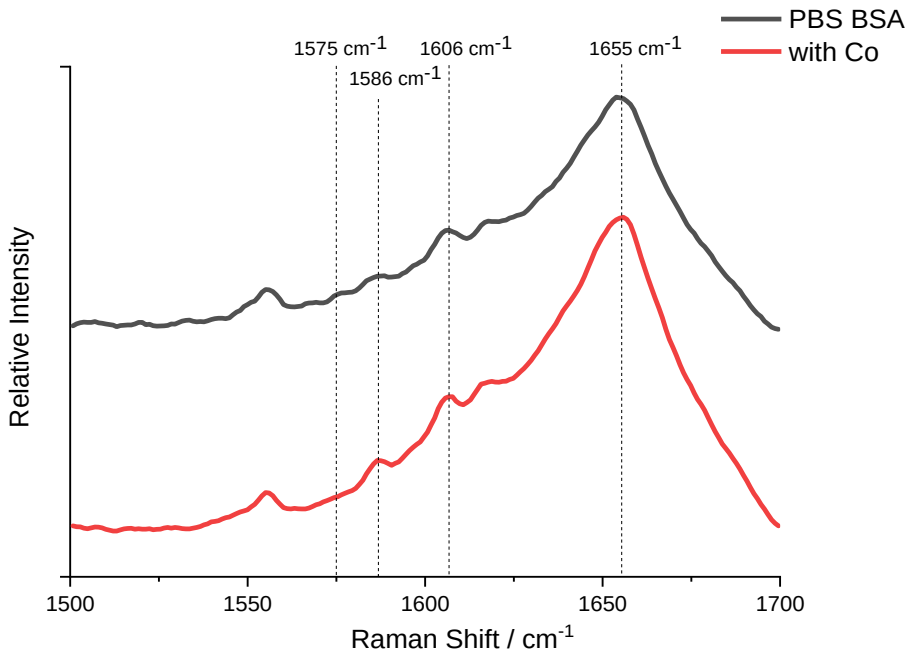

Figure 7.2 Comparison of the Amide I peak of BSA with/without the influence of cobalt ions (1500 – 1700 cm^{-1})

Visible changes within the Amide I peak can be seen from the spectra. Firstly there is a broadening of the Amide peak, which indicates that there is the presence of metal-ligand interactions [175]. The carbon double bond within the imidazole side chain of histidine produces a weak bond around 1575cm^{-1} (See Figure 7.3); this band is depleted when cobalt ions are present with an increase in the broadening/intensity of the peaks at 1586 and 1606cm^{-1} [175]. These feature changes are down to changes in the chemical shift of the C_4=C_5 band, which is known to be sensitive to the site at which a metal ion binds, if in the N_π – metal from the peak is 1580 ± 10cm^{-1} with the N_τ appearing at 1600 ± 6cm^{-1} [175,176]. These peak features indicate that the Co (II) ion binds to both the N_π and N_τ atom of the histidine chain

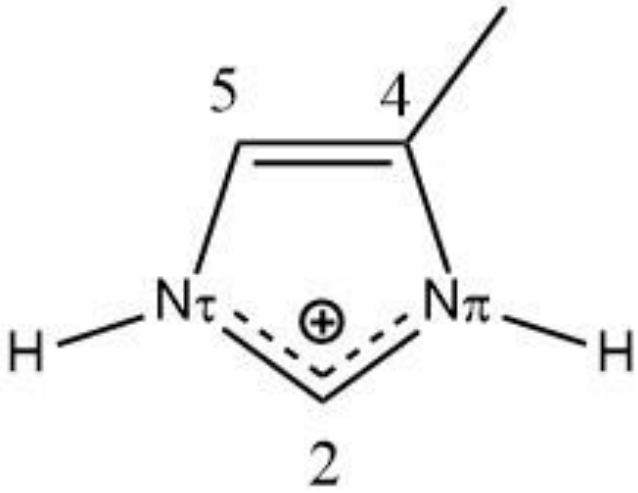

Figure 7.3 Schematic of imidazole side chain

Other areas within the spectrum can depict histidine binding to the cobalt ligand; these are depicted in Figures 7.4. In Figure 7.4a, the band at 982 cm^{-1} increases in intensity, which corresponds to the ring breathing mode of imidazole bound at the N_T site. This can be deduced as the intensity of the peak at 990 cm^{-1} corresponds to the histidyl moiety in its cationic form, which when bound to a metallic ion is shifted to lower wavelengths [177,178]. The other strong peaks in this Figure, which both correspond to Phe, appear at 1000 cm^{-1} and 1032 cm^{-1} [141]. Within Figure 7.4b, there is a visible stronger peak at around 1278 cm^{-1} when cobalt ions are present, which correspond to the ring breathing mode of a side chain of histidine ligated to the metal ion at the N_π site [177]. A stronger shoulder peak is also observed between 1405-1420 cm^{-1} which is known to be due to the significant rearrangement of charges from both the COO^- and C=O/C-N^-group [178]. The other peaks present in this Figure correspond to the C_α-H deformation and the CH_2 twist/wag at 1342 cm^{-1}, with the shoulder at 1318 cm^{-1} corresponding to amide III as well as the CH_2 twist/wag [141].

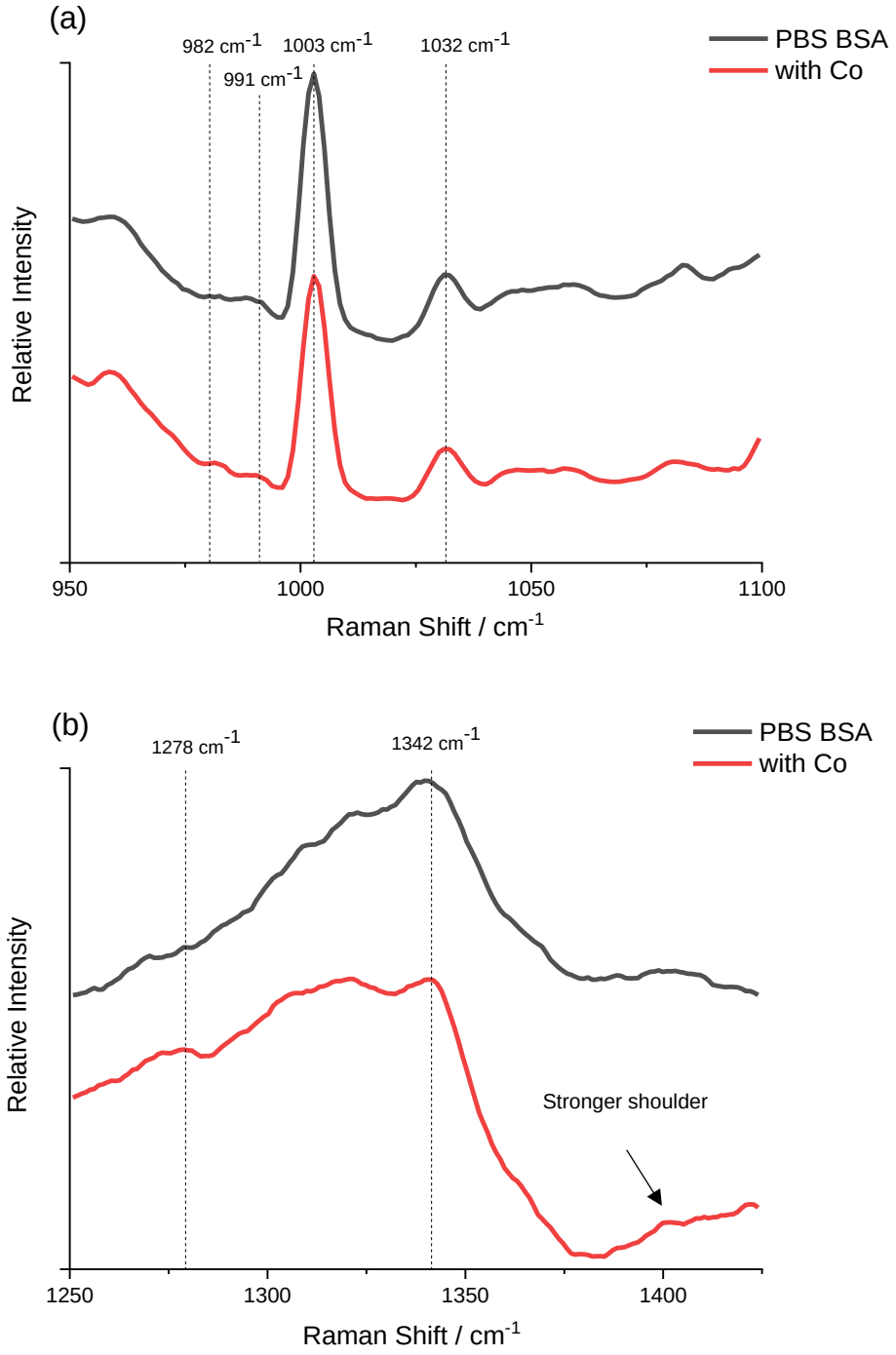

Figure 7.4 Effect that cobalt ions have on BSA in regions that show characteristics of histidine bonding (a) (950 – 1100 cm^{-1}) (b) (1250 – 1425 cm^{-1})

7.2.2 Effect of Chromium ions on BSA

In the presence of chromium ions, the BSA formed a hydrogel. This was not seen with BSA and any of the other metallic ions investigated within this research but has been noted by researchers previously [49].

The fingerprint region for BSA in the presence of chromium ions is shown in Figure 7.5. From the spectra, the intensity of the C-H deformation peak has dramatically increased due to the change in the state of the BSA. This makes all of the peaks possess a higher general intensity than the aqueous BSA form it is compared against.

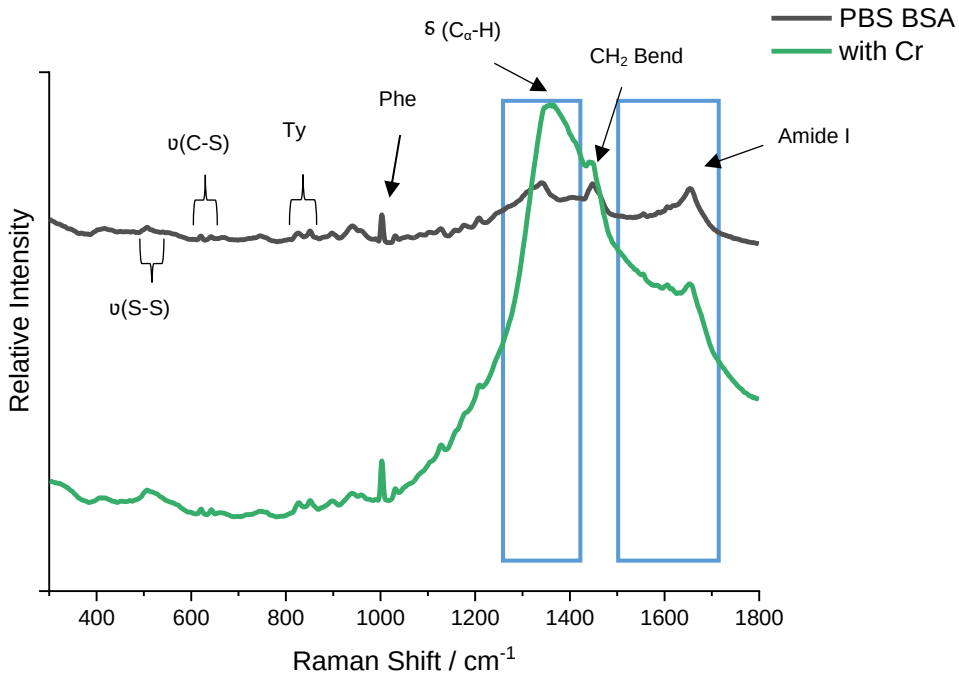

Figure 7.5 Comparison of the Raman fingerprint region between 100g/L BSA with/without chromium ions (300 – 1800 cm^{-1})

A close up of Amide I with chromium ions is shown in Figure 7.6. The Amide I peak around 1655 cm^{-1} possess less intensity but is broader than its counterpart. This indicates that the protein has undergone a structural change, moving away from its normally favoured α-helix structure. The investigation into this comes in the following section. The other peaks present in this region have been shifted to slightly lower wavenumbers due to intermolecular hydrogen bonds now being present between the hydrocarbons of the aromatic rings [179]. As seen in cobalt-containing conditions, the C_4=C_5 imidazole side chain of histidine at 1575 cm^{-1} is diminished, which leads to an increase in the intensity of the region around 1600 cm^{-1} [175,176]. As explained previously this indicates that Cr (III) ion binds to the N_τ atom of the histidine chain.

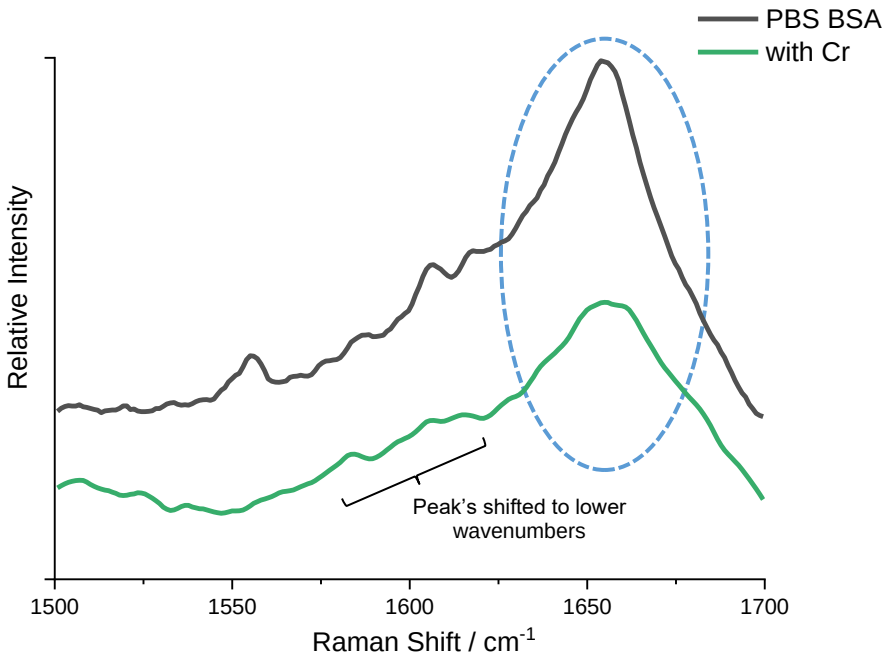

Figure 7.6 Comparison of the Amide I peak of BSA with/without the influence of chromium ions (1500 – 1700 cm^{-1})

Further information about the interactions of the His and Asp parts of the protein are depicted between 1250 – 1450 cm^{-1} in Figure 7.7 [177,178]. The lack of a shoulder peak around 1278 cm^{-1} would indicate that the metal doesn't bind via the N_{π} site, but there is a stronger shoulder seen at 1290 cm^{-1} which indicates the presence of metal bridging with His. The presence of this peak and the previously seen N_{τ} at 1606 cm^{-1} suggests the bridging occurs through the N_{τ} site [175,177]. The peak corresponding to the COO/C=O/C-N^{-} between 1405 – 1420 cm^{-1} is diminished in the presence of chromium as the bonds have become fixed in place due to aggregation of the complex [143]. The main peak of the C_{α}-H deformation and the CH_2 twist/wag at 1342 cm^{-1} is shifted to a lower frequency when exposed to chromium; this is a direct result of the formation of hydrogen bonds as they stabilise the structure lowering the restoring force of the bond [180].

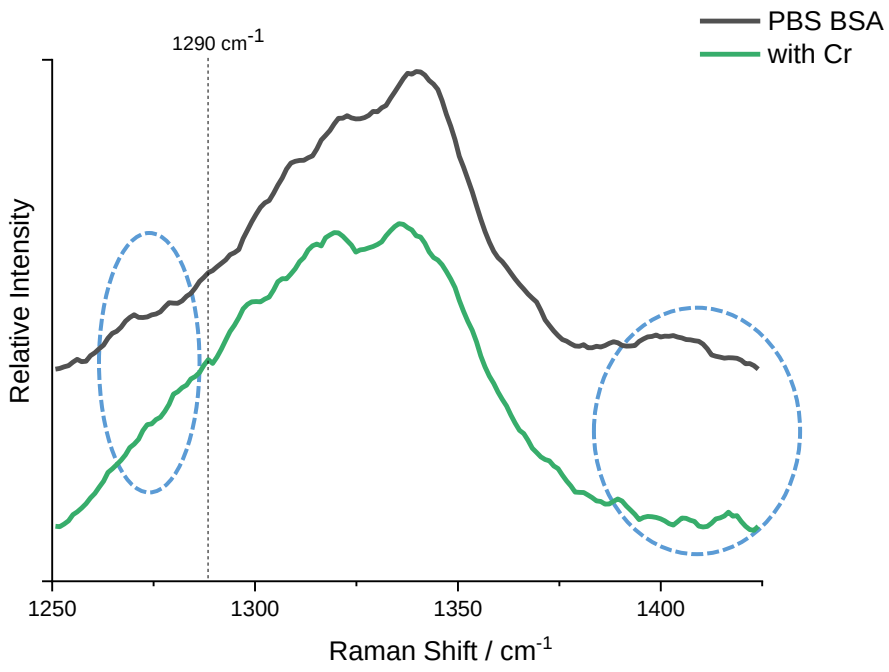

Figure 7.7 Comparison of the C_{α}-H deformation peak of BSA with/without the influence of chromium ions (1250 – 1425 cm^{-1})

The presence of this hydrogen bonding between aggregates is easy to see via analysing the region between 2800 – 3800 cm^{-1}, shown in Figure 7.8. The main peaks within this region are as follows: υ(C-H) 2800 - 3000 cm^{-1}, υ(=C-H) 3000 - 3100 cm^{-1}, υ(N-H) 3300 - 3500 cm^{-1} and υ(O-H) 3100 - 3650 cm^{-1} [141,142]. It can be seen that the major O-H/N-H possess both a higher peak position and intensity with a shorter width in chromium conditions. This is due to the formation of new hydrogen bonds that increase the wavenumbers of the -OH bonds as well as giving rise to new hydrogen bonds that involve the N-H bonds (3315 – 3340 cm^{-1}) [180]. These bonds imply that the intermolecular hydrogen bonding is now present between the molecules, which are vital to the stability of the aggregated molecule [181].

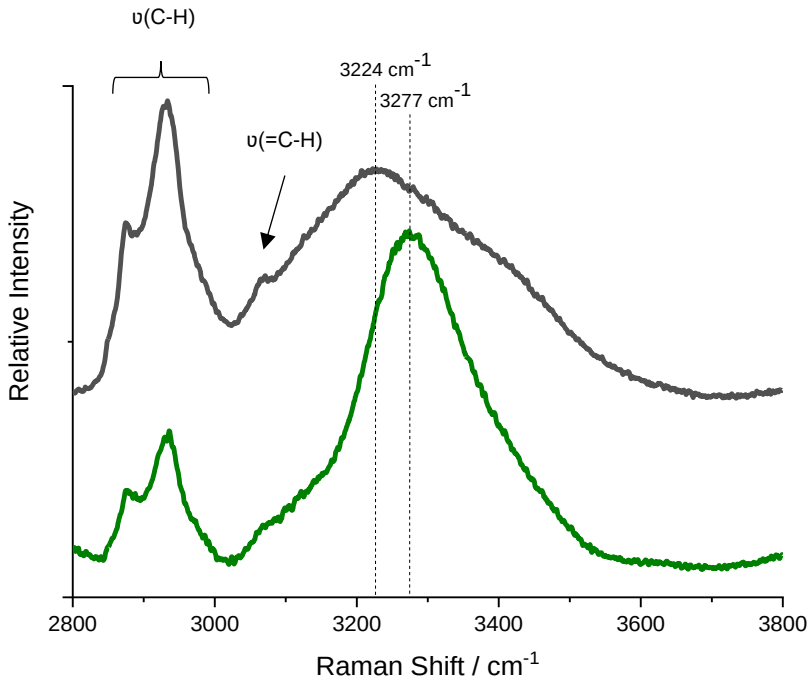

Figure 7.8 Comparison of the upper Raman shift region of BSA with/without the influence of chromium ions (2800 – 3800 cm^{-1})

7.2.3 Effect of Molybdenum ions on BSA

The fingerprint region for BSA in the presence of molybdenum is shown in Figure 7.9. From this comparison, it can be seen that there is a strong peak at 900 cm^{-1} as well as a peak at 320 cm^{-1} which are not present in any of the other spectra.

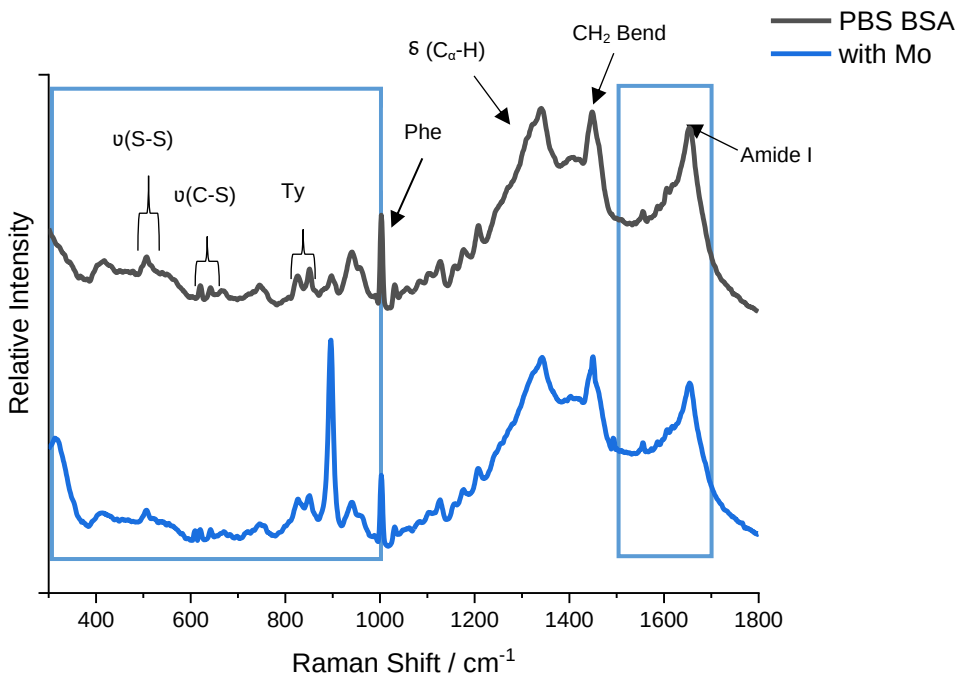

Figure 7.9 Comparison of the Raman fingerprint region of 100g/L BSA and with molybdenum ions (300 – 1800 cm^{-1})

A close up of the amide peak in the presence of molybdenum is shown in Figure 7.10; it is seen that the molybdenum has little/no effect on the broadness of the Amide I peak as well as the positioning and intensity of the surrounding peaks. This would indicate that the metal ion has no interaction with the histidine side chain of the protein. To confirm this, the regions between 950 – 1100 cm^{-1} and 1250 – 1425 cm^{-1} were also examined, but there was little difference in terms of intensity and position.

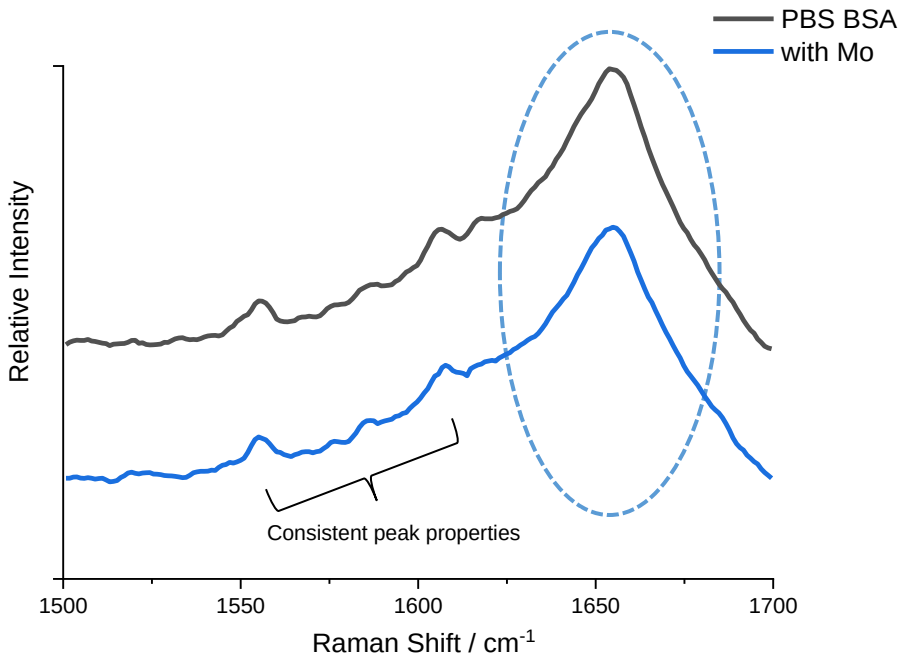

Figure 7.10 Comparison of the Amide I peak of BSA with/without the influence of molybdenum ions (1500 – 1700 cm^{-1})

As seen in the overall fingerprint region, there is the formation of two new peaks; a close up of the spectra between 300 – 1000 cm^{-1} is indicated in Figure 7.11 to investigate this further. From the analysis of the molybdenum salt previously and literature, it appears that the strong peak at 900 cm^{-1} is due to the υ(O-Mo), from the powder, there is also a peak at 800 cm^{-1} that relates to υ(O-Mo_2), which is not seen in this spectrum [141,182]. The peak present at 320 cm^{-1} is known to be υ(S-Mo) [181]. Upon close inspection of the spectra, there is also a new peak formed around 600 cm^{-1}, which comes at the expense of intensity from the υ(C-S) peak; this occurs due to the environment of the bonds being affected by the addition of the molybdenum ion [141].

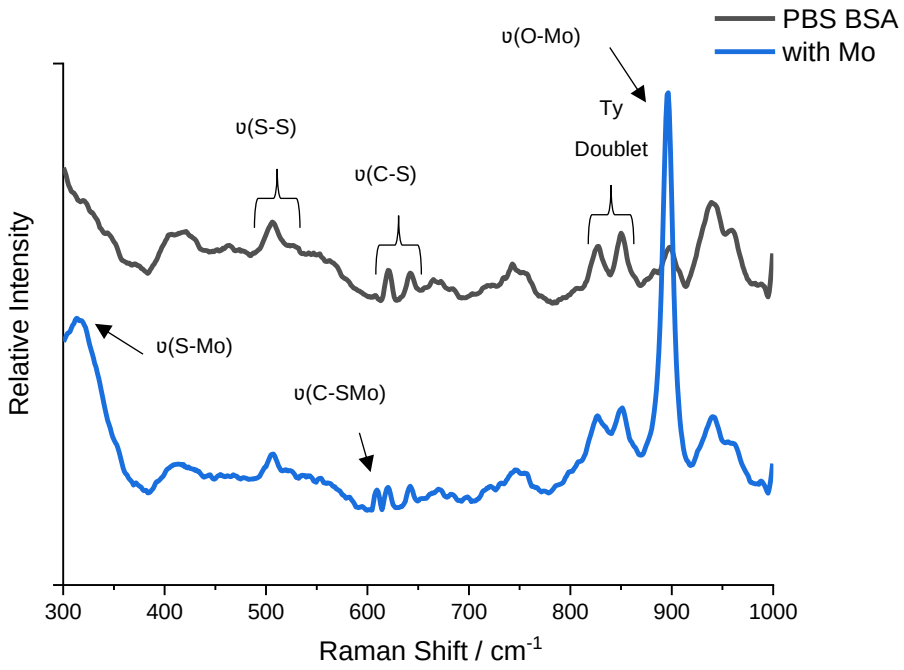

Figure 7.11 Comparison of the 300 – 1000 cm^{-1} region of BSA with/without the influence of molybdenum ions

7.3 Metal Ion Effects on the Secondary Structure of BSA

The secondary structure of the protein; how the amino acid chains are structured can be determined from the Amide I peak from Raman spectroscopy. This is due to the different conformations of the protein exhibiting different Raman shifts: α-helix (1650 – 1657 cm^{-1}), β-sheet (1670 – 1690 cm^{-1}), Coils (1680 – 1696 cm^{-1}) and Random (1626 – 1640 cm^{-1}) [180]. From the Raman experiments conducted, obvious changes were seen within the albumin molecules in the presence of chromium, with the peak being broader with much less intensity. This indicates that the protein has undergone a structural change away from its favoured α-helix form; the dissected Amide I peak in the presence of chromium is shown in Figure 7.12a. A comparison of the conformations against other environments shown in Figure 7.12b.

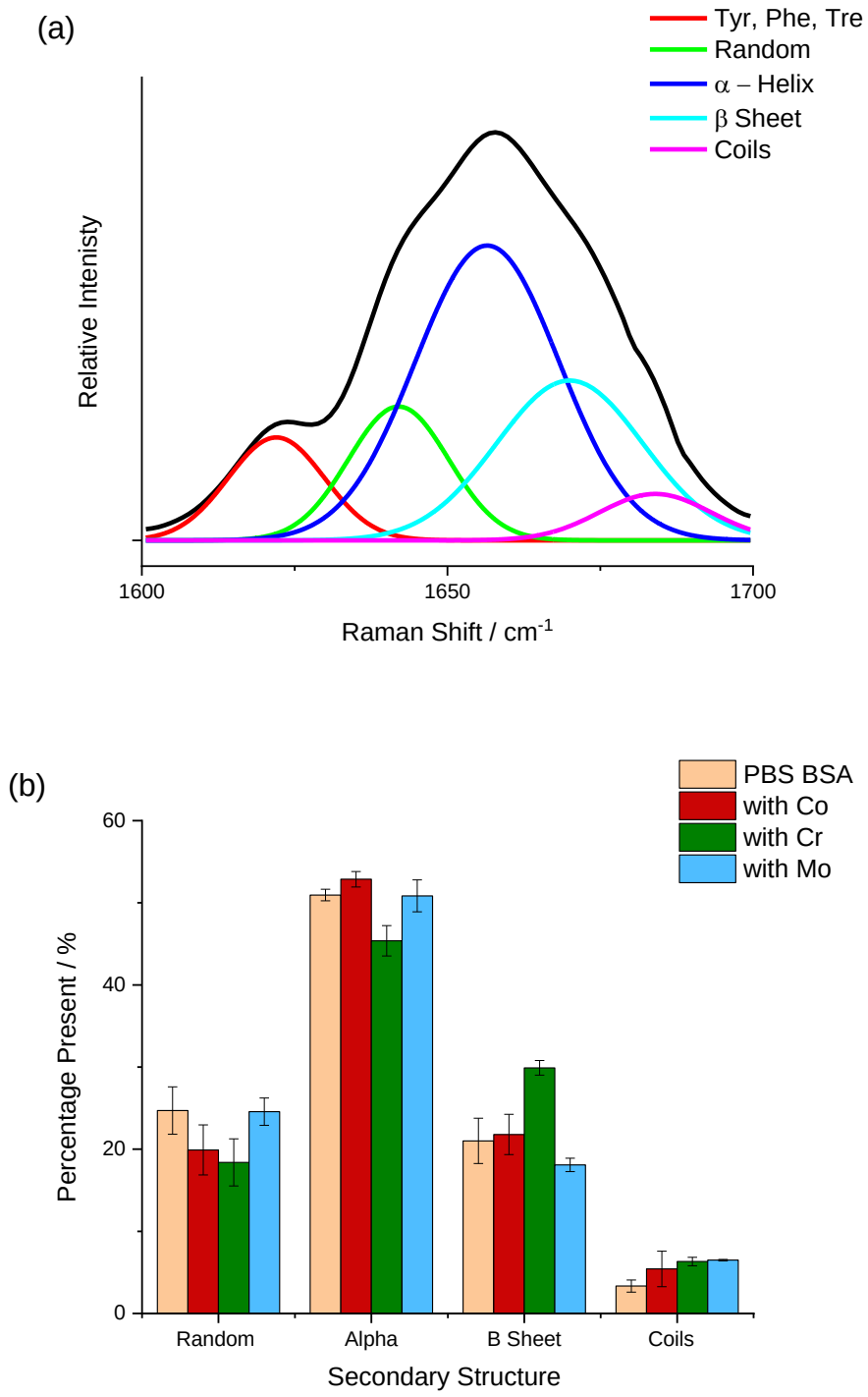

Figure 7.12 Effect of metal ions on the secondary structure of BSA (a) Dissection of the Amide I peak from Raman for BSA in the presence of chromium (b) Comparison of the secondary structures of BSA in different metallic environments

The use of circular dichroism can support these changes indicated from the Raman spectroscopy. The spectra obtained are indicated in Figure 7.13; the α helical content of BSA is well characterised throughout the literature with two negative bands appearing at 209 and 222 nm, which is due to the π-π* and the n-π* transitions of the amide groups [142,144]. The presence of cobalt leads to these bands becoming more prominent, indicating that the percentage of α-helical content is increased while the opposite effect is seen when chromium ions are present. This is due to the more negative band seen at 197 nm alongside the decreased intensity of the characterised BSA bands, indicating that some α-helix content is lost to the expense of β sheets [144]. These findings are in accordance with the Raman findings on secondary structure.

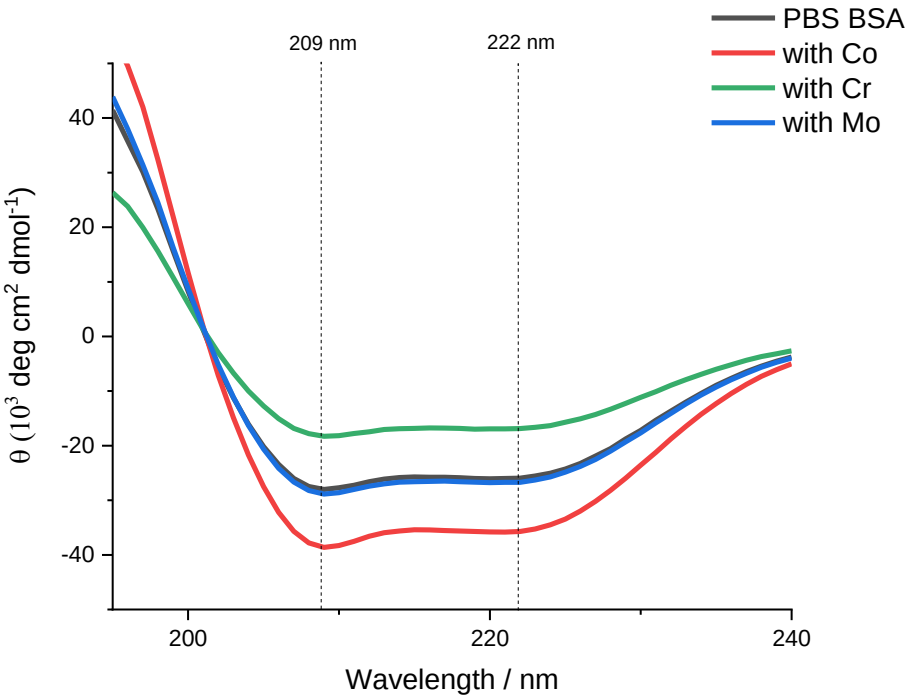

Figure 7.13 Comparison of the circular dichroism spectra of BSA in different metallic environments

7.4 Metal Ion effects on the Disulphide Bond of BSA

The conformer forms of the S-S bonds that help hold the protein molecules together are affected by the presence of metallic ions due to the bonding into specific sites. A comparison of the different forms is shown in Figure 7.14, with these bands being fitted as shown previously in Figure 3.17. The conformations adopted by the S-S are altered depending on the ion present, indicating that the metal ions bind to different sites on the protein.

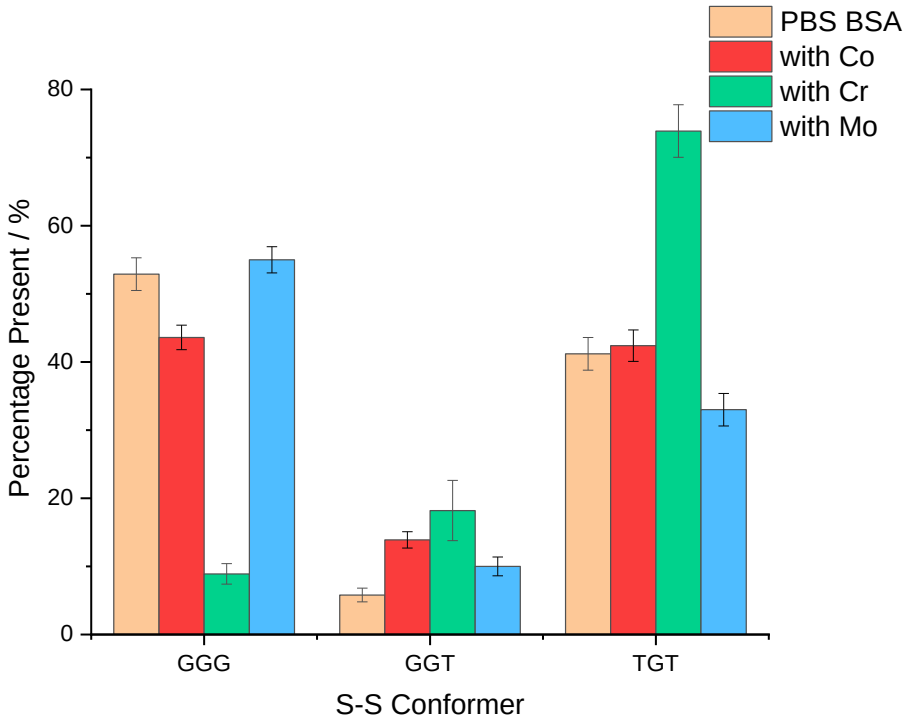

Figure 7.14 Conformation of the S-S bonds of BSA in different metallic environments

The effect of both cobalt and molybdenum ions only lead to slight changes within the conformations due to inducing strain on the protein when it interacts with the site leading to a shift in conformation to become more energetically stable. However, chromium ions lead to a drastic change in the conformation, with the previously favoured GGG conformer being almost all depleted in favour of the GGT and TGT.

7.5 Discussion

By investigating how each metal ion binds with the BSA, a deeper insight into explaining the observed trends can be deducted. This section will give a detailed explanation and critique of the observations that have been noted throughout this chapter.

7.5.1 Determination of the Binding Sites for the Metallic Ions

From the experiments undertaken, it is clear that the presence of metallic species has a drastic effect on the conformation and properties of both the secondary and tertiary structures of albumin. The ions are seen to have different effects due to the number of electrons in their outer d shells, their respective oxidation states, their favoured coordination geometry and their respective Lewis acid properties.

7.5.1.1 Cobalt Binding Site

The cobalt-containing BSA species gave distinct peaks that correspond to the histidine binding sites (982 cm^{-1}, 1278 cm^{-1}, 1606 cm^{-1}) alongside the stronger shoulder peak seen at 1405 – 1420 cm^{-1} which indicates the rearrangement of COO^-/C=O and C-N^- [142,175]. As the metal ion was shown to bind to both the N_τ and N_π sites of histidine, it indicates that the ions can bind to the NTS and the MBS site even though they require different geometries. This is due to the versatility of the Co(II) ion, which is known to adopt four, five and six co-ordinate complexes [183]. The ion possesses a d^7 configuration which can exist in a high spin quartet state as well as a low spin doublet state. The broadening of the amide I as well as the rearrangement of C-N- could also indicate an affinity for binding Site B.

Sokolowska [184] used isothermal titration calorimetry to distinguish that Co(II) can bind to the same three binding sites of HAS and was able to order them per their binding affinities as Site B>MBS ≈ NTS. This could be due to the complex being octahedral, which is the most natural binding site of Co(II) within an aqueous solution; overall it's hard to determine why Site B is the most favoured as the site is non-localised [66].

7.5.1.2 Chromium Binding Site

The presence of chromium leads to the aggregation of protein molecules through the formation of crosslinks which involves the formation of non-reversible interconnections between individual albumin molecules [178]. In the case of hydrogel formation, the bound metal ion undergoes chelation to

enhance its thermodynamic stability. It remains bound for a long time in retrospect to the lifetime of the folded state of the protein due to extremely slow ligand exchange rates [185,186]. This enables the metal to be available for crosslinking as the bound metal ion is now exposed to other protein molecules with favourable binding sites.

From the analysis of the secondary structure of the BSA with both Raman and CD, it appears that for the hydrogel to form, some of the α-helical content has to be converted into β sheets enabling the correct orientation for crosslinking. This, in turn, would alter the conformation of the disulphide bond, accounting for the drastic changes seen from the previously favoured GGG to the TGT form. Only slight changes are seen with the other metallic ions as the protein adapts to the interactions of the ion.

The process of chelation of this metal species can take one of the following forms where there is no evidence of metal-metal bridging in a shift in secondary structure towards β sheet [185].

His – M – His

Asp – M – His

Cys – M – His

Where M is a metal ion

Analysis of the spectra can give us details upon which process the crosslink is formed through between the album molecules. Asp involved chelation can be ruled out due to the diminished COO/C=O/C-N^- peak indicated within Figure 7.10. The conformation of the tertiary structure alongside no evidence of a υ(S-Cr) bond enables us to also rule out crosslinking through Cys. Therefore the crosslink occurs through the His(N_τ) – Metal - His(N_τ), as there was an indication of a metal N_τ bond due to a peak arising at 1606 cm^{-1} as well as the formation of a peak at 1290 cm^{-1} which represents histidine metal bridging [175]. The shift to a higher conformation of β sheets of the proteins secondary structure in the presence of this metal ion enables the bond to be formed, as it gives the right orientation/conformation for the ion to interact intermolecularly with other β sheets [186].

Further insight as to why chromium binds in this way can be determined from its electronic properties. Chromium (III) has a d^3 electronic configuration with a tendency to form only octahedral complexes; as there are only $3e^-$ in the d

shell, there is only the possibility of existing in the high spin state. Due to having a high oxidation state with a low d electron count (d^0-d^3), π donor ligands are preferred for the metal ion. These are ligands with one or more lone pairs of electrons within the p orbitals on the donor atom that can donate into the empty orbital on the metal, such as the imidazole ligand. This is due to the imidazole having a high energy HOMO (highest occupied molecular orbital) [187]. This is opposite to the Co(II), which prefers π-acceptor ligands due to the ion having a lower oxidation state alongside a high electron count ($<d^6$).

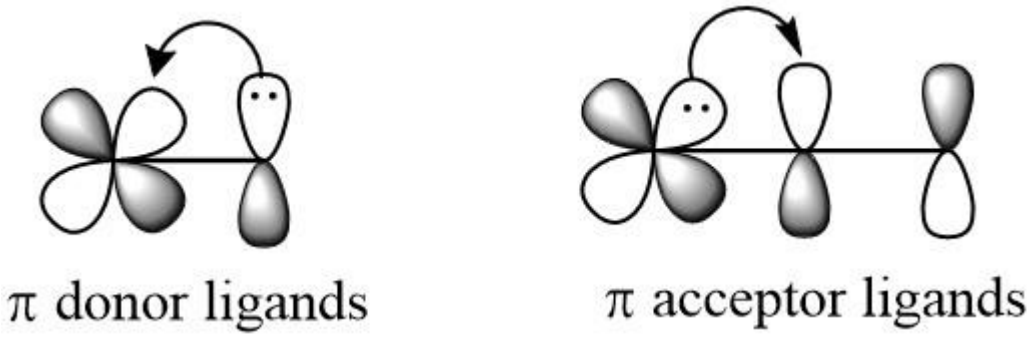

Figure 7.15 Schematic indicating the way π donor and acceptor ligands complex to species

A possible model for this interaction is shown in Figure 7.16. Mirua [175] observed crosslinking through this method with Zn(II) ions in the presence of amyloid β – peptides. These species would alter the viscosity of the fluid within the hip environment due to the aggregation of multiple albumin molecules; in reality, this is not observed due to a higher level of cobalt released from the implant, which has been shown to have a greater affinity for the albumin over chromium [49]. Yang et al. [49] undertook a competitive binding study between cobalt and chromium with albumin and determined that the binding of chromium is severely inhibited in the presence of cobalt, suggesting that they share a similar binding site which has been proven within this study.

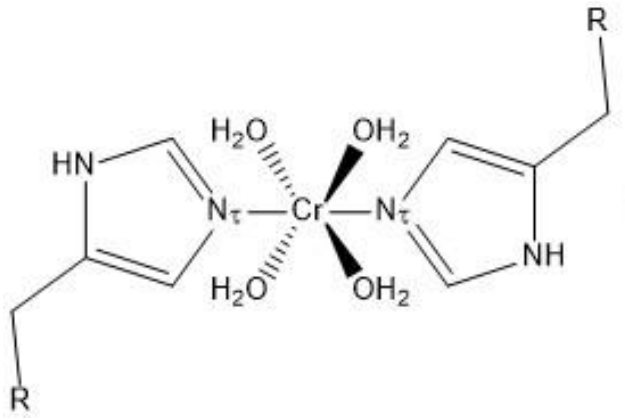

Where R is the rest of the protein molecule

Figure 7.16 Model for the aggregation of BSA through crosslinking involving chromium (III) ions

7.5.1.3 Molybdenum Binding Site

Molybdenum has a very different effect on BSA compared to the other two metal ions investigated. There were observations of a molybdenum-sulphur bond (320 cm^{-1}, 609 cm^{-1}) alongside a lack of interaction with the metal ion and the main active sites on the protein (His, Tyr, Asp), indicating that this metal ion binds to the free thiol at Cys-34. This is due to this specific binding location not possessing spatial location for simultaneous coordination [66].

The electronic configuration of Mo(VI) is d^0. This ion is governed by oxo-species when in a higher oxidation state. This is due to possessing properties that are typical of a class A acceptor (high affinity for oxide/oxygen donor atoms and light halides), which is indicated via the high intensity of the υ(O-Mo) bond**.** Metal ions with a d^0/d^{10} configuration commonly exist in the tetrahedral geometry. The molybdenum ion is also known to have a high affinity for sulphur which is illustrated by its occurrence as a sulphide ore, MoS_2. Wagman [189] determined from the differences between the heats of formation of oxides and sulphides that Mo has a higher affinity for sulphides than Cr does. From the spectra, there is no presence of bridging oxides; therefore, there is only one metal ion bound to each BSA molecule. When in this form, they are present as a tetrahedral oxyanion; this geometry could also be another limitation of the Cys-34 binding and why chromium ions do not interact with this site.

The Cys-34 thiol has been reported to have a low pK_a indicating that it is highly likely to lose its proton, enabling the Mo-S bond to form [190]. This could occur via nucleophilic substitution, involving the attack of the lone pair of electrons

from the sulphur into the molybdenum ion, which in turn leads to one of the O-Mo bridging bonds being broken to form both the protein molybdenum species and a MoO_4^{2-}. This bond is highly enthalpic driven, which could explain why it is the favoured metal for coordination out of the constituents [66].

7.6 Conclusion

The interactions between the metal ions and protein have been quantified to help explain the corrosion mechanisms that take place between the alloy and its environment. The following conclusions have therefore been reached.

1) The possible protein-metal ion interactions that can occur are as follows:
    - Cobalt ions can bind to the NTS, MBS and Site B of the protein molecule due to it being a versatile ion.
    - Chromium ions cause the formation of a hydrogel by forming protein aggregates due to crosslinking of histidine residues.
    - Molybdenum ions bind to the Cys-34 binding site of the molecule; this is highly thermodynamically favoured due to the formation of a Mo-S bond.

Chapter 8
Insight

8.1 Introduction

The drivers for this specific piece of research stem from the need for a longer-lasting implant that can meet the needs of the highly active younger population. MoM devices meet these criteria due to low wear rates and excellent corrosion resistance, but the release of metal ions into the body can lead to adverse effects within the patient. Fully understanding the mechanisms behind this phenomenon are vital in enhancing the functionality of these implants and providing people with a more reliable implant.

This thesis presents a comprehensive investigation into the effects that simulated bodily fluids can have on CoCrMo under a range of different conditions, which was key to gaining a deeper insight into components of the electrolyte interactions with the alloy and their resultant effects on the corrosion resistance. The aims and objectives set out at the start of the thesis have been achieved by combining electrochemical characterisation alongside a variety of different post-test assessment techniques. The main takeaways from this research were determining the deeper aspects of how BSA affects the corrosion behaviour of CoCrMo, indicating that BSA can interfere with a repassivation phase alongside drawing molybdenum into the solution through the formation of a Mo-S bond lowering its content within the passive film.

This chapter aims to bring all the result chapters together, hoping to tie all the links between the data obtained and provide detailed crosslinking with already existing published work.

8.2 Effect of the electrolyte

Electrochemical testing has shown that the presence of phosphates lead to an increase in the resistance of the alloy, indicated by more noble values of E_{corr} and i_{corr} alongside lower obtained values of $i_{p.}$ The phosphates have been seen to adsorb onto the surface of the alloy as observed via SEM and AFM, protecting the alloy from the environment, this accounts for the electrochemical data observed. This is a chemisorption process in which a coordinated type bond is formed between the alloy and the phosphate, this was further evidenced via XPS which showed the presence of a strong metal phosphate bond (~133 eV). The formation of this bond was seen for all applied

electrochemical conditions indicated via a smoother R_a and increased R_p. The use of XPS also determined an increase in the quantity of Cr(III) within the passive film, indicating that the absorption of these species helps promote chromium presence within the film. It is well known within the literature that increases in chromium enhance the resistance of the film [92,105,123]. Yan et al. [191] noted that the presence of inorganic or organic species could alter the characteristics of the passive film and, therefore, the corrosion resistance of the alloy. The affinity of chromium and phosphates can be seen in the ICP-MS data obtained, seeing as in phosphate-containing environments, the quantity of chromium released is increased. Therefore it can be concluded that the phosphates increase the resistance of CoCrMo by adsorbing onto the surface, providing extra protection and by altering the composition of the passive film.

The use of SEM and TEM has observed BSA adsorption onto the surface, which also occurs via chemisorption. AFM has indicated that BSA adsorbs onto the surface of the alloy via the side-on model; the layer is typically 4 nm thick, suggesting it is only one monolayer thick. However, BSA acts as a cathodic inhibitor due to lowering obtained values of E_{corr} whilst increasing the i_p [14]. The effect of BSA on the corrosion resistance of CoCrMo is dependent on the applied electrochemical condition. In the case of OCP, the resistance of the film was observed to be weaker, indicated by lower obtained values of R_p, due to the flow of oxidants being inhibited to the surface by the adsorbed protein [100]. Whereas for passive conditions, the resistance is enhanced due to the speed of oxide formation not being affected by the relatively large BSA molecule, which only inhibits slow oxide growth processes [145]. BSA has been shown to possess a unique affinity for molybdenum within the alloy, as indicated by increased quantities within the passive film and bulk solution when the protein is present. These effects have been noted before by multiple researchers where a supposed higher affinity was suggested [30,102,174]. This has now been determined from investigating specific binding sites of BSA and determining the BSA binds to molybdenum through an entropically favoured Mo-S bond formation [66].

8.3 Effect of the applied potential

It has been shown that the potential applied to CoCrMo governs the surface properties and corrosion behaviour of the alloy. An implanted alloy can experience different conditions due to standard everyday use, so the

characterisation of these conditions is vital for obtaining a clearer picture. Cathodic conditions can be induced by the removal of the oxide film, which occurs due to walking and running via wear [105]. The area of the metal which is exposed is cathodically polarized due to possessing a lower potential than the oxide covered surface. If the implanted joint becomes inflamed, transpassive conditions can be induced [192,193]. This occurs due to the production of radicals (oxygen and hydroxy) as a response to the conditions. However, this creates a highly aggressive environment for the alloy, vastly enhancing corrosion [192,193]. A schematic depicting the effects of the applied conditions is displayed in Figure 8.1.

Under the cathodic conditions applied (-1V_{RE}), a reduction of the oxide film (low R_p and increased CPE_{out}) occurs as the applied potential is lower than the standard reduction potential of the elemental composition [128]. Differences between XPS oxide composition in the passive state and after a repassivation phase consolidate reduction occurs, but to what extent is difficult to characterise. However, the reduction of this layer only leads to minimal ion loss due to the alloy acting as a cathode (flow of electrons towards the alloy). This is in concordance with the smooth surface observed with AFM (R_a = 7.99 ± 0.03). The use of AFM also indicated enhanced irreversible BSA absorption, providing complete coverage in comparison to other conditions. This could play a key role in the formation of the biofilm, which gives an implanted alloy its biocompatibility [80].

Under both OCP and Passive conditions (+0.1V_{RE}), the alloy is covered with an oxide film. This film has been visible with the use of TEM-EDX and XPS analysis. When electrochemically passivated, the oxide film was seen to be thicker, calculated to be between 1.1 – 1.8 nm from EIS and observed via TEM/EDX to be between 1.5 – 2.0 nm. The protectivity of the film is also enhanced, characterised via lower ion levels detected from the electrolyte post-test via ICP-MS.

When a trans-passive potential (+1V_{RE}) is applied, corrosion of the surface readily occurs as the surface is exposed to the electrolyte. The R_p values from EIS are heavily diminished, with the electrolyte being responsible for the obtained values. Corrosion is characterised via the magnitude of the ions lost observed via ICP-MS and the increased surface roughness (R_a = 9.59 ± 0.07) determined from AFM, which would be due to the formation of pits on the surface of the alloy.

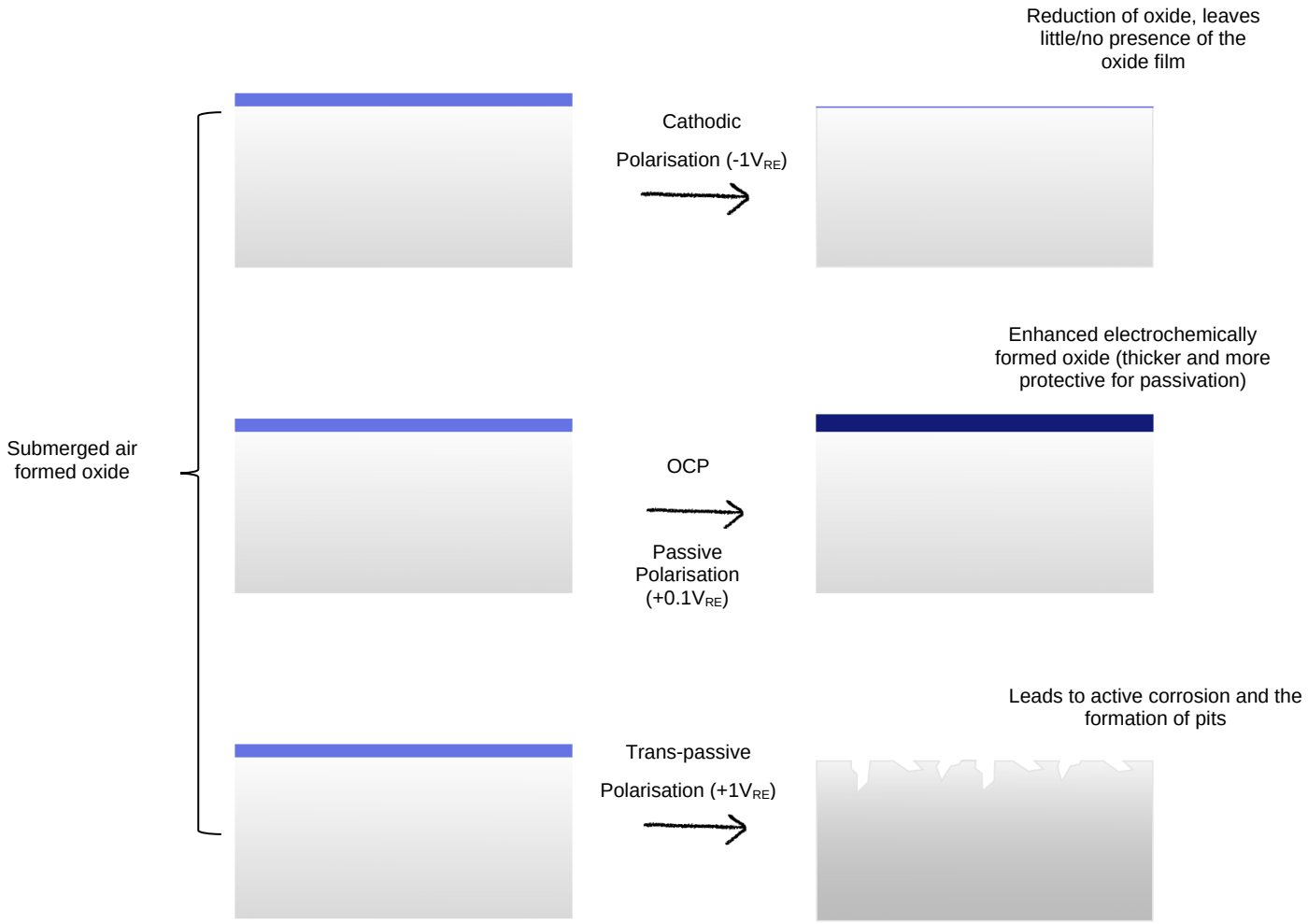

Figure 8.1 Comparison of applied potential on the surface properties of CoCrMo (a) Cathodic (-1V$_{RE}$) (b) OCP/Passive (+0.1V$_{RE}$) (c) Trans-passive (+1V$_{RE}$)

8.4 Repassivaiton Phase

The formation of the passive film is key to the corrosion resistance of CoCrMo as it limits corrosion by acting as a shield between the alloy and the environment. Once this passive film is compromised/removed, the extremely reactive bulk alloy is exposed to the environment, so the ability of the alloy to repassivate at a high rate is vital to limit the amount of corrosion that occurs each repassivation phase. The obtained results portray that the composition of the electrolyte affects the repassivation rate, the composition of the oxide film and the quantity of metal ions released into the environment.

The quickest rate of repassivation was observed in a PBS environment due to lower obtained values of the coverage phase (τ_1) which was seen to be the dominant time constant. This could be due to the oxidising power of phosphates which help to aid the reformation of the film [88,100]. The presence of phosphate oxides were observed via XPS, which occur due to PO^{3-}_4 becoming trapped in the O^{2-} lattice sites during the growth process of the oxide [84]. This would aid in the speed of film formation as the time is not as limited by the need for the diffusion of oxygen to the surface of the alloy. The integrity of this film was also observed to be the most protective, indicated by the lowest steady-state current obtained and the highest repassivation index value. By XPS analysis, it was seen that the presence of molybdenum within this reformed film increased with lower levels of chromium. This indicates the importance that molybdenum plays in the corrosion resistance of the alloy. ICP-MS analysis noted a drastic increase in the quantity of chromium lost to the solution, which again highlights the affinity between phosphates and chromium to form phosphate chromium ion complexes (Equation 4.2). A summary of both these processes are shown in Figure 8.2.

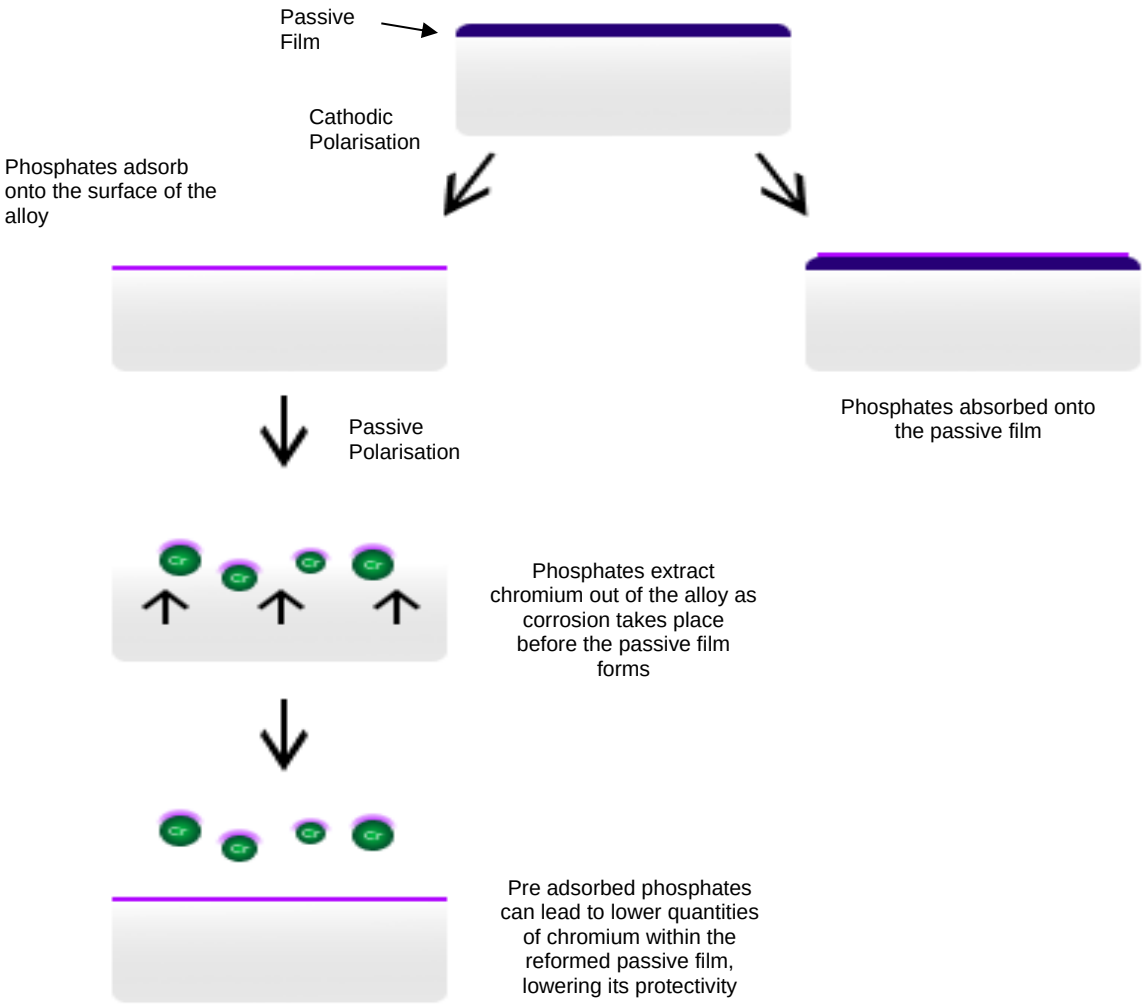

Figure 8.2 Schematic showing the process of chromium extraction in the presence of phosphates when electrochemical repassivation is undertaken against passive polarisation

BSA was seen to massively hinder the repassivation rate by inhibiting both of the coverage (τ_1) and growth (τ_2) phases of oxide formation. This would be due to inhibiting dissolved oxygen to the surface by adsorbing onto the surface; the effects are much more drastic for BSA over PBS due to the size of the molecule [92,155]. This phenomenon was seen in detail by the use of AFM, as the cathodic application gives full protein coverage. A longer τ_1 leads to enhanced levels of corrosion, explaining why the highest dissolution of CoCrMo was seen for BSA containing environments. EELS analysis also depicted that BSA molecules interfere with the repassivation phase and can even disrupt its uniformity. As the thickening of the film is reduced alongside increasing the overall porosity of film, it can account for some of the increased metal ion production from the alloy as the ions could diffuse through the newly

formed film. There is a decrease in the content of molybdenum within the film upon repassivation due to the ion now being easily accessible to the BSA molecules permitting them to simply diffuse away into the environment; this is not possible when the oxide film is intact. The process is depicted in Figure 8.3. The dissolution of this ion accounts for over 50% of the total charge lost in some cases. Over time this could have drastic effects on the performance of the alloy due to molybdenum being shown to increase the corrosion resistance and its low quantity within the alloy. There have been reported beneficial effects of BSA seen on the corrosion behaviour on CoCrMo, where Y.Yan [80] observed the formation of a biofilm that hindered metal ion released. From this project, this statement is only verified when the system is in a stable passive stable with negative effects being observed if the oxide layer is compromised/removed.

In terms of the overall rates of repassivation, J.R.Golberg and D.Sun noted that it could occur on the millisecond timescale [118,156]. However, this is very dependent on the size and complexity of the particular area under examination, with this specific study being on the whole sample and not a single scratch. When mechanical depassivation is considered, there can be other factors that needed to be accounted for, such as the deformation of the area, which may lead to changes in the corrosion potential of the surface, causing a faster rate of repassivation [168]. A scratch test is also known to leave oxide present on either side of the depassivation zone, which enables repassivation to occur via lateral growth, which isn’t possible in this project conducted.

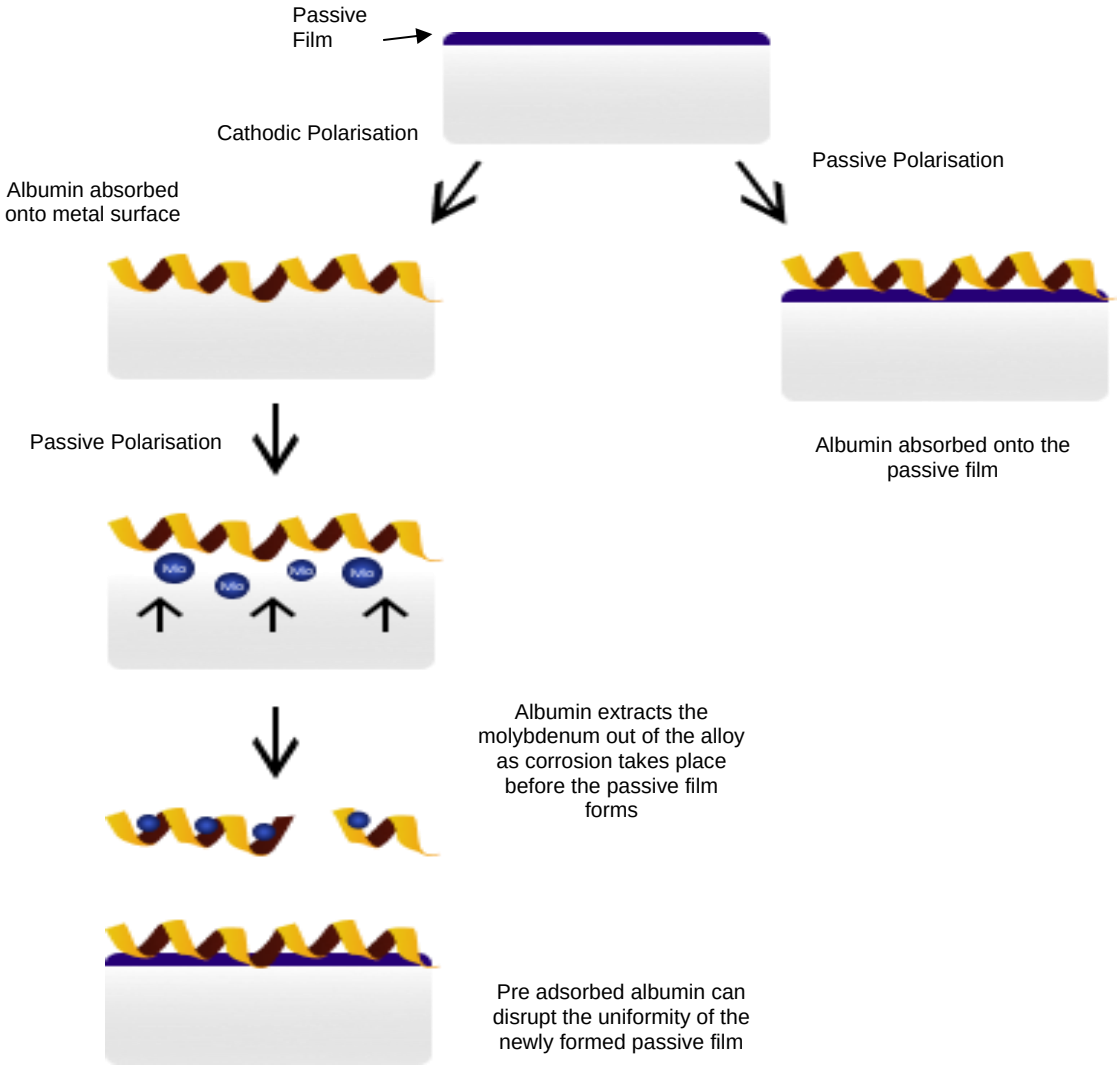

Figure 8.3 Schematic showing the process of molybdenum extraction in the presence of BSA when electrochemical repassivation is undertaken against passive polarisation. Published previously within [125]

8.5 Bodily interactions with dissolved metal ions of CoCrMo

From the use of Raman spectroscopy and Circular Dichroism, it has been clear to see that the preferential binding affinity of BSA and molybdenum stems from the binding site at which they interact. Molybdenum binds through the free Cys-34 bond-forming a highly thermodynamically favoured bond [66]. Cobalt ions bind through the NTS, MBS and Site B through weak and most likely reversible bonding. In contrast, chromium leads to structural changes within the protein through crosslinking of histidine chains.

If the environment considered was from an in-vivo perspective, being exposed to synovial fluid, then the interactions of the metal ions with cells also need to be considered. There could be other slight interactions of the metal species with other proteins present in the fluid, but as stated previously, research has shown that the metal ions bind much stronger to albumin than any other protein present [49,50]. This finding, alongside albumin being the most abundant protein present in serum and tissue fluid, implies that this protein heavily dominates any metal-protein interaction.

Cobalt (II) ions have been shown in previous research to bind strongly to cells alongside having a high affinity for proteins; this could indicate that the ion also binds to tissue cells which tend to remain localised around the implant [49,51]. This phenomenon would explain why there have been noted build up deposits of cobalt (II) around the implant [194,195].

Chromium (III) ions bind strongly to protein molecules but have little affinity for cells [50,51]. The hexavalent form has the opposite binding preferences to the trivalent form, as it has been shown to easily pass the membranes of cells but has a weak binding affinity for proteins as it lacks a specific binding site [50,51]. This form of chromium is of particular interest, however, as it is highly toxic, being classed as a class 1 carcinogen [51]. These ions are readily formed from the implant when the alloy is under transpassive conditions, which leads to the oxidation of the trivalent form to the hexavalent state. From this data, it is clear that the valency of the ion has a drastic impact on the properties of the ion; these two forms of chromium account for why there have been notable increases of the ion present within the serum (localised) as well as disseminated throughout the body [51,194].

Molybdenum is known to have specific uptake requirements to be absorbed via cells, especially when in the presence of other anions [196]. Even though studies have shown that molybdenum has the highest affinity for albumin out of the alloy constituents, the quantity released is minimal compared with the other ions due to its percentage within the alloy [102,171,197]. Although the dissolution is governed by the cobalt release, the affinity of molybdenum and albumin is of extreme importance nonetheless regarding the formation of an organic deposit [82,198,199]. The occurrence of the film stems from the high affinity of the attraction of the protein molecules with molybdenum within the alloy. Upon depassivation of the film, the bare metal is now exposed, which leads to the adsorption of albumin on the surface [81,200]. It’s important to note that this only inhibits the rate of repassivation. During the normal friction

process within the hip, this protein layer is then denatured, leading to the formation of a tribofilm, which is known to be vital to the performance of the alloy as it lowers the contribution of adhesion and abrasion to wear [79,197].

8.6 In-Vivo Application

The significance of the passive film to the resistance of the alloy has been echoed throughout this work, which is governed by its composition. Specifically, the level of chromium (III) oxide that is present which was shown in comparative data between OCP and passive induced conditions (+0.1V_{RE}). To enhance the longevity of the alloy and minimise the number of ions released into the patient, this film needs to be resistant to both repassivation (electrochemical and wear induced) and inflamed conditions. These are key features that need to be considered when designing new surfaces/materials for the use of implantation within the body.

This thesis has also highlighted the importance of the protein metal interactions in regards to the formation of the biofilm on the surface of the alloy which is key to providing an extra layer of protection to the alloy and aiding in the reduction of friction. It has been concluded that this film arises due to interactions between the Cys 34 binding site and the molybdenum ion, with cobalt and chromium interactions playing no role in film formation. To utilise the beneficial effects of this deposited organic layer to its maximum, surface engineering methods or even alterations to the composition of CoCrMo could be undertaken. An increase in molybdenum content to the alloy could ensure that the biofilm is formed in greater quantities or with higher levels of adhesion.

Chapter 9
Conclusions, Limitations and Future Work

9.1 Conclusions

A thorough analysis has been conducted on the effects of simulated bodily fluids and applied electrochemical conditions on CoCrMo. From the data attained throughout this thesis, the following conclusions have been deduced.

9.1.1 Surface properties of CoCrMo

- The passive film of CoCrMo is typically between 1 – 2 nm thick and is primarily formed of Cr(III) oxide and hydroxide, with small contributions from cobalt and molybdenum oxide.
- The effects and properties of the surface of a CoCrMo alloy are highly influenced by the composition of the surrounding electrolyte, the applied potential as well as temperature.

9.1.2 Effect of the electrolyte

Phosphates

- Reduce the rate of corrosion as they adsorb onto the surface of the alloy via chemisorption, acting as a shield between the alloy and its surroundings.
- This adsorption alters the composition of the passive film by increasing the quantity of chromium and molybdenum within the oxide film at the expense of cobalt. Its presence leads to a higher level of BSA adsorption.
- Tend to reduce the number of metal ions released as they adsorb onto the surface inhibiting ion flow.

BSA

- The effects of albumin are two-fold: it can inhibit the access of oxidants to the alloy leading the adsorbed organic layer/passive film to be weaker, increasing the corrosion rate but can alter the passive film due to the molecule being a cathodic inhibitor increasing the resistance of corrosion in the passive domain. The molecule also adsorbs onto the surface via chemisorption.
- BSA adsorbs onto the surface of the alloy via the side-on model; the layer is typically 4nm thick, suggesting it is only one monolayer thick. This adsorption enhances the rate of corrosion by promoting the

electron transfer process. Alterations to the composition of the passive film are also observed, increasing the quantity of molybdenum within the film due to supposed high affinity.

- The presence of albumin leads to increased dissolution of molybdenum from the alloy. The higher the concentration of molybdenum, the greater the effect.

9.1.3 Effect of applied domain

Cathodic Domain (-1.0V_{RE})

- Current is determined from the reduction oxygen reaction, which leads to major/complete reduction of the oxide film.
- Almost halts any dissolution of the alloy by negatively polarising the metal.
- Observe the highest level of BSA deposition, indicating that the adsorption process is dominated via hydrophobic interactions.

OCP

- There is an oxide film formed that protects the alloy. The thickness of the film is between 0.5-1.0nm for the environments analysed.
- The oxide film restricts the flow of ion movement, leading to reduced metal ion loss.

Passive (+0.1V_{RE})

- Passive domain (+0.1V_{RE}), a thicker oxide film is formed, which enhances the corrosion resistance of the alloy. The thicknesses obtained were between 1.0-1.8nm.
- The thicker oxide film restricts the flow of ion movement, even more, leading to reduced metal ion loss.
- Deposition of BSA occurs agglomerates on small fractions of the alloy.

Transpassive Domain (+1.0V_{RE})

- There is a presence of a non-barrier layer; the oxide film is broken down under these conditions, with localised corrosion occurring on the surface.
- It gives off a high amount of metallic ions due to no protective film being present, so corrosion readily occurs.
- Only small levels of BSA deposition suggests the BSA prefers to bind to metal ions that are released into the solution.

9.1.4 Effect of Temperature

- An increase in temperature increases the rate of the corrosion rate of CoCrMo alongside increasing the cathodic reaction rates.

9.1.5 Repassivation Process

- The rate of repassivation has been noted to vary with the environment in which it occurs, the fastest repassivation rate was observed in a phosphate-containing environment, whereas the presence of BSA, leads to slower repassivation rates seeing as the oxidant is being inhibited due to the proteins size which blocks the active sites on the surface. Repassivation under a higher passive potential leads to a higher rate of coverage but has little/no effect on the growth phase.
- The higher the rate of repassivation, the less ion dissolution occurs as the alloy is exposed less to the environment. In the presence of phosphates, the overall dissolution is lower, although there is an increased percentage of chromium lost due to these ions being drawn to the surface when the cathodic-passive transition occurs. Albumin is seen to increase the over dissolution, with massive increases seen in the quantity of molybdenum released as they complex favourably over the other metallic ions present.
- The effect of repassivation can alter the reformation of the passive film, depending on the contents of the electrolyte.
    - Phosphates lead to an increase of chromium and molybdenum within the passive film.
    - BSA increases the quantity of chromium within the film even further but leads to a decrease in molybdenum content as the protein can extract the ion into the solution. It appears to also interfere with the consistency of the film.

9.1.6 Interactions between BSA and the dissolved metal ions from CoCrMo

- The possible protein-metal ion interactions that can occur are as follows:
    - Cobalt ions can bind to the NTS, MBS and Site B of the protein molecule due to it being a versatile ion.
    - Chromium ions cause the formation of a hydrogel by forming protein aggregates due to crosslinking of histidine residues.

- Molybdenum ions bind to the Cys-34 binding site of the molecule; this is highly thermodynamically favoured due to the formation of a Mo-S bond.

9.2 Limitations

This research has provided some key foundations and novel findings into the corrosion behaviour of CoCrMo; however, there are a few general limitations that need to be highlighted. Limitations with the repassivation investigation were addressed previously within Section 3.3.3.2.1.

- **Electrolyte Composition** - In total bovine serum contains around 22 unique proteins. The focus of this study was on BSA, which is present in the highest concentration and possesses high mobility. However, this study does not take into account how other protein species and differing protein-protein interactions affect both the corrosion resistance of the alloy and its dissolution rate.
- **Tribological processes** - In-vivo, there is simultaneous action of both mechanical and corrosion processes. This study has specifically focused on just the electrochemical processes that occur to get a clear understanding of the fundamentals. The use of tribology and electrochemistry must be looked at simultaneously to obtain a more realistic picture of how these interactions work.
- **Metal ion binding to BSA** – From the metal ions that can bind with BSA from CoCrMo, the molybdenum ion was deduced to possess the highest affinity due to ICP-MS work undertaken in this research and the literature. A competition study between the possible ions (Co, Cr, Mo) in realistic quantities and BSA must be done separately to confirm these results.

9.3 Future Work

The work conducted in this thesis has helped provide a complete overview of electrochemical interactions of CoCrMo with simulated bodily environments. Giving a deeper insight into how protein molecules interact with CoCrMo and the dissolved ions that the alloy produces over its lifetime. However, further studies are vital to seeing how these results can complement more realistic processes and predict in vivo performance.

- **Realistic Environment** – As stated within the limitations, a more realistic electrolyte and processes that the alloy experience could be incorporated to thoroughly examine how each component affects the corrosion resistance and ion release of the alloy. This study was focused on the interactions of BSA, which is present in the highest concentration and possesses high mobility so arrives first at the implant determining the majority of surface/environment interactions. However, bovine serum has 22 unique proteins, so this study doesn't take into account how other protein species and differing protein-protein interactions influence the corrosion behaviour of the alloy. Comparisons of a biofilm and a tribofilm would also be intriguing, as maybe the wear denatured protein can interact with the alloy and its ions in different ways.
- **Other Comparable Alloys** – This study was carried out only on LC CoCrMo; electrochemical analysis on HC CoCrMo would build up a comparison profile on how the quantity of carbon within the alloy affects the corrosion behaviour of the alloy and its interactions with the surrounding environment. An increase in carbon content would lead to the formation of different carbides alongside increasing their quantity formed leading to further strengthening of the alloy. The presence of these species could lead to differences within passive film and biofilm formation on the alloy.
- **Long Term Effects** – Research into changes of the passive film after multiple electrochemical repassivation phases would provide an insight into long term implantation. Creating a profile on the molybdenum content would be interesting to observe if the content will keep reducing after multiple phases or if a plateau is established.
- **Ellipsometry** – By using in-situ ellipsometry a profile of the thickness of the oxide and protein film formation could be monitored as a function of time. This technique would be able to determine the differences in thickness of the oxide film under various electrochemical conditions and clarify the extent of oxide film removal that occurs under cathodic conditions. The rate of protein deposition and overall thickness on the surface of the alloy would help consolidate the conditions where protein interactions are favoured.
- **XPS Etching** – An interesting find of this thesis was that BSA could interfere and disrupt the uniformity of a reformed oxide film. The use of XPS etching would provide key insights into this feature, providing

scans of the composition of the passive film every 10th of a nanometer to see the extent of the disruption alongside building up a depth profile of a passive and reformed oxide film.

List of References

1. National Joint Registry. National Joint Registry for England and Wales: 17th Annual Report 2020. Date Last Accessed (15/2/2021) https://bit.ly/3bnKvwL
2. National Institute for Health and Clinical Excellence. Osteoarthritis: the care and management of osteoarthritis. Date Last Accessed (5/10/2020) https://bit.ly/2F0yFw6.
3. A. Balamurugan, S. Rajeswari, G. Balossier, A.H.S Rebelo, J.M.F Ferreira," Corrosion aspects of metallic implants – an overview," Materials and Corrosion, 2008, 59, pp. 855-869
4. A.G. Cobb, T.P Schmalzried," The clinical significance of metal ion release from cobalt-chromium metal-on-metal hip joint arthroplasty," Journal of Engineering in Medicine, 2006, 220, pp. 385-398
5. MHRA. Medical Device Alert: All metal-on-metal (MoM) hip replacements 2012. Date Last Accessed (19/01/2021) https://bit.ly/3oXLadJ
6. FDA. Concerns about Metal-on-Metal Hip Implants. Date Last Accessed (19/01/2021) https://bit.ly/2Kt7z3D
7. G. Manivasagam, D. Dhinasekaran, A. Rajamickam," Biomedical implants: corrosion and its preventions – a review," Recent Patents on Corrosion Science, 2010, 2, pp. 40-54
8. M. Roberts," Rise in hip replacements for under '60s," 2016, BBC News. Date Last Accessed (13/7/2020) https://bbc.in/36MU2MZ
9. S.M. Kurtz, E. Lau, K. Ong, K. Zhao, M. Kelly, K.J. Bozic," Future young patient demand for primary and revision joint replacement: national projections from 2010 to 2030," Clin Orthop Relat Res, 2009, 467(10), pp. 2606-2612
10. H. Derer, M. Shahinpoor," Recent patents and designs on hip replacement prosthesis," The Open Biomedical Engineering Journal, 2015, 9, pp. 92-102
11. D. Snyder, R. Chapell, W. Bruening, K. Schoelles, J. Kaczmarek, E. Kuserk, E. Errinoff," Horizon scan on hip replacement surgery," Agency for Healthcare Research and Quality, 2006
12. J. Foran," Total hip replacement," 2020, OrthoInfo: American Academy of Orthopaedic Surgeons. Date Last Accessed (13/7/2020) Reproduced with permission from OrthoInfo. © American Academy of Orthopaedic Surgeons. https://bit.ly/3nBvDzM

13. S.R. Knight, R. Aujlia, S.P Biswas," Total hip arthroplasty – over 100 years of operative history," Orthopeadic Reviews, 2011, 3(2), 16
14. London Implant Retrieval Centre. Patient Information. Date Last Accessed (23/8/2020) https://bit.ly/2GNHNFm
15. G.K. McKee, J. Watson-Farrar," J. Replacement of arthritic hips by the McKee-Farrar prosthesis," JBJSBr, 1966, 48-B(2), pp. 245-259
16. P. King," Complete replacement arthroplasty of the hip by the ring prosthesis," JBJSBr, 1968, 50(B), pp. 720-731
17. J. Charnley," Arthroplasty of the hip. A new operation," The Lancet, 1961, 1(7187), pp. 1129-1132
18. E. Riska," Ceramic endoprosthesis in total hip arthroplasty," Clinical Orthopeadics, 1993, 297, pp. 87-94
19. J. Foran," Total hip replacement," 2020, OrthoInfo: American Academy of Orthopaedic Surgeons. Date Last Accessed (13/7/2020)
20. Y. Dong, T. Li, K. Xiao, Y.Y. Bian, X. Weng," Ceramic on ceramic or ceramic-on-polyethylene for total hip arthroplasty: A systemic review and meta-analysis of prospective randomized studies," Chin Med J, 2015, 128(9), pp. 1223 – 1231
21. D. Cash, V. Khanduja," The case for ceramic-on-polyethylene as the preferred bearing for a young adult hip replacement," Hip Int, 2014, 24(5)
22. S. Affatato, M. Goldoni, M. Testoni, A. Toni," Mixed oxides prosthetic ceramic ball heads. Part 3: effect of the ZrO_2 fraction on the wear of ceramic on ceramic hip joint prostheses. A long term in vitro wear study," Biomaterials, 2001, 22(7), pp. 717 – 723
23. P. Sury, M. Semlitsch," Corrosion behaviour of cast and forged cobalt based alloys for double-alloy joint endoprosthesis," Journal of Biomedical Materials Research, 1978, 12, pp. 723-741
24. Y. Yan, A. Neville, D. Dowson," Tribo-corrosion properties of cobalt-based medical implant alloys in simulated biological environments," Wear, 2007, 263(7), pp. 1105-1111
25. M. Bryant, A. Neville," Corrosion and mechanical properties," Orthopaedics and Trauma, 2016, 30:3, pp. 176-191
26. Z. Wang, Y. Yan, L. Qiao," Protein adsorption on implant metals with various deformed surfaces," Colloids and Surfaces B: Biointerfaces, 2017, 156, pp. 62 – 70

27. R. Varano, J. Bobyn, J. Medley, S. Yue,” The effect of microstructure on the wear of cobalt based alloys used in the metal-on-metal hip implants,” Proc Inst Mech Eng H, 2005, 220, pp. 145-159
28. R. Pourzal, R. Theissmann, M. Morlock, A. Fischer,” Microstructural alterations within different areas of articulating surfaces of a metal-on-metal hip resurfacing system,” Wear, 2009, 267, pp. 689-694
29. M.G. Miciuna, P.Vizureanu, D.C.Achitei, N. Ghiban, A.Sandu, N. Forna,” Structural characterization of some CoCrMo alloys with medical applications,” Rev.Chim, 2014, 65(3), pp. 335-338
30. I. Milosev, H.H Strenblow,” The composition of the surface passive film formed on CoCrMo alloy in simulated physiological solution,” Electrochimica Acta, 2003, 48(19), pp. 3767-2774
31. G. Cui, S. Li, H. Liu, G. Gao,” Effect of carbon on the microstructure and sliding wear performance of CoCrMo matrix composites from room temperature to 1000^{o}C,” J Mater Res Technol, 2019, 8(5), pp. 4778-4787
32. E. Bettini, T. Eriksson, M. Bostrom, C. Leygraf, J. Pan,” Influence of metal carbides on dissolution behaviour of biomedical CoCrMo alloy: SEM, TEM and AFM studies,” Electreochimica Acta, 2011, 56, pp. 9413-9419
33. J.A Disegi, L. Eschbach,” Stainless steel in bone surgery,” Injury, 2000, 31, pp. D2-D6
34. M. Zhang,” Biocompatibility of material,” 2004, Heidelberg: Spring-Verlag
35. K. Yang, Y. Ren,” Nickel-free austenitic stainless steels for medical applications,” Sci Technol Adv Mater, 2010, 11(1), pp. 1-13
36. T. Ma, P. Wan, Y. Cui, G. Zhang, J. Li, J. Liu, Y. Ren, K. Yeng, L.Lu,” Cytocompatibility of high nitrogen nickel-free stainless steel for orthopedic implants,” J. Mater. Sci. Technol, 2012, 28(7), pp. 647-653
37. A. Yamamoto, Y. Kohyama, D. Kuroda, T. Hanawa,” Cytocompatibility evaluation of Ni-free stainless steel manufactured by nitrogen adsorption treatment,” Materials Science and Engineering: C, 2004, 24(6-8), pp. 737-743
38. H. Wilert, L. Broback, G. Buchhorn, P. Jensen, G. Koster, I. Lang, P. Ochsner, R. Schenk,” Crevice corrosion of cemented titanium alloy stems in total hip replacements,” Clin Orthop Relar Res, 1996, 333, pp. 333-351

39. M. Semlitsch,” Titanium alloys for hip joint replacements,” Clinical Materials, 1987, 2(1), pp. 1-13
40. C.N. Elias, J.H.C. Lima, R. Valiev, M.A. Meyers,” Biomedical applications of titanium and its alloys,” JOM, 2008, pp. 46-48
41. P. B Tchounwou, C. G Yedjou, A.K Patolla, D.J Sutton,” Heavy metals toxicity and the environment,” Experientia Supplementum, 2012, 101, pp. 131-164
42. I. Catelas, J. Bobyn, J. Medley, J. Krygier, D. Zukor, O. Huk,” Size, shape, and composition of wear particles from metal-metal hip simulator testing: effects of alloy and number of loading cycles,” Journal of Biomedical Materials Research Part A, 2003, 67(1), pp. 312 – 327
43. J. Drummond, P. Tran, C. Fary,” Metal-on-metal hip arthroplasty: a review of adverse reactions and patient management,” J Funct Biomater, 2015, 6(3), pp. 486-499
44. B. H. Bosker, H.B. Ettema, M. Rossum, M.F. Boomsma, B.J. Kollen, M.Maas, C. Verheyen,” Pseudotumor formation and serum ions after large head metal-on-metal stemmed total hip replacement. Risk factors, time course and revisions in 706 hips,” Arch Orthop Trauma Surg, 2015, 135, pp. 417-425
45. K. Yukata, S. Nakai, T. Goto, Y. Ikeda, Y. Shimaoka, I. Yamanaka, K. Sairyo, J.I. Hamawaki,” Cystic lesion around the hip joint,” World J Orthop, 2015, 6(9), pp. 688-704
46. G. Matharu, A. Judge, D. Murray, H. Pandit,” Prevalence of and risk factors for hip resurfacing revision a cohort study into the second decade after the operation,” The Journal of Bone and Joint Surgery, 2016, 98(17), p. 1444-1452
47. K. Czarnek, S. Terpilowska, A.K. Siwicki,” Selected aspects of the action of cobalt ions in the human body,” Cent Eur J Immunol, 2015, 40(2), pp. 236-242
48. L. Leyssens, B. Vinck, C. Straeten, F. Wuyts, L. Maes,” Cobalt toxicity in humans – a review of the potential sources and systemic health effects,” Toxicology, 2017,387, pp. 43-56
49. J. Yung, J. Black,” Competitive binding of chromium, cobalt and nickel to serum proteins,” Biomaterials, 1994, 15, pp. 262-268
50. K. Merrit, S.A. Brown, N.A. Sharkey,” The binding of metal salts and corrosion products to cells and proteins in vitro,” J.Biomed.Master.Res, 1984, 18, pp. 1005-1015

51. G. Afolaranmi, J. Tetty, R. Meek, M. Grant," Release of chromium from orthopeadic arthroplasties," Open Orthop J, 2008, 2, pp. 10-18
52. L.E. Eiselstein, D.M. Proctor, T.C. Flowers," Trivalent and hexavalent chromium issues in medical implants," Materials Science Forum Vols, 2007, 539-543, pp. 698-703
53. A. Vyskocil, C. Viau," Assessment of molybdenum toxicity in humans," Appl Toxicol, 1999, 19(3), pp. 185-192
54. P. Matsumoto," Trends in Ionization energy of transition-metal elements," Journal of Chemical Education, 2005, 82(11), pp. 1660 – 1661
55. V. Zviagin," Ellipsometric determination of cation disorder in magnetically ordered spinal ferrite thin films," PhD Thesis, Leipzig University, 2019
56. P. Atkins," Inorganic Chemistry," Oxford University Press, 5th Edition, 2010, Chapter 7, 19
57. N. Eliaz," Corrosion of Metallic Biomaterials: a review," Materials, 2019, 12(3):407
58. A. Fam, G. Lawry, H. Kreder," Anatomy of joints general considerations and principles of joint extraction," Musculoskeletal Examination and Joint Injection Techniques, 2006, Mosby, Ch.1
59. A. Burkandt, A. Katzer, K. Thaler, V. Baehr, R.E. Friedrich, W. Ruther, M. Amling, J. Zustin," Proliferation of the synovial lining cell layer in suggested metal hypersensitivity," In Vivo, 2011, 25, pp. 679-686
60. P.A. Lalor, P.A. Revell," The presence of a synovial layer at the bone-implant interface: An immunohistological study demonstrating the close similarity to true synovium," Clin. Mater, 1993, 14, pp. 91-100
61. M. Kung, J. Markantonis, S. Nelson, P. Campbell," The synovial lining and synovial fluid properties after joint arthroplasty," Lubricants, 2015, 3, pp. 394-412
62. M. Talha, Y. Ma, P. Kumar, Y. Lin, A. Singh," Role of protein adsorption in the bio corrosion of metallic implants – a review," Colloids and Surfaces B: Biointerfaces, 2019, 176, pp. 494-506
63. F. Ding, W. Peng," Biological activity of natural flavonoids as impacted by protein flexibility: an example of flavonoids," Mol. Biosyst, 2015, 11, pp. 1119-1133
64. M.X. He, D. Carter," Atomic structure and chemistry of human serum albumin," Nature, 1992, 258, pp. 4377-4387

65. T. Topala, A. Bodoki, L. Oprean, R. Oprean," Bovine serum albumin interactions with metal complexes," Clujjul Med, 2014, 87(4), pp. 215-219
66. W. Bal, M. Sokolowska, E. Kurowska, P. Faller," Binding of transition metal ions to albumin: sites, affinities and rates," Biochimica et Biophysica Acta, 2013, 1830, pp. 1687-1690
67. E. Martins, T. Drakenberg," Cadmium (II), zinc (II), and copper(II) ions binding to bovine serum albumin. A ^{113}Cd NMR study," Inorganica Chimica Acta, 1982, 67, pp. 71-74
68. P.J Sadler, J.H Viles," ^{1}H and ^{113}Cd NMR invesigations of $Cd^{(2+)}$ and $Zn^{(2+)}$ binding sites on serum albumin: competition with $Ca^{(2+)}$, $Ni^{(2+)}$, $Cu^{(2+)}$, and $Zn^{(2+)}$," Inorg Chem, 1996, 35, pp. 4490-4496
69. G. Navarra, A. Tinti, M. Leone, V. Militello, A. Torreggiani," Influence of metal ions on the thermal aggregation of bovine serum albumin: aggregation kinetics and structural changes," Journal of Inorganic Biochemistry, 2009, 103(12), pp. 1729-1738
70. W. Bal, J. Christodoulou, P.J Sadler, A. Tucker," Multi-metal binding site of serum albumin," J. Inorg. Biochem, 1998, 70, pp. 33-39
71. G. Fanali, Y. Cao, P. Ascenzi, M. Fasano," Mn(II) binding to human serum albumin: A ^{1}H-NMR relaxometric study," J.Inorg. Biochem, 2012, 117, pp. 198-203
72. E. Mothes, P. Faller," Evidence that the principal Co(II) binding site in human serum albumin is not at the N-terminus: implication on the albumin cobalt binding test for detecting myocardial ischemia," Biochemistry, 2007, 46, pp. 2267-2274
73. P. Silva-Bermudez, S.E. Rodil," An overview of protein adsorption on metal oxide coatings for biomedical implants," Surface and Coatings Technology, 2013, 233, pp. 147-158
74. A. Carre, V. Lacarriere," How substrate properties control cell adhesion. A physical-chemical approach," 2010, 24(5), pp. 815-830
75. M. Talha, Y. Ma, P. Kumar, Y. Lin, A. Singh," Role of protein adsorption in the bio corrosion of metallic implants – a review," Colloids and Surfaces B: Biointerfaces, 2019, 176, pp. 494-506
76. Y. Liao, R. Pourzal, M.A Wimmer, J.J Jacobs, A. Fischer, L.D Marks," Graphitic tribological layers in metal-on-metal hip replacements," Science, 2011, 344, pp. 1687-1690

77. M.A Wimmer, J. Loos, R. Nassutt, M. Heitkemper, A. Fischer," The acting wear mechanisms on metal-on-metal hip joint bearings: in vitro results," Wear, 2001, 250, pp. 129-
78. M.P Heuberger, M.R Widmer, E. Zobeley, R. Glockshuber, N.D Spencer," Protein-mediated boundary lubrication in arthroplasty," Biomaterials, 2005, 26, pp. 1165-1173
79. M.A Wimmer, C. Sprecher, R. Hauert, G. Tager, A. Fischer," Tribochemical reaction on metal-on-metal hip joint bearings – a comparison between in-vitro and in-vivo results," Wear, 2003, 255, pp. 1007-1014
80. Y.Yan, A. Neville, D. Dowson," Biotribocorrosion of CoCrMo orthopeadic implant materials-accessing the formation and effect of the biofilm," Tribology International, 2007, 40, pp. 1492-1499
81. Y. Li, C. Shi, L. Guan, Y. You, W. Tang," Correlation between protein adsorption and electrochemical corrosion behaviour of niobium for bio-implant application," Journal of Solid State Electrochemistry, 2020, 24, pp. 1325-1336
82. E. Martin, R. Pourzal, M. Mathew, K. Shull," Dominant role of molybdenum in the electrochemical deposition of biological macromolecules on metallic surfaces," Langmuir, 20013, 29, pp. 4812-4822
83. S. Tait, "An introduction to electrochemical corrosion testing for practicing engineers and scientists," 1994, Pair O Docs Pubns
84. D. Landolt," Corrosion and Surface Chemistry of Metals," 2007, EPFL Press
85. R. Beadling," Biotribocorrosion of hard-on-hard bearing surfaces in orthopaedic hip replacements," PhD Thesis: University of Leeds
86. D. Talbot, J. Talbolt," Corrosion science and technology," 2007, 2nd Edition, Boca Raton: CRC Press
87. P. W. Atkins, J.D. Paula," Physical Chemistry," Oxford University Press, 2006, 8th Ed, Ch. 24-25
88. C. Vidal, A. Juan, A. Munoz," Adsorption of bovine serum albumin on CoCrMo surface: effect of temperature and protein concentration," Colloids and Surfaces B: Biointerfaces, 2010, 80, pp. 1-11
89. P. Saha, S. Chowdhury," Insight into adsorption thermodynamics," Thermodynamics, 2011, pp. 349-364
90. F. Bentiss, M. Lebrini, M. Lagrenee," Thermodynamic characterization of metal dissolution and inhibitor adsorption processes in mild steel/2,5-

bis(n-thienyl)-1,3,4-thiadiazoles/hydrochloric acid system," Corrosion Science, 2005, 47, pp. 2915-2931
91. M. Fontana, N. Greene," Corrosion Engineering," 1967, New York, Mc Graw Hill
92. S. Virtanen, I. Milosev, E. Gomez-Barrena, R. Trebse, J. Salo, Y.T Konttinen," Special modes of corrosion under physiological and simulated physiological conditions," Acta Biomaterialia, 2008, 4, pp. 468-476
93. M. Sivakumar, U. Mudali, S. Rajeswari," Investigation of failures in stainless steel of orthopaedic implant devices: fatigue failure due to improper fixation of a compression bone plate," Journal of Materials Science Letters, 1994, 13, pp. 142-145
94. H.H Uhlig, I.M Feng, W. Tierney, A.McClellen," A fundamental investigation of fretting corrosion," National Advisory Committee for Aeronautics, 1953
95. S.W Watson, F.J Friedersdorf, B.W Madsen, S.D Cramer," Methods of measuring wear-corrosion synergism," 1995, Wear, 2, pp. 476-484
96. Z.R Muslim, A. Abbas," The effect of pH and temperature on corrosion rate stainless steel 216L used as a biomaterial," International Journal of Basic and Applied Science, 2015, 4(2)
97. D. Sun, J.A Wharton, R.J.K Wood," Effects of proteins and pH on tribocorrosion performance of cast CoCrMo – a combined electrochemical and tribological study," Tribology – Materials, Surfaces and Interfaces, 2008, 2:3, pp. 150-160
98. C. Liu, Y. Zhang, C. Zhang, W. Wang, W. Huang, P. Chu," Synergistic effect of chloride ion and albumin on the corrosion of pure magnesium," Front Mater Sci, 2014, 8(3), pp. 244-255
99. Y. Hedberg, X. Wang, J. Hedberg, M. Lundin, E. Blomberg, I. Wallinder," Surface-protein interactions on different stainless steel grades: effects of protein adsorption, surface changes and metal releases," J Mater Sci: Mater Med, 2013, 24, pp. 1015-1033
100. A. Munoz, S. Mischler," Interactive effects of albumin and phosphate ions on the corrosion of CoCrMo implant alloy," Journal of the Electrochemical Society, 2007, 154(10), pp. C562-C570
101. Y.Yan, H. Yang Y. Su, L. Qiao," Albumin adsorption on CoCrMo alloy surfaces," Sci Rep, 2015, 5:18403

102. N. Espallargas, C. Torres, A. Munoz," A metal ion release study of CoCrMo exposed to corrosion and tribocorrosion conditions in simulated body fluids," Wear, 2015, 332-33, pp. 669-678
103. R.L Williams, D.F Williams," Albumin adsorption on metal surfaces," Biomaterials, 1998, 9, pp. 206-212
104. C. Vidal, A. I Munoz," Electrochemical aspects in biomedical alloy characterisation: electrochemical impedance spectroscopy," Intech, 2011, 13, pp. 283-306
105. R. Namus, J. Nutter, J. Qi, W. Rainforth," The influence of protein concentration, temperature and cathodic polarisation on the surface status of CoCrMo biomedical grade alloys," Applied Surface Science, 2020, 499. 143908
106. C.T Chu, P.D Fuqua, J.D Barrie," Corrosion characterisation of durable silver coatings by electrochemical impedance spectroscopy and accelerated environmental testing," Applied Optics, 2006, 45(7), pp. 1583-1593
107. M.H Metikos, Z. Pilic, R. Babic, D. Omanovic," Influence of alloying elements of the corrosion stability of CoCrMo implant alloy in hank's solution," Acta Biomaterialia, 2006, 2(6), pp. 693-700
108. J.A Helsen, H.J Breme," Metals as biomaterials," John Wiley and Sons, Ltd, 1998
109. P. Zeng, W.M. Rainforth, R.B. Cook," Characterisation of the oxide film on the taper interface from retrieved large diameter metal on polymer modular total hip replacements," Tribology International, 2014, 89, pp. 86-96
110. L. Wang, A. Shinbine, J. Luo," Electrochemical behavior of CoCrMo implant in Ringer's solution," Surf. Interface Anal, 2013, 45, pp. 1323-1328
111. C. Vidal, A.I. Munoz, C. Olsson, S. Mischler," Passivation of a CoCrMo PVD alloy with biomedical composition under simulated physiological conditions studied by EQCM and XPS," Journal of The Electrochemical Society, 2012, 159(5), pp. C233-243
112. K.K Aligizaki, D.D Macdonald," Diagnostics analysis of the growth of passive films on aluminium," Electrochemical Society Proceedings, 2000, 23, pp. 211-219
113. E. Skikora, D. D Macdonald," Defining the passive state," Solid State Ionics, 1997, 94, pp. 141-150

114. T. Hoar,” The production and breakdown of the passivity of metals,” Corrosion Science, 1967, 94, pp. 341-355
115. K.E Heusler, L. Fischer,” Kinetics of pit initiation at the alloy Fe_5Cr,”Materials and Corrosion, 1976, 27(11), pp. 788-791
116. D. Landolt, S. Mischler, M. Stemp,” Electrochemical methods in tribocorrosion: a critical appraisal,” Electrochimica Acta, 46, 2001, pp. 3913 – 3929
117. S. Mischler, A. Munoz,” Wear of CoCrMo alloys used in metal-on-metal hip joints: A tribocorrosion appraisal,” Wear, 297, 2013, pp. 1081 - 1094
118. J. Ambrose,” Repassivation Kinetics,” Treatise on Materials Science and Technology, 1983, 23, pp. 175-204
119. J. Gilbert,” Electrochemical behaviour of metals in the biological mileu,” Comprehensive Biomaterials II, 2017, Ch 2
120. J.R Goldberg, J.L Gilbert,” Electrochemical response of CoCrMo to high speed fracture of its metal oxide using an electrochemical scratch test method,” Division of Biological Materials and Department of Biomedical Engineering, 1997, 27(3), pp. 421-431
121. D. Sun, J.A Wharton, R.J.K Wood,” Abrasive size and concentration effects on the tribo-corrosion off cast CoCrMo alloy in simulated bodily fluids,” Tribology International, 2009, 42, pp. 1595-1604
122. J. Lee,” Effects of alloying elements, Cr, Mo and N on repassivation characteristics of stainless steels using the abrading electrode technique,” Materials Chemistry and Physics, 2006, 99(2-3), pp. 224-234
123. J. Sin,” Investigation of the corrosion and tribocorrosion behaviour of metallic biomaterials,” PhD Thesis: Lulea University of Technology, 2015
124. G. Berry, J. Bolton, J. Brown, S. McQuaide,” The production and properties of wrought high carbon Co-Cr-Mo alloys,” Cobalt-Base Alloys for Biomedical Applications, ASTM STP 1365, 1999
125. B. Thornley, R. Beadling, M. Bryant, A. Neville,” Investigation of the repassivation process of CoCrMo in simulated biological fluids,” Corrosion, 2020, 76, pp. 538-552
126. S. Rahdar, A. Rahdar, S. Ahmadi, J. Trant,” Adsorption of bovine serum albumin (BSA) by bare magnetite nanoparticles with surface oxidative impurities that prevent aggregation,” Can J Chem, 2019, 97, pp. 577-583

127. D. Enos, L. Scribner," The potentiodynamic polarisation scan," Solartron Analytical – Technical Report 33," 1997, 2, pp. 1-13
128. Y.Yan," Corrosion and tribo-corrosion behaviour of metallic biomaterials," PhD Thesis: The University of Leeds, 2006
129. A.F Alhosseini, N. Attarzadeh," The mechanism of transpassive dissolution of AISI 321 stainless steel in sulphuric acid solution," International Journal of Electrochemistry, 2011, 10, pp. 40-61
130. A. Salman," Application of nanomaterials in environmental improvement," Intech, 2020, ch 6
131. Gatan," 4D STEM," Date Last Accessed (21/07/2020) https://bit.ly/3kkBdVg
132. Crystallography Open Database. Last Accessed (11/02/2021) https://bit.ly/2RzZg9v
133. J. Verbeeck, S. Hens, P. Potapov, S. Schryvers," Electron energy loss spectrometry," Encyclopedia of Analytical Science (2nd Edition), 2005, pp. 324-331
134. R. Brydson," Electron energy loss spectroscopy," BIOS Scientific Publishers, 2000
135. EELS Data Base. Last Accessed (11/02/2021) https://bit.ly/373ysDk
136. J.F Watts, J. Wolstenholme," An introduction to surface analysis by XPS and AES," 2003, Jon Wiley and Sons
137. A. V. Naumkin, A. Kraut-Vass, S.W. Gaarenstroom, C.J. Powell," NIST X-ray photoelectron spectroscopy database," NIST Standard Reference Database 20, Version 4.1
138. A. Downes, A. Elfick," Raman spectroscopy and related techniques in biomedicine," Sensors 2010, pp. 1871-1889
139. G. Socrates," Infrared and Raman characteristic group frequencies: tables and charts," Wiley ed. 3, 2004
140. C. Wang, C. Huang, L. Lin, W. Chen," The effect of disulfide bonds on protein folding, unfolding and misfolding investigated by FT-Raman spectroscopy," J. Raman Spectrosc, 2016, 47, pp. 940-947
141. C. David, S. Foley, M. Enescu," Protein S-S bridge reduction: a Raman and computational study of lysozyme interaction with TCEP," Physical Chemistry Chemical Physics, 2009, 11, pp. 2532-2542
142. C. Wiedemann, P. Bellstedt, M. Gorlach," CAPITO – a web server based analysis and plotting tool for circular dichroism data," Bioinformatics, 2013, 29, pp. 1750-1757

143. A. Munoz, C. Vidal," Influence of electrochemical conditions on CoCrMo behaviour in simulated body fluid by step polarisation technique," ECS Transactions, 2010, 28(24), pp. 23-25
144. E. Bettini, C. Leygraf, J. Pan," Nature of current increase for a CoCrMo alloy: transpassive dissolution vs water oxidation," Int.J.Electrochem.Sci, 2013, 8, pp. 11791-11804
145. M. Pourbaix," Electrochemical corrosion of metallic biomaterials," Biointeractions, 1984, 5, pp. 122-134
146. T. Szauer, A. Brandt," Adsorption of oleates of various amines on iron in acidic solution," Electrochimica Acta, 1981, 26(9), pp. 1209-1217
147. G. Gece," Drugs: a review of promising novel corrosion inhibitors," Corrosion Science, 2011, 53, pp. 3873-3898
148. B. Mertwn, A. Skaja, D. Tordanato, D. Little," Re-evaluating electrochemical impedance spectroscopy for the field inspector's toolbox: a first approach," Corrosion and anti-corrosives, 2014
149. A.F Alhosseini, N. Attarzadeh," The mechanism of transpassive dissolution of AISI 321 stainless steel in sulphuric acid solution," International Journal of Electrochemistry, 2011, 10, pp. 40-61
150. D. Macdonald," On the tenuous nature of passivity and its role in the isolation of HLNW," Journal of Nuclear Materials, 2008, 379, pp. 24-32
151. D. Jones, N.Greene," Electrochemical measurement of low corrosion rates," Corrosion, 1996, 22(7), pp. 198-205
152. M. Haeri, S. Goldberg, J.L Gilbert," The voltage-dependant electrochemical impedance spectroscopy of CoCrMo medical alloy using time-domain techniques: generalized Cauchy-Lorentz, and KWW- Randles functions describing non-ideal interfacial behaviour," Corrosion Science, 2011, 53, pp. 582-588
153. X. Cheng, S.G Roscoe," Corrosion behaviour of titanium in the presence of calcium phosphate and serum proteins," Biomaterials, 2006, 25, pp. 7350-7356
154. D. Sun, J.A Wharton, R.J.K Wood," Micro-and nano-scale tribo-corrosion of cast CoCrMo," Tribol Lett, 2011, 41, pp. 525-533
155. S. Pyun, E. Lee," Effect of halide ion and applied potential on repassivation behaviour of Al-1wt.%Si-0.5wt.%Cu alloy," Electrochimica Acta, 1995, 40(12), pp. 1963-1970
156. A.W.E Hodgson, S. Kurz, S. Virtanen, V. Fervel, C.O.A Olsson, S. Mischler," Passive and transpassive behaviour of CoCrMo in simulated biological solutions," Electrochim Acta, 20004, pp. 2167-2178

157. G.T Burnstien, A.J Davenport," The current-time relationship during anodic oxide film growth under high electric field," J.Electrochem.Soc, 1989, 136(4), pp. 936-941
158. Z. Wang, Y. Yan, L. Qiao," Nanocrystalline layer on the bearing surfaces of artificial hip implants induced by biotribocorrosion processes," Biosurface and Biotribology, 2015, 1, pp. 130 – 134
159. M. Bryant," Fretting-crevice corrosion of cemented metal on metal total hip replacements," PhD Thesis: University of Leeds, 2013
160. M. Biesinger, B. Payne, A. Grosvenor, L. Lau, A. Gerson, R. Smart," Resolving surface chemical states in XPS analysis of first row transition metals, oxides and hydroxides: Cr, Mn, Fe, Co and Ni," 2011, 257, pp. 2717-2730
161. M. Aronniemi, J. Sainio, J. Lahtinen," Chemical state quantification of iron and chromium oxides using XPS: the effect of the background subtraction method," Surface Science, 2005, 578, pp. 108-123
162. C.Vidal, A.I Munoz," Effect of thermal treatment and applied potential on the electrochemical behaviour of CoCrMo biomedical alloy," Electrochimica Acta, 2009, 54, pp. 1798-1809
163. H. Chen, Z. Qin, M. He, Y. Liu, Z. Wu," Application of electrochemical atomic force microscopy (EC-AFM) in the corrosion study of metallic materials," Materials, 2020, 13(3): 668
164. M. Jenko, M. Gorensek, M. Godec, M. Hodnik, B. Batic, C. Donik, J. Grant, D. Dolinar," Surface chemistry and microstructure of metallic biomaterials for hip and knee endoprostheses," Applied Surface Science, 2012, 427, pp. 584-593
165. H.M Ahmed, J.A Byrnem, W. Ahmed," Characteristic of silicon doped diamond like carbon thin films on surface properties and human serum albumin adsorption," Diam.Relat.Mat, 2015, 55, pp. 108-116
166. M. Tencer, R. Charbonneau, N. Lahoud," AFM study of BSA adlayers on Au stripes," Appl. Surf.Sci, 2007, 253, pp. 9209-9214
167. M.P Gispert, A. Serro, R. Colaco, B. Saramango," Bovine serum albumin adsorption onto 316L stainless steel and alumina: a comparative study using depletion protein radiolabeling quartz crystal microbalance and atomic force microscopy," Surf. Interface Anal, 2008, 40, pp. 1529-1537
168. X. Li, Y. Yan, H. Zhang, Y. Sum L. Qiao," Depassivation-repassivation behaviour of a CoCrMo alloy under tribological contact in simulated body fluids," Int. J. Electrochem. Sci, 2017, pp. 2495-2505

169. V.Maskiewicz, P. Williams, S. Prates, J. Bowsher, I. Clarke," Characterisation of protein degradation in serum-based lubrications during simulation wear testing of metal-on-metal hip prosthesis," J. Biomed Mater Res Part B: Appl Biomater, 2010, 94(2), pp. 429-440
170. O. Klok, A. Munoz, S. Mischler," An overview of serum albumin interactions with biomedical alloys," Materials, 2020, 13, pp. 1-26
171. A. Serro, M.P Gispert, M. Martins, P. Brogueira, R. Colaco, B. Saramago," Adsorption of albumin on prosthetic materials: implication for tribological behaviour," Journal of Biomedical Materials, 2006, pp. 581-589
172. P.V Dulm, W. Norde," The adsorption of human plasma albumin on solid surfaces with special attention to the kinetic aspects," J Colloid Interface Sci, 1983, 91, pp. 248-255
173. I. Smith, M. Baumann, L. McCabe," Electrostatic interactions as a predictor for osteoblast attachment to biomaterials," J Biomed Mater Res A, 2004, 70, pp. 436-441
174. C. Vidal, A.I. Munoz, C.A. Olsson, S. Mischler," Adsorption of BSA on passivated CoCrMo PVD Alloy: an EQCM and EXP investigation," J. The Electrochemical Society, 2014, pp. C294-C301
175. T. Miura, K. Suzuki, N. Kohata, H. Takeuchi," Metal binding modes of Alzheimer's amyloid β-peptide in insoluble aggregates and soluble complexes," Biochemistry, 2000, 39, pp. 7024-7031
176. H. Takeuchi," Raman structural markers of tryptophan and histidine side chains in proteins," Biopolymers, 2003, 72, pp. 305-317
177. J. Mesu, T. Visser, F. Soulimani, B. Wechhuvsern," Infrared and Raman spectroscopic study of pH-induced structural changes of L-histidine in an aqueous environment," Vibrational Spectroscopy, 2005, 30, pp. 114-125
178. A. Torreggiani, G. Navarra, A. Tinti, M. Di Foggia, V. Meilitello," Chemical and physical characterization of thermal aggregation of model proteins modulated by zinc(II) and copper(II) ions," Biomedical Spectroscopy and Imaging, 2016, 5, pp. 197-205
179. G. Ionita," Characterisation and tailoring the properties of hydrogels using spectroscopic methods," in Emerging Concepts in Analysis and Application of Hydrogels, IntechOpen, 2006, Ch. 3
180. A. Barth," Infrared spectroscopy of proteins," Biochimica et Biophysica Acta, 2007, 1767, pp. 1073-1101

181. I. Rybarek,” A guide through the dental dimethacrylate polymer network structural characterization and interpretation of physico-mechanical properties,” Materials, 2019,12, pp. 4047
182. Y. Deng, L. Ting, P. Neo, Y. Zhang, A. Peterson, B. Yeo,” Operando Raman spectroscopy of amorphous molybdenum sulfide (MoSx) during the electrochemical hydrogen evolution reaction: identification of sulfur atoms as catalytically active sites for H+ reduction,” American Chemical Society, 2016, 6, pp. 7790-7798
183. H. Goodwin,” Spin crossover in transition metal compounds II,” Top Curr Chem, 2004, 29, pp. 1750-1757
184. M. Sokolowska, M. Rylik, J. Pozanski, W. Bal,” Spectroscopic and thermodynamic determination of three distinct binding sites for Co(II) ions in human serum albumin,” Journal of Inorganic Biochemistry, 2009, 103, pp. 1005-1013
185. F. Arnold, J. Zhang,” Metal-mediated protein stabilization,” Trends in Biotechnology, 1994, 15(5), pp. 189-192
186. K. Suzuki, T. Miura, H. Takeuchi,” Inhibitory effect of copper(II) on zinc(II) induced aggregation of amyloid β-peptide,” Biochemical and Biophysical Research Communications, 2001, 285, pp. 981-996
187. J. Richardson, D. Richardson,” Natural beta-sheet proteins use negative design to avoid edge-to-edge aggregation,” Proc. Natl. Acad. Sci, 2002, 99, pp. 2754-2759
188. S. Asperger, B. Cizmek,” σ and π bonding modes of Pyridine and Imidazole type ligands in the transition states of their reactions with [Co(II) (protoporphyrin IX dimethyl ester)(MeO)(MeOH)] in Methanol,” Inorg. Chem,1996, 25, pp. 5232-5236
189. D. Wagman, W. Evans, I. Halow, V. Parker, S. Bailey, R. Schumm,” Selected values of chemical thermodynamic properties,” Nat. Bur. Stds, 1952
190. A. Stewart, C. Blindauer, S. Berezenko, D. Sleep, P. Sadler,” Interdomain zinc site on human albumin,” PNAS, 2003, 100(7), pp. 3701-3706
191. Y. Yan, A. Neville, D. Dowson, S. Williams,” Tribocorrosion in implants – assessing high carbon and low carbon Co-Cr-Mo alloys by in situ electrochemical measurements,” Tribology International, 2006, 29, pp. 1509-1517
192. M. Koronfel, A. Goode, J. Weker, S. Tay, C. Stitt, T. Simones, J. Frederick, W. Mosselmans, P. Quinn, R. Brydson, A. Hart, M. Toney,

A. Porter, M. Ryan," Understanding the reactivity of CoCrMo-implant wear particles," Materials Degradation, 8, 2018

193. Y. Liu, J. Gilbert," The effect of simulated inflammatory conditions and Fenton chemistry on the electrochemistry of CoCrMo alloy," J. Biomed Mater Res Part B, 106B, 2018, pp. 209 – 220
194. F. Hennig, H. Raithel, K. Schaller, J. Dohler," Nickel-, chrom-, and cobalt- concentrations in human tissue and body fluids of hip prosthesis patients," J. Trace Elem Electrolytes Health Dis, 1992, 6(4), pp. 239-243
195. J.P. Simpson, V. Geret, S.A. Brown, K. Merrit," Retrieved fracture plates: implant and tissue analysis," Implant Retrieval: Material and Biological Analysis, 1980, 13, pp. 395-442
196. R. Mendal, F. Bittner," Cell biology of molybdenum," Biochimica et Biophysica Acta, 2006, 1763, pp. 621-635
197. T.A. Simones, A.P. Brown, S.J. Milne, R.M.D Bryson," Bovine serum albumin binding to the CoCrMo nanoparticles and the influence of dissolution," Journal of Physics, 2015, 644
198. M. Lyvers, D. Bijukumar, A. Moore, P. Saboria, D. Royhamn, M. Wimmer, K. Shull, A. Mathew," Electrochemically induced tribolayer with molybdenum for hip implants: tribocorrosion and biocompatibility study," Thin Solid Films, 2017, 644, pp. 82-91
199. M.A. Wimmer, M. Laurent, M. Mathewm C. Nagellim Y. Liao, L. Marks, J. Jacobs, A. Fischer," The effect of contact load on CoCrMo wear and the formation and retention of tribofilms," Wear, 2015, 332-333, pp. 643-649
200. M.A. Wimmer, A. Fischer, R. Buscher, R. Pourzal, C.Sprecher, R. Hauert, J. Jacobs," Wear mechanisms in metal-on-metal bearings: the importance of tribochemical reaction layers," Journal of Orthopaedic Research, 2009, 28, pp. 436-443

Appendix – Image Reproduction Permissions

The use of several figures within this thesis required permissions, this section displays the approval documents obtained for use of these figures.

Figure 2.26 The major applications of biomaterials within the human body [3]

JOHN WILEY AND SONS LICENSE TERMS AND CONDITIONS

Jun 22, 2021

This Agreement between Mr. Blake Thornley ("You") and John Wiley and Sons ("John Wiley and Sons") consists of your license details and the terms and conditions provided by John Wiley and Sons and Copyright Clearance Center.

License Number	5066401095899
License date	May 12, 2021
Licensed Content Publisher	John Wiley and Sons
Licensed Content Publication	Materials and Corrosion
Licensed Content Title	Corrosion aspects of metallic implants — An overview
Licensed Content Author	J. M. F. Ferreira, A. H. S. Rebelo, G. Balossier, et al
Licensed Content Date	Nov 10, 2008
Licensed Content Volume	59
Licensed Content Issue	11
Licensed Content Pages	15
Type of Use	Dissertation/Thesis
Requestor type	University/Academic
Format	Print and electronic
Portion	Figure/table
Number of figures/tables	1
Will you be translating?	No
Title	Corrosion Behaviour of CoCrMo in Simulated Biological Environments
Institution name	University of Leeds
Expected presentation date	Jul 2021
Portions	Figure 1
Requestor Location	Mr. Blake Thornley 4 Belmont Drive Coalville, Leicestershire LE67 3LQ United Kingdom Attn: Mr. Blake Thornley
Publisher Tax ID	EU826007151
Total	**0.00 GBP**

Figure 2.27 Shows the components of an artificial hip replacement [12]

DM

Decker, Monica <mdecker@aaos.org>
Tue 18/05/2021 00:30
To: Blake Thornley [cm12bjt]

Dear Blake,

Your request for permission was forwarded to my attention, thank you. You have permission to use the image referenced below from OrthoInfo in your thesis provided that you use the following credit line:

Reproduced with permission from OrthoInfo. © American Academy of Orthopaedic Surgeons. https://orthoinfo.org/
Sincerely,
Monica Decker

AAOS
American Academy of Orthopaedic Surgeons
American Association of Orthopaedic Surgeons

Monica Decker
Compliance Specialist
Office of General Counsel
9400 West Higgins Road, Rosemont, IL 60018
847.384.4047
mdecker@aaos.org

BT

Blake Thornley [cm12bjt]
Wed 12/05/2021 10:29
To: orthoinforequests@aaos.org

Dear Sir/Madam,

I am writing to obtain permission to use the following Figure from your website within my thesis which I will be submitting later this year.

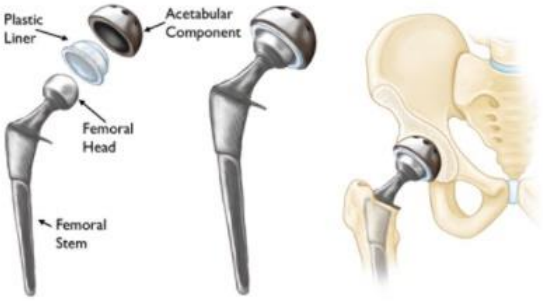

The article the Figure is from is 'Total Hip Replacement', the following is the caption I plan to use: Shows the components of an artificial hip replacement [12]
Where [12], is the reference to your website.

Thanks
Blake

Figure 2.28 Indicates the formation of a cystic lesion within a male patient by use of Coronal short tau inversion recovery magnetic resonance [45]

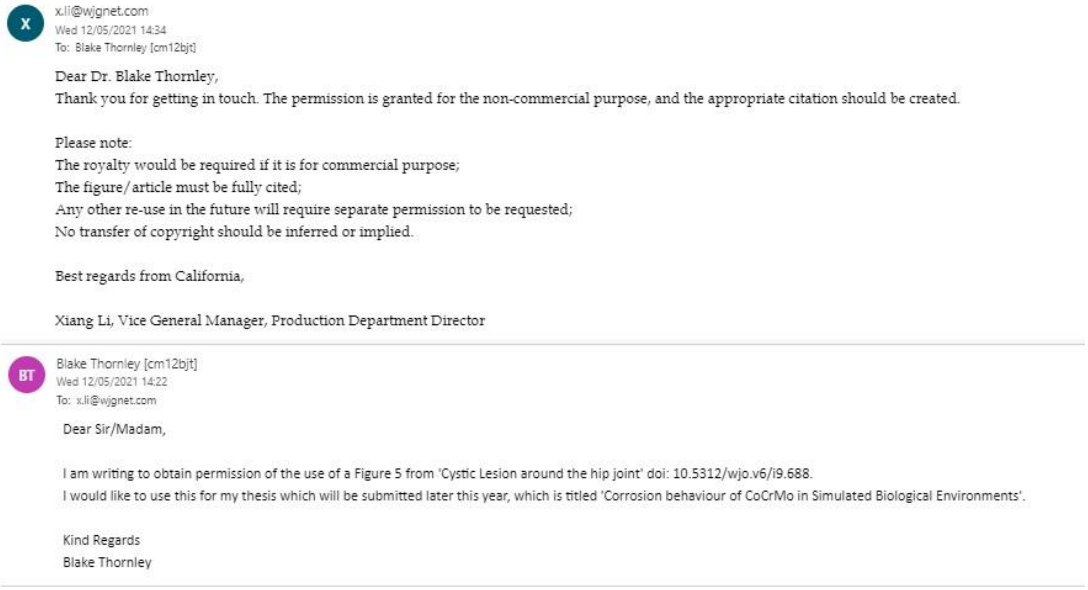

x.li@wjgnet.com
Wed 12/05/2021 14:34
To: Blake Thornley [cm12bjt]

Dear Dr. Blake Thornley,
Thank you for getting in touch. The permission is granted for the non-commercial purpose, and the appropriate citation should be created.

Please note:
The royalty would be required if it is for commercial purpose;
The figure/article must be fully cited;
Any other re-use in the future will require separate permission to be requested;
No transfer of copyright should be inferred or implied.

Best regards from California,

Xiang Li, Vice General Manager, Production Department Director

Blake Thornley [cm12bjt]
Wed 12/05/2021 14:22
To: x.li@wjgnet.com

Dear Sir/Madam,

I am writing to obtain permission of the use of a Figure 5 from 'Cystic Lesion around the hip joint' doi: 10.5312/wjo.v6/i9.688.
I would like to use this for my thesis which will be submitted later this year, which is titled 'Corrosion behaviour of CoCrMo in Simulated Biological Environments'.

Kind Regards
Blake Thornley

Figure 2.29 Schematic of an albumin molecule indicating the subdivision of HSA into domains (I, II and III) and subdomains (A and B) [63]

CCC | Marketplace™

This is a License Agreement between Blake Thornley ("You") and Royal Society of Chemistry ("Publisher") provided by Copyright Clearance Center ("CCC"). The license consists of your order details, the terms and conditions provided by Royal Society of Chemistry, and the CCC terms and conditions.
All payments must be made in full to CCC.

Order Date	12-May-2021	Type of Use	Republish in a thesis/dissertation
Order License ID	1118390-1	Publisher	ROYAL SOCIETY OF CHEMISTRY
ISSN	1742-2051	Portion	Image/photo/illustration

LICENSED CONTENT

Publication Title	Molecular bioSystems	Country	United Kingdom of Great Britain and Northern Ireland
Author/Editor	Royal Society of Chemistry (Great Britain)	Rightsholder	Royal Society of Chemistry
Date	06/01/2005	Publication Type	e-Journal
Language	English	URL	http://www.rsc.org/Publishing/Journals/m...

REQUEST DETAILS

Portion Type	Image/photo/illustration	Distribution	U.K. and Commonwealth (excluding Canada)
Number of images / photos / illustrations	1	Translation	Original language of publication
Format (select all that apply)	Electronic	Copies for the disabled?	No
Who will republish the content?	Publisher, not-for-profit	Minor editing privileges?	No
Duration of Use	Life of current edition	Incidental promotional use?	No
Lifetime Unit Quantity	Up to 499	Currency	GBP
Rights Requested	Main product		

NEW WORK DETAILS

Title	Corrosion Behaviour of CoCrMo in Simulated Biological Environments	Institution name	University of Leeds
Instructor name	Blake Thornley	Expected presentation date	2021-07-01

ADDITIONAL DETAILS

Order reference number	N/A	The requesting person / organization to appear on the license	Blake Thornley

REUSE CONTENT DETAILS

Title, description or numeric reference of the portion(s)	Figure 2	Title of the article/chapter the portion is from	NA
Editor of portion(s)	NA	Author of portion(s)	Royal Society of Chemistry (Great Britain)
Volume of serial or monograph	NA	Issue, if republishing an article from a serial	N/A
Page or page range of portion	19	Publication date of portion	2005-06-01

Figure 2.30 Shows the formation of a biofilm on the surface of a metal [82]

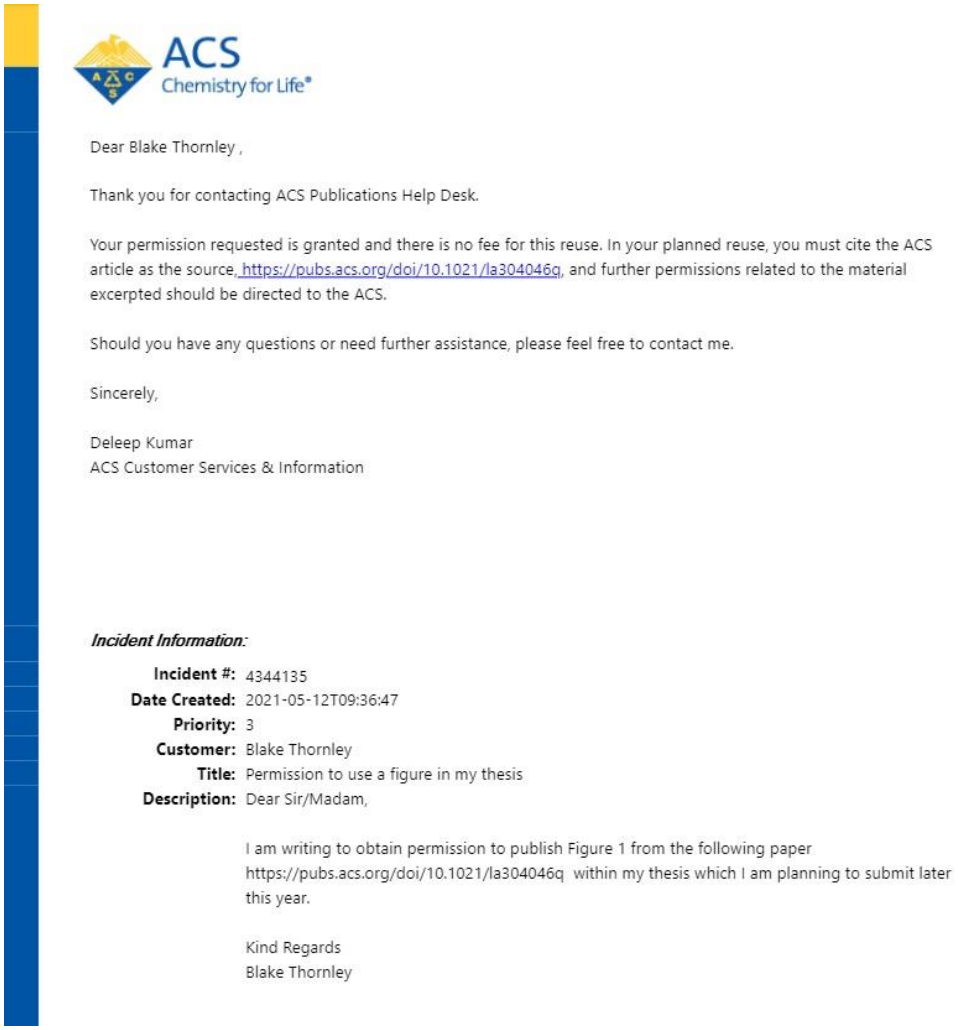

ACS Chemistry for Life®

Dear Blake Thornley ,

Thank you for contacting ACS Publications Help Desk.

Your permission requested is granted and there is no fee for this reuse. In your planned reuse, you must cite the ACS article as the source, https://pubs.acs.org/doi/10.1021/la304046q, and further permissions related to the material excerpted should be directed to the ACS.

Should you have any questions or need further assistance, please feel free to contact me.

Sincerely,

Deleep Kumar
ACS Customer Services & Information

Incident Information:

Incident #: 4344135
Date Created: 2021-05-12T09:36:47
Priority: 3
Customer: Blake Thornley
Title: Permission to use a figure in my thesis
Description: Dear Sir/Madam,

I am writing to obtain permission to publish Figure 1 from the following paper https://pubs.acs.org/doi/10.1021/la304046q within my thesis which I am planning to submit later this year.

Kind Regards
Blake Thornley

Figure 2.31 Effect of temperature and quantity of BSA on the corrosion rate of CoCrMo (Arrhenius plot) [88]

ELSEVIER LICENSE
TERMS AND CONDITIONS

Jun 22, 2021

This Agreement between Mr. Blake Thornley ("You") and Elsevier ("Elsevier") consists of your license details and the terms and conditions provided by Elsevier and Copyright Clearance Center.

License Number	5066510809558
License date	May 12, 2021
Licensed Content Publisher	Elsevier
Licensed Content Publication	Colloids and Surfaces B: Biointerfaces
Licensed Content Title	Adsorption of bovine serum albumin on CoCrMo surface: Effect of temperature and protein concentration
Licensed Content Author	C. Valero Vidal,A. Olmo Juan,A. Igual Muñoz
Licensed Content Date	Oct 1, 2010
Licensed Content Volume	80
Licensed Content Issue	1
Licensed Content Pages	11
Start Page	1
End Page	11
Type of Use	reuse in a thesis/dissertation
Portion	figures/tables/illustrations
Number of figures/tables/illustrations	1
Format	both print and electronic
Are you the author of this Elsevier article?	No
Will you be translating?	No
Title	Corrosion Behaviour of CoCrMo in Simulated Biological Environments
Institution name	University of Leeds
Expected presentation date	Jul 2021
Portions	Figure 8
Requestor Location	Mr. Blake Thornley 4 Belmont Drive Coalville, Leicestershire LE67 3LQ United Kingdom Attn: Mr. Blake Thornley
Publisher Tax ID	GB 494 6272 12
Total	**0.00 GBP**

Figure 2.32 Potentiodynamic curves depicting the effects of albumin on the corrosion potential of CoCrMo in NaCl and PBS solutions [100].

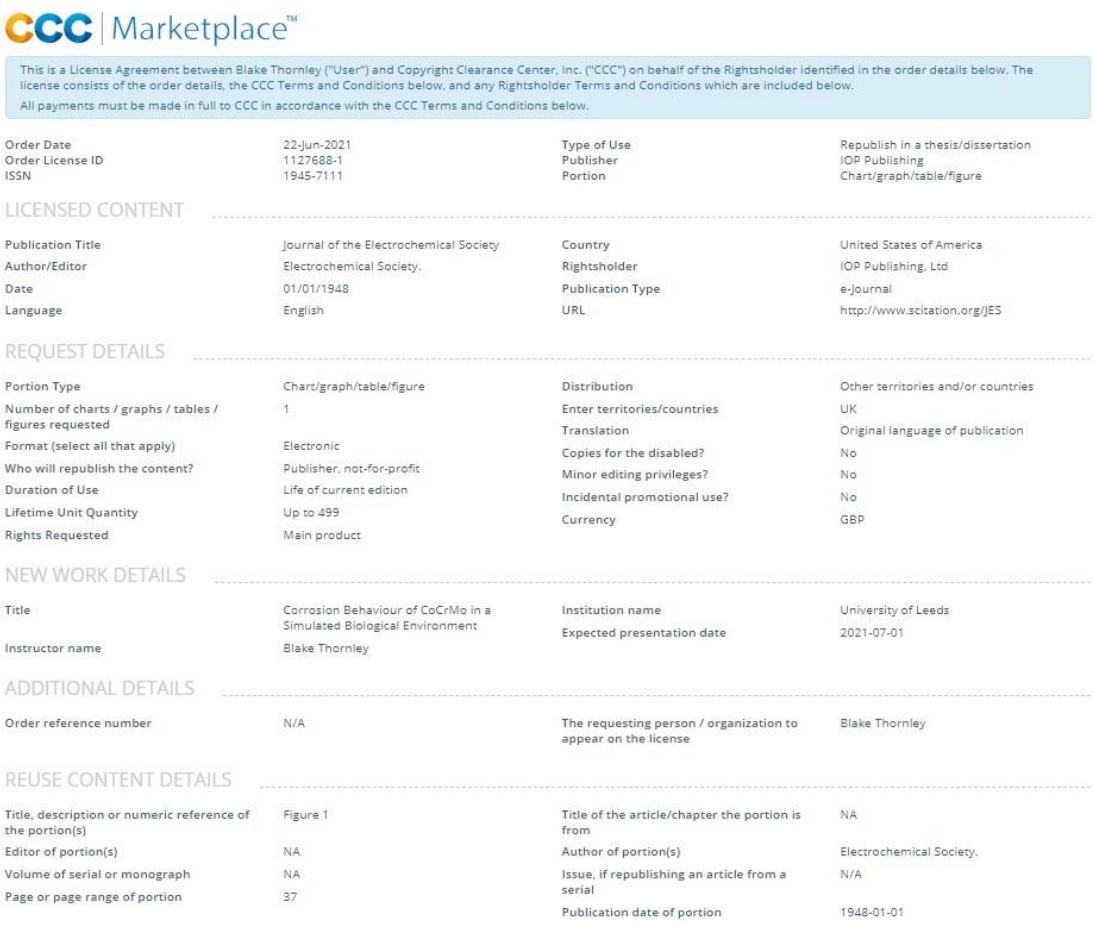

CCC | Marketplace™

This is a License Agreement between Blake Thornley ("User") and Copyright Clearance Center, Inc. ("CCC") on behalf of the Rightsholder identified in the order details below. The license consists of the order details, the CCC Terms and Conditions below, and any Rightsholder Terms and Conditions which are included below.

All payments must be made in full to CCC in accordance with the CCC Terms and Conditions below.

Order Date	22-Jun-2021	Type of Use	Republish in a thesis/dissertation
Order License ID	1127688-1	Publisher	IOP Publishing
ISSN	1945-7111	Portion	Chart/graph/table/figure

LICENSED CONTENT

Publication Title	Journal of the Electrochemical Society	Country	United States of America
Author/Editor	Electrochemical Society.	Rightsholder	IOP Publishing, Ltd
Date	01/01/1948	Publication Type	e-Journal
Language	English	URL	http://www.scitation.org/JES

REQUEST DETAILS

Portion Type	Chart/graph/table/figure	Distribution	Other territories and/or countries
Number of charts / graphs / tables / figures requested	1	Enter territories/countries	UK
		Translation	Original language of publication
Format (select all that apply)	Electronic	Copies for the disabled?	No
Who will republish the content?	Publisher, not-for-profit	Minor editing privileges?	No
Duration of Use	Life of current edition	Incidental promotional use?	No
Lifetime Unit Quantity	Up to 499	Currency	GBP
Rights Requested	Main product		

NEW WORK DETAILS

Title	Corrosion Behaviour of CoCrMo in a Simulated Biological Environment	Institution name	University of Leeds
		Expected presentation date	2021-07-01
Instructor name	Blake Thornley		

ADDITIONAL DETAILS

Order reference number	N/A	The requesting person / organization to appear on the license	Blake Thornley

REUSE CONTENT DETAILS

Title, description or numeric reference of the portion(s)	Figure 1	Title of the article/chapter the portion is from	NA
Editor of portion(s)	NA	Author of portion(s)	Electrochemical Society.
Volume of serial or monograph	NA	Issue, if republishing an article from a serial	N/A
Page or page range of portion	37	Publication date of portion	1948-01-01

Figure 2.33 Typical anodic dissolution behaviour of an active-passive metal [25]

ELSEVIER LICENSE
TERMS AND CONDITIONS

Jun 22, 2021

This Agreement between Mr. Blake Thornley ("You") and Elsevier ("Elsevier") consists of your license details and the terms and conditions provided by Elsevier and Copyright Clearance Center.

License Number	5066520050395
License date	May 12, 2021
Licensed Content Publisher	Elsevier
Licensed Content Publication	Orthopaedics and Trauma
Licensed Content Title	Corrosion and mechanical properties
Licensed Content Author	M. Bryant,A. Neville
Licensed Content Date	Jun 1, 2016
Licensed Content Volume	30
Licensed Content Issue	3
Licensed Content Pages	16
Start Page	176
End Page	191
Type of Use	reuse in a thesis/dissertation
Portion	figures/tables/illustrations
Number of figures/tables/illustrations	1
Format	both print and electronic
Are you the author of this Elsevier article?	No
Will you be translating?	No
Title	Corrosion Behaviour of CoCrMo in Simulated Biological Environments
Institution name	University of Leeds
Expected presentation date	Jul 2021
Portions	Figure 6
Requestor Location	Mr. Blake Thornley 4 Belmont Drive Coalville, Leicestershire LE67 3LQ United Kingdom Attn: Mr. Blake Thornley
Publisher Tax ID	GB 494 6272 12
Total	**0.00 GBP**

Fig 3.2, 3.5, 3.8, 4.1a, 4.11, 4.12, 4.16, 4.20, 4.21, 4.22, 5.19, 5.20, 8.2

Table 4.1, 4.4, 4.6, 4.8, 6.8.

B. Thornley, R. Beadling, M. Bryant, A. Neville," Investigation of the repassivation process of CoCrMo in simulated biological fluids," Corrosion, 2020, 76, pp. 538-552 [125]

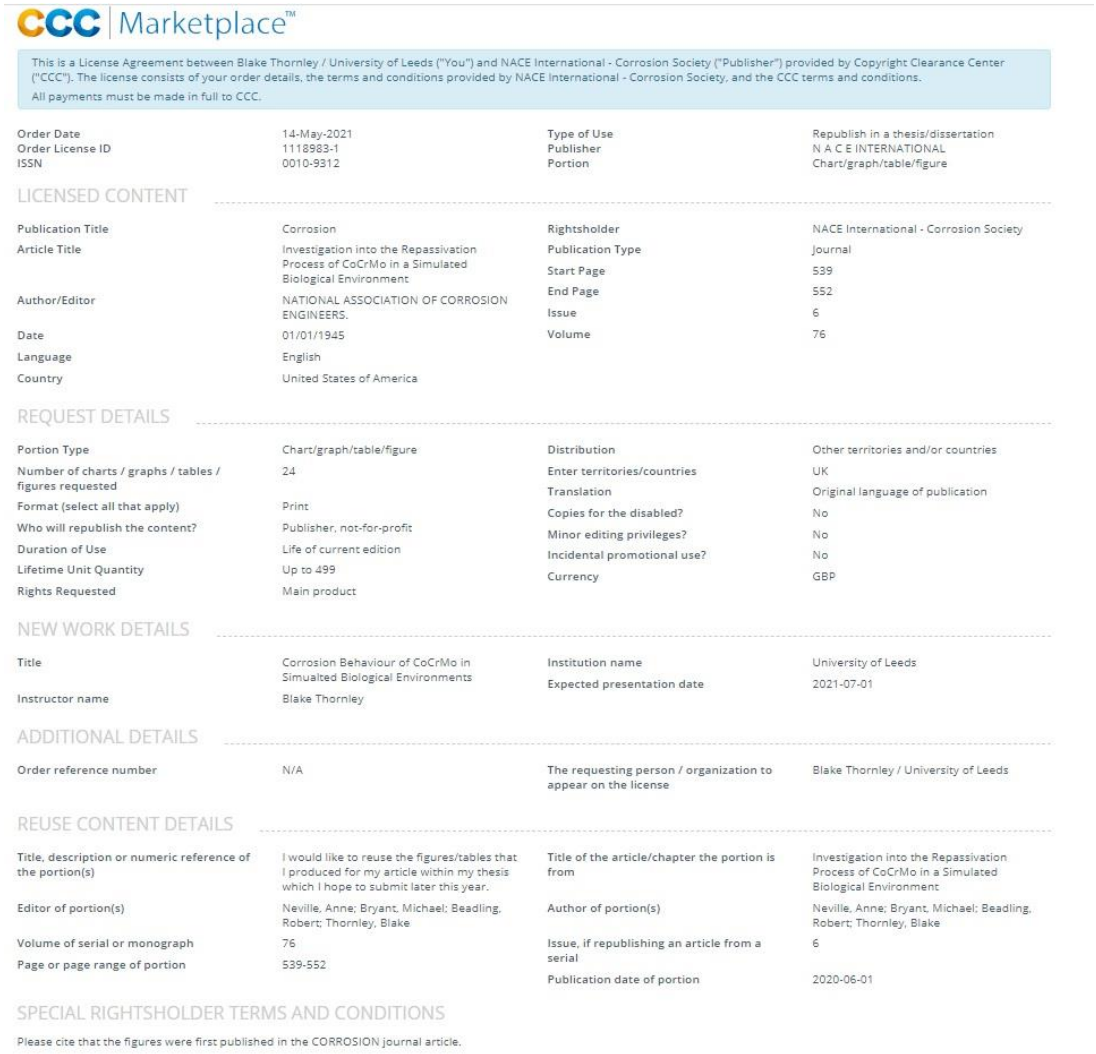

CCC Marketplace™

This is a License Agreement between Blake Thornley / University of Leeds ("You") and NACE International - Corrosion Society ("Publisher") provided by Copyright Clearance Center ("CCC"). The license consists of your order details, the terms and conditions provided by NACE International - Corrosion Society, and the CCC terms and conditions.

All payments must be made in full to CCC.

Order Date	14-May-2021	Type of Use	Republish in a thesis/dissertation
Order License ID	1118983-1	Publisher	N A C E INTERNATIONAL
ISSN	0010-9312	Portion	Chart/graph/table/figure

LICENSED CONTENT

Publication Title	Corrosion	Rightsholder	NACE International - Corrosion Society
Article Title	Investigation into the Repassivation Process of CoCrMo in a Simulated Biological Environment	Publication Type	Journal
		Start Page	539
Author/Editor	NATIONAL ASSOCIATION OF CORROSION ENGINEERS.	End Page	552
		Issue	6
Date	01/01/1945	Volume	76
Language	English		
Country	United States of America		

REQUEST DETAILS

Portion Type	Chart/graph/table/figure	Distribution	Other territories and/or countries
Number of charts / graphs / tables / figures requested	24	Enter territories/countries	UK
		Translation	Original language of publication
Format (select all that apply)	Print	Copies for the disabled?	No
Who will republish the content?	Publisher, not-for-profit	Minor editing privileges?	No
Duration of Use	Life of current edition	Incidental promotional use?	No
Lifetime Unit Quantity	Up to 499	Currency	GBP
Rights Requested	Main product		

NEW WORK DETAILS

Title	Corrosion Behaviour of CoCrMo in Simualted Biological Environments	Institution name	University of Leeds
		Expected presentation date	2021-07-01
Instructor name	Blake Thornley		

ADDITIONAL DETAILS

Order reference number	N/A	The requesting person / organization to appear on the license	Blake Thornley / University of Leeds

REUSE CONTENT DETAILS

Title, description or numeric reference of the portion(s)	I would like to reuse the figures/tables that I produced for my article within my thesis which I hope to submit later this year.	Title of the article/chapter the portion is from	Investigation into the Repassivation Process of CoCrMo in a Simulated Biological Environment
Editor of portion(s)	Neville, Anne; Bryant, Michael; Beadling, Robert; Thornley, Blake	Author of portion(s)	Neville, Anne; Bryant, Michael; Beadling, Robert; Thornley, Blake
Volume of serial or monograph	76	Issue, if republishing an article from a serial	6
Page or page range of portion	539-552	Publication date of portion	2020-06-01

SPECIAL RIGHTSHOLDER TERMS AND CONDITIONS

Please cite that the figures were first published in the CORROSION journal article.

Figure 3.22 EELS spectra for the standard amorphous carbon spectrum [109]

ELSEVIER LICENSE TERMS AND CONDITIONS

Jun 22, 2021

This Agreement between Mr. Blake Thornley ("You") and Elsevier ("Elsevier") consists of your license details and the terms and conditions provided by Elsevier and Copyright Clearance Center.

License Number	5066530709366
License date	May 12, 2021
Licensed Content Publisher	Elsevier
Licensed Content Publication	Tribology International
Licensed Content Title	Characterisation of the oxide film on the taper interface from retrieved large diameter metal on polymer modular total hip replacements
Licensed Content Author	P. Zeng,W.M. Rainforth,R.B. Cook
Licensed Content Date	Sep 1, 2015
Licensed Content Volume	89
Licensed Content Issue	n/a
Licensed Content Pages	11
Start Page	86
End Page	96
Type of Use	reuse in a thesis/dissertation
Portion	figures/tables/illustrations
Number of figures/tables/illustrations	1
Format	both print and electronic
Are you the author of this Elsevier article?	No
Will you be translating?	No
Title	Corrosion Behaviour of CoCrMo in Simulated Biological Environments
Institution name	University of Leeds
Expected presentation date	Jul 2021
Portions	Figure 5b
Requestor Location	Mr. Blake Thornley 4 Belmont Drive Coalville, Leicestershire LE67 3LQ United Kingdom Attn: Mr. Blake Thornley
Publisher Tax ID	GB 494 6272 12
Total	**0.00 GBP**

Figure 3.23 Schematic of the XPS process [136]

JOHN WILEY AND SONS LICENSE TERMS AND CONDITIONS

Jun 22, 2021

This Agreement between Mr. Blake Thornley ("You") and John Wiley and Sons ("John Wiley and Sons") consists of your license details and the terms and conditions provided by John Wiley and Sons and Copyright Clearance Center.

License Number	5066530971096
License date	May 12, 2021
Licensed Content Publisher	John Wiley and Sons
Licensed Content Publication	Wiley Books
Licensed Content Title	Comparison of XPS and AES with Other Analytical Techniques
Licensed Content Date	Jan 28, 2005
Licensed Content Pages	10
Type of Use	Dissertation/Thesis
Requestor type	University/Academic
Format	Print and electronic
Portion	Figure/table
Number of figures/tables	1
Will you be translating?	No
Title	Corrosion Behaviour of CoCrMo in Simulated Biological Environments
Institution name	University of Leeds
Expected presentation date	Jul 2021
Portions	XPS Process
Requestor Location	Mr. Blake Thornley 4 Belmont Drive Coalville, Leicestershire LE67 3LQ United Kingdom Attn: Mr. Blake Thornley
Publisher Tax ID	EU826007151
Total	**0.00 GBP**

Figure 3.24 Obtained CD spectra for a 100% content of α-helix (-), β-strand (--) and irregular (..) [142]

OXFORD UNIVERSITY PRESS LICENSE TERMS AND CONDITIONS

Jun 22, 2021

This Agreement between Mr. Blake Thornley ("You") and Oxford University Press ("Oxford University Press") consists of your license details and the terms and conditions provided by Oxford University Press and Copyright Clearance Center.

License Number	5066531501028
License date	May 12, 2021
Licensed Content Publisher	Oxford University Press
Licensed Content Publication	Bioinformatics
Licensed Content Title	CAPITO—a web server-based analysis and plotting tool for circular dichroism data
Licensed Content Author	Wiedemann, Christoph; Bellstedt, Peter
Licensed Content Date	May 15, 2013
Type of Use	Thesis/Dissertation
Institution name	
Title of your work	Corrosion Behaviour of CoCrMo in Simulated Biological Environments
Publisher of your work	University of Leeds
Expected publication date	Jul 2021
Permissions cost	0.00 GBP
Value added tax	0.00 GBP
Total	**0.00 GBP**
Title	Corrosion Behaviour of CoCrMo in Simulated Biological Environments
Institution name	University of Leeds
Expected presentation date	Jul 2021
Portions	Figure 1
Requestor Location	Mr. Blake Thornley 4 Belmont Drive Coalville, Leicestershire LE67 3LQ United Kingdom Attn: Mr. Blake Thornley
Publisher Tax ID	GB125506730
Total	**0.00 GBP**